Improved Modelling and Implementation Guidance of Energy Dissipation Devices

by

Robin Xie

Supervised by

Professor Geoffrey Rodgers

Professor Timothy Sullivan

Associate Professor Gregory MacRae

A thesis submitted for the degree of

Doctor of Philosophy

in Earthquake Engineering

at the University of Canterbury, Christchurch, New Zealand

2019

ABSTRACT

There is a range of innovative energy dissipation method available to modify the seismic response of both new and existing structures. Viscous damper and friction brace are two well-known types of energy dissipators that have attracted interests from practitioners and researchers for many years. However, current design methodologies for friction braces rely on the past experimental results that were carried out at a component level, and current viscous damper design frameworks do not specifically consider the flexibility of the damper system and connections. Such design approaches may be considered as unconservative and can cause the devices to behave different than expected under large load reversals. This thesis presents the findings of the research carried out to achieve better understanding in the energy dissipation mechanism of friction braces and viscous dampers, which lead to an improved design frame for structures equipped with friction braces and viscous dampers.

Quasi-static testing of Asymmetrical Friction Connection (AFC) and Symmetrical Friction Connection (SFC) braces was conducted. The braces were tested alone, where an axial load was applied directly to the specimens, as well as within a one storey full scale steel frame. It was found that the friction braces developed stable sliding behaviour with repeatable hysteresis loops. The average effective friction coefficient of 0.18 for the AFC braces and 0.31 for the SFC braces. It was also found that due to bolt slackening and surface degradation, the maximum strength degradation in the AFC and SFC braces was 10% and 15%, respectively. Additionally, frame compatibility actions caused brace bending in-plane with bolt bearing on the slotted hole sides, and prying and p-delta effect caused bracing member to deform out-of-plane. Based on the observed mechanisms of AFC and SFC within a bracing system, a simplified numerical hysteresis model has been developed as a part of this thesis and implemented into OpenSees as a tool to approximate the hysteretic behaviour of a friction connection.

The inherent elastic flexibility of viscous dampers can alter the phasing of damper and structural forces. This thesis also investigates how damper sub-system stiffness affects overall seismic response. By undertaking a suite of analyses with damped single degree-of-freedom systems it is shown that a damper with significant flexibility can experience median peak displacements 40% higher than those of a damper with rigid support, depending on the added damping, damper sub-system stiffness, and period of vibration. To limit the impact of phasing

effects, the damper sub-system stiffness should be five to ten times the stiffness of the main lateral load resisting system. A design example has been carried out to present how the damper sub-system to main structure lateral stiffness ratio can be calculated. Additionally, a modified design frame has been proposed as a part of this study to account for damper sub-system stiffness.

ACKNOWLEDGEMENT

First, I want to acknowledge my supervisors, Prof. Geoff Rodgers, A. Prof. Timothy Sullivan, and A. Prof. Gregory MacRae at the University of Canterbury. Thank you for giving me the opportunity to pursuit such high academic achievement. As well as for the opportunities to present my work at various conferences. I could not have been where I am without your invaluable guidance, support and encouragement. I want to acknowledge my mentor Jose Chanchi for his assistance and guidance in the early years of my postgraduate study. Man thanks to the technical staff at the University of Canterbury Structures Laboratory who provided me a tremendous amount of help in setting up of my experimental specimens, Mosese Fifita, Stuart Toase, John Maley, Alan Poynter, and Russell McConchie, also thanks for keeping me safe and alive, and entertained during my time working with you. To Dr. Tony Abu, and Dr. Chris McGann who appointed me as their senior tutor. Thank you for your trust in me and the help you have provided outside of my postgraduate studies. My colleagues/mentors/friends, Trevor Yeow and T.L. Chang, who are the first go-to persons whenever I am stuck. Thank you for your patience with me and never get tired of answering my questions. My gratitude also extends to Elizabeth Ackermann, the mother of the department. No one can truly survive through postgraduates without you. I would also acknowledge the kind technical support from Francois Bissey at UC HPC.

This project is supported by QuakeCoRE, a New Zealand Tertiary Education Commission-funded Centre, through QuakeCoRE Flagship 4 research funding. The QuakeCoRE publication number is 0460. Acknowledgement is also extended to MBIE Natural Hazard Research Platform (NHRP) and John Jones Steel for their support of this study.

To my parents, thank you for putting food on my plate and roof over my head growing up, and the sacrifice you had to make to ensure I lived through my childhood and teenage years comfortably, and thank you for providing me the opportunity to study and live abroad.

To my partner, Maija Kosinanonth, thank you for your support, understanding and encouragement in life. Thank you for walking me through the ups and downs over the past years. I am grateful that I have you as my co-pilot. I would also like to extend my gratitude to Maija's family for providing me a comfortable place as I finalise this thesis. Thanks to the cats for keeping me company day and night, and not sitting on my laptop as I scramble.

To my friends and colleagues throughout my undergraduate and postgraduate years, T.L.C, Trevor Yeow, Ali Rad, Nikoo Hazaveh, Tushar Chaudhari, Mahdi Hatami, Ribu Dhakal, Karim Tarbali, Dennis Pau, Claudio Cappellaro, Lee Huang, Ben Fu, Shannon Brown, Steff Booth and many more. Thank you for your company, entertainment and wisdom over the years. The E303 boys - Ethan Thomson, Robin Lee, and Xavier Bellagamba, it was a pleasure to share an office with you. Best thing to know is we will always have stories to tell over a pint.

Finally, to my whānau at The Lion Pit, Liam Giles, Andy Spice and the rest of the WOF2 boys, Stacey Te Kuru, Navajo Stirling, Big Junior, Ninos Mikhaeil, Jordan Smart, George Roberts, Mohi Wahi, Shiva Mishra, Regy Yamat, Emilia Sa'u, Paul Wolf, Ata Fakalelu, Pou Sefesi, Rian Rees, Sarah Jones, and everyone else whom I have shared the mat with. You have no idea how much you have helped me in life. Thank you for keeping me humble and sane.

"Be grateful with everything you have and you will be successful in everything you do."

- Conor McGregor

To a better tomorrow

Table of Contents

List of Figures

List of Tables

1. INTRODUCTION

1.1. Motivation

Most current earthquake design standards around the world aim primarily to prevent life loss during a design level seismic event. Although adequate conventional capacity design can help provide life safety during severe seismic events, significant structural and non-structural damage may occur [Cook, 2018]. The structures designed according to such standards may be referred to as being "damage-prone" under such shaking and they may have to be repaired or demolished, there may be significant repair costs and associate downtime [Elwood *et al.*, 2015].

Recent building designs have adopted a range of innovative new energy dissipation techniques to modify the seismic response of both new and existing structures [MacRae, 2008]. Therefore, yielding of major structural components can be prevented during design level earthquakes. Structures that are designed by using such techniques are often called "low damage" structures in New Zealand. They are expected to undergo very limited damage and return to service shortly after design level events. Such low-damage structures may include those with viscous dampers, those with friction dissipaters, those on base isolators, and those that have strong components to minimise yielding. Structures with easily replaceable energy dissipating elements are also more desirable than traditional yielding structures, as they may be reinstated faster. Facilitating the appropriate design and uptake of these new energy dissipation methods in the field is the ultimate goal of this research, so as to have a meaningful impact and mitigate seismic risk. Several tranches of research are required to provide a clear implementation pathway and enable wider uptake of these energy dissipation mechanisms.

Bracing systems are effective in improving the lateral capacity of a frame. Bracing systems that are equipped with energy dissipators can add strength to a structure and allow non-linear and ductile response within the bracing system to provide energy dissipation mechanisms. Energy dissipation devices such as viscous dampers and friction devices can be easily implemented into bracing systems. Bracing systems equipped with these two devices currently appear to be popular among researchers and practitioners in most seismic regions around the world, and they are considered as potential robust low damage solutions for new structures and retrofitting strategies for existing structures. Therefore, for this research, the focus will be placed on friction braces and viscous dampers devices.

New Zealand has already seen viscous dampers and friction devices being implemented into modern structural designs to create cost-effective systems that are easily repairable and expected to undergo no or little damage during a design earthquake. [Pettinga *et. al,* 2013, Gledhilll *et al.,* 2008]. However, practitioners often struggle with their current design frameworks due to lack of understandings in their energy dissipation mechanisms, and often unconservative assumptions are made. Therefore, there is a need to conduct more detailed studies on the viscous dampers and friction braces to obtain better understandings in their mechanisms. As a result, better guidance can be provided on the design and modelling of viscous damper and friction braces to improve the uptake of these two devices, and to help ensure and optimise outcome in a typical structures and innovative retrofit strategies.

1.2. Literature review

1.2.1. Conventional braces

In a conventional design strategy, concentric steel bracing system is considered as the cost-effective solution to provide lateral restraints of a structure under earthquake and wind loadings. By adding a bracing system to frame, the brace could significantly improve the lateral strength and stiffness of the frame without adding a substantial amount of structural weight Chimeh & Homami [2012]. There are many forms of concentrically braced frames and a few examples are presented in Figure 1-1 below.

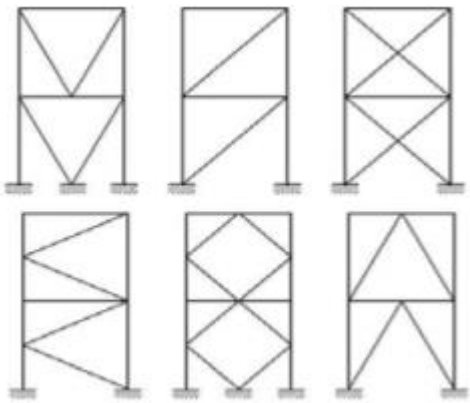

Figure 1-1. Examples of concentrically braced frame [Chimeh & Homami, 2012]

However, under large compressive axial force, the conventional bracing members are prone to buckling, which induces unbalanced force in the adjacent beam, as well as produces a hysteresis profile that is asymmetrical as shown in Figure 1-2 below. This behaviour indicates

a steel brace behaves much better in tension than in compression due to the effect of local buckling as illustrated in Figure 1-2 below. Therefore, a poorly designed brace layout could result a building to be strong in one direction but much weaker in the other direction. Although the yielding of braces offers some energy dissipation mechanism to the structure, and damage is most likely localised within the bracing system, but conventional braces are not easily replaceable components and repairs often come at a substantial cost.

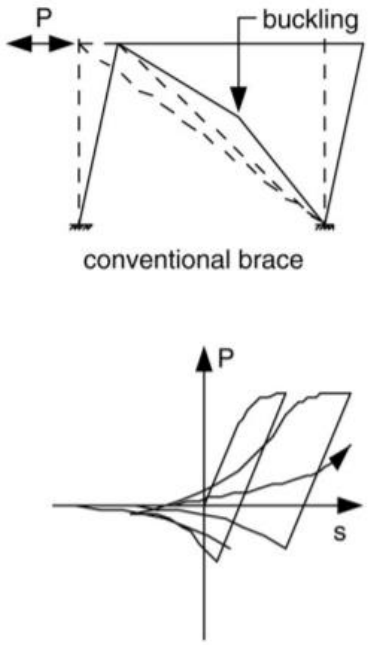

Figure 1-2. Nonlinear hysteretic behavior of a conventional brace [Xie et al., 2005]

Another approach to achieve adequate performance while using conventional bracing system is not by relying on the nonlinear behaviour of the braces, but instead by increasing the strength of the braces so they can remain elastic under design load. Such design strategy allows a structure to avoid any permanent damage and residual stress during and after a design level earthquake [Buchanan *et al.*, 2011]. However, the elastic design approach could be significantly more expensive than a basic design where yielding in braces is allowed. Additionally, adding such a strong bracing system could see a substantial increase in the stiffness of a structure which leads to an increase in demand in the building foundations. Therefore, the elastic design approach could be extremely difficult to be carried out as a retrofit strategy for existing structures, as it could require strengthening work to be done on the existing foundations.

1.2.2. Buckling-restrained braces (BRB)

To mitigate the short-coming of a conventional steel brace described in the previous section, buckling-restrained brace (BRB) has been introduced as a bracing system that can achieve equal hysteresis profile in both tension and compression zones. Such hysteresis profile is achieved by restraining the buckling of a steel bracing member by a buckling restraining unit that surrounds the bracing member. An idealised BRB nonlinear hysteretic behaviour under load reversals is shown in *Figure 1-3* below where the BRB has the same stiffness and maximum strength in the tension and compression quarters. Over the past decades, frames equipped with BRBs have become a popular choice as a lateral load resisting system in seismic regions, especially in Japan for their adequate performance in earthquakes [Xie *et al.*, 2005].

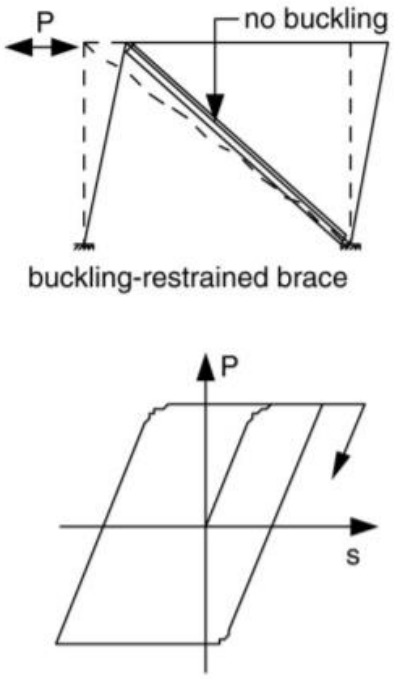

Figure 1-3. Nonlinear hysteretic behavior of a buckling-restrained brace [Xie et al., 2005]

Sabelli *et. al.*, [2003] has provided a few examples of a BRB layout as shown in Figure 1-4. In general, a BRB comprises a ductile metal core that is slotted through a continuous steel tube that is filled with concrete or mortar. For such configuration, unbonding material is used between the steel core and the infill material to allow the steel core to deform freely under axial load reversals. When the BRB is under compression, the buckling of the steel core is restricted by the infill material and the steel core.

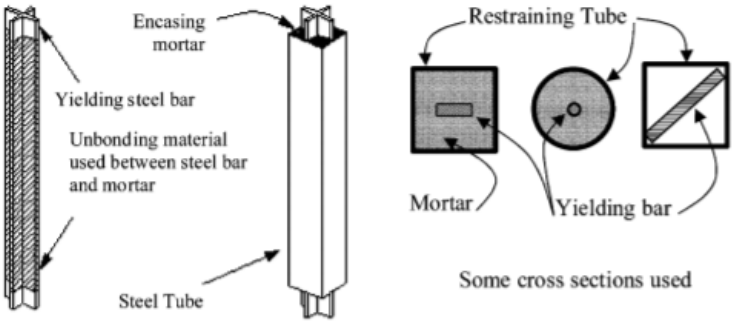

Figure 1-4. BRB layout [Sabelli et al., 2003]

However, BRBs often require strong end connections due to the high overstrength of the BRB. The transition segments at both ends need to be designed to behave elastically under the maximum design load of the BRB to avoid out-of-plane buckling deformations. The adjacent beams to the bracing system need to have enough capacity to resist the moment demands transferred from the BRB if bolted end connections are used [Wijanto, 2012]. Additionally, low cycle fatigue, 3D performance, and gusset designs are the main issues of structures equipped with BRB systems [MacRae and Clifton, 2015]. Currently there is insufficient testing and analysis of BRB systems under realistic earthquake demands and multi-directional loading [Cook, 2018].

1.2.3. Friction braces

Low damage solutions involving friction devices have been tested in steel moment resisting frame beam-to-column joints [Christopoulos *et al.*, 2002, Clifton, 2005, MacRae *et al.*, 2010, Latour *et al.*, 2015, Cavallaro *et al.*, 2018], and in base connections [Borzouie *et al.*, 2014]. Friction braces are braces equipped with friction devices, which dissipate seismic energy through frictional sliding at the interfaces of two or more elements. Friction connections may (i) be easy and fast to construct, (ii) be economical to apply to structures, (iii) have a high initial (pre-sliding) stiffness, (iv) have some dynamic recentring characteristics, (v) have components that are easily replaced, and they (vi) may dissipate significant amounts of energy [MacRae *et al.*, 2010].

Asymmetrical Friction Connection (AFC) and Symmetrical Friction Connection (SFC) are two types of friction devices that may be suitable for the bracing system of a structural frame. These two friction devices both consist of several plates that are clamped together by means of high tensile bolts, and long slots are cut on the plate that transfers external load through the

connection details, this plate can be identified as a slotted plate. A fixed plate is often used to connect the friction connection to a primary structure component such as a column, beam or a bracing member. Once the external load overcomes the clamping force provided by the bolts, the slotted plate can slide for a distance that equals the length of the slots with minimal increments in force. The key difference between an AFC and an SFC is that an AFC has an asymmetrical alignment, so when the load is applied at the centreline of the slotted plate, it is transferred eccentrically from the slotted plate to the fixed plate and then to the adjacent structural component. The eccentricity induces a moment in the AFC, which can cause the AFC and the adjacent sub-system to deflect out-of-plane. Conversely, an SFC adopts a symmetrical alignment so the external force can be transferred concentrically from the slotted plate to the structural component that the SFC is attached to. Simple illustrations that highlight the key features of an AFC and SFC are presented in Figure 1-5 below.

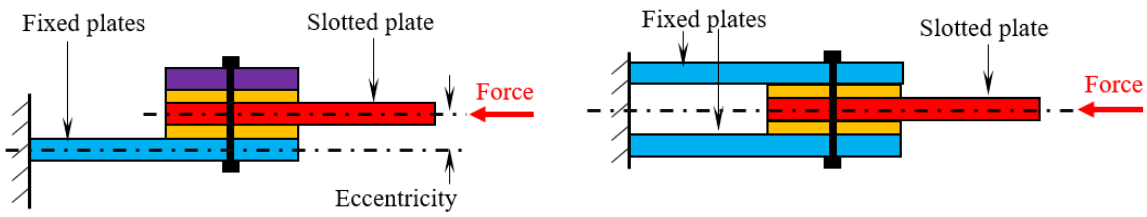

a. AFC b. SFC

Figure 1-5. Illustrations of AFC and SFC

The Asymmetrical Friction Connection (AFC) was first proposed as an energy dissipater for steel moment resisting frames on the bottom flange of steel beams at the column face by Clifton [2005]. This AFC configuration was referred to as the Sliding Hinge Joint (SHJ). In the SHJ, energy dissipation occurs as the column rotates relative to the beam end overcoming the friction resistance from the clamping force provided by the bolts. A sliding friction connection allow beam rotation, in place of the formation of a plastic hinge within the beam. Tests of the connection subassembly, as well as beam-column joints equipped with this type of connection, have demonstrated that this technology can reliably dissipate energy with little damage to the major structural elements [MacRae *et al.*, 2010].

SHJ has been implemented in several New Zealand buildings, including a steel multi-storey student accommodation building in Welllington, New Zealand [Gledhill *et al.*, 2008]. In this building, SHJ's are used between columns, foundations and within beams to achieve a cost-

effective solution for a Damage Avoidance system, which should be designed to withstand a severe earthquake with minimal and repairable damage.

Tests of AFC components by Chanchi *et al*., [2013] with high hardness shims, such as Bisalloy 400 and Bisalloy 500 (with Brinell hardness values of 400 and 500 respectively), considering coating and corrosion effects exhibited stable hysteretic behaviour for sliding displacements greater than 50 mm. The sliding strength, considering both sliding interfaces, was similar for the tests with two M16 Grade 8.8 bolts of length-to-diameter ratios (*L/d*) less than 4 from components tests. Since the moment-axial-shear (MPV) interaction effects described by MacRae *et al.,* [2010] were not significant, Golondrino *et al.,* [2012] recommended using a constant effective coefficient of friction, μ_{eff}, computed as the sliding force divided by the total bolt proof force, rather than considering MPV interaction directly.

Borzouie *et al.,* [2015] carried out an experimental study of AFC assemblies using black coated Grade 10.9 bolts with short threaded lengths inside the grip length. A few bolt fractures occurred during testing, and therefore Borzouie *et al.,* [2015] recommended that the threaded length for Grade 10.9 bolts, when used in sliding connections, should be at least 1.33 times the threaded length required in the grip length for Grade 8.8 bolts specified in AS/NZS1252 [2016]. This is due to the ultimate strength of Grade 10.9 bolts is 1.33 times greater than that of Grade 8.8 bolts. In general, as a conclusion of the experimental study, galvanisesd Grade 8.8 bolts are preferred for friction connections as they have adequate strength and they are more ductile than higher grade bolts with non-galvanised coats.

AFCs at the end of, or within, braces are shown in the schematics in Figure 1-6a and b [Butterworth, 1999, MacRae, 2008, and Chanchi *et al.,* 2012]. These AFC braces dissipate energy via friction when the braces slide in axial deformation. The friction strength limits the force that can be transferred from the brace to the rest of the frame. An AFC brace can be connected to a frame using gusset plates.

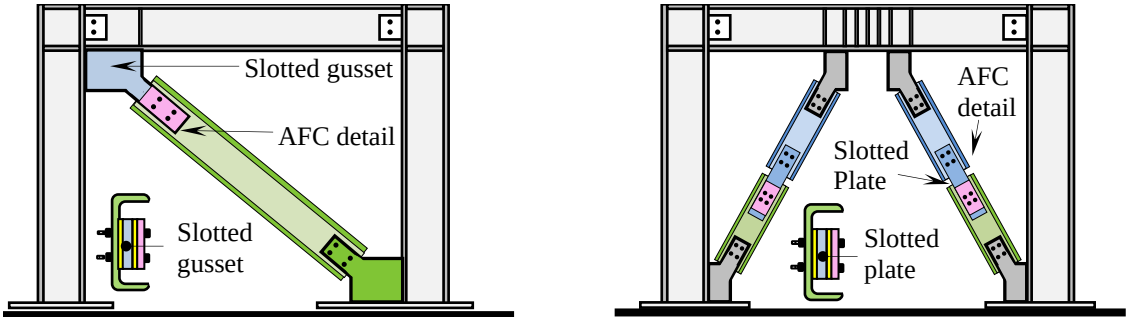

a. Brace with AFC detail at one end (Singly braced frame)

b. Brace with AFC detail within the brace (Eccentrically braced frame)

Figure 1-6. Applications of AFC braces in moment resisting frames

Galvanised Grade 8.8 structural bolts are used as clamping bolts due to their high ductility and adequate strength. For each clamping bolt, one Belleville washer is inserted between the bolt nut and the flat structural washer. The Belleville washer acts as a spring in the bolt assembly to reduce the loss of initial bolt tension during sliding and to improve the consistency on the sliding strength values as shown in Figure 1-7 [Chanchi *et al.*, 2012 and Ramhormozian *et al.*, 2015]. However, Belleville washers are not expected to affect the maximum shear resistance of an AFC.

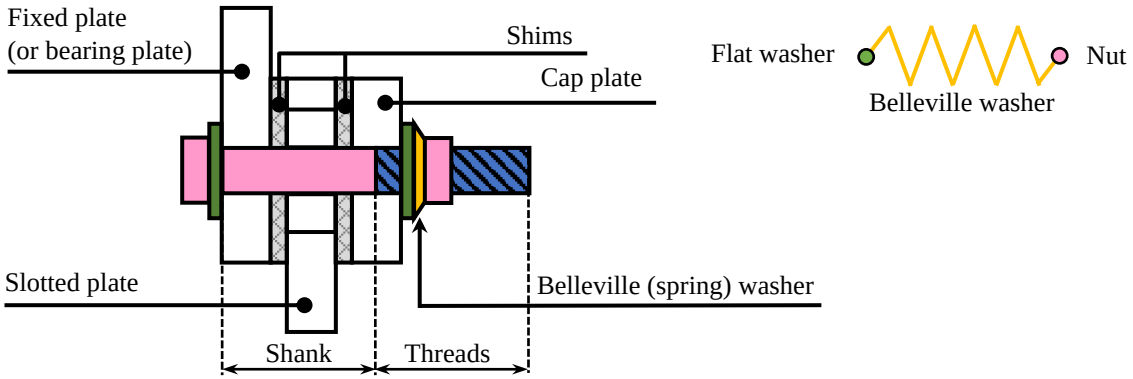

Figure 1-7. Bolt assembly model [Chanchi *et al.*, 2012]

Thin plates, termed shims, are placed at the interfaces between the slotted plate and the bracing member, and at the interfaces between the slotted plate and the cap plate to improve the hysteretic behavior of the AFC detail, as well as reducing the overall damage to the AFC detail during a seismic event. The use of mild steel slotted plates and shims with higher Brinell hardness such as Bisalloy 500 shims are recommended in AFC details in order to achieve stable hysteretic behavior [Chanchi *et al.*, 2012]. A bearing plate can be welded on the inner web of

the bracing member to prevent any bearing issue resulting from the force transmitted from the bolts to the bracing member, as shown in Figure 1-8. It is to be noted that the AFC can also be applicable not only to channel sections but also to other profiles such as I-shaped profile [Chanchi *et al.*, 2012].

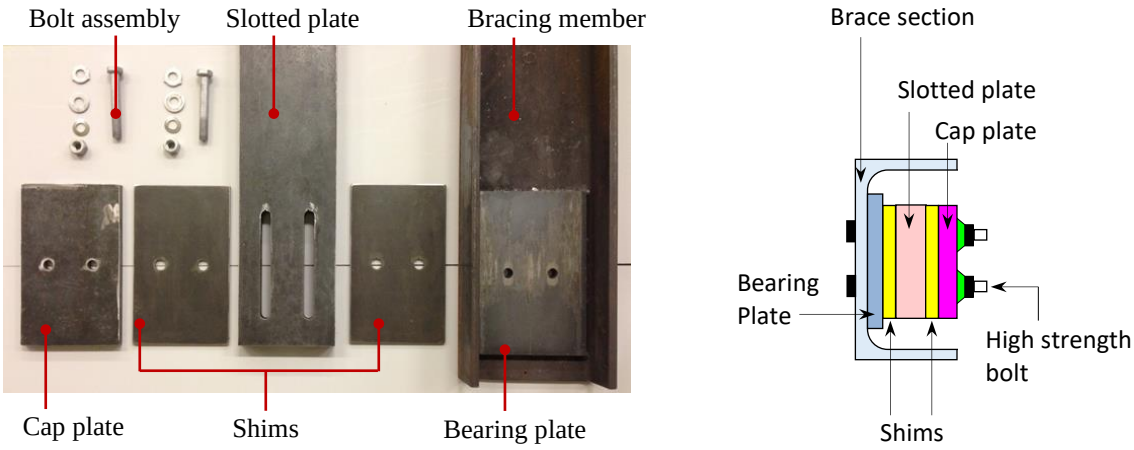

a. AFC components b. AFC assembly cross section

Figure 1-8. AFC brace components and cross section

Unlike yielding dissipaters where energy dissipation relies on the yielding of certain components of the device, energy dissipation in friction connections is developed when the slotted plate is pushed or pulled to a force that is equal to or greater than the shear resistance from the clamping force provided by the clamping bolts. Theoretically, all components within the bracing system remain elastic throughout the process of energy dissipation, and therefore the friction brace can offer stable performance over large cycles without component replacements. The force that fully activates the sliding mechanism, that is sliding is occurring on both sides of the slotted plate, is termed the maximum shear resistance, or the peak sliding force, and the magnitude of this force can be described using Equation 1.1 [MacRae *et al.*, 2010] below. The peak sliding force (F_s) a friction connection depends on the (i) number of clamping bolts (n_b), (ii) number of sliding interfaces (n_s), (iii) tension provided by the clamping bolts (N_{tf}), and (iv) the effective friction coefficient (μ_{eff}) which is directly related to the material properties of the sliding interfaces. The term ϕ represents the understrength or the overstrength factor of the connection assembly, it can be used to predict the lower and upper bound of the peak friction force. [MacRae *et al.*, 2010] has recommended an average value of 0.21 to be

used as the μ_{eff} of an AFC. Furthermore, the understrength and overstrength factors for a friction connection should be 0.7 and 1.4, respectively, as recommended by MacRae & Clifton [2015].

$$\phi F_s = \phi \times n_b \times n_s \times N_{tf} \times \mu_{eff} \quad (1.1)$$

Chanchi *et al.*, [2012] conducted tests on AFC specimens with M16 Grade 8.8 galvanised clamping bolts where the slotted plate from each specimen was pushed and pulled up to 110 mm each direction. The clamping bolts were tightened up to torque values of 20, 50, 150, 250, 350, 410 and 500 N-m from the finger tightened condition without application of additional lubrication on bolts as specified by AS/NZS 1252 [2016]. All bolts tested had a grip length of 76 mm and a total length of 110 mm. The testing setup of this experiment is shown in Figure 1-9.

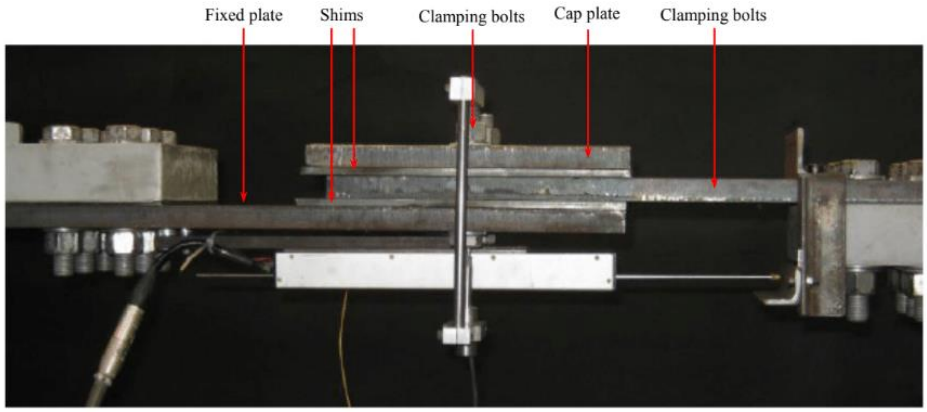

Figure 1-9. AFC test setup by Chanchi *et al.*, [2012]

The results of the tests described above indicated that the stability and shape of the hysteresis loops of AFC were heavily influenced by the bolt torque, which relates to the bolt clamping force. For torque levels below 50 N-m, which was equivalent to the snug tightened condition, unstable hysteretic behaviour was observed from the AFC details and the hysteresis loop shapes were constricted (Figure 1-10a). At torque values of 100 N-m, the hysteresis behaviour was stable with almost rectangular hysteresis loops for sliding lengths up to 50 mm (Figure 1-10b). For a torque of 350 N-m, aimed at achieving the proof load of a M16 bolt, the AFC produced stable and almost rectangular hysteresis loops across the total sliding length of 220 mm (Figure 1-10c). Therefore, the value for N_{tf} in Equation 2 should equal to the proof load of one clamping bolt.

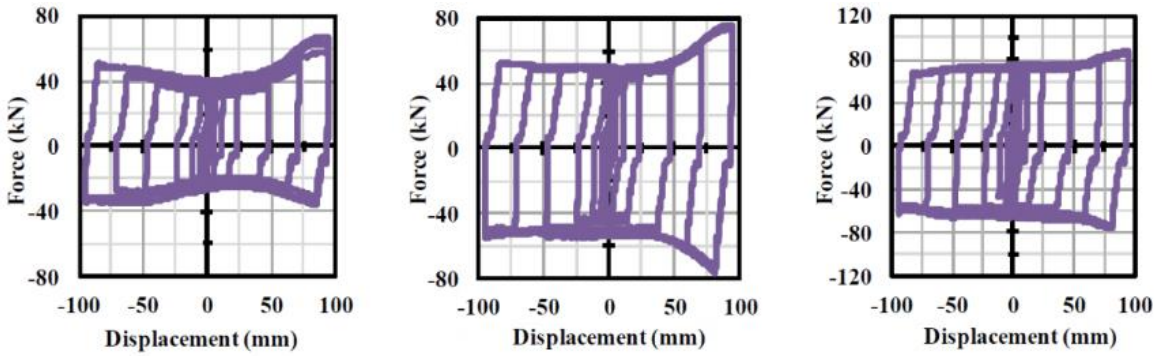

a. 50 N-m torque b. 100 N-m torque a. 150 N-m torque

Figure 1-10. Applications of AFC braces in moment resisting frames

Additionally, Cavallaro *et. al.*, [2018] conducted investigations on the relaxation of friction damper bolt assemblies in relation with time, and the outcome shows bolt assemblies that are tightened to their yield load can exhibit up to 10% loss of their initial tension in 50 years, and 50% of the total tension loss can occur in the first 18 hours, and 70% of the total loss can occur in the first 30 days. Loss of bolt tension causes a reduction in the peak sliding force. However, given the long term loss is no more than 10%, using a understrength factor of 0.7 as suggested by MacRae & Clifton [2015] is sufficient to account for the bolt relaxation. This study also suggests Belleville washers are not effective in reducing bolt relaxation.

The concept of SFC braces used as dissiapters in framed buildings was initially introduced by Pall & Marsh [1982]. In the initial proposal of this type of braces the SFC was assembled with non-metallic shims made of a heavy-duty brake lining pad material. Testing of the SFC sub-assembly showed that the hysteresis loop is square, repeatable, and that the brake lining pads exhibited a negligible fade when subjected to many cycles comparable to the cycles that a brace can undergo during a severe earthquake. Pall & Marsh [1982] also proposed a structural system where the SFC was placed in both directions of an X brace system, where the braces were connected with four links that activate the sliding at the connection details in both directions, as shown in Figure 1-11a. Results from inelastic time-history analysis showed that the frame equipped with the X brace system performed better during ground motion simulations than conventionally braced frames and moment resisting frames.

The experimental validation of the SFC X bracing system proposed by Pall & Marsh [1982] was carried out by Filiatrault & Cherry [1987] when a scaled-down 3 storey building was tested on a shake table. The model structure was initially assembled with an SFC X bracing system,

and it was assembled twice more with a moment resisting frame system and with a conventional yielding X bracing system. Results of this experimental study confirmed that the SFC X bracing system had a superior seismic performance when compared with the two other types. This is because no damage occurred within the primary structure that was attached to the X bracing system, whereas large inelastic deformations were observed in the other two systems when subjected to earthquake records with peak accelerations of 0.90g. Also based on the experimental results, Filitrault & Cherry [1987] proposed a refined SFC X bracing numerical model. Filiatrault & Cherry [1988] compared this refined numerical model with a system that was equipped with a base isolator using ground motion simulations, and the analytical results showed the SFC X bracing structural model performed better than the base isolated structure under low frequency earthquakes. Filitrault & Cherry [1988] also suggested the friction device could offer a more consistent way of protecting structures during earthquakes when compared to a base isolator. This is because less shear force and displacements were observed in the friction structure.

FitzGerald *et al.,* [1989] proposed a type of SFC brace assembled with two channel profiles back to back as bracing members and a gusset plate. The friction connection details were located at one end of the brace. The SFC details, which include the channels and cover plates, were fitted at each side of the gusset plate, and the channels were slotted to enable sliding. High tensile bolts were used to clamp the cover plates, the channels and the gusset plate together, as shown in Figure 1-11b. Quasi-static testing of this SFC brace showed that the hysteresis loops were rectangular and comprised two post-yielding zones associated with the sliding of the friction connection details. Results also showed that the hysteresis loops were stable when using steel-steel interfaces without inserting any type of shims between the cover plates and the channels.

Tremblay [1993] proposed a type of SFC brace assembled with a circular hollow section (CHS) as the bracing member and the SFC was attached at one end of brace. The SFC was assembled by using shims, slotting the gusset plate, and by sandwiching the gusset plate and the shims with two connecting plates welded to the CHS, as shown in Figure 1-11c. Two prototypes of this SFC brace configuration were tested, one prototype was assembled using mild steel shims and the other one using Cobalt alloy shims. Testing of the prototypes was undertaken in quasi-static conditions. Results showed that the sliding surfaces of the SFC braces using mild steel shims underwent significant degradation and the hysteresis loops were unstable, and with low

predictability when compared with the performance of the braces using Cobalt alloy shims. For this reason, the use of dissimilar materials at the sliding interfaces of SFC was suggested in order to achieve a stable and predictable hysteretic behaviour of an SFC brace.

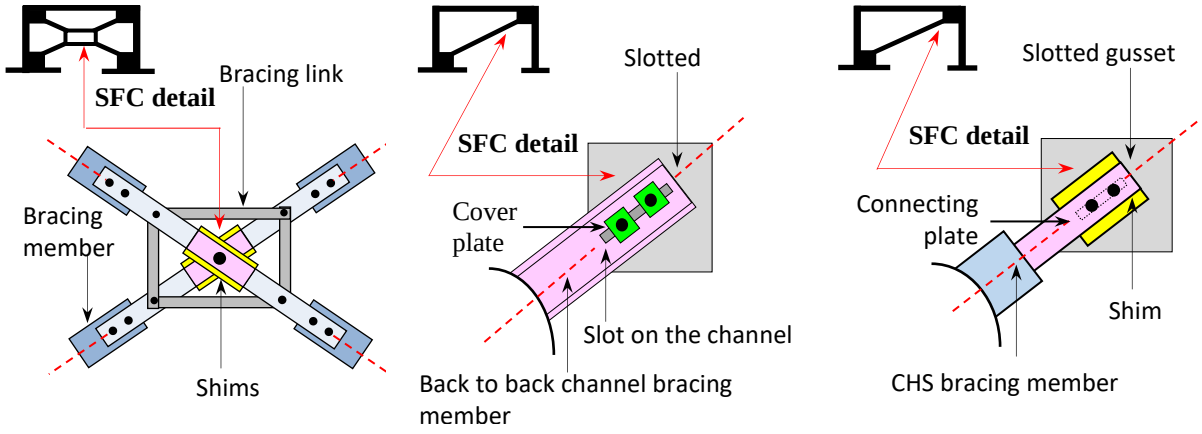

a. Pall & Marsh (1982) b. FitzGerald *et al.* (1989) c. Tremblay (1993)

Figure 1-11. SFC for different brace configurations proposed on different research works

Chanchi *et al.*, [2013] tested samples of SFC assemblies with dissimilar sliding interfaces by sliding a mild steel slotted plate over metallic shiims of different Brinell hardness (BH) such as aluminium, brass, Bisalloy 80, Bisalloy 400, and Bisalloy 500, as shown in Figure 1-12. The SFC was assembled by clamping the slotted plate and the shims together with the fixed plates, shown in Figure 1-12a, by means of Grade 8.8 high tensile strength bolts. An illustration of the cross section of the assembly is shown in Figure 1-12b.

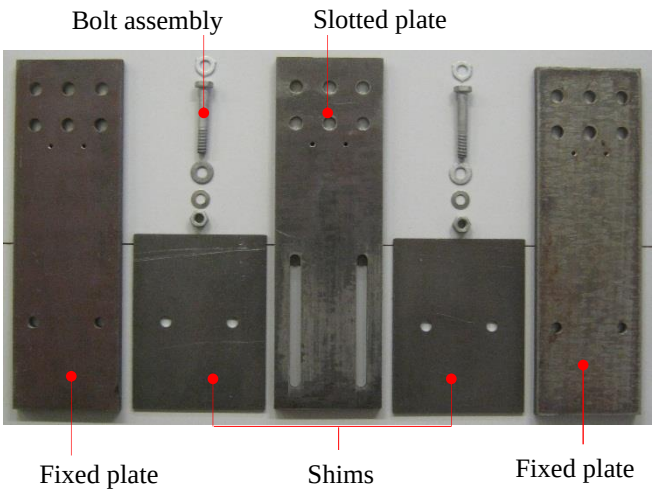

a. SFC components

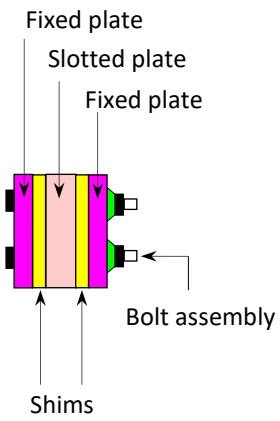

b. SFC cross section

c. SFC assembly 3D view

Figure 1-12. SFC components and assembly tested by Chanchi *et al.* [2013]

Results of this experimental study, which are presented in Figure 1-13, show that by using a shim material with a Brinell hardness of at least 2.5 times the Brinell hardness of the slotted plate. For the case of a mild steel slotted plate, the recommended materials for the shims are Bisalloy 400 and 500. The degradation mechanism observed by Chanchi *et al.*, [2013] for such assembly was adhesive, which produced very stable hysteresis loops and low material degradation on the sliding interfaces.

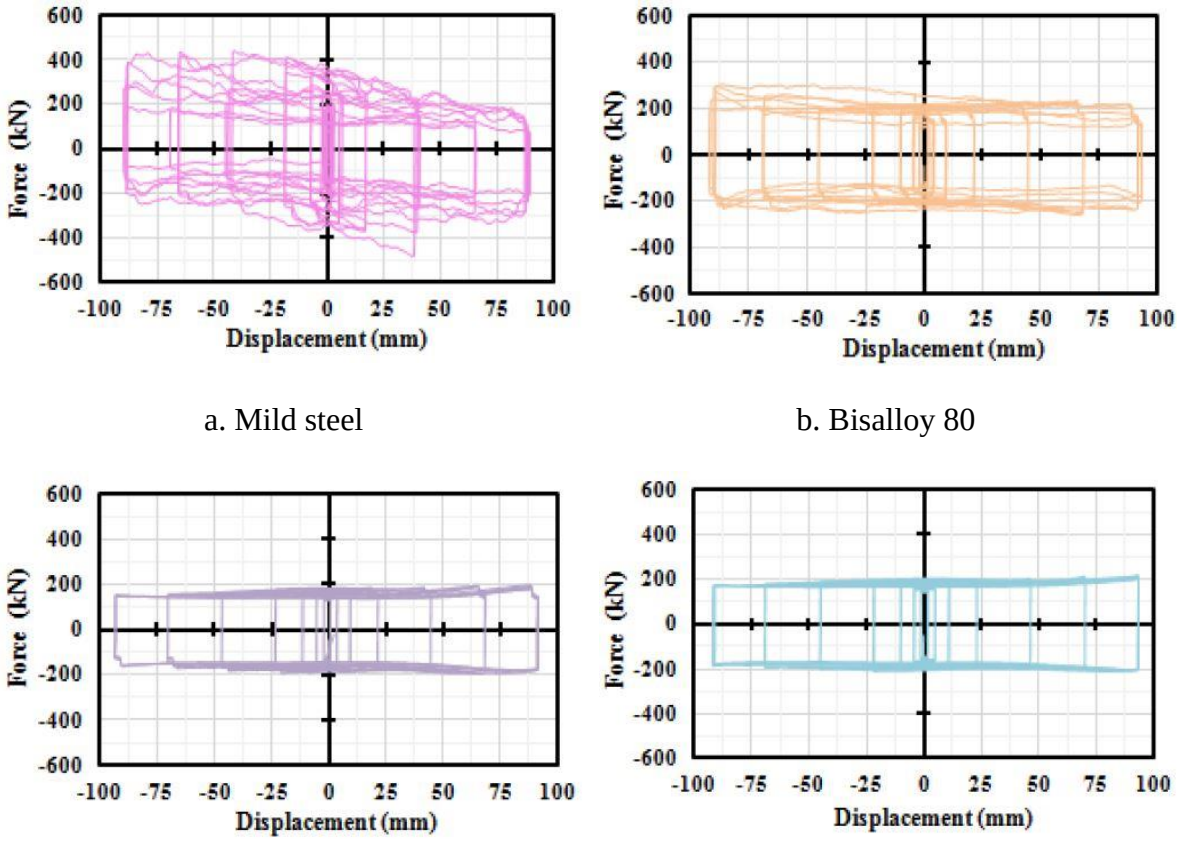

a. Mild steel

b. Bisalloy 80

c. Bisalloy 400

d. Bisalloy 500

Figure 1-13. Hysteresis loops of SFC using different shim materials by Chanchi *et al.*, [2013]

Latour *et al.*, [2015] carried out a series of tests on different shim materials. This study suggests that steel – steel sliding interface is not desirable, which agrees with the experimental outcome from Chanchi *et al.*, [2013] as shown in Figure 1-13a above. Additionally, Latour *et. al.*, [2015] tested a rubber-based shim that has similar properties to those of a brake pad. The experimental result of this shim material shows stable behaviour, as shown in Figure 1-14 below. However, it produced lower effective friction coefficient than metallic shims.

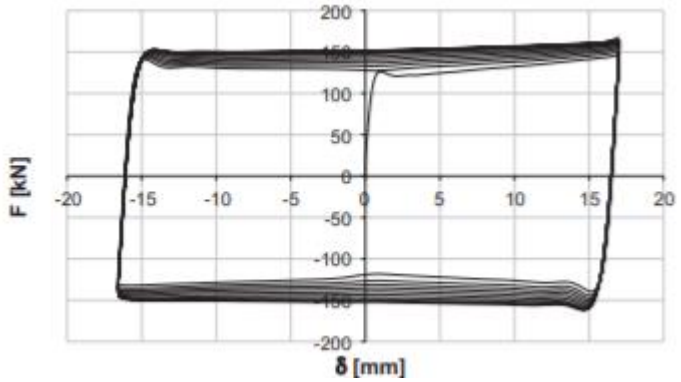

Figure 1-14. Hysteresis loops of SFC using rubber-based shim materials by Latour *et al.*, [2015]

Equation (1.1) described earlier can also be used to predict the peak sliding force of an SFC assembly. The understrength and overstrength factors, and bolt clamping force for an SFC are the same as those of an AFC assembly. For the effective friction coefficient, based on the experimental results from Chanchi *et. al.*, [2013], it is recommended an average value of 0.45 to be used.

More recently, component testing on friction connections has been carried out by Hatami *et al.*, [2019] using M24 bolts under quasi-static condition. During this experimental study temperature change within the friction connection details was monitored, and the temperature rose by 28 degrees Celsius after 24 cycles of load reversals with an accumulative travel of 2625 mm. The temperature rise was proportional to the amount of energy dissipated by a friction connection.

1.2.4. Viscous dampers

The use of viscous fluid dampers in civil engineering to reduce vibrations started in the 1990s [Christopoulos *et al.*, 2006]. Nowadays, viscous dampers are widely applied to buildings and bridges in high seismic regions, and the number of viscous damper manufacturers appears to be growing over recent years. Viscous dampers are a common choice of supplement damping for structures in seismic regions because they (i) can improve structural response, and (ii) do not introduce significant additional structural stiffness and thus limit the demand on foundations. Additionally, the application of viscous dampers in new and existing structures can be cost effective [Pettinga *et al.*, 2013]. Rad *et al.*, [2019] conducted nonlinear time history analysis on two 4-storey composite steel structures of the same dimensions, one structure was

equipped with viscous dampers and the one was base isolated. The analytical results from this study showed the two low damage systems generated similar peak accelerations and drifts. For this reason, Rad *et al.*, [2019] has stated that when considering options for seismic energy dissipations in structures, viscous dampers can be a suitable alternative to base isolators.

In a structural system equipped with viscous damper, the damping force is induced by the flow of viscous fluid (e.g. silicone oil) through the piston head of the damper, and it is velocity dependent. In general, the damping force can be defined using Equation (1.2) below.

$$F = C|v|^{\alpha}.sign(v) \tag{1.2}$$

Where F is the damping force, v is the velocity, C is the damping constant, and α is the exponent constant that defines the linearity of a viscous damper. Figure 1-15a and b plot the force-velocity curves and force-displacement curves, respectively, for linear and nonlinear viscous dampers.

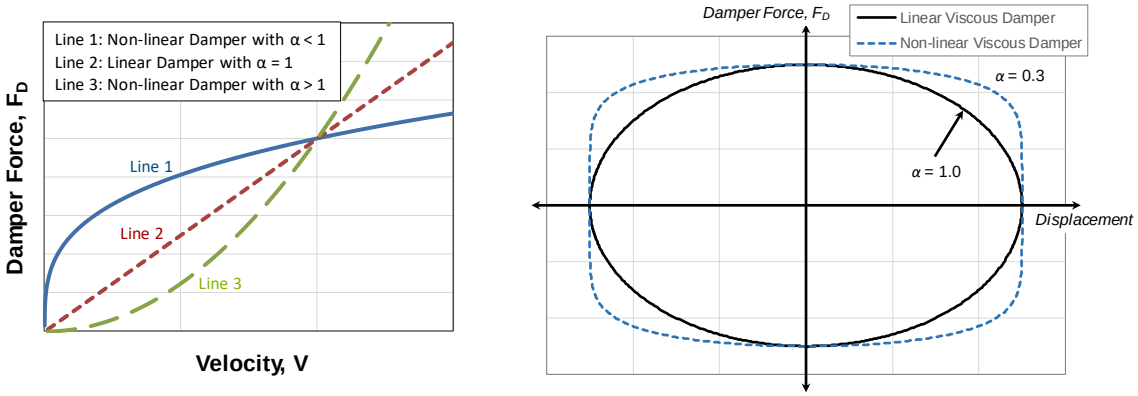

a. Force-velocity curves of viscous dampers

b. Force-displacement curves of viscous dampers

Figure 1-15. Linear and nonlinear viscous dampers force-velocity and force-displacement relationships

A linear viscous damper adopts an α value of 1, and if α is greater or less than 1 it makes the viscous damper nonlinear. Typically, in practice, a nonlinear viscous damper possesses an α value between 0.1 – 0.3 [Sullivan and Lago, 2012]. As shown in Figure 1-15b above, if oscillated to the same level of displacement, a nonlinear viscous damper is able to dissipate more energy (which is presented by the area enclosed by the force-displacement curve) than a

linear viscous damper. In practice, nonlinear dampers are generally considered favourable as they lead to less variation in resistive force as the velocity imparted into the damper changes, which results in less required overstrength within the connecting elements.

As the forces in viscous dampers are velocity dependent, non-standard design and analysis strategies are required. Many different methods can be found in the literature such as Ramirez *et al*. [2000], Lin *et al*. [2003], Kim *et al*. [2003], Silverstri *et al*. [2010], Sullivan and Lago [2012], Lavan [2012], Lavan [2015], and Puthanpuravil *et al*. [2017]. Lavan & Levy [2005, 2006 and 2009] proposed methodologies for the optimal design of supplemental damping for frame structures. These three research works address 'fully-stressed-design' which aims to minimise the amount of supplemental damping required while the design constraints are fully utilised.

As shown above, there has been extensive research aimed at determining the size and number of linear and nonlinear dampers to achieve a given level of overall system damping. However, most of the contributions listed above do not specifically consider the flexibility of the damper system and connections, and thus do not account for the influence of the elastic deformation of the damper sub-system.

Some insight into the significance of damper sub-system stiffness has been provided by Dong *et al*. [2016] as part of a large-scale experimental investigation of a multi-story steel frame building structure with nonlinear viscous dampers. The test structure underwent both design basis and maximum considered ground motions using real-time hybrid simulation. Results from this experimental study concluded that a steel frame would perform significantly better during all levels of seismic events than a bare conventional steel moment resisting frame. Additionally, this literature also provided the interesting observation that the deformations of structural components and connections adjacent to the dampers caused the local deformations of viscous dampers to be different to the story drift. This phenomenon, referred to as the "brace flexibility" effect by the authors, caused the changes in phase shifts between the damper and structural responses, and as a result, the brace flexibility effect added stiffness to the steel frame equipped with viscous dampers (Figure 1-16). The term "brace" here indicates the damper sub-system that provides connection between the damper and the main structure. Furthermore, Dong [2016] used an equivalent linear elastic-viscous model to simulate a damper-sub-system component in order to further investigate the effect of sub-system stiffness on the response of

a frame structure. This study stated that a more flexible sub-system stiffens a structure and the sub-system stiffness also affects the effective damping of the structure.

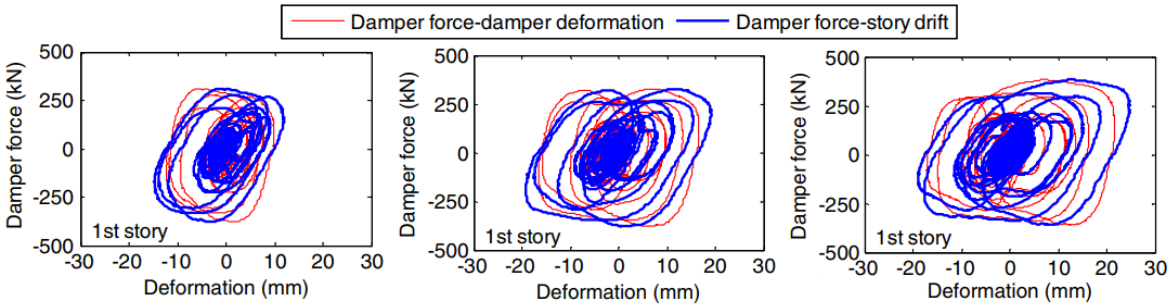

Figure 1-16. Damper is partially out-of-phase with the structure due to sub-system flexibility [Dong *et al.*, 2016].

Some research works have discussed the effect of brace stiffness on the behaviour of SDOF systems. Reinhorn *et al.* [1995] uses Maxwell and Kevin-Voigt models to address the effect of brace stiffness on a component level, and this study focuses primarily on forces and stiffness. Fu & Kasai [1998] carried out parametric studies using harmonic excitations and outlines the benefit of having high brace-to-frame stiffness ratio in terms of added stiffness to the overall system and energy dissipation. Londono *et al.* [2013] and Londono *et al.* [2014] propose methods to optimise brace and damper size. However, these works focus only on linear damper systems and do not consider nonlinear dampers.

Several studies have proposed approaches for the optimal design of MDOF structures with viscous dampers while taking the brace flexibility into consideration, such as Takewaki & Yoshitomi [1998], Singh *et al.* [2003], Park *et al.* [2004], Viola & Guidi [2009], Chen & Chai [2011], Castaldo *et al.* [2014], Lavan [2015], Pollini *et al.* [2017], and Pollini *et al.* [2018]. Although some of these studies consider both linear and nonlinear viscous damper systems, the proposed methods by these studies involve complex computational and numerical analysis of such systems. Therefore, these methods may not be practical in a design office.

1.3. Research objectives and scope

1.3.1. Friction connections

To date, there has been extensive testing on friction devices at a component-level as outlined in several research studies such as Pall & Marsh [1982], Filiatrault & Cherry [1987],

Golondrino *et al.,* [2012] Chanchi *et al.,* [2013], Hatami *et al.,* [2019]. Some experimental studies have been carried on beam-column joints using friction connections as described in Clifton [2005] and Latour *et al.,* [2015]. However, there appear to have been no large-scale experimental testing of friction connection used as a part of a bracing system. It may be seen that for the AFC and SFC to be used in actual structures as brace dissipaters, there is a need to first understand the hysteretic behaviours of the friction braces. Therefore, the first part of this research is to carry out experimental testing of the friction braces to answer the following questions:

(i) Does the hysteresis behaviour of a friction brace differ when tested as a component versus inside a frame?

(ii) Is there strength and material degradation within the friction connections after several cycles of testing?

(iii) What are the parameters that govern the design of a friction connection?

The use of time-history analysis is becoming substantially more common in design offices. However, currently there do not appear to be numerical tools to incorporate non-standard elements to simulate the behaviours of friction connections. The experimental results can then be used to develop device equations in order to incorporate a new friction element model into numerical packages such as OpenSees. This model will enable detailed time-history analysis of a frame using frictional bracing elements to be undertaken by a practitioner and increase likelihood of wider uptake.

Appropriate detailing of the connections between the friction braces and the primary structure is essential for advantageous field performance. Based on the experimental results, recommendations can be provided as an outcome of the experimental studies to outline the key detailing concepts and underlying design principles of structures equipped with friction braces.

1.3.2. Viscous dampers

Current seismic design procedures available for structures equipped with viscous dampers are mainly intended to identify the amount of damping required to limit the structural displacements to a desired amount, and this can result in a set of damper coefficients over the height of the structure. However, most methods appear to presume conventional detailing for

the connections between viscous dampers and the primary structures and no allowance appears to be made for the flexibility of connections. While Dong *et al.*, [2016] has shown that phasing effects associated with the flexibility of the support system can influence the dynamic response of structures with dampers, detailed guidance is not provided in the literature to how to account for the flexibility of the damper sub-system, which includes all the components of the viscous damper-structure connection. Furthermore, the definition of what constitutes a "rigid" or sub-system connection is unclear.

Although some methods have been proposed to account for brace flexibility in the design of a viscous damper system, most of these methods only consider linear damper systems and some cannot be easily incorporated into a practical design process.

For the reasons above, the objective of this study is to investigate how the damper sub-system stiffness changes the response of a structure when considering both linear and nonlinear viscous dampers, and to what extent the sub-system stiffness can affect the equivalent damping provided to the system. The result of this study will be used to provide a practical indication of how stiff a sub-system needs to be to enable it to be effectively considered as rigid during design. Finally, based on the findings of this study, modifications to the current design framework can be made, to help ensure an optimal and practical outcome in typical structures and as part of innovative retrofit strategies.

1.4. Thesis overview

This section provides an overview of the contents in Chapter 2 to Chapter 5.

In Chapter 2, the experimental study carried out on AFC braces is described. The contents within Chapter 2 includes discussions on the energy dissipation mechanism of AFC braces by themselves, as well as within a steel frame. Discussions on strength degradations, design considerations and modelling method of AFC braces are also provided.

Chapter 3 describes the testing of SFC braces by themselves and inside a steel frame. Contents within this chapter include discussions on SFC brace energy dissipation mechanisms, strength degradations, design considerations and modelling method.

Chapter 4 presents the findings from the investigations on how damper sub-system stiffness affects overall system seismic response. Based on the findings, a modified design framework is proposed.

Chapter 5 highlights the key findings of this research topic. A comparative study on viscous dampers and friction braces has also been presented.

2. EXPERIMENTAL STUDIES OF ASYMMETRICAL FRICTION CONNECTION

2.1. Overview

A subset of the results presented within this chapter has been submitted to the following conferences/journals. The work presented within this chapter is an extended version of the information presented within these publications.

Chanchí, J. C., Xie, R., MacRae, G., Chase, G., Rodgers, G., & Clifton, C. (2014, March). Low-damage braces using asymmetrical friction connections (AFC). In NZSEE Conf., The New Zealand Society for Earthquake Engineering, Wellington, New Zealand.

Xie, R., Golondrino, J. C., MacRae, G. A., Chase, G., Rodgers, G., & Clifton, C. (2015). Braced frame using asymmetrical friction connections (AFC). In 8th Conference on Behaviour of Steel Structures in Seismic Areas (STESSA).

Xie, R., Chanchi Golondrino, J., MacRae, G. A., & Clifton, G. C. (2018). Braced Frame Symmetrical and Asymmetrical Friction Connection Performance. In Key Engineering Materials (Vol. 763, pp. 216-223). Trans Tech Publications.

This chapter describes the experimental studies carried on Asymmetrical Friction Connection (AFC) when it is used as part of a friction brace energy dissipator. The experiments were carried out as an extension to the early experimental work conducted by Chanchi *et al.*, [2012, 2013] to investigate the sliding mechanism of an AFC brace under quasi-static condition and define the design parameters of an AFC brace. The testing results are also used to quantify the strength and material degradation of an AFC brace after several cycles of axial loading, so a component replacement strategy can be proposed. This chapter describes the materials, instrumentation, assembly methods and loading protocols that were used for the experiments.

The experimental program is divided into two main parts, and the first part was to test three AFC brace specimens by themselves as component tests. The aim of the AFC brace tests was to investigate the hysteretic behaviour of an AFC in a brace without the influence of frame actions. Each brace specimen was subject to three sets of 48 cycles of load reversals. Strength degradation was accessed after every 24 cycles, and material degradation was accessed after every 48 cycles. At the end of each stream, certain components within the AFC were replaced

to investigate the most effective retrofit strategy for an AFC brace without having to replace the entire AFC.

In the second part of the experimental program, the AFC brace was fitted on to a singly braced frame. The aim of the frame tests was to investigate the behaviour of an AFC brace when it was part of a singly braced frame, and if it behaved differently to when it was tested by itself within a component test. The test results of the AFC braced frame were also compared to the hysteretic behaviour of the same frame but without the AFC brace, to investigate the influence of an AFC brace could have on a steel frame. Two sample braces were tested, and each brace was subject to only 48 cycles of load reversals with no component replacements between cycles. At the end of the 48 cycles all brace components were replaced except the bracing member.

Based on the results obtained from the brace tests and braced frame tests, important design parameters for an AFC brace have been defined, these include the effective friction coefficient, understrength and overstrength factors. Design recommendations have also been proposed, and a design example is presented for a singly braced frame equipped with an AFC brace.

At the end of the chapter, a new numerical multi-linear model is proposed and implemented into OpenSees. The performance of the model is tested in a displacement-controlled analysis and the analytical results are compared to the experimental results obtained from the AFC brace tests.

2.2. AFC in a brace

2.2.1. Materials and assembly methodology

The AFC brace tests were carried out first to fully investigate the hysteretic behaviour of the Asymmetrical Friction Connection details when they are attached to a brace. The AFC brace testing samples were assembled using Grade 300 steel hot rolled profiles with parallel flange channel section, 250PFC, with 2860 mm length. At the location of the AFC, a Grade 300 plate with 16 mm thickness was fillet-welded all around on to the web of the channel section using a weld leg size of 10 mm to avoid any bearing issue related to the transfer of load from the bolts to the web. The AFC was assembled with a Grade 300 steel cap plate, two Bisalloy 500 shims with Brinell hardness of 500BH, a Grade 300 steel slotted plate with two 200 mm elongated holes, and two M16 Grade 8.8 galvanised bolts of 130 mm in length with single layers of Belleville washers and two flat washers. The bolt assembly is the same as the

configuration shown in Figure 1-7. Thickness of 16 mm, 6 mm, and 32 mm were used for the cap plate, shims, and slotted plate, respectively. Six M24 Grade 8.8 bolts were used at the two ends of the brace to prevent slip occurring during the quasi-static testing. An illustration of the experimental assembly is shown in Figure 2-1. All sliding surfaces were mechanically cleaned using a wire brush to remove surface mills, and any surface flaws were removed using a grinder.

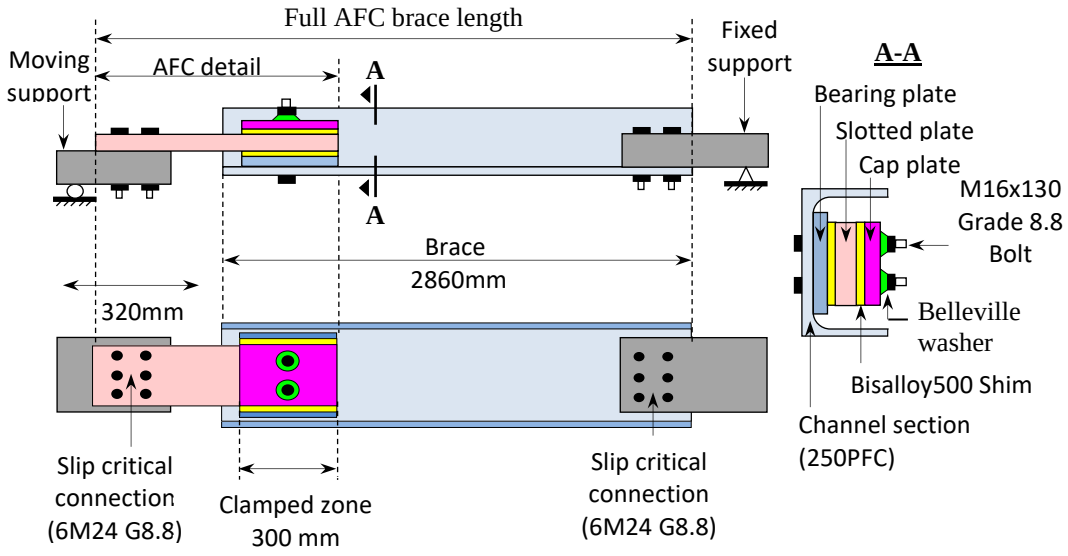

Figure 2-1. Assembly of AFC braces

The torque control method was adopted to tighten the clamping bolts at the AFC detail by using a calibrated manual torque wrench, and the bolts were tensioned up to their proof load. To achieve this, the elongation of the bolts at proof load was found using the tension-elongation relationship (Figure 2-2a), and the bolt elongation was then used to extrapolate the torque required from the torque wrench (proof load torque) using the torque-elongation relationship (Figure 2-2b). Using this methodology, the proof load torque was defined to be 310 N-m from the hand tight condition, and this proof load torque corresponded to 1/4 to 1/2 turn of nut rotation when comparing with the nut rotation method. The tension-elongation relationship and the torque-elongation relationship was produced based on the results of bolt tightening tests carried out by Chanchi *et al.,* [2014] using bolts with the same bolt diameter and same bolt grip length as those used in the AFC detail. It is worth noting that this method is not currently accepted by the NZ Steel Structures Standard for structural applications. However, it was used here to systematically control the bolt tension from experimental relationships.

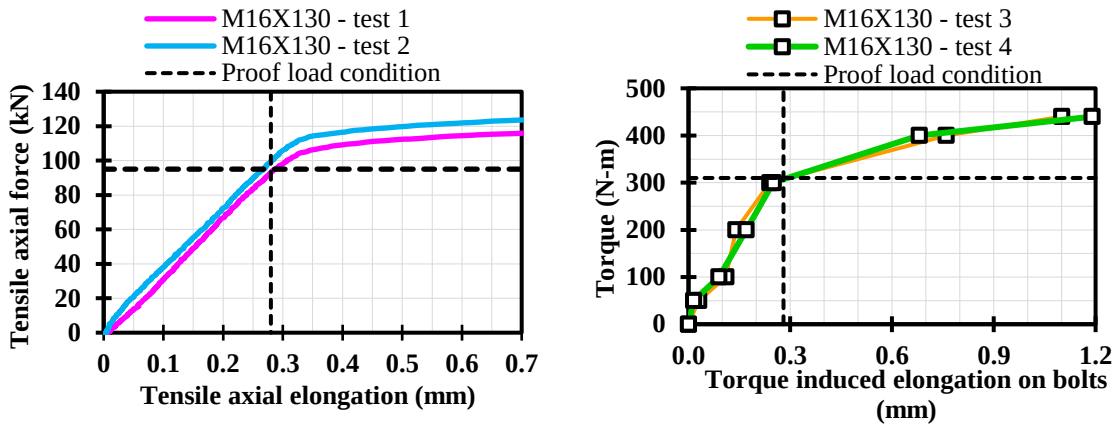

a. Tensile testing relationship b. Torque – bolt elongation relationship

Figure 2-2. Relationships used for assembling AFC detail [Chanchi et al., 2014]

2.2.2. Experimental setup, instrumentations and loading regime

The AFC brace tests were carried out by placing the braces in a horizontal setup constituted by a fixed and a moving support, as shown in Figure 2-3. The fixed support of the brace test setup was assembled with a bracket bolted on to a reaction frame, and the moving support was assembled with a bracket that was attached to an actuator which was bolted onto a reaction tower. This setup was instrumented with a load cell in series with the actuator. One string extensometer was placed horizontally across the brace length to measure the travel distance of the AFC detail, and four string extensometers were placed vertically at each quarter of the brace length to measure the vertical movements of the brace, as shown in Figure 2-3.

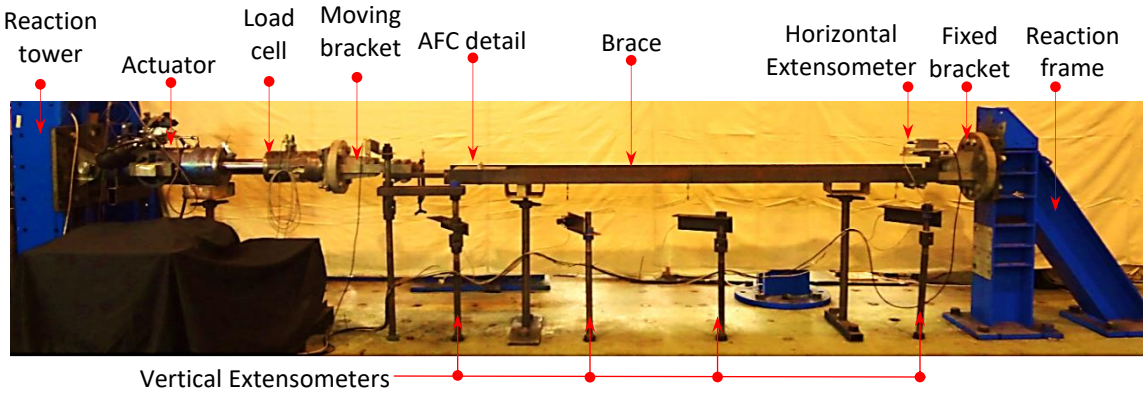

Figure 2-3. AFC brace test setup

Testing was based on subjecting the AFC braces to a cyclic displacement regime with a constant velocity of 3 mm/s. The displacement regime for the AFC brace tests comprises 20 sawtooth cycles with amplitudes between 3 mm and 90 mm, which correspond to 3 and 90% of the slot length of the AFC detail (Figure 2-4).

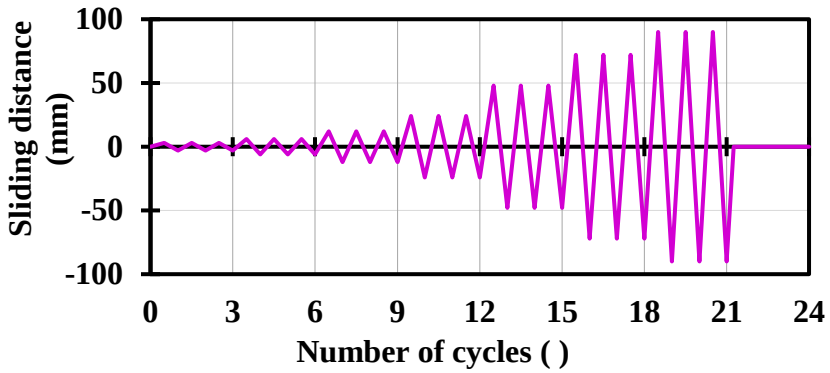

a. Graphic illustration of loading regime

No. of Cycles	Ram X Displacement (mm)
3	3
3	6
3	12
3	24
3	48
3	72
3	90

b. Cycles and Displacements

Figure 2-4. Displacement regime for AFC brace tests

A total of three sample sets of AFC details were tested with the channel brace attached. Testing of each sample comprised three streams, namely brand-new materials, bolt replacements and shim replacements. See the brief descriptions of each stream of testing below:

(i) Brand-new materials: undamaged new materials were used. The purpose of this stream was to investigate the behavior of AFC brace without the influence of strength and material degradation.

(ii) Bolt replacements: the 2 M16 clamping bolts were replaced at the beginning of this stream. Strength degradation was expected after several cycles of testing. This stream was to investigate whether the strength of a used AFC brace could be restored by replacing the clamping bolts.

(iii) Shim replacements: both the clamping bolts and shims were replaced at the beginning of this stream to investigate the effect of shim and bolts replacements on restoring the strength of a used AFC brace. The slotted plate surfaces were also cleaned by brushing off the debris from the previous test runs.

(iv) Slotted plate replacements: after the previous three streams were completed, the slotted plate was replaced by a new sample slotted plate, and the shims and bolts were also replaced. At this stage the AFC brace was considered to have brand new materials. Throughout the entire AFC brace tests, the 250PFC channel bracing member remained unreplaced.

Two runs of testing were conducted for each testing stream. No bolt-tensioning was applied after the first runs, so that the degradation of sliding surfaces and loss of bolt tension could be estimated when comparing hysteresis loops of the first and second run. A minimal of 30 minutes interval was allocated between the two runs to allow the AFC details to cool down from friction heat. The testing plan is summarized in Table 2-1 below.

Table 2-1. Matrix of AFC brace tests and test names

STREAMS	**Sample A**		**Sample B**		**Sample C**	
	1st Run	2nd Run	1st Run	2nd Run	1st Run	2nd Run
Brand New Materials	A1	A2	B1	B2	C1	C2
Bolt Replacements	A3	A4	B3	B4	C3	C4
Shim Replacements	A5	A6	B5	B6	C5	C6

2.3. AFC in a singly braced frame

2.3.1. Materials and assembly methodology

Testing of the frame comprises two stages: (i) an initial stage where the frame was tested three times without the application of the AFC brace, and (ii) a final stage where the frame was tested together with the AFC brace. In the final stage the AFC brace was bolted onto the top and bottom gusset using slip critical connections of 6 M24 Grade 8.8 high strength structural bolts with an ultimate strength of 830 MPa as shown in Figure 2-5.The AFC brace cross section configuration is the same as shown in Figure 2-1.

The AFC brace was assembled by parts while suspended from the frame in the following order: (i) attached the channel section to the bottom gusset, (ii) attached the slotted plate to the top gusset, and (iii) placed the shims and the cap plate at the AFC detail, and (iv) installed the bolts using the same bolt tightening method as that of the AFC brace tests (i.e. torque control method described in Section 2.1.1). This installation process was adopted to ensure the slotted plate was in-line with the channel before the bolts were tightened.

The columns and beams of the testing frame were assembled using Grade 300 200UC59.5 steel hot rolled I-sections. The beam between column faces was 2830 mm length. It comprised of two short beams of 360 mm and one longer 2080 mm spliced beam as shown in Figure 2-5. Each end of the long beam was connected to one end of the short beams using 20 mm thick Grade 300 steel plates clamped onto both sides of the beam webs using four M24 Grade 8.8 bolts. The gap between each short beam and the long beam was 15 mm. Each of the column sections was 2875 mm in length. The columns were continuous and welded to 50 mm base plates. The base plates were bolted to pin connections which were bolted on to the floor. Beam-column joints were assembled by welding the beam to the column. A Grade 300 gusset plate with 40 mm thickness and six standard holes of 25 mm diameter was used to bolt the AFC braces on to the frame at each end of the braces. Global center-to-center dimensions of the frame were 3040 mm wide, 3020 mm tall, with a brace length was 2860 mm. The bases of the testing frame were pinned in order to limit frame action affects, where the beam and column connection opened and closed, putting additional forces on the gusset plate at the beam-column connection. The two bolted beam-to-beam connections were also considered as pin connections in their design. Such frame configuration was chosen to create a mechanism frame so that majority of the lateral load demand was taken by the brace, and the beams and columns were not likely to fail or deform significantly, so they could be reused in other tests. This frame configuration allows easy replacement of components.

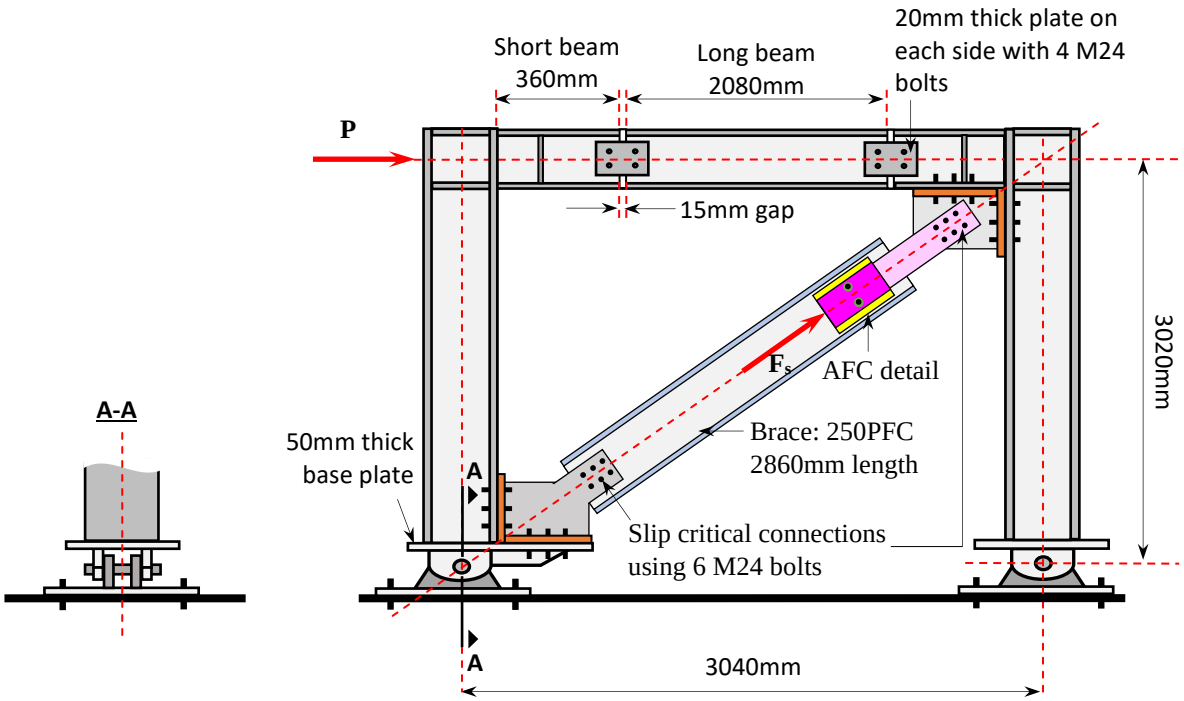

Figure 2-5. Testing frame equipped with an AFC brace

The gussets were welded to the connecting plates which were bolted to the beam and column flanges. This assembly method was adopted so that the gussets could easily be replaced if damaged during testing. The top gusset was eccentrically bolted on to the short beam and the column with an eccentricity of 48 mm to line up with the AFC detail with the bracing member, and the bottom gusset was concentrically bolted on to the column and the pinned base connection. The brace – gusset connections are illustrated in Figure 2-6 below. The bolts at the beam-to-beam connections and the gusset-to-column connections were snug tightened with an air impact wrench.

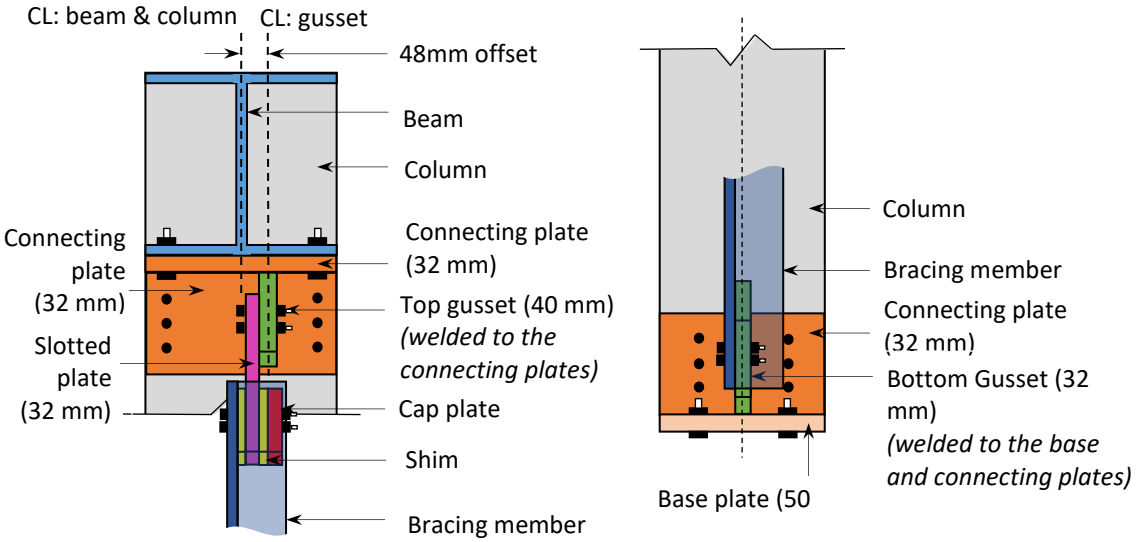

a. Top gusset b. Bottom gusset

Figure 2-6. Gusset details

2.3.2. Experimental setup, instrumentations and loading regime

Unidirectional testing of the braced frame was carried out using the setup in Figure 2-7. Like the AFC brace tests, this setup was instrumented with a load cell in series with the actuator. A rotatory potentiometer was placed on the top of the right-hand side column to measure the total lateral displacement of the frame, and a string extensometer was placed perpendicular to the brace (behind the brace) to measure any unintended out-of-plane movements of the AFC brace.

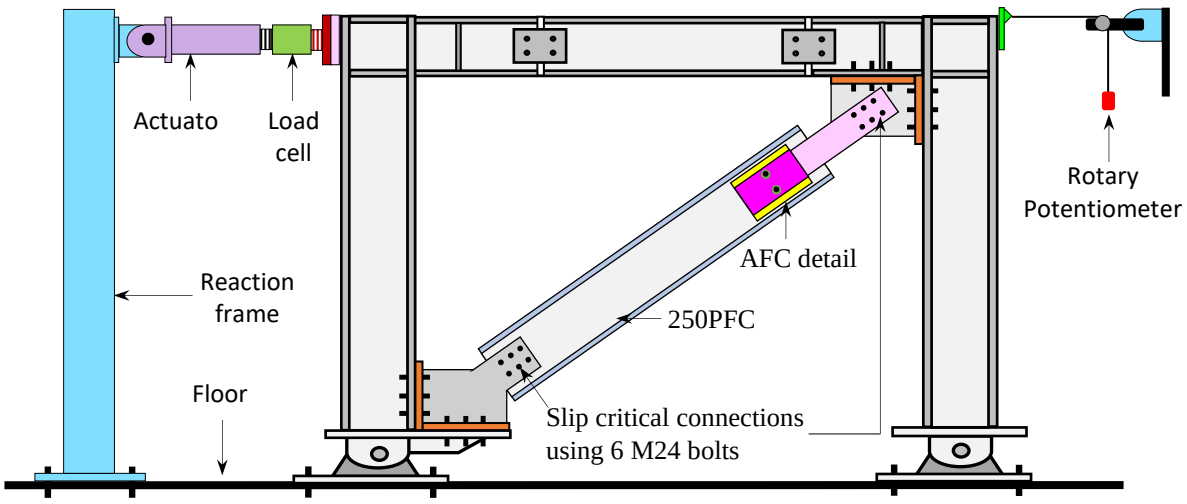

a. Frame test setup illustration

b. AFC braced frame

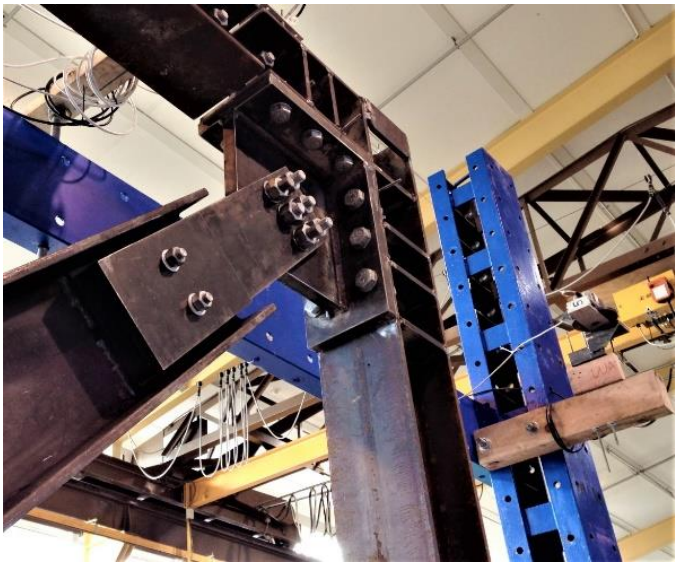

c. AFC braced frame

d. The top gusset offset

Figure 2-7. Frame test setup

The braced frame testing setup was subject to the same 20 sawtooth cyclic loading profile as that of the testing of the AFC brace by itself as shown in Figure 2-8. The braced frame was pushed pulled in the horizontal direction with the lateral displacement ranged between 3 mm and 90 mm, which corresponded to 0.1% - 3% lateral frame drift.

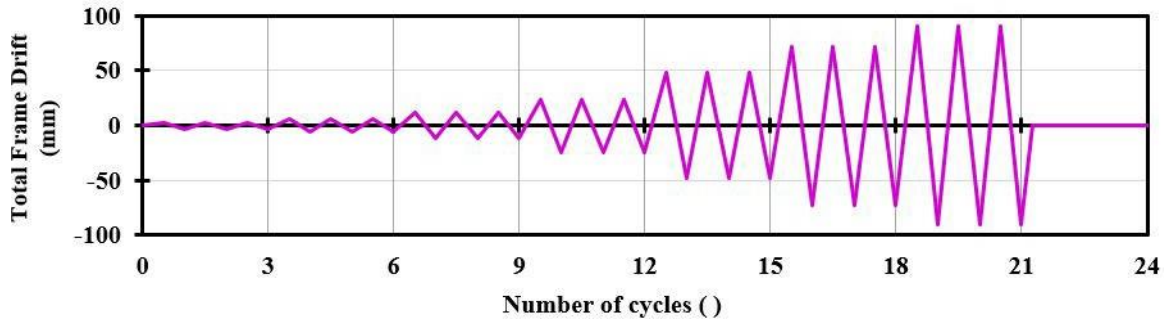

Figure 2-8. Frame test displacement protocol

2.4. Experimental results and observations

2.4.1. AFC in a brace

2.4.1.1. Hysteretic behaviour of AFC in a brace

This section focuses on the hysteretic behavior of an AFC brace that was tested using brand new materials, so the basic sliding mechanism of an AFC brace can be understood without the influence of pre-existing material degradations. The results from the testing of sample A will be used as examples for discussions and they will be compared to the results of the other three samples at the end.

The first a few cycles of the first run of sample A are plotted in Figure 2-9. The horizontal force-displacement curve indicates the stage where full sliding mechanism was activated. The force that triggered full sliding is termed as the peak sliding strength of the AFC brace.

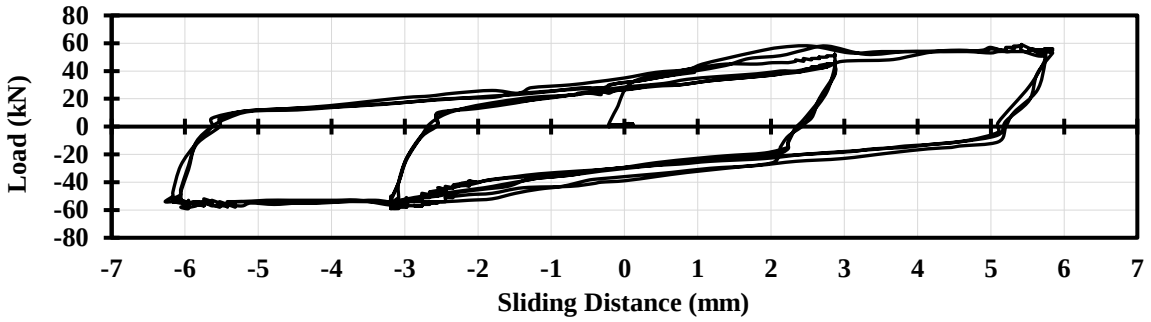

Figure 2-9. Early cycles of the first run

Figure 2-10a shows that the peak shear resistance increased after each low displacement cycle, which is marked as Δ in the figure. There were three contributing factors to this phenomenon. (i) The inclination of the bolts in the AFC detail as sliding of the slotted plate occurred. The maximum increase in the peak sliding force could be partly due to the horizontal force vector acting on the bolts when they tilted to the maximum angle (Figure 2-10b). The horizontal force vector was acting in the opposite direction as the applied driving force, thus provided additional shear resistance to the AFC. This increase in AFC strength was limited by the bolt-hole oversize which limited the maximum bolt inclination. Chanchi [2019] provides a more in depth discussion on the impact of bolt inclination on the hysteretic behaviour of friction connections. (ii) Thermal expansion. As stated by Hatami *et al.*, [2019], surface temperature within a friction connection increases due to friction induced heat, which results thermal expansion. As the plates became slightly thicker as the AFC was heated, it pushed the clamping bolts outwards and induced additional tension in the clamping bolts. And (iii), the residual torsional stress stored in the bolts from the bolts tightening process. As no lubricant was applied on to the bolt threads while the bolts were tightened, the bolts could undergo elastic torsional deformation while the proof load torque was being achieved. Once the bolts had experienced some yielding due to the first two contributing factors described above, the torsional residual stress was released. This means that in subsequent cycles the bolt had no residual stresses, and they were able to provide higher axial forces.

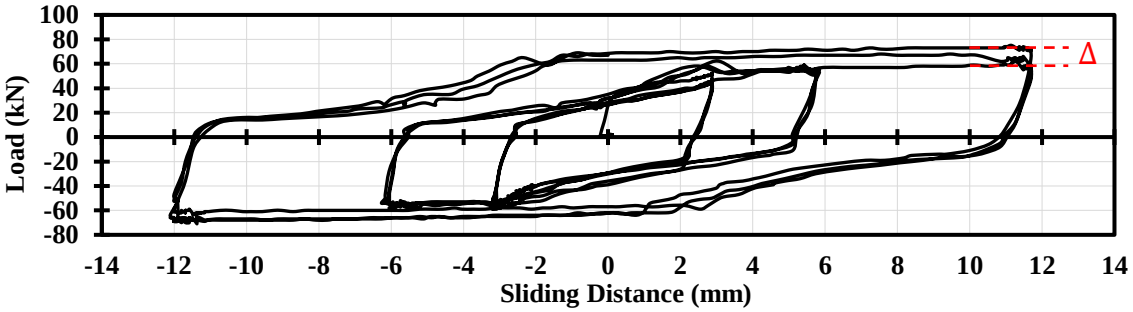

a. Low displacement hysteresis loops of the first run

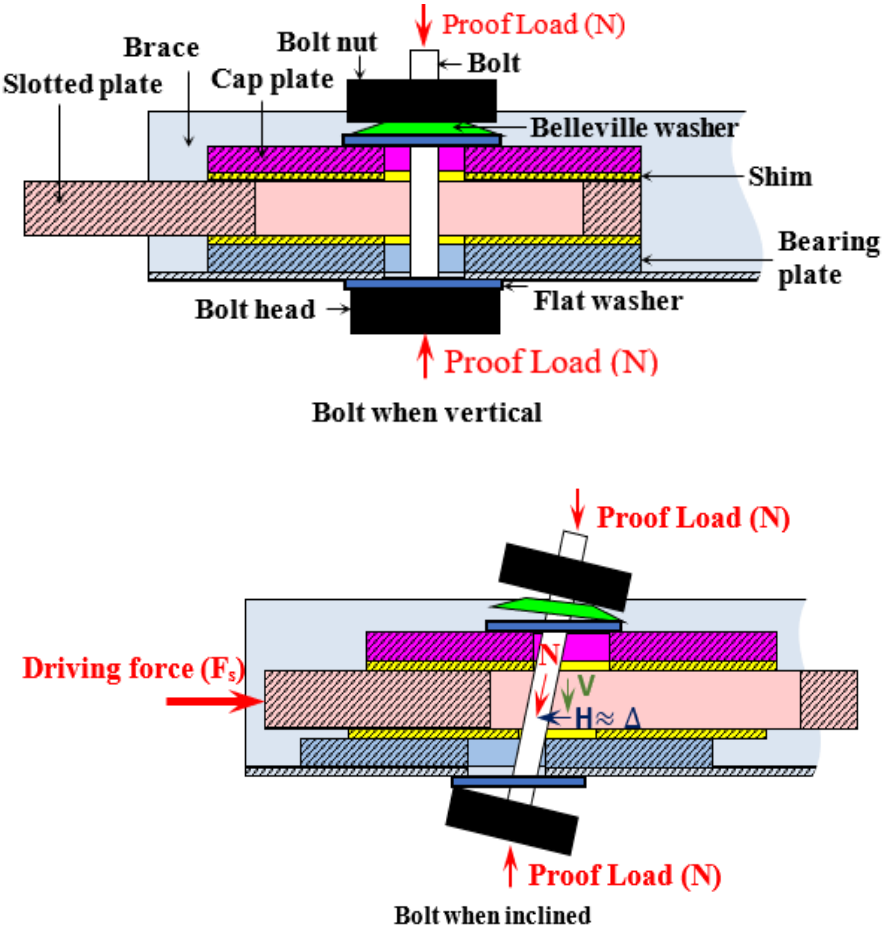

b. Force vectors acting on the bolts

Figure 2-10. Bolt inclination effect

For displacement amplitude greater than 3 mm, the AFC brace hysteresis loops were stable and repeatable as shown in Figure 2-11a. In general, the sliding mechanism of an AFC brace for cycles larger than -3 mm to 3mm could be characterized by four stages labelled I, II, III and IV in Figure 2-11b. The four stages included the stiffness of the AFC brace changing from a very

steep behavior (stage I), to a lower stiffness (stage II and III), and to an almost horizontal tendency with close to zero stiffness (stage IV) during full sliding.

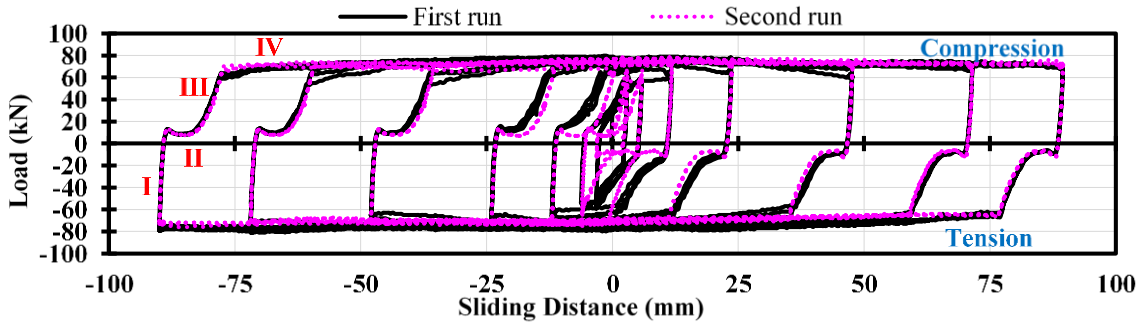

a. Hysteresis loops from AFC brace test

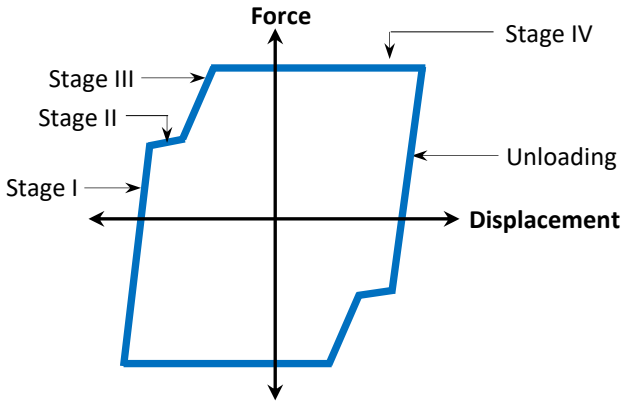

b. Large displacement sliding mechanism illustration

Figure 2-11. AFC brace sliding mechanism development

The changes in the hysteretic behavior of the AFC brace through all the stages are caused by movements at different sliding interfaces, which are described in Figure 2-12. Stages II to IV behaviors are discussed in detail below.

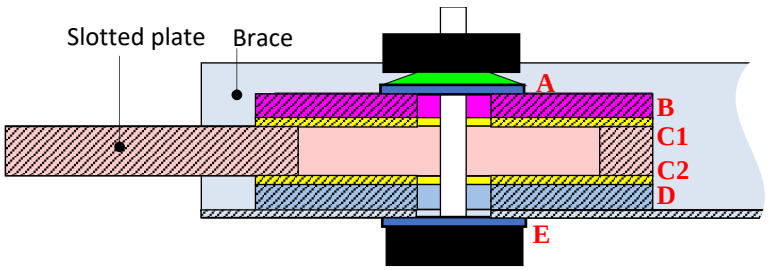

A: Belleville washer – flat washer
B: Top plate – top shim
C1: Top shim – slotted plate
C2: Slotted plate – bottom shim
D: Bottom shim – bearing plate
E: Channel web – flat washer

Figure 2-12. Sliding interfaces within an AFC detail.

(ii) Stage II. The eccentricity between the slotted plate and the channel brace generated a moment at the location of the AFC. This moment was initially resisted by the friction at interfaces C2, as shown in Figure 2-13a. When the resisting moment was overcome, initially sliding occurred at C2, which also triggered sliding at interface D. At this stage, the cap plate, top shim, slotted plate and the bottom shim slide together as a whole for a distance slightly larger than half the bolt-hole oversize of the bottom shim due to bolt tilting (Figure 2-13b). Sliding at interface E began when the edges of the bolt-holes of the bottom shim bore on to the side of the clamping bolts which pushed the bolts for a distance that was equal to the bolt-hole oversize of the bearing plate and the channel web (Figure 2-13c). The designed bolt-hole oversize within the AFC details was 2 mm larger than the clamping bolts diameter. Therefore, for a pair of M16 bolts, the bolt-holes of the cap plate, shims and channel webs were 18 mm in diameter. The slots of the slotted plate were 18 mm wide. At this stage the bolts were free to displace which caused a sudden reduction in stiffness that makes the force-displacement (hysteresis) response nearly flat during this regime. Figure 2-11a shows that stiffness reduction at Stage II became more noticeable as interface E smoothened due to the surface is polished from the frictional motion, which made the bolt head easier to slip. It was observed that during large displacement cycles, sliding at interface D and E occurred almost simultaneously, and sliding at interface E may occur without the bottom shim bearing on the side of the bolts. This phenomenon was also a result of the slackening of the bolts (loss of bolt tension), which provided less clamping force to the overall clamping zone, thus making sliding and slipping easier.

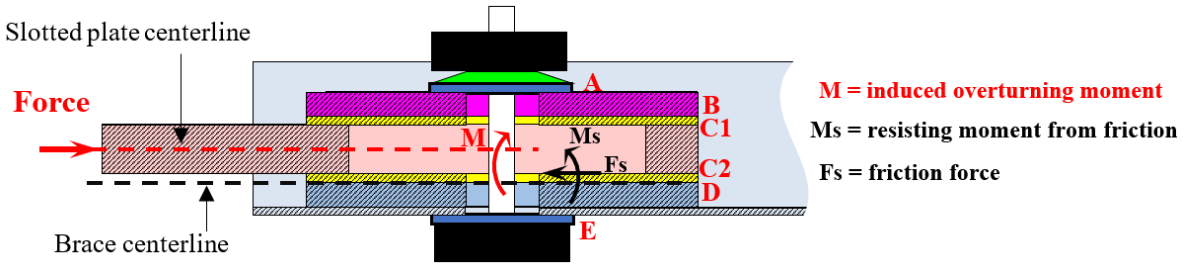

a. Stage II: overturning moment due to applied axial force and resisting moment from the friction at interface C2.

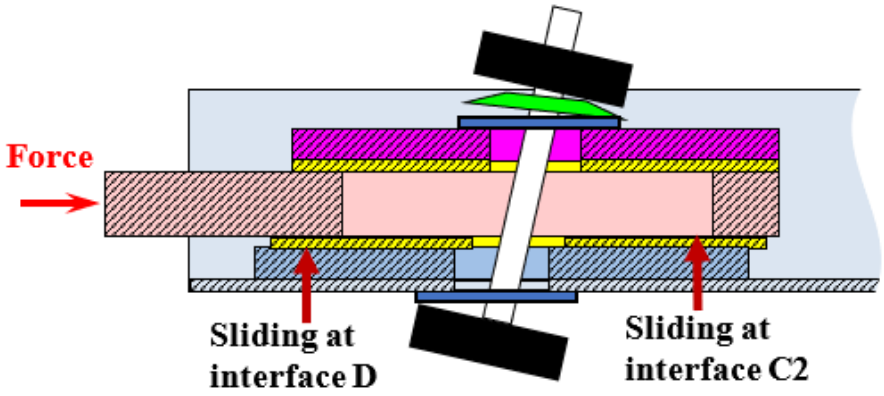

b. Stage II: first sliding occurred at interface D and C2

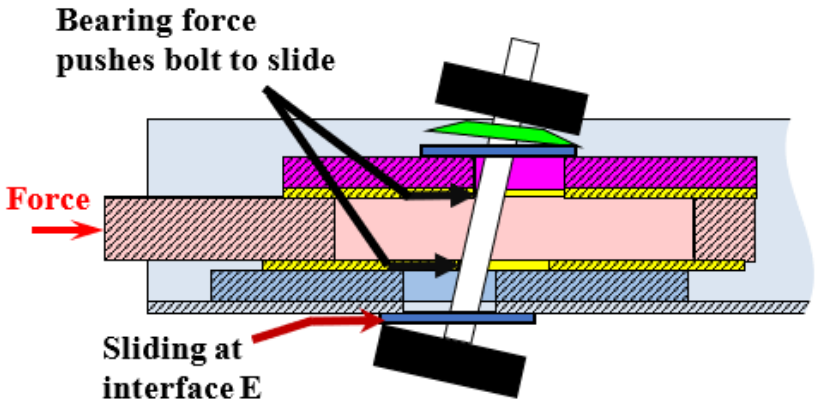

c. Stage II: bottom shim pushed the bolts to induce sliding at interface E

Figure 2-13. Sliding mechanisms at stage II

(iii) Stage III. The bolts came into bearing with the channel web and the cap plate, thus rapidly increasing the stiffness of the AFC brace, as shown in Figure 2-14. Although the stiffness of the AFC brace recovered at this stage, but it was still less than that of the initial stage as shown in Figure 2-11a, as the stiffness at Stage III primarily depended on the flexural stiffness of the

clamping bolts. If more slender bolts were used the Stage III stiffness would reduce. Once Stage III was reached, the shear resistance of the AFC brace increased until Stage IV was reached.

As shown in Figure 2-14 below, the bolts tilted before they came to full bearing. Therefore, the sliding distance from stage II to stage III was the sum of the bolt-hole oversize and the horizontal length of the tilted bolts, which was a fraction of the clamping length of the bolts. This suggests that if the clamping length increases due to thicker connection details and longer bolts are used, the sliding distance from stage II to stage III would also increase.

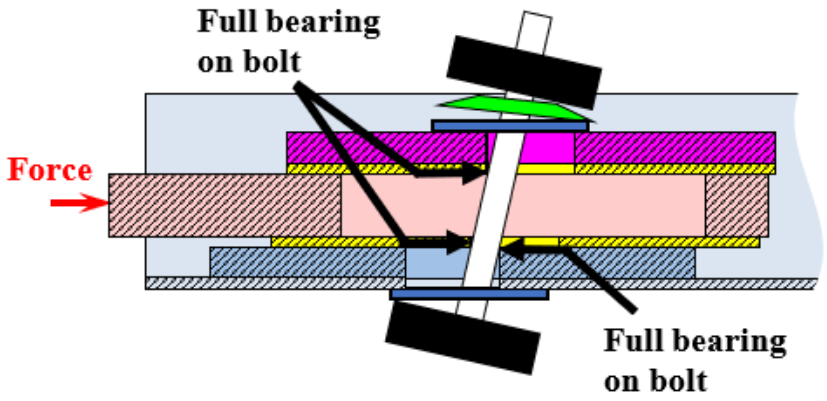

Figure 2-14. Stage III: bolts bore against the top shim, bottom shim and the bearing plate

(iv) Stage IV is termed the full sliding zone as that the sliding mechanism of the slotted plate was fully activated (sliding at interface C1 and C2), and the slotted plate could be driven up to the maximum design sliding distance (Figure 2-15). As shown in Figure 2-11a, the stiffness of the AFC brace at stage IV had an almost horizontal tendency as the slotted plate slid after the sliding resistance was overcome in both interface C1 and C2.

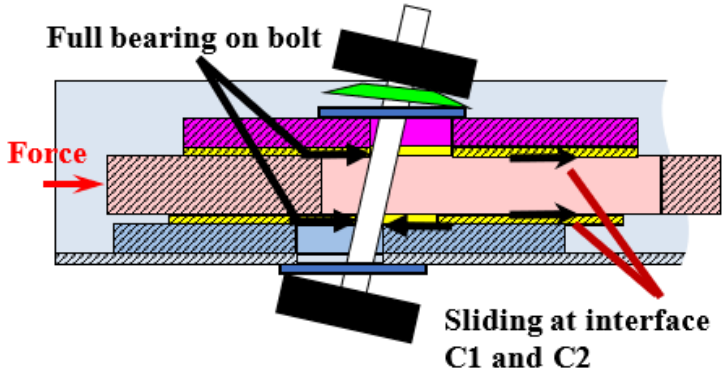

Figure 2-15. Stage IV: full sliding

The first three cycles of the second run (sliding between -3 mm and 3 mm) produced asymmetrical hysteresis loops as shown in Figure 2-16. This was due to the plates (the slotted plate, shims and cap plate) within the AFC details were initially out of alignment as a result of the first run. Therefore, the bolts were bearing on to the plates when moving in one direction and they were free to displace when the force direction was reversed. The plateau line labelled as 'Peak 1' in Figure 2-16 was due to the residual stress on the AFC brace from the actuator after the first run was completed, and the plateau line labelled as 'Peak 2' was due to the bolts pushing the out-of-alignment plates across the interfaces which caused a plateau to appear on the force-displacement response.

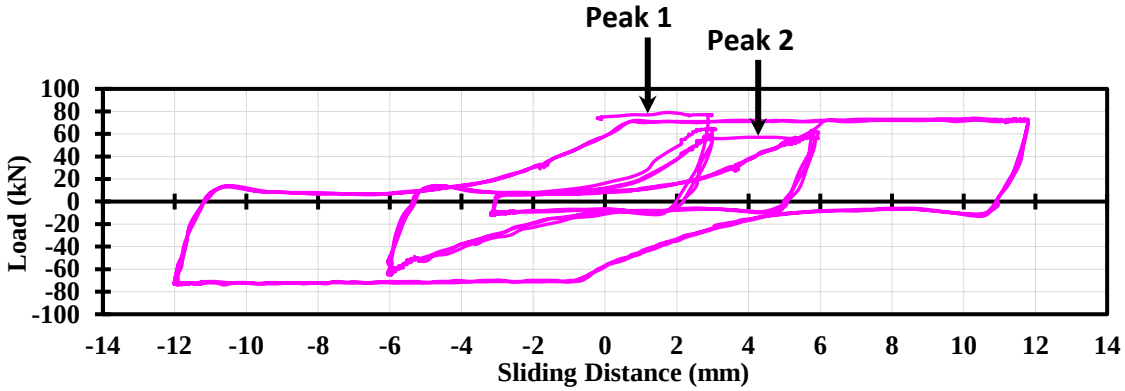

Figure 2-16. Early cycles of the second run

Comparing the early cycles of the second run with those of the first run, although the peak sliding strength of both runs are almost overlapping in Figure 2-17, the second run had lower pre-full sliding stiffness. This phenomenon can be explained by the stage II surface degradation and bolt slackening which have been discussed earlier. Since the bolt slackening and surface degradation reached a stable state at the end of the first run and the start of the second run, no further stage II stiffness reduction was observed in the second run. Therefore, apart from the first cycles, the second run had an overall more stable hysteretic behaviour than the first run.

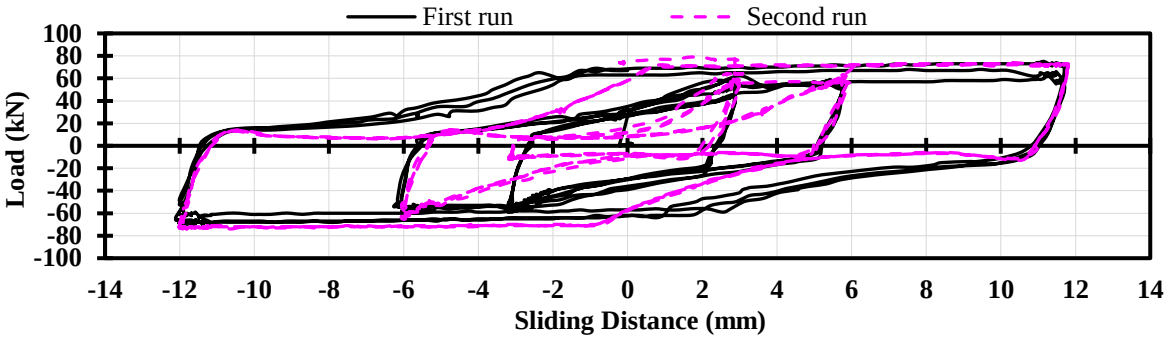

Figure 2-17. Early cycles of the first run and the second run

The first and second run hysteresis loops of sample brace B and C are shown in Figure 2-18a and b, respectively, below. In general, sample brace B and C produced repeatable hysteresis loops with almost flat full sliding (stage IV) curves, and these results are consistent with the observations described above for sample A. For this reason, the AFC brace configuration shown in Figure 2-1 can provide stable and predictable performance over a large amount of travels without the need of bolt retightening and component replacements.

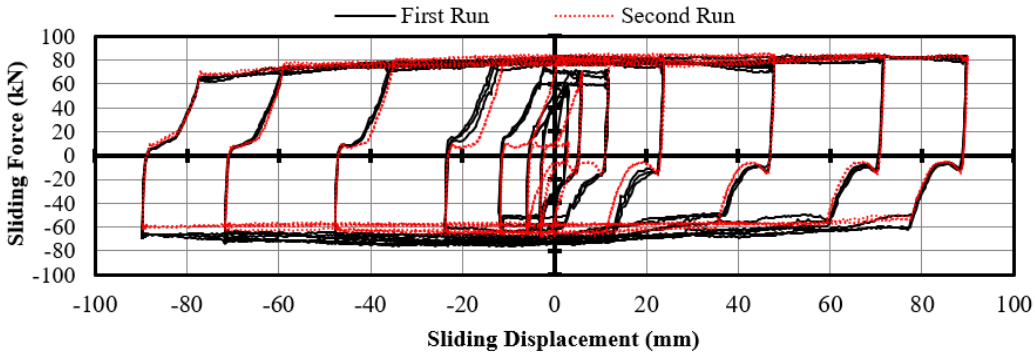

a. Sample B results

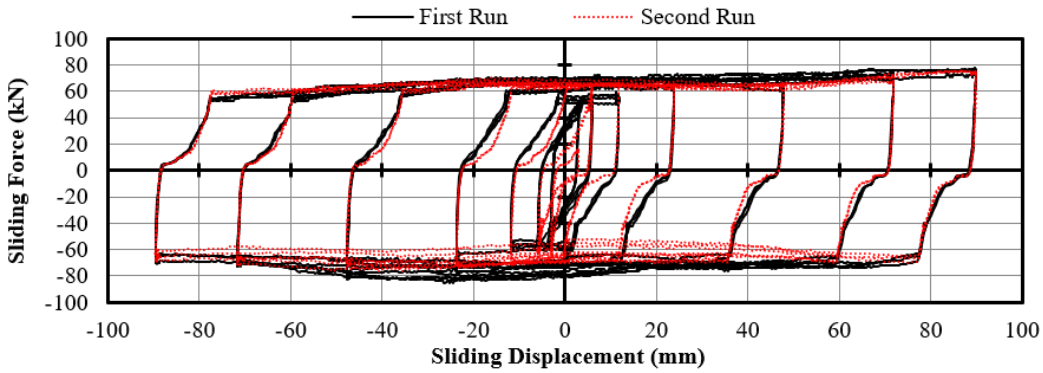

b. Sample C results

Figure 2-18. Hysteresis loops of sample B and C

2.1.1.1.Strength degradation

Strength degradation can be classified into two categories namely intra-test strength loss, which includes strength degradations that occur between the cycles of the same test run, and inter-test strength loss, which describes the differences between the overall maximum shear resistances of different test runs. Intra-test strength loss occurred during the tests was the result of (i) bolt slackening which reduced the sliding force at which the hysteresis loop transited from Stage I to Stage II, and (ii) surface degradations on all sliding surfaces within an AFC detail. Degraded material could be described as fine debris that could be associated with adhesive sliding mechanisms. In this type of sliding mechanism, the product of degradation would either adhere to the sliding surfaces or be pushed out of the clamped zone producing loss of bolt tension, which would reduce the connection's shear resistance [Grigorian & Popov, 1994]. Figure 2-19 below shows surface degradations on the slotted plate and the shims after four runs of testing. It can be seen although scratch marks were present on the plate surfaces but there was no sign of major material deterioration after 80 cycles of testing.

a. Slotted plate deterioration

b. Shim deterioration at the end of the third testing stream (refer to section 2.1.2)

Figure 2-19. Material degradations within the AFC details

As mentioned in the previously, surface degradation at interface E led to significant Stage II stiffness reduction as the smoothened surface made it easier for the bolt head and bottom flat washer to slip. For bolts with large L/d ratios (for this experiment, L/d > 8), bolt yielding and permanent deformation could also contribute to intra-test strength loss. Inter-test strength loss

was partly due to thermal shrinkage as AFC components cooled down after the first test run was completed and the total clamping thickness reduced over time, and since no bolt retightening was applied, tension in the clamping bolts reduced. As shown in Figure 2-11a, the maximum strength loss from the first cycle of the first run to the last cycle of the second run was approximately 10%. This is the combination of both intra-test and inter-test strength loss.

Given that the strength degradation that AFC braces exhibited for a total of 40 cycles distributed across the effective slot of the AFC detail was only up to 10%, and considering that the adopted displacement regime was characterized by a cumulative travel that was approximately 150 times of that referenced by Grigorian & Popov [1994] as the maximum observed in structural systems using braces with slotted bolted connections subjected to severe earthquakes; it can be argued that based on the test results, AFC braces are a low damage solution that can be implemented in new structural systems to dissipate seismic energy, or as a possible solution to upgrade the seismic strength of existing structural systems. As stated earlier, one Belleville washer was placed in each bolt assembly to reduce the loss of bolt tension. However, during the experiments it was observed that the Belleville washer at each bolt assembly was squashed flat when the bolts were tightened to their proof load. Therefore, special considerations need to be made with Belleville washer for them to improve the performance [e.g. Ramhormozian *et al.*, 2017]. However, while the cost of one Belleville spring may be three times of the cost of a bolt-nut combination, and there is increased installation time and labour cost, the possibility of minimizing the loss of bolt tension, and limiting the need for bolt replacement after an event may render it cost effective. It is suggested that further experiment and cost analysis are required on AFC braces using Belleville washers to clearly quantify the benefits and/or disadvantages of using Belleville washers in a friction connection.

2.4.1.2. Strength restoration – bolts and shims replacements

As mentioned earlier, the testing plan for the AFC braces included replacing the bolts and shims as an attempt to restore the peak sliding strength back to the ‘brand new’ condition, without replacing the slotted and cap plate. Recall from earlier, after two runs of testing using ‘brand new’ materials, bolts were replaced, and two more runs were conducted using the new bolts. Then both the bolts and shims were replaced before performing the last two runs using the same slotted plate. Figure 2-20, Figure 2-21 and Figure 2-23 show the hysteresis loops of sample A, B and C, respectively, at bolt and shim replacements.

The results for sample A showed that after the bolts were replaced. For the displacement cycles up to 48 mm, bolt replacements restored the peak sliding force back to 70 – 80 kN, which was similar to the range of peak sliding forces for brand new materials, and the hysteretic behaviour of the brace was stable. However, at the first 72 mm displacement cycle, the shims and the cap plate started to become out-of-alignment due to surface degradations and debris adhering on to the sliding surface, which lead to non-uniform sliding. Misalignments induced additional MPV actions on to the clamping bolts, which explains the increase in peak sliding force when the brace was pulled from 48 mm to -72 mm, as shown in Figure 2-20a. This caused the bolts to yield and permanently deform which reduced the clamping force provided by the bolts, therefore from this cycle onwards, both peak strength and stability of the brace reduced. At this stage, although the brace was still able to provide energy dissipation, the peak sliding force became unpredictable as it ranged from 30 kN to 100 kN at different sliding displacements, especially in the second run where bolt-yielding and surface degradation were worsened.

After both the bolts and shims were replaced, some strength was restored initially, and comparing to Figure 2-20a, the hysteretic stability was improved in general as the degraded shims were replaced with brand new shims, as shown in Figure 2-20b. However, plate misalignments still occurred due to the rough surfaces of the heavily degraded slotted at this stage, which led to bolt-yielding due to high MPV actions and significant strength degradations.

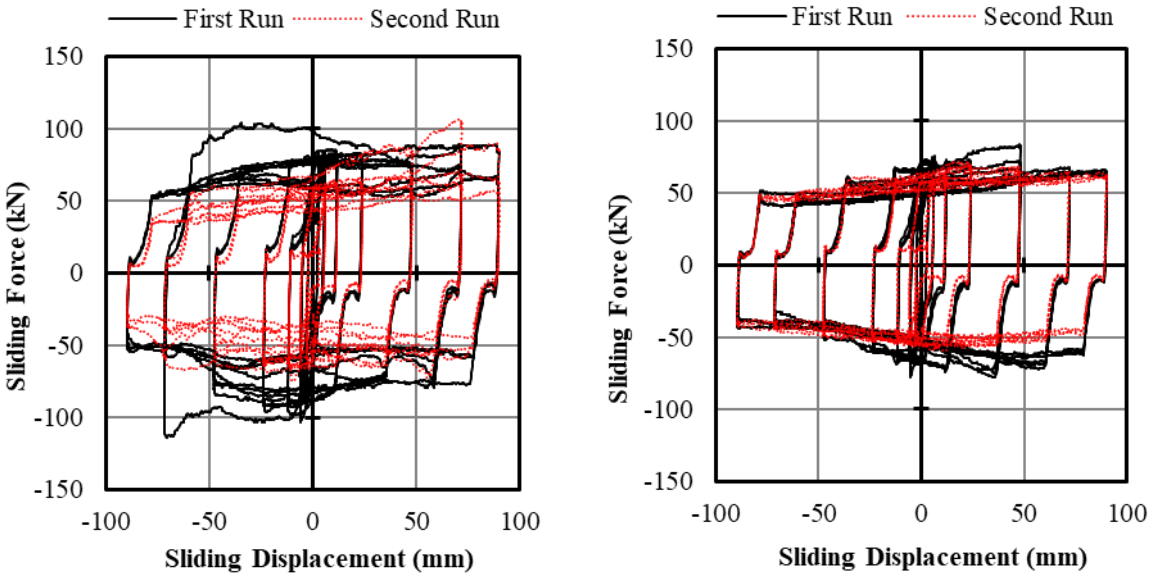

a. Bolt replacements b. Shim replacements

Figure 2-20. Sample A results after bolts and shim replacements

Figure 2-20a shows that sample B produced more stable hysteresis loops than sample A when only the bolts were replaced after the initial two runs, and the maximum strength degradation was close to 10% for sliding displacements less than 90 mm. As the slotted plate was pulled towards the first 90 mm displacement cycle, the bolts reached the end of the slots which caused a sudden spike in strength as the bolts underwent high MPV actions that led to bolt-yielding. Although the setup was not designed for the bolts to reach the slot ends, this occurred could due to a combination of permanent bolt deformation and instrumentation error, which meant that the actual travel of the slotted plate was more than what was measured by the extensometer. After this cycle, the brace strength degraded significantly, up to 20 kN at the end of the first run.

In the second run, the same phenomenon occurred which yielded the bolts further and caused higher strength degradation. At the end of the second run, the peak sliding force was approximately 30 kN lower than the peak sliding force at the beginning of the first run. The strength degradation for these two runs were primarily attributed to bolt slackening due to permanent deformations, and the smooth hysteresis loops indicated the surface degradations were not heavy during these two runs.

Although this phenomenon was unintentional, the positive take from this observation was the bolts did not fracture due to high accidental MPV actions, and this suggested the high ductile grade 8.8 galvanised bolts should be used for friction connections to minimise the chance of bolt fracture if slotted plate travels more than the design displacement.

Figure 2-21 shows the hysteretic behaviour of sample B after the replacements of the clamping bolts and shims. The first run was stable, strength degraded up to approximately 25 kN at the end of the first run. The convex full sliding curve at 90 mm displacement cycles indicated minor surface degradations as the sliding interfaces became smoother near the center of the slots. This can be explained by Figure 2-22 which shows the clamping stress distribution provided by the bolts. The clamping stress is the highest at the location of the bolts, and it decrease as the distance away from the bolt increases [Ito (1979)]. The debris from the surface degradations was pushed out of the interfaces, therefore, the surface degradations did not affect the stability of the brace. In the second run, the surface degradations worsened, and the debris started to adhere on to the sliding interfaces affecting the stability of the brace. Similar to what was observed during the testing of sample A, plate misalignments occurred, and the bolts were

yielded as a result of high MPV actions, which led to significant strength degradations. The largest peak strength difference between the first and second run was approximately 40 kN.

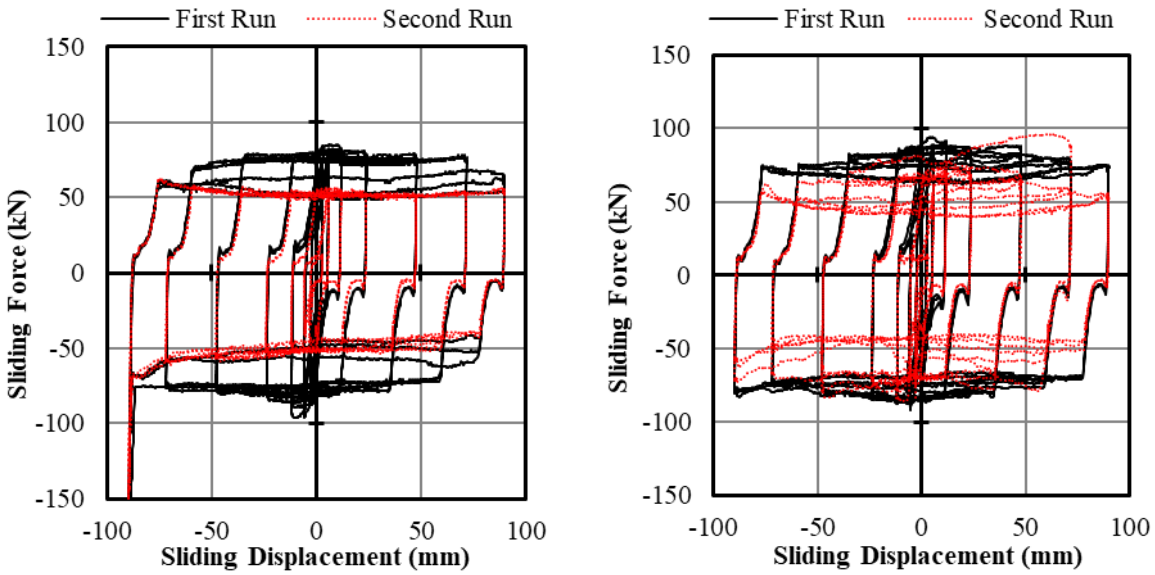

a. Bolt replacements b. Shim replacements

Figure 2-21. Sample B results after bolts and shim replacements

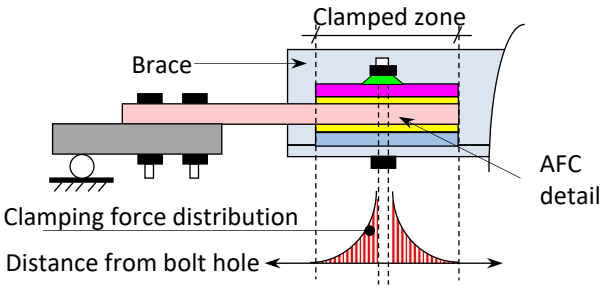

Figure 2-22. Bolt clamping stress distribution theory according to Ito [1979]

Figure 2-23 below shows that the hysteresis loops of sample C after bolt and shim replacements also reflect the observations made during the testing of sample A and B. In the very last run after shim replacements the full sliding behaviour became unpredictable with the peak sliding force varying between 45 kN to almost 100 kN, as shown in Figure 2-23b. This was the result of heavily degraded slotted plate, although the degradation of the shims was not severe, as shown in Figure 2-23b.

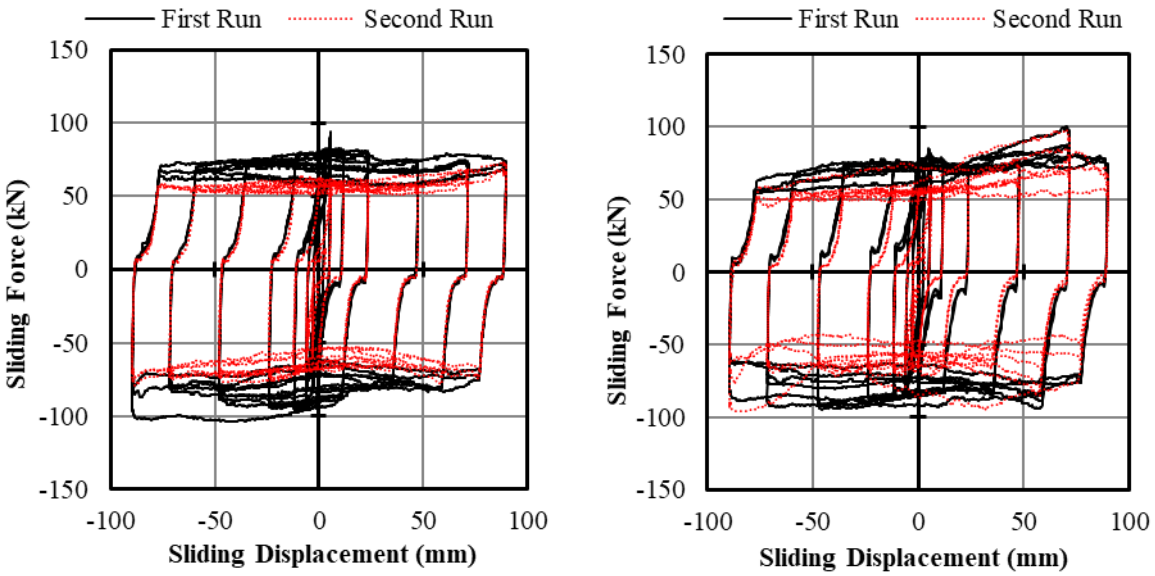

a. Bolt replacements

b. Shim replacements

Figure 2-23. Sample C results after bolts and shim replacements

As a conclusion to be observations made above, bolt slackening or tension loss can lead to reductions in the peak sliding force of a friction brace, but it only slightly affects the stability of the hysteretic behaviour of a friction brace. Heavy material degradation can affect the performance stability of a friction brace, and as mentioned earlier, it can also indirectly induce high MPV actions on the clamping bolts that leads to bolt-yielding and strength degradation. For this reason, the amount of material degradation on the surfaces where sliding occurs is the factor that governs how many cycles can a friction brace undergo before it loses its stability and start to show significant strength loss.

As a retrofit strategy for friction braces, it is recommended to access the conditions of the sliding interfaces after a major seismic event. Figure 2-24a below shows a slightly degraded slotted plate and Figure 2-24b shows a heavily degraded slotted plate. If only minor material degradation is shown on the surface, then only the clamping bolts need to be replaced. If the slotted plate or a shim is heavily degraded with deep scars shown on the surfaces, as displayed in Figure 2-24b, then that plate needs to be replaced. The results presented above indicate that a friction brace can still produce unstable full sliding behaviour if the slotted plate has damaged surfaces, but the shims are almost new. When accessing the surfaces of a set of friction connection details, it is also essential to clean them and brush off any debris left between the sliding interfaces from previous seismic events.

a. Lightly degraded slotted plate after one run of testing (sample B)

b. Severely degraded slotted plate with deep scars after six runs of testing (sample B)

Figure 2-24. Material degradations on the surface of the slotted plate

2.4.1.3. Out-of-plane behaviour

Brace out-of-plane behaviour as it bends about its weak axis occurs with an AFC brace during an axial test. Out-of-plane deflections were exhibited along the AFC brace because the load transferred from the slotted plate to the channel was eccentric, thus the brace was subjected to a moment that produces bending around of one of the principal axis of the brace [Chanchi *et al.*, 2014]. Figure 2-25 shows an illustration of how the moment was created at the location of the AFC detail when an AFC brace was subject to compression. The magnitude of this moment depended on (i) the total clamping force used to assemble the connection, (ii) the effective friction coefficient, (iii) the distance between centroids of the slotted plate section and the brace section and, (iv) the bolt inclination. Because of this bending moment, the non-clamped zones of the slotted plate and the brace bent, so that when the sliding mechanism was activated, the edge of the slotted plate act as a point load and pried against the bottom shim when in compression, as shown in Figure 2-25b.

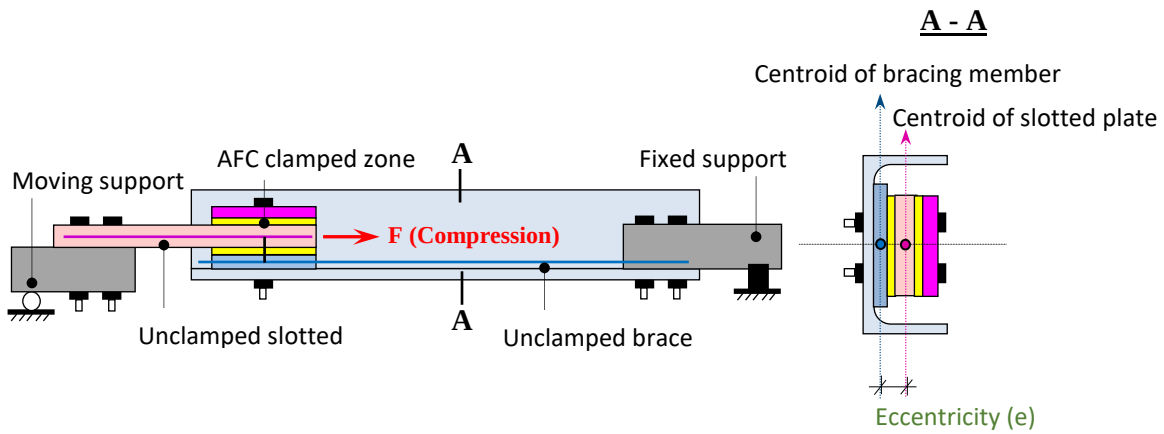

a. Eeccentricity between the brace member and the slotted plate

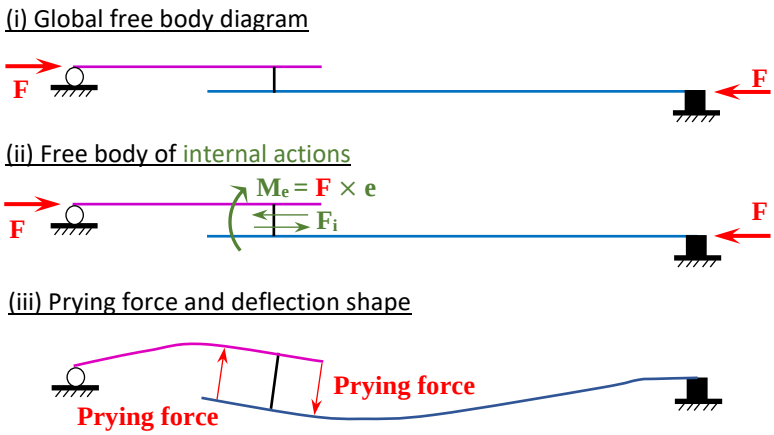

b. Free body diagram and the prying forces

Figure 2-25. Out-of-plane deflections and prying forces in AFC brace in compression

When in tension, this force was reversed, and the slotted plate pried against the cap plate. As the prying forces were concentrated loads acting at one location instead of uniform distributed loads across a sliding interface, they affected the stability of the AFC detail. For that reason, the lines showing the full sliding regions of the hysteresis loops were not perfectly smooth as expected in friction devices as shown in Figure 2-11a.

Maximum deflections were developed at full strokes (+/- 90 mm), Figure 2-26 summarises the maximum vertical (out-of-plane) deflections recorded at various locations along the brace span. It shows the maximum vertical deflections of the AFC brace when it was loaded in tension and compression were 3.8 mm and 3.2 mm, respectively.

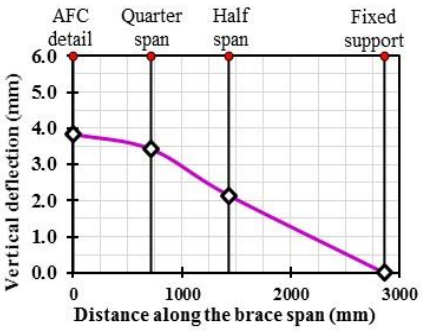

a. Vertical deflections of braces in tension for a sliding distance of 90mm

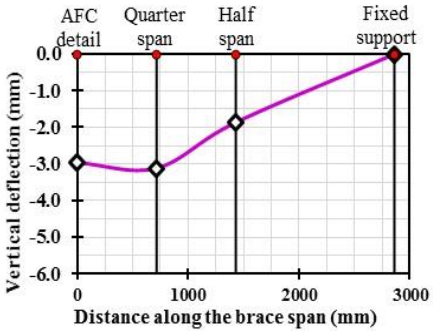

b. Vertical deflections of braces in compression for a sliding distance of 90mm

Figure 2-26. Vertical deflections in AFC braces in tension and compression

2.4.2. AFC in a singly braced frame

2.4.2.1. Hysteretic behaviour of the unbraced frame

Before the AFC brace was fitted on the experimental frame setup, the frame was subject to load lateral load reversals unbraced. This test was to set a benchmark by determining the hysteretic behavior of the bare frame so it could be compared with the hysteresis loops of the frame after it was equipped with a friction brace.

The hysteretic behaviour of the bare frame presented in Figure 2-27 is approximately bilinear with no post-elastic stiffness. The initial elastic stage was from the lateral stiffness of the frame. The final stage with constant load was caused by the generation of two hinge mechanisms at the connections of the long beam with the two short beams. Hinges were developed when the axial force on the beam overcame the shear resistance induced by the clamping forces from the bolts, which were snug tightened using an air impact wrench, at the beam-to-beam connections. This allowed the central beam section to rotate so that the frame behaved with two frictional hinges at the beam and two pins at the base of columns. This process is illustrated in Figure 2-28a and b. Figure 2-28c shows signs of material damage (the curved scratch marks) on the beam webs due to the rotations of the connecting plates. The maximum force achieved by the bare frame was 15 kN.

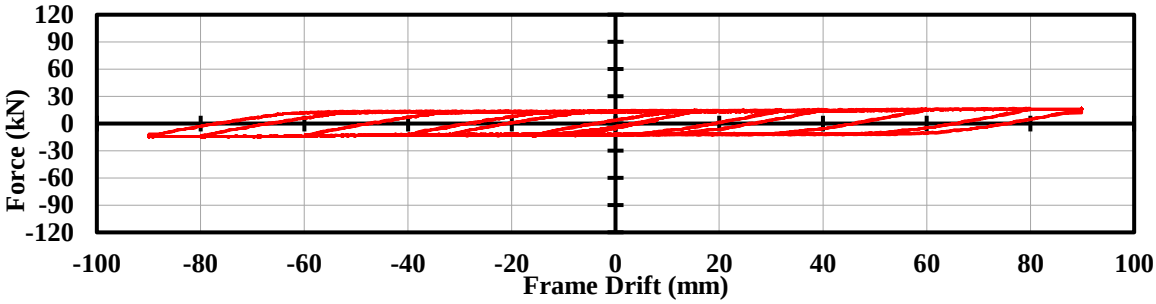

Figure 2-27. Hysteretic behaviour of the bare frame

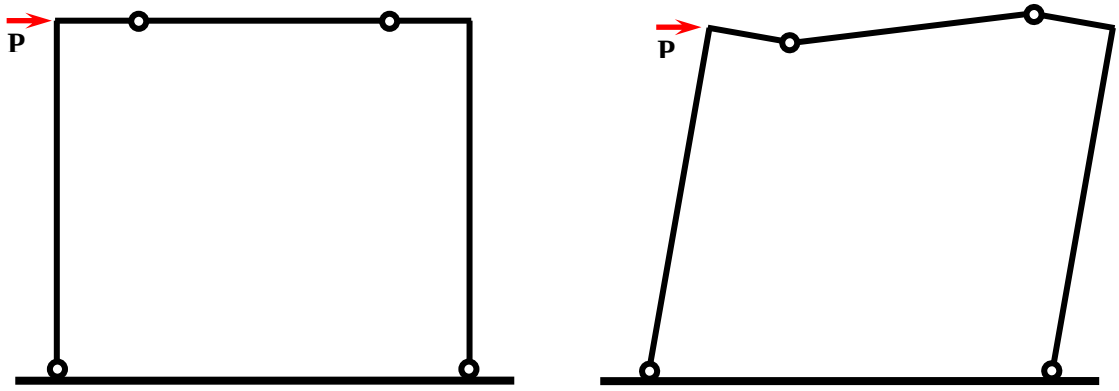

a. Mechanism frame with four hinges

b. Deformed shape of the mechanism frame

c. Material degradation on the beam webs due to rotations at the beam-to-beam connections

Figure 2-28. Frictional hinges at beam-beam connections

2.4.2.2. Hysteretic behaviour of the singly braced frame

Figure 2-29 shows the hysteretic behaviour of the overall AFC frame (i.e. bare frame plus a single diagonal AFC brace). The hysteretic loops of the AFC frame can be described as stable, and similar to those of the AFC brace shown in Figure 2-11a, they can also be divided in the same four stages as described in Section 2.3.1.1. Comparing to the hysteresis loops of the brace tests, the stage IV lines of the frame tests are slightly sloped, this was due to the elastic deformation of the frame components. As the full sliding mechanism was developed in the AFC brace, the primary structural components and brace sub-system components remained elastic. If the AFC brace was tested as a part of a moment resisting frame with fixed bases, the post-yielding slope would be expected to be much steeper. The maximum frame force at the peak drift is approximately sum of the maximum force of the bare frame (Figure 2-27) and the maximum force of the AFC brace alone (Figure 2-11a). For that reason, it can be said that the behaviour of AFC frame was significantly influenced by the behaviour of the AFC brace.

When comparing the hysteresis loop of the bare frame with the hysteresis loop of the AFC frame, the force at the initiation of nonlinear behaviour in the AFC frame is four times greater than the similar force in the bare frame showing that by adding the AFC brace to the bare frame the strength could be increased. Energy dissipation, which is represented by the total area enclosed by the hysteresis loops, was also improved without inducing any damage to the primary components of the frame. For these reasons, the AFC brace significantly enhanced the lateral performance of the frame.

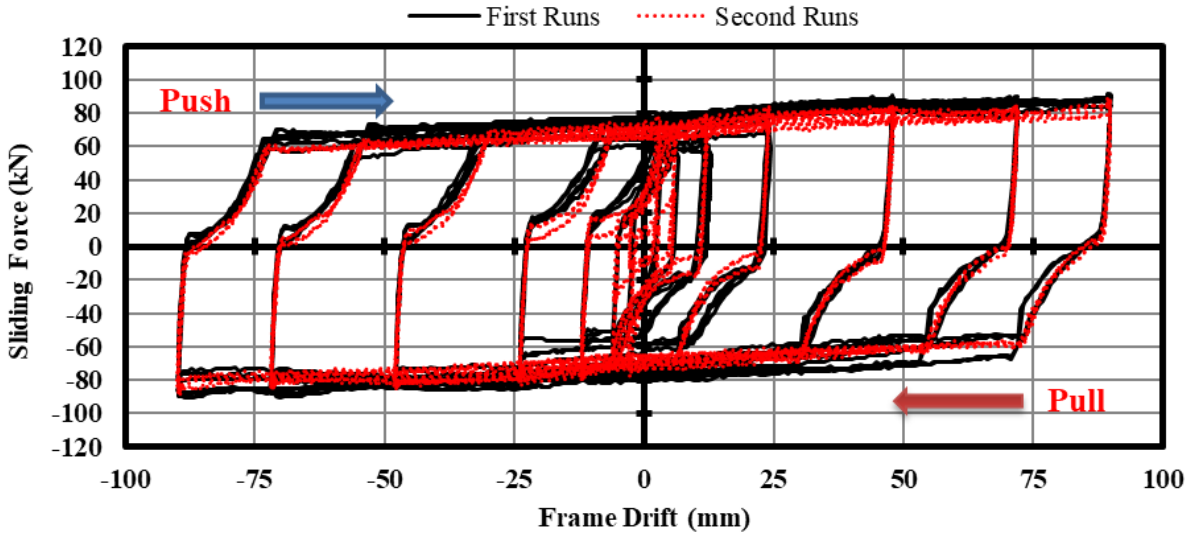

Figure 2-29. Hysteretic behaviour of the singly braced frame

2.4.2.3. Bearing of the sliding bolts

When the AFC braced frame was pushed laterally, the beam-column joints rotated, which caused the slotted plate to slide at a small angle adjacent to the bracing member. As the AFC brace was not subjected to a pure axial elongation, which caused in-plane rotations at the AFC, and the two M16 bolts started to rub against the sides of the slots during sliding. The rubbing started when the frame drift was less than 1%, and as a result, scratches were left on the bolt surfaces as shown in Figure 2-30. This phenomenon did not have a significant impact on the performance stability of the AFC. However, as mentioned earlier the stage IV lines of the brace frame are slightly sloped as shown in Figure 2-29, and the bolt bearing phenomenon was believed to be the one of the reasons. Since the bolts were rubbing against the slot edges which added extra force required to slide the slotted plate. Also, as the frame displacement increased, the beam-column joints rotated more, which induced more in-plane rotation at the location of AFC causing the bolts to bear harder against the slotted plate. For this reason, the sliding strength of the braced frame was higher at larger drifts. This in-plane rotation induced bearing force is illustrated in Figure 2-31.

Figure 2-30. Scratches shown on the shank surfaces of the bolt

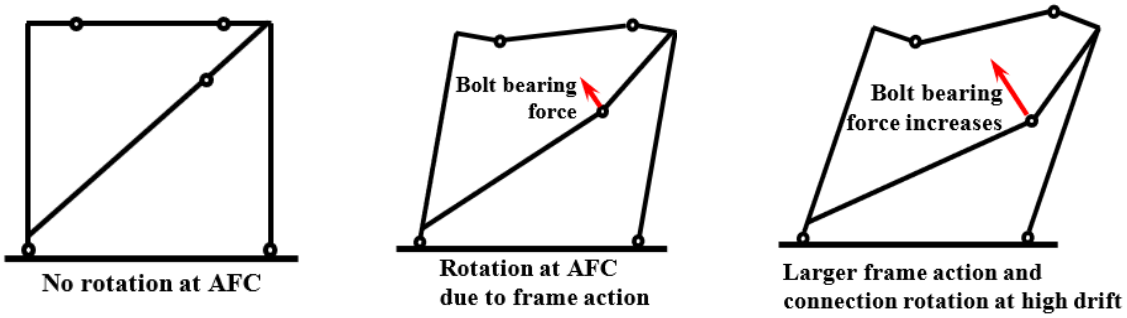

a. Frame at zero drift b. Frame at small drift c. Frame at high drift

Figure 2-31. Vertical deflections in AFC braces in tension and compression

2.5. Effective coefficient of friction

Equation 2.1 [Chanchi *et al.*, 2014] can be used to calculate the effective friction coefficient (EFC) of an AFC brace. $F_{sliding}$ is the average sliding force assessed across the tensile and compressive full sliding zones (stage IV), F_{proof} represents the proof load of the clamping bolts. This equation considers two shear planes and two clamping bolts.

$$\mu_{eff} = \frac{F_{sliding}}{2 \times 2 \times F_{proof}} \tag{2.1}$$

The average effective friction coefficients (EFC) of the AFC brace tests and the AFC braced frame tests are shown in Figure 2-32a and b, respectively, at various locations. The effective friction coefficient varies with changes in sliding distance, this was a result of uneven material degradations at sliding interfaces, as well as tilting of the clamping bolts which caused slight variations in the clamping force. The value for the effective friction coefficient ranges from 0.16 to 0.195 for AFC brace tests and 0.188 to 0.194 for braced frame tests, which indicates that all the recorded values of EFC are lower than the assumed value of 0.21. Therefore, the average EFC shall be reduced to 0.18 based on the experimental results. The understrength and overstrength factors shall be kept at 0.7 and 1.4, respectively, to cover the lower and upper bounds of the peak sliding force.

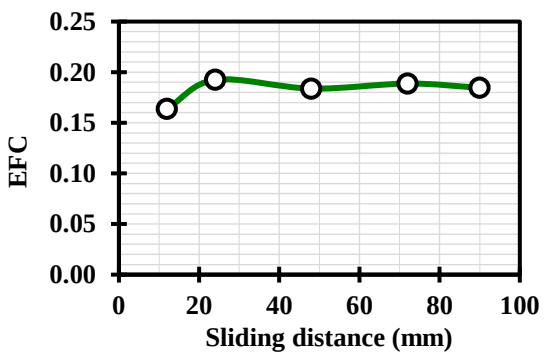

a. Effective coefficient of friction of AFC braces tested alone

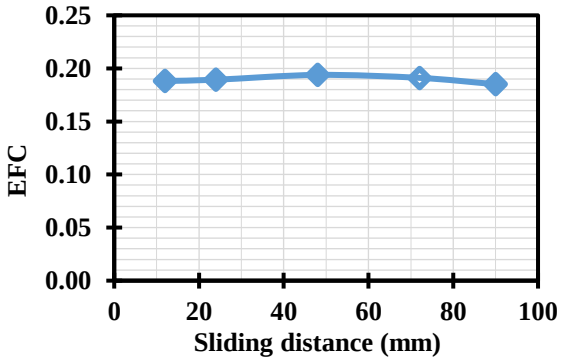

b. Effective coefficient of friction of AFC braces tested as part of a braced frame

Figure 2-32. Effective friction coefficient

2.6. Design recommendations of AFC braces

2.6.1. Capacity design procedure

Step 1: Prediction of sliding force.

The dependable sliding force of an AFC brace ($\phi_u F_s$) gives a lower bound value of force that can trigger full sliding in an AFC detail. The dependable sliding force can be defined by Equation 1.1.

$$\phi_u F_s = \phi_u \times n_b \times n_s \times \mu \times N_{tf} \quad (1.1)$$

Where:

ϕ_u = Understrength factor to account for the overestimation of μ, use 0.7 as recommended by MacRae & Clifton [2015]

n_b = Number of bolts

n_s = Number of sliding surfaces

μ = Friction coefficient, use 0.18 for Bisalloy 500 – Mild Steel interface

N_{tf} = Proof load of bolt used

For AFC, the dependable sliding force is primarily controlled by the number of bolts and size of the bolts used (n_b and N_{tf}). μ can also be changed based on the materials used at the sliding interface. However, this is not recommended as tests conducted by Chanchi *et. al.*, [2015] proved that Bisalloy 500 – Mild Steel interface produces the most stable and symmetrical hysteresis loops.

To perform capacity design, it is essential to calculate the potential overstrength of an AFC, by using an overstrength factor (ϕ_o) of 1.4 as recommended by MacRae & Clifton [2015]. This gives an upper bound of the full sliding force.

Step 2: Design of the bracing member.

The section compressive capacity of the bracing member shall satisfy:

$\phi_u N_s \geq N_s^*$

$N_s^* = \phi_o F_s$

ϕ_o = Overstrength factor, use 1.4 as recommended by MacRae & Clifton (2015).

$\phi_u N_s = \phi_u \times K_f \times A_n \times f_y$ *(NZS3404, Eqn. 6.2.1.)* (2.2)

Where:

ϕ_u = Strength reduction factor, use 0.7 [MacRae & Clifton 2015].

A_n = Net cross – section area of the brace.

f_y = Minimum yield stress of the brace.

K_f = Form factor *(NZS3404, Clause 6.2.3)*

$= \frac{A_e}{A_g}$ *(NZS3404, Clause 6.2.2.)* (2.3)

The nominal compressive member axial capacity of the brace shall satisfy:

$\phi_u N_c \geq N_c^*$

$N_c^* \geq \phi_o F_s$

ϕ_o = Overstrength factor, use 1.4 [MacRae & Clifton 2015].

$\phi_u N_c$ = min $(\phi_u N_{cx}, \phi_u N_{cy})$, need to check both x and y axis.

$\phi_u N_c = \phi_u \times \alpha_c \times K_f \times f_y \times A_n$ *(NZS3404, Clause 6.3.3)* (2.4)

Where:

ϕ_u = Strength reduction factor, use 0.7 [MacRae & Clifton 2015].

A_n = Net cross – section area of the brace.

f_y = Minimum yield stress of the brace *(NZS3404, Clause 6.2.2)*

α_c = Member slenderness reduction factor, NZS3404 table 6.3.3(2). Determined using member section constant α_b (table 6.3.3(1)) and modified member slenderness (λ_n). Since both x and y need to be checked, therefore α_{cx}, α_{cy}, λ_{nx} and λ_{ny} are required.

α_b = 0.5 for flame cut plate to account for residual stress.

$$\lambda_n = \frac{L_e}{r}\sqrt{K_f}\sqrt{\frac{f_y}{250}} \quad (2.5)$$

The effective length of the brace in compression can be defined as:

$$L_e = K_e L \text{ (NZS3404, Clause 6.3.2)} \quad (2.6)$$

Where:

K_e = The member effective length factor determined in accordance with Clause 4.8.3.2.

The brace should be considered as a sway cantilever member with one end fixed and free rotation at the other end. According to Clause 4.8.3.2, which describes members with idealized end restraints, for such case $K_e = 1.2$ should be used for the brace.

The nominal section tensile capacity of the slotted shall satisfy:

$$\phi_u N_t \geq N_t^* \text{ (NZS3404, Clause 7.2.1)}$$

$$\phi_u N_t = min\left(\phi_u A_g f_y, \phi_u 0.85 k_{te} A_n f_u\right) \text{ (NZS3404, Eqn. 7.2.1 \& 7.2.2)} \quad (2.7)$$

Where:

A_g = The gross area of the cross section of the slotted plate.

A_n = Net cross – section area of the slotted plate.

f_y = The minimum yield stress of the slotted plate.

k_{te} = The correction factor for force distribution, determined in accordance with NZS3404, Clause 7.3. For the case of the slotted plate, k_{te} shall be taken as 1.0 according to Clause 7.3.1.

f_u = The ultimate tensile strength of the slotted plate.

f_u = 430 MPa for 21 $mm \leq t \leq 150\ mm$ *(AS/NZS3678)*

As a conclusion, the resultant axial load capacity of the slotted plate is defined as:

$$\phi_u N = min\ (\phi_u N_s\ , \phi_u N_c\ , \phi_u N_t) \tag{2.8}$$

The brace can be subject to three types of moment, they are (i) in-plane moment due to the rotation (M_x^*) of the beam – column joint, (ii) out-of-plane moment due to laterally load acting in the transverse direction (M_y^*), and (iii) eccentricity due to the asymmetrical configuration of the AFC brace (M_e^*) (Figure 17). Design of the brace needs to satisfy both section considerations and member considerations using the general methods from NZS3404.

For section considerations, the following shall be satisfied:

f_1 = Factor of safety *(NZ3404, Clause 8.3.4.1).*

$$= \frac{N^*}{\phi_u \times N_s} + \frac{M_x^*}{\phi_u \times M_{sx}} + \frac{M_e^* + M_y^*}{\phi_u \times M_{sy}} \leq 1 \tag{2.9}$$

Where:

M_s = Section moment capacity *(NZS3404, Eqn. 5.2.1).*

$$= Z_e f_y \tag{2.10}$$

If design compressive force dominates the axial capacity of the brace (compression member), the following shall be satisfied for member considerations:

f_2 = Factor of safety *(NZS3404, Clause 8.4.5.1).*

$$= \left(\frac{M_x^*}{\phi_u \times M_{cx}}\right)^{1.4} + \left(\frac{M_e^* + M_y^*}{\phi_u \times M_{iy}}\right)^{1.4} \leq 1 \quad (2.11)$$

Where:

M_{cx} = Member moment capacity about the x-axis.

$$= min(M_{ix}\ ,\ M_{ox})$$

M_i = Member in-plane moment capacity *(NZS3404, Clause 8.4.2.2.1).*

$$= M_s\left(1 - \frac{N^*}{\phi_u N_c}\right) \quad (2.12)$$

M_{ox} = Member out-of-plane moment capacity *(NZS3404, Clause 8.4.4.1.1).*

$$= M_{bx}\left(1 - \frac{N^*}{\phi_u N_{cy}}\right) \quad (2.13)$$

M_{bx} = Nominal member x(strong)-axis moment capacity without full lateral restraint. *(NZS3404, Eqn. 5.6.1.1(1))*

$$= \alpha_m \alpha_s \phi_u M_{sx} \quad (2.14)$$

α_m = Moment modification factor *(NZS3404, Eqn. 5.6.1.1(2); or table 5.6.1).*

$$= \frac{1.7 M_m^*}{\sqrt{\left[(M_2^*)^2 + \left(M_3^*\right)^2 + (M_4^*)^2\right]}} \leq 2.5 \quad (2.15)$$

M_m^* = Maximum design bending moment in the segment.

$M_2^*\ , M_4^*$ = Design bending moments at the quarter points of the segment.

M_3^* = Design bending moment at the mid – point of the segment.

α_s = Slenderness reduction factor *(NZS3404, Eqn. 5.6.1.1(3)).* (2.16)

$$= \quad 0.6\left\{\sqrt{\left[\left(\frac{M_{sx}}{M_{oa}}\right)^2 + 3\right]} - \left(\frac{M_{sx}}{M_{oa}}\right)\right\}$$

M_{oa} = Reference buckling moment *(NZS3404, Eqn. 5.6.1.1(4)).*

$$= \quad \sqrt{\left\{\left(\frac{\pi^2 E I_y}{{L_e}^2}\right)\left[GJ + \left(\frac{\pi^2 E I_w}{{L_e}^2}\right)\right]\right\}} \tag{2.17}$$

G, E = Elastic moduli.

I_y, I_w, J = Section constants.

L_e = Effective length of the bracing member.

If design tensile force dominates the axial capacity of the brace (tension member), the following shall be satisfied for member considerations:

f_3 = Factor of safety *(NZS3404, Clause 8.4.5.2).*

$$= \quad \left(\frac{M_x^*}{\phi_u \times M_{tx}}\right)^{1.4} + \left(\frac{M_e^* + M_y^*}{\phi_u \times M_{ry}}\right)^{1.4} \leq 1 \tag{2.18}$$

Where:

M_{tx} = $min(M_{rx}, M_{ox})$

M_{ry} = Nominal section moment capacity reduced by axial tension *(NZS3404, Clause 8.3.3.1).*

$$= \quad M_{sy}\left(1 - \frac{N^*}{\phi_u N_t}\right) \tag{2.19}$$

Step 3: Design of slotted plate

The slotted plate is made of Grade 300 Mild Steel. The unclamped section of the slotted plate L_u can be considered as a cantilever because the clamped section is a significant portion of the total length of the slotted plate (Figure 2-33). The unclamped section of the slotted plate is subject to tensile and compressive axial load due to the sliding force (F_s). The unclamped

section is also subject to bending due to in-plane bending, out-of-plane bending, and eccentricity.

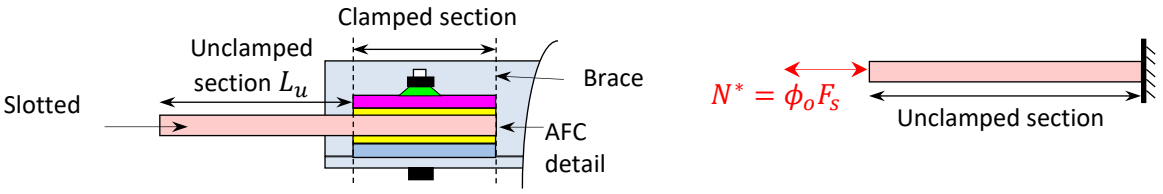

a. AFC detail

b. Unclamped section of the slotted plate

Figure 2-33. AFC slotted plate configuration

The design of the slotted plate shall follow the same procedure as that of the design of the brace, and all criteria described by Equation (2.2) – (2.19) shall be satisfied.

Step 4: Gusset Design

Thornton Buckling Capacity Method [Thornton, 1984], using a Whitmore width and maximum Thronton length, should be used to carry out a conservative design of a gusset. Thronton Buckling Capacity Method has been found conservative in experimental tests by Yam and Cheng [1993] and Gross [1990], and it is a widely used design method and it has been implemented into standards such as AISC [AISC, 2005]. The Thornton gusset buckling capacity P_{cr} can be defined by using Equation (2.20) – (2.22) below.

$$\lambda_c = \frac{KL}{\pi r}\sqrt{\frac{F_y}{E}} \tag{2.20}$$

$$P_{cr} = (0.658)^{\lambda_c^2} b_e t_g F_y \qquad \lambda_c \leq 1.5 \tag{2.21}$$

$$P_{cr} = \left(\frac{0.877}{\lambda_c^2}\right) b_e t_g F_y \qquad \lambda_c \leq 1.5 \tag{2.22}$$

In the equations above, the terms are defined as λ_c = gusset slenderness; K = effective length factor; L = maximum Thornton Length; F_y = gusset yield strength; r = gusset radius of gyration; E = elastic modulus; b_e = Whitmore Width; and t_g = gusset thickness. Chou *et al.*, [2012]

recommended to use an effective length factor of 2 when calculating the maximum Thronton length to prevent out-of-plane sway buckling failures.

Although the Thronton method is considered more conservative than other existing methods, finite element analysis carried out by Westeneng *et al.*, [2016] found that gusset plates designed using this method can still buckle at lower strength than predicted. However, this research work was carried out based on a frame assembly that used Buckling Restrained Brace as the bracing system. Therefore, it is unclear whether the Thronton method described above is conservative enough when designing a gusset for a friction brace, and the gusset-brace interactions were outside of the scopes of this thesis. To minimize the potential impact of gusset buckling, an effective length factor of 3 was used to design the gussets used for the braced frame tests. A design example for an AFC brace configuration presented in Figure 2-1 can be found in Appendix A.

2.6.2. Consideration of stage II and III stiffness

As stated in Section 2.4.1.1, the AFC hysteretic behaviour at stage II and III is dependent on the surface condition of the sliding interfaces and it could also be affected by the slackening of the clamping bolts, making it difficult to predict. Therefore, for simplicity, practitioners may choose to neglect stage II and III of the hysteretic response in the design process by assuming the friction behaviour as a simplified Elastic-Perfectly Plastic (EPP) loop as illustrated in Figure 2-34.

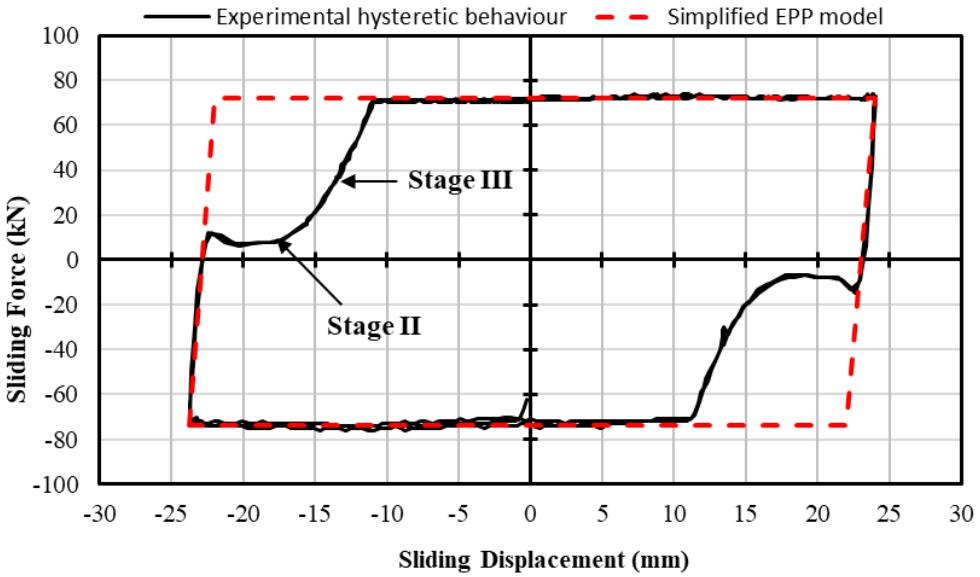

Figure 2-34. Simplified AFC hysteresis profile – Elastic-perfectly plastic (EPP)

The equivalent hysteretic damping ratios of the simplified profile and the experimental profile can be calculated using Equation (2.23) as a method to quantify the impact of simplifying the AFC brace hysteresis profile.

$$\zeta_{hy} = \frac{1}{4\pi}\frac{E_d}{E_s} \tag{2.23}$$

While noting that the total effective viscous damping (EVD) of the system, ζ_{eff}, is the sum of inherent viscous damping, ζ_0, and effective hysteretic damping, ζ_{hy}, as described by Equation (2.24).

$$\zeta_{eff} = \zeta_0 + \zeta_{hy} \tag{2.24}$$

In Equation 2.23, E_d is the energy dissipated by the AFC brace, which is defined by the area enclosed by the hysteresis loop, and E_s is the stored potential energy corresponding to the area of the shaded triangle, shown in Figure 2-35.

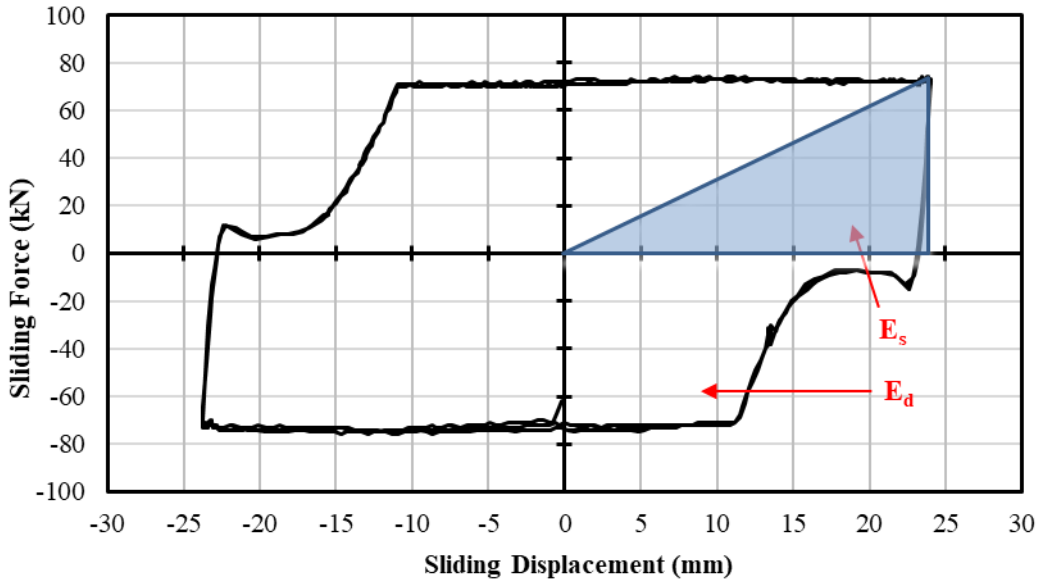

Figure 2-35. Estimation of equivalent damping ratio

By calculating the E_d of both profiles, it is determined that by neglecting stage II and III, the simplifying assumption may overestimate the enclosed hysteretic area by up to 25%. Therefore, this simplifying assumption introduces some non-conservative error if practitioners choose to

neglect the stiffness changes in stage II and III. However, when considering that ζ_{hy} is only one of the contributors to total system damping, the error may not have significant impact on the overall outcome of displacement-based design. For a structure responding to a ductility demand that corresponds to 15% EVD for bilinear hysteresis, the differences in EVD from the two models is likely to result in less than 3% difference in the prediction of peak displacement values. However, it is important to note that this is a non-conservative assumption as it overestimates hysteretic damping and EVD.

While this discussion has considered area-based damping, it is recognised that EVD expressions are generally calibrated to the results of Non-Linear Time-History Analysis (NLTHA) [Pennucci *et al.*, 2011]. Nevertheless, the area-based reasoning provided in this Section is considered a reasonable means of showing that the likely differences in EVD values for systems with AFC braces and those approximated using the simplified bilinear hysteresis model would be relatively small.

2.7. AFC model

Currently in OpenSees there are two general types of friction material models available. The first type is the Coulomb friction model, and the second type is velocity dependent friction model. The Coulomb model does not capture the changes in the stiffness of an AFC brace as its sliding mechanism is developed through the four stages described earlier. Also, there is currently no experimental data to indicate the impact of velocity on the effective friction coefficient of a friction connection. For this reason, the velocity dependent models are not currently suitable for the modelling of AFC. Therefore, there is a need to develop a new multi-linear hysteresis model that can approximate the hysteretic behaviour of an AFC. The new model needs have the same yielding force in both tension and compression, and users should be allowed to define the pre-yielding stiffness at different stages.

To address the need for a new numerical hysteresis model, the *AFC* model has been constructed and proposed by the author, with the kind assistance from T.L. Chang from the University of Canterbury. The *AFC* model is a uniaxial material model which hysteresis profile is generically based on the experimental hysteresis loops of an AFC brace. The model has been implemented into suanPan [2009] and it can also be used on the OpenSees platform. The hysteretic model that has four definable variables, an illustration of the model's hysteretic behaviour is shown in Figure 2-36 below. K_1 is the initial pre-sliding loading and unloading stiffness, which is

dependent on the axial stiffness of an AFC before any sliding or slipping takes place. K_2 approximates the changes in stiffness at stage II and III using a single linear curve. K_3 is the stiffness at full sliding, which should be zero for a friction connection. It is worth noting that the *AFC* hysteresis model can also be used to simulate other hysteresis profiles that have similar features as the illustration shown in Figure 2-36. For a case where it is appropriate, K_3 can be defined as a value larger than zero to represent post-yield strain hardening. Lastly, F_y is the yielding force which is the same for both tension and compression.

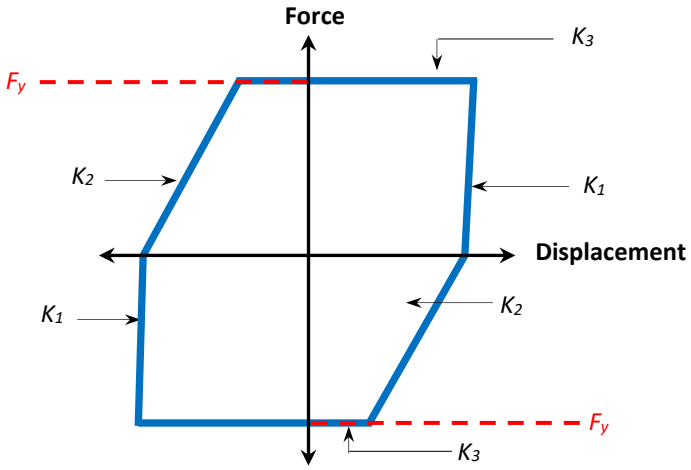

Figure 2-36. AFC numerical model

A displacement-controlled simulation has been conducted in OpenSees using the numerical *AFC* hysteresis model. In the simulation, K_2 is defined as 50% of the flexural stiffness of two clamping bolts in cantilever bending. Such value was defined for K_2 as it is a simplified approximation of stage II and III, and it does not consider the pre-mature yielding at stage II. Therefore, this is a conservative approach to minimise the overestimation of the amount of energy dissipated by an AFC. The hysteretic response of the AFC model is plotted in Figure 2-37 below, and the computational results are compared against the experimental results from an AFC brace test. It can be seen that the numerical hysteresis model provides a reasonable approximation of the quasi-static behaviour of an AFC brace. However, one major drawback of this *AFC* model at this stage is that it does not consider strength degradations, therefore as shown in the figure below that the numerical model's overestimation of peak sliding force is higher at large sliding cycles, because in reality an AFC exhibits more strength degradation as the accumulative sliding distance increases.

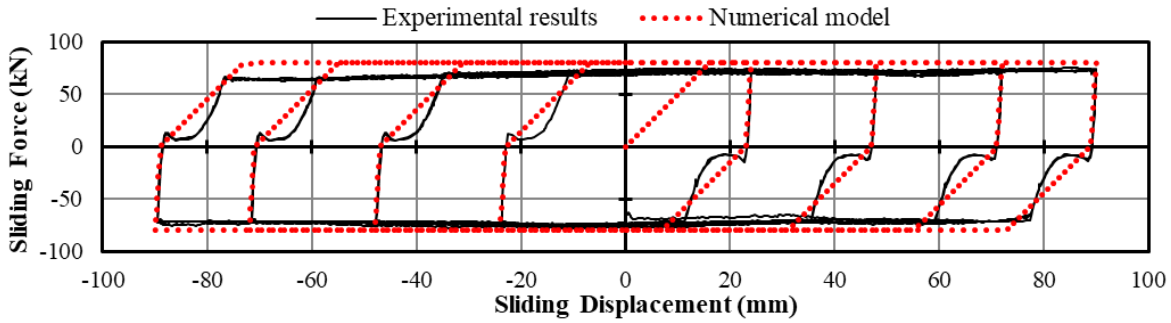

Figure 2-37. AFC OpenSees model response comparing to experimental results

2.8. Conclusions

This chapter describes the hysteretic behaviour of AFC brace by itself as well as the hysteretic behavior of a singly braced frame equipped with an AFC brace (AFC frame). It has shown that:

(i) The hysteretic behaviour of AFC brace by itself and AFC braced frame was stable and almost rectangular. The sliding mechanism could be divided into four stages with different stiffness. The changes in the brace stiffness were caused by the sliding at the plate interfaces within the AFC details.

(ii) Strength degradation of AFC braces was estimated as 10%, for the case where no change of the AFC components or bolt re-tensioning was made after subjecting braces up to 40 cycles distributed across the full stroke of the connection. Reductions in strength were attributed to loss of bolt tension presented and sliding surfaces degrade. The low strength deterioration indicated that friction braces would be a reliable solution to energy dissipation.

(iii) The AFC braced frame produced similar hysteretic behavior as when the AFC braces were tested alone. The post-yielding stiffness of the braced frame at full sliding was slightly sloped due to (i) the elastic deformations of the frame components, and (ii) the clamping bolts were bearing on the slotted hole sides as the brace bent in-plane due to frame actions.

(iv) AFC braces also increased the ductility of frames allowing them to undergo high drifts without yielding any frame member and with low damage on the brace.

(v) AFC braces underwent out-of-plane deflections as a result of bending moment generated in the load transfer mechanism from the slotted plate to the brace member. Maximum out-of-plane deflection measured from the experiments ranged from 3.2 mm to 3.8 mm.

(vi) The measured effective coefficient of friction from the experiments ranged from 0.16 to 0.195, this was lower than the initially estimated effective friction coefficient of 0.21. Therefore, it is recommended to instead use an average effective friction coefficient of 0.18 for AFC's in braces, while the recommended understrength and overstrength factors should remain as 0.7 and 1.4, respectively. A general design guideline of AFC braces has been provided.

(vii) AFC braced frames can be considered as low damage structural systems given that stable hysteretic behaviour could be achieved over an amount of cycles comparable to a typical severe earthquake, and also because AFC braced frames could dissipate seismic energy via friction and exhibit large drifts without yielding any member or component of the primary structural system.

(viii) Lastly, an initial OpenSees AFC model has been proposed as a part of this study. The model captures the general behavior of an AFC brace and can be used to estimate the energy dissipation of an AFC.

3. EXPERIMENTAL STUDIES OF SYMMETRICAL FRICTION CONNECTION

3.1. Overview

A subset of the results presented within this chapter has been submitted to the following conferences/journals. The work presented within this chapter is an extended version of the information presented within these publications.

Chanchi Golondrino, J., Xie, R., MacRae, G. A., Chase, J. G., Rodgers, G. W., & Clifton, C. (2015). Low damage brace using a Symmetrical Friction Connection (SFC) detail. In NZSEE Conf., The New Zealand Society for Earthquake Engineering, Wellington, New Zealand.

Xie, R., Chanchi Golondrino, J., MacRae, G. A., & Clifton, G. C. (2018). Braced Frame Symmetrical and Asymmetrical Friction Connection Performance. In Key Engineering Materials (Vol. 763, pp. 216-223). Trans Tech Publications.

While Chapter 2 has presented both brace and frame testing of AFCs, it is also of interest to understand how SFC connections may alter the behaviour.

The primary focus of the SFC brace and SFC braced frame tests was to understand the basic hysteretic behaviour of an SFC when it is used as a brace dissipator, and whether the flexibility of the bracing member would significantly affect the energy dissipation mechanism of an SFC. Also, since the strength restoration and retrofit strategies for a friction connection were already investigated as parts of the AFC brace tests, the experimental study of SFC brace was to focus on testing braces with brand new materials only.

The experiment plan used to test SFC braces was similar to that for AFC braces presented in Chapter 2. The first part of the experiment consisted of the testing of SFC braces by themselves as a component-level test in a horizontal setup, and the second part was to place an SFC brace in a singly braced frame. Two brace specimens were tested in each part, and each specimen was subject to 48 cycles of load reversals before all SFC components were replaced with brand new materials. All tests were completed under quasi-static conditions. Loading protocols used were the same as those used for the experiment of AFC braces in Chapter 2.

Discussions on the results of this chapter focus on the sliding mechanisms of SFC braces and how the hysteresis loops were created. Discussions are also provided on the strength degradation of the SFC brace specimens after 48 cycles of testing without component

replacements and bolt retightening. At the end of the chapter, based on the test results of the friction braces by themselves presented in both Chapter 2 and 3, comparisons are then made between SFC braces and AFC braces in terms of strength, hysteretic behaviour, and cost.

3.2. SFC in a brace

3.2.1. Materials and assembly methodology

The SFC brace test specimen assembled using two 250PFC channel sections placed back to back as shown in Figure 3-1b.The SFC details were attached at one end of the channels, and the connection details were characterized by one 32 mm thick slotted plate with two 200 mm length slots, and two 8 mm thick Bisalloy 500 shims. Two M16 galvanised Grade 8.8 clamping bolts of 100 mm length were used. One Belleville washer and two flat washers were equipped on each clamping bolt. The full length of the SFC brace test specimen was 3225 mm. The length of the SFC details was 300 mm. The unclamped zone of the slotted plate and the channels were 415 mm and 2860 mm, respectively, as shown in Figure 3-1a. Six M24 Grade 8.8 bolts were used at the moving and fixed ends of the assembly to prevent slipping.

This SFC brace configuration is chosen as it uses the same number of clamping bolts as the AFC brace configuration presented in Chapter 2, and it also has the same number of sliding interfaces as the AFC brace configuration. Therefore, such SFC brace configuration provides better and more relevant comparisons between the SFC and AFC brace results.

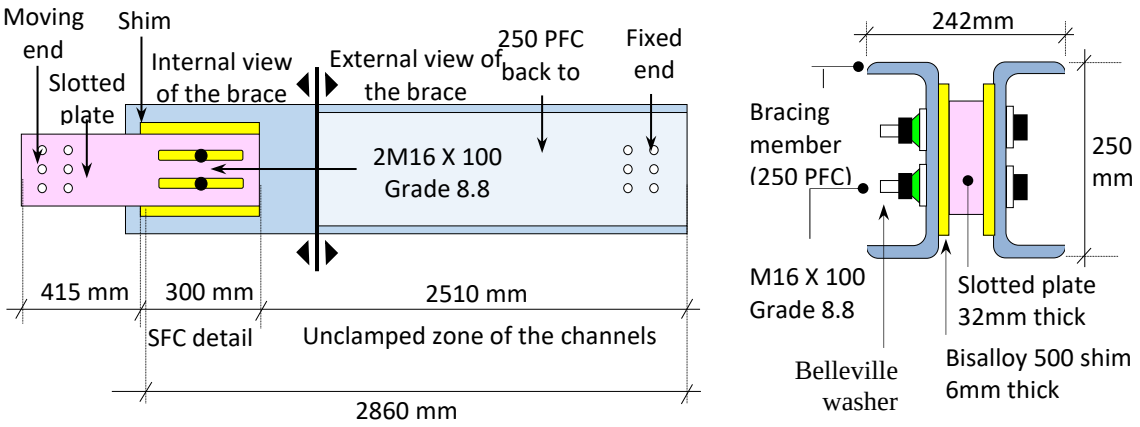

a. Longitudinal configuration of the SFC brace b. SFC brace cross section

Figure 3-1. SFC brace components and SFC detail cross section

The clamping bolts were tightened to their proof loading using the same torque control method as that used for the AFC brace tests, which is described in Section 2.1.1 and Figure 2-2. However, the bolts used for the SFC braces were shorter than those used for the AFC braces, therefore, new torque-elongation and tension-elongation relationships are required. These are shown in Figure 3-2. Using this methodology, a torque value of 200 N-m from the hand tightened condition was defined as the proof load torque for M16 bolts of 100 mm in total length. This torque value corresponded to a nut rotation between ¼ and ½ turn when considering the more commonly used nut rotation method.

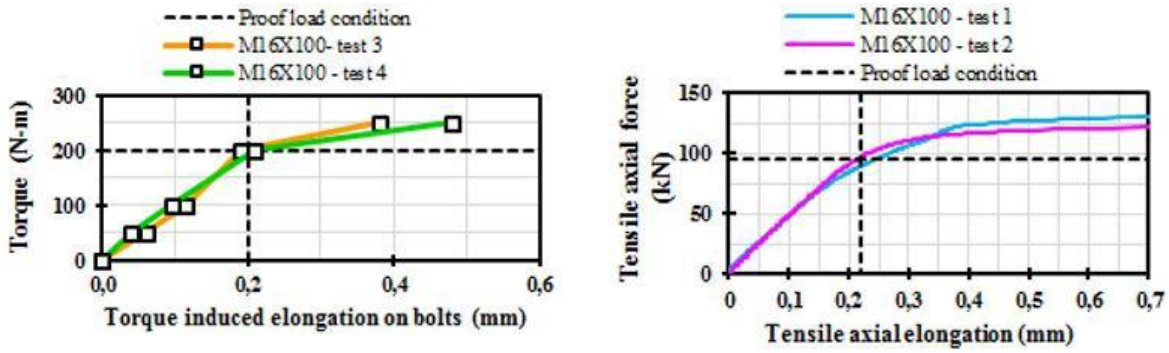

a. Torque-elongation relationship b. Tension-elongation relationship

Figure 3-2. Torque control method for M16 x 100 mm bolts

3.2.2. Experimental setup, instrumentations and loading regime

The SFC brace tests were carried out by placing the braces in a horizontal setup constituted by a fixed and a moving support. The fixed end of the brace was bolted to a bracket which was bolted on to a short reaction frame, as shown in Figure 3-3c. The moving support consisted of a slotted plate that was attached to a load cell and an actuator. Loads from the actuator drove the slotted plate as the strokes of the actuator developed. This setup was also instrumented with one extensometer that was placed horizontally across the brace length to measure the horizontal deflection of the SFC brace. Four extensometers were placed vertically at the location of the SFC details, quarter length, half length and the fixed end of the brace to measure the vertical movement of the brace, as shown in Figure 3-3a. Testing of SFC braces was carried out by feeding the actuator a displacement control regime, which is the same regime as that of the AFC brace tests shown in Figure 14. The slotted plate was pushed and pulled between 3 and 90% of the total slot length (3 mm – 90 mm).

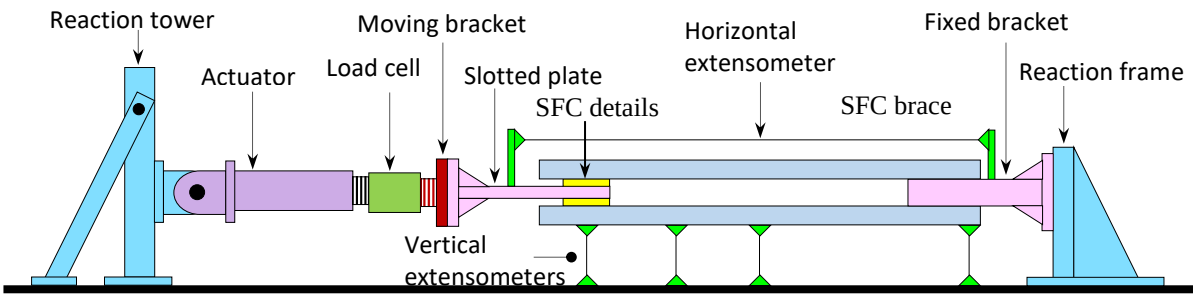

a. SFC brace test setup overview

b. The moving support – the actuator and load cell

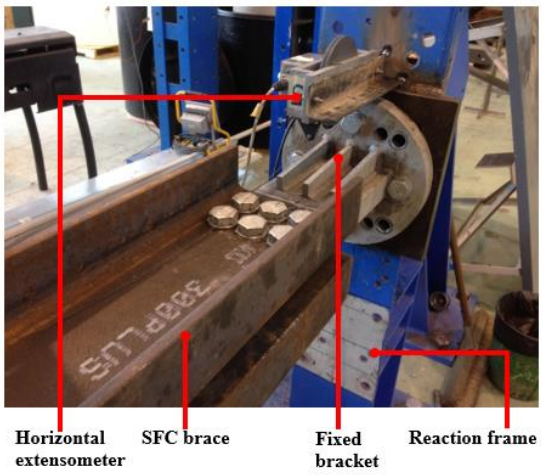

c. The fixed support

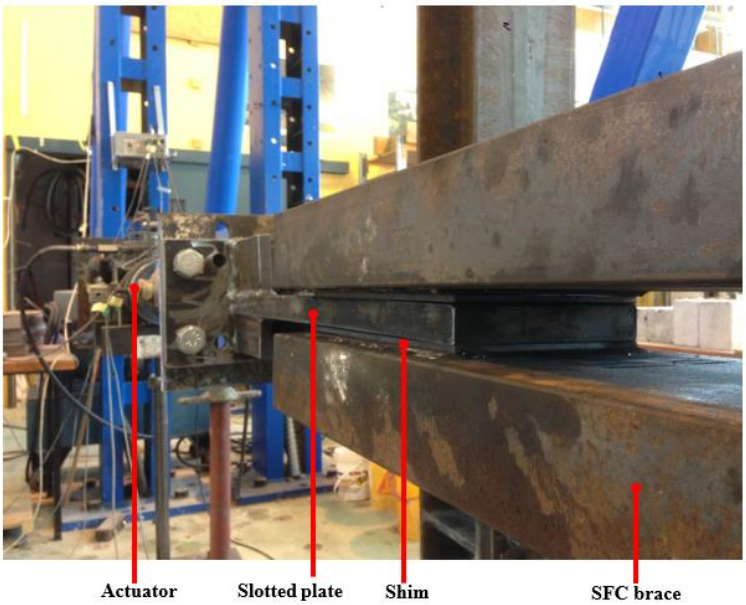

d. The SFC details

Figure 3-3. SFC brace test setup

3.3. SFC in a singly braced frame

3.3.1. Testing methodology

The SFC brace was placed in a frame by bolting the brace on to a gusset at each end. The bottom brace-gusset connection was fixed, and six M24 bolts were used to prevent slip and rotation of the brace. The SFC details were attached to the opposite end of the brace where sliding was allowed. The SFC details of the braced frame consisted of two Bisalloy 500 shims, two M16 x 100 mm clamping bolts, and a slotted gusset that was sandwiched by the channel bracing members and the shims, as shown in Figure 3-4. By having a slotted gusset as part of the SFC details was a simple and efficient method to minimise the eccentricity when the SFC brace was subjected to an axial load. The same torque control method was used to tighten the SFC clamping bolts of the braced frame as that used for the SFC brace tests. The top (slotted) and bottom gussets were concentrically welded to connecting plates which were bolted to the beam and column flanges, as shown in Figure 3-5.

The frame that used to attach the SFC brace on was the same as that used for the AFC braced frame tests. The configuration and dimensions of the frame is shown in Figure 3-4a, and the same instrumentation was adopted for the SFC braced frame tests as that shown in Figure 2-7a. The SFC braced frame was also pushed and pulled up to 3% lateral drift using the 20 sawtooth cycle displacement regime shown in Figure 2-8.

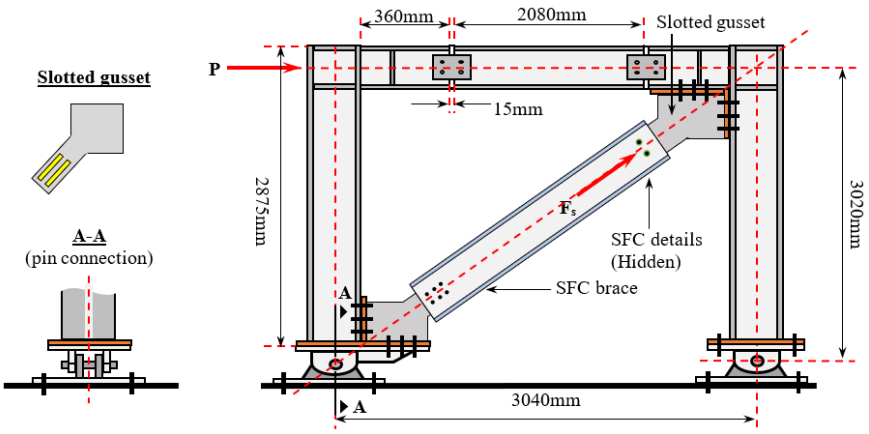

a. SFC braced frame test setup illustration

b. SFC braced frame

c. The SFC details

d. The top slotted gusset

Figure 3-4. Singly braced frame equipped with an SFC brace

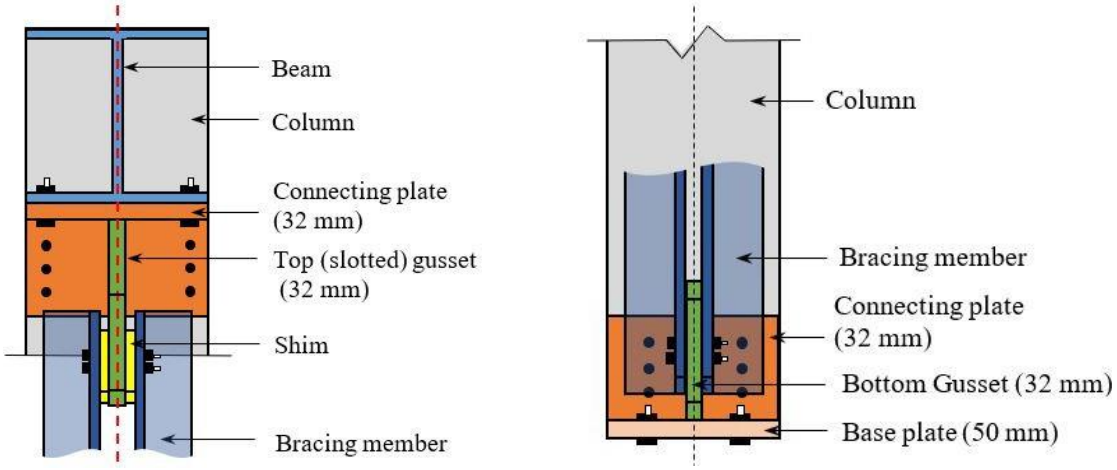

a. Configuration of the top gusset b. Configuration of the bottom gusset

Figure 3-5. Top and bottom gusset configuration

3.4. Experimental results and observations

3.4.1. SFC in a brace

3.4.1.1. Discussions on the hysteretic behaviour of an SFC in a brace

The force-displacement response of the SFC brace is plotted in Figure 3-6a, where the hysteresis loops for all sliding distances have similar shapes, which indicates the SFC provided stable dissipation mechanism to the brace. Based on the test results, the lower and upper bound of the peak sliding force of the SFC brace specimens tested were 96 kN and 143 kN, respectively. Similar to AFC braces, the sliding mechanism of an SFC brace can also be characterized by four stages labelled as I, II, III and IV in Figure 3-6a. The four stages were developed as the stiffness of the brace changed from a very steep slope (stage I), to a lower stiffness (stage II and III), and to almost zero stiffness (stage IV), where full sliding occurred.

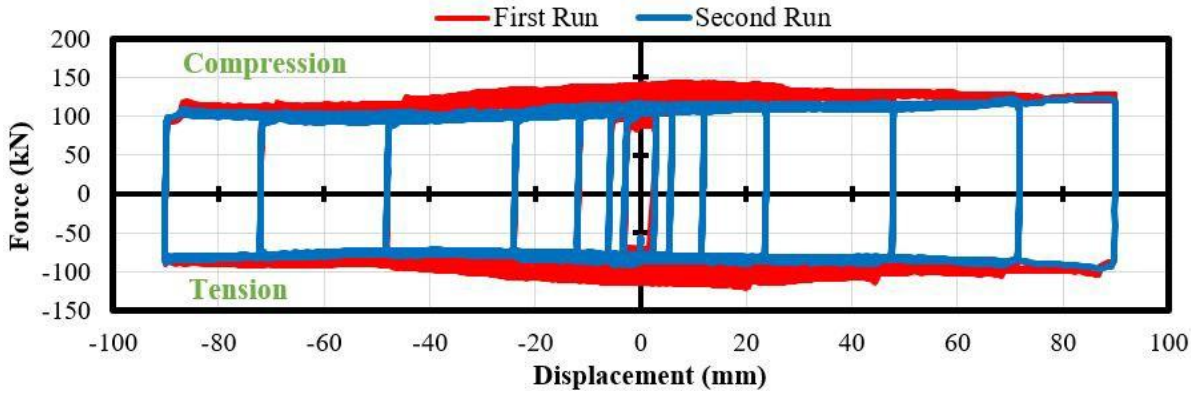

a. Configuration of the top gusset

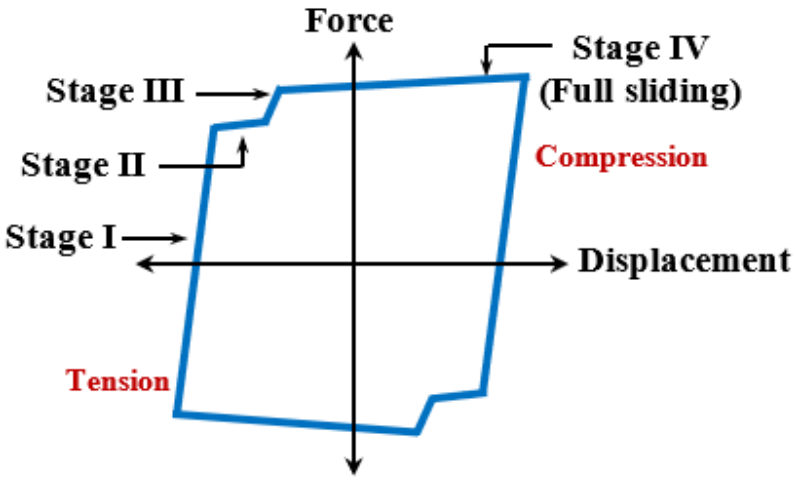

b. Sliding mechanism of an SFC brace

Figure 3-6. Hysteresis loops and sliding mechanism of the SFC brace alone

The changes of the brace stiffness shown in Figure 3-6 resulted from sliding at six plate interfaces within the SFC details. These interfaces are labelled as A, B, C, D, E and F in Figure 3-7.

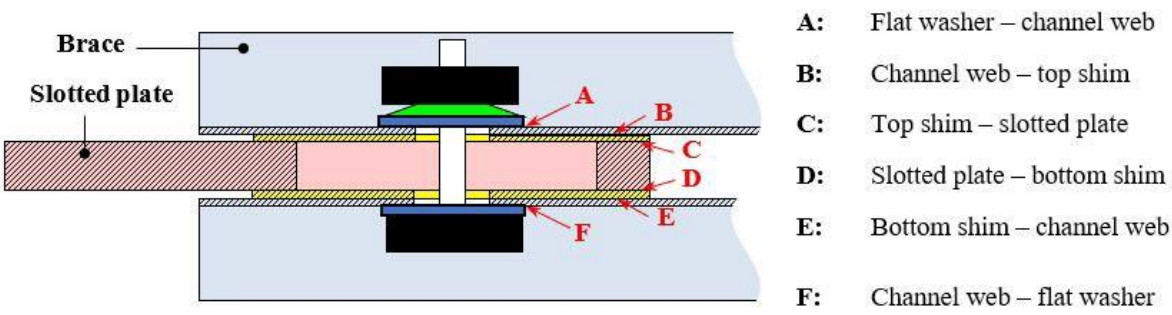

Figure 3-7. Sliding interfaces within an SFC brace

Each stage of the sliding mechanism can be described as: (i) Stage I: pre-sliding, where the axial force in the brace was less than the clamping force at the SFC details, and no sliding occurred at any of the six interfaces described above. The force in the brace increased linearly in a steep tendency with a stiffness that was equivalent to the elastic stiffness of steel.

(ii) Stage II: limited sliding. Initial sliding occurred at first interfaces A, B, E and F almost simultaneously. At this stage the slotted plate, shims and bolts slid for a distance equal to the bolt-hole oversize of the channel webs. This is illustrated in Figure 3-8. The SFC brace experienced a reduction in stiffness due to the limited sliding of some of the details.

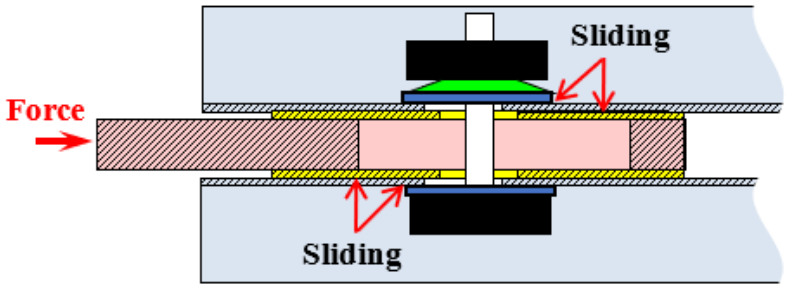

Figure 3-8. Stage II: first sliding occurred at washer-channel and channel-web interfaces (A, B, E and F)

(iii) Stage III: bolt bearing. Stage II is developed into stage III when the bolts started to bear against the bolt-hole edges of the channel webs and the shims, as illustrated in Figure 3-9. At this stage the clamping bolts were locked in place, and the SFC brace experienced a rapid increase in stiffness, and the force in the SFC brace increased linearly.

Comparing to the stage II and III of the AFC brace results discussed in Chapter 2 (Figure 2-11a), the stage II and III of the SFC braces was not as obvious and they occurred very close to stage

IV full sliding. Therefore, they did not have much effect on the overall hysteretic behaviour of an SFC brace. The reason behind this was, unlike the AFC braces, the slotted plate of the SFC plate was not subject to any moment caused by eccentricity that could lead to premature slipping at one of the interfaces. During sliding, there was no significant bolt tilting, the maximum slipping distance from stage II to stage III, where the bolts were locked in place by the shims and the channel webs are shown in Figure 3-9 below, was equal to the bolt-hole oversize. The bolt-holes were 18 mm in diameter for a pair of M16 clamping bolts. Therefore, the stage II and III occurred over a short displacement (2 – 4 mm) as shown in Figure 3-6a.

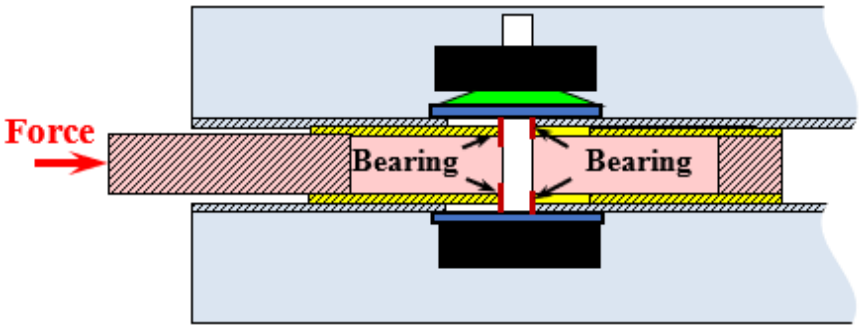

Figure 3-9. Stage III: sliding bolts in full bearing

(iv) Stage IV: full sliding. The increase in force at stage III continued until the force overcame the friction on both sides of the slotted plate, while the clamping bolts were in full bearing. At this stage, sliding occurred on both sides of the slotted plate, and the slotted plate could be driven up to ± 100 mm with little or no force increments, and the stage IV full sliding stiffness was almost horizontal, as shown in Figure 3-6a.

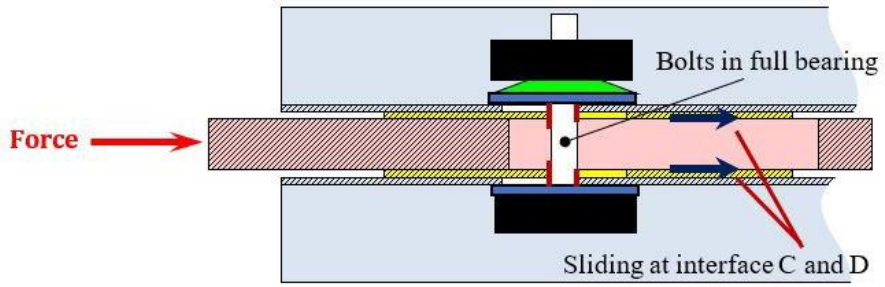

Figure 3-10. Stage IV: full sliding

3.4.1.2. Prying effect within the SFC details

Figure 3-11 shows that the force increase when the brace was sliding in compression and the force decreases when the brace was sliding in tension, causing the hysteresis loops to be slightly trapezoidal. It is shown more clearly in Figure 3-11a below where one 48 mm cycle is plotted. When the SFC was pushed axially, the brace members buckled elastically towards the slotted plate, and due to the eccentricity between the slotted plate and each of the channel braces, the axial compressive force caused an anti-clockwise moment on the top channel, and a clockwise moment on the bottom channel. This resulted the SFC details to close and prying forces from the channels were pushing against the slotted plate, making it more difficult to slide, as shown in Figure 47b. The moments caused the channel braces to buckle further and increased the eccentricity which led to higher moments on the channels that led to higher prying forces. Therefore, the sliding force was increasing gradually from approximately 95 kN to almost 120 kN as the slotted plate was being pushed. This is also known as the p-delta effect, and it is illustrated in Figure 3-11b. As the force reversed and the brace was in tension, the SFC details opened as the channel braces bent outwards and the p-delta effect was no longer affecting the brace performance. Therefore, there was only slight variations in the peak sliding force less than 15 kN when the slotted plate was pulled along the slot lengths.

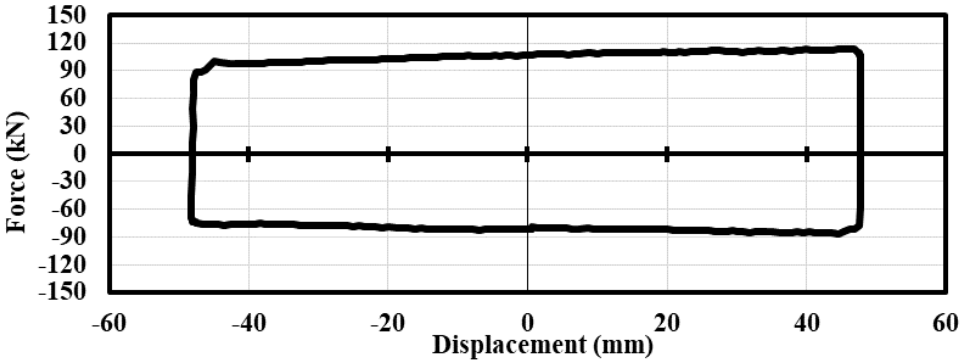

a. Trapezoidal hysteresis loop

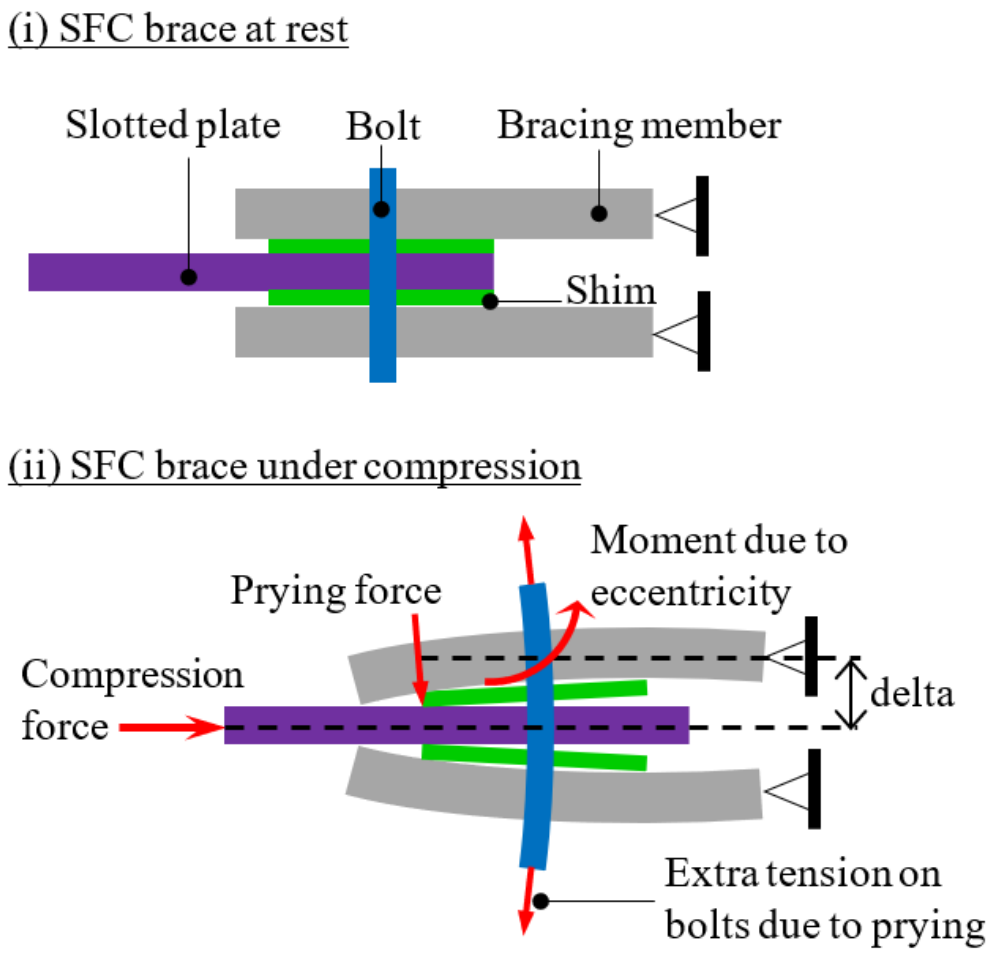

b. Illustration of the p-delta effect

Figure 3-11. P-delta effect

Another observation made during the SFC brace tests was that all the slotted plates used in the test had initial out-of-straightness to some degree, and this was believed to be result of the non-

uniform distribution of thermal stresses presented when welding the slotted plate together with some stiffeners and the fixed braced (Figure 3-12), which caused the slotted plate to warp, as shown in Figure 3-13. Because of this, prying was developed between the surfaces of the slotted plate and the shims when the initially bent slotted plate slid across the clamped zone of the SFC details. The prying also caused extra tension on the clamping bolts as shown in Figure 3-13.

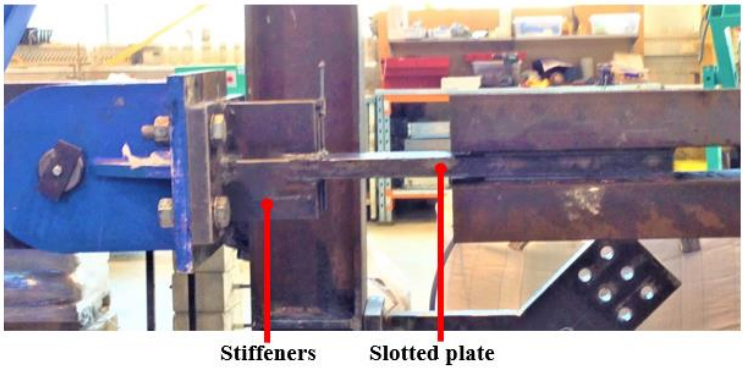

a. Slotted plate side view

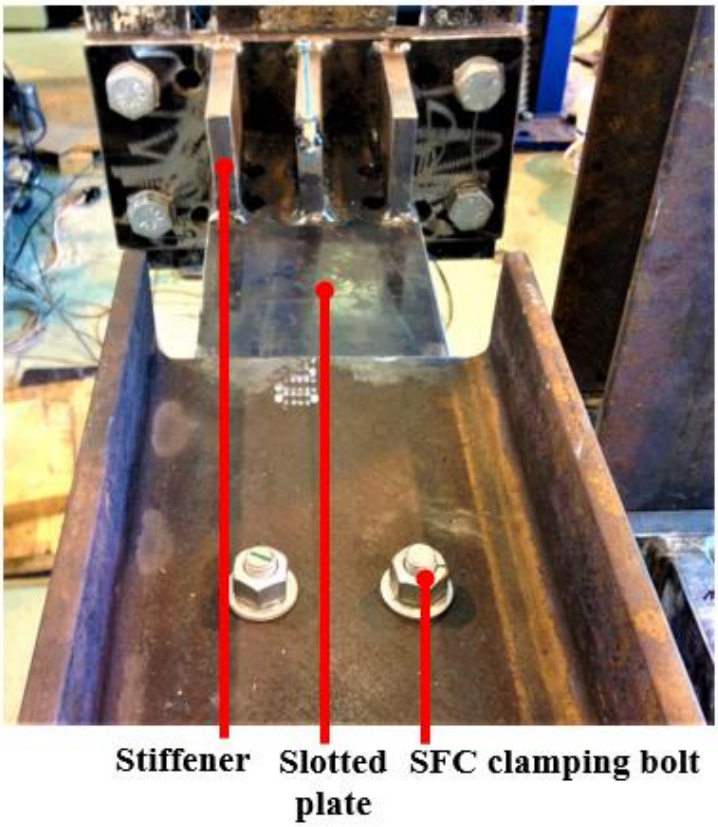

b. Slotted plate top view

Figure 3-12. Heavy welding on the slotted plate

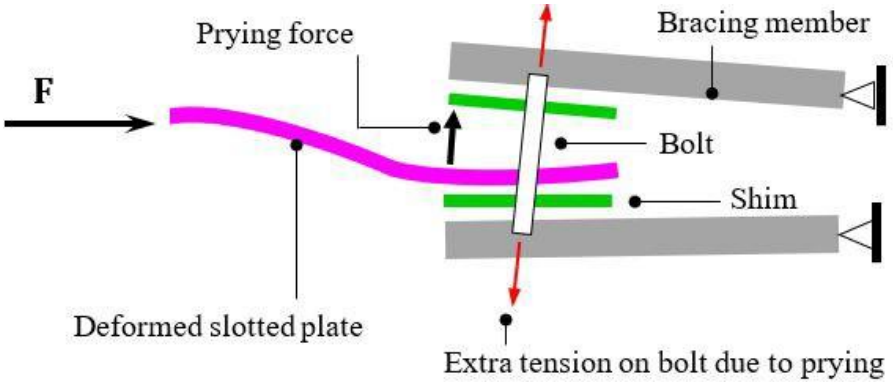

Figure 3-13. Prying due to deformed slotted plate

3.4.1.3. Variations in the peak sliding force in the early cycles

Figure 3-14 shows a comparison between a 3 mm cycle and a 6 mm cycle. Similar to what was observed from the AFC brace tests, the peak sliding force of the SFC brace also increased by approximately 20 kN in the early cycles. This is marked as 'Δ' in Figure 3-14 below. This was partially attributed to the same three factors discussed in Section 2.4.1.1, which are (i) bolt inclination, (ii) thermal expansion due to friction heat, and (iii) residual stress in the clamping bolts due to torsion applied during the bolt tightening process. The bolt inclinations in an SFC could be caused by the differences in clamping stress distribution and surface conditions at the interfaces. If sliding at interface A and B was triggered slightly earlier than sliding at E and F, due to more slippery surfaces, the clamping bolts could slightly tilt until they reached full bearing, similar to what is shown in Figure 2-10b. The bolt inclinations during the SFC brace tests were less obvious than those observed during the AFC brace tests. In addition to the three factors, the prying forces due to the p-delta effect described in the previous section also contributed to 'Δ', as the prying forces were proportional to the sliding displacement.

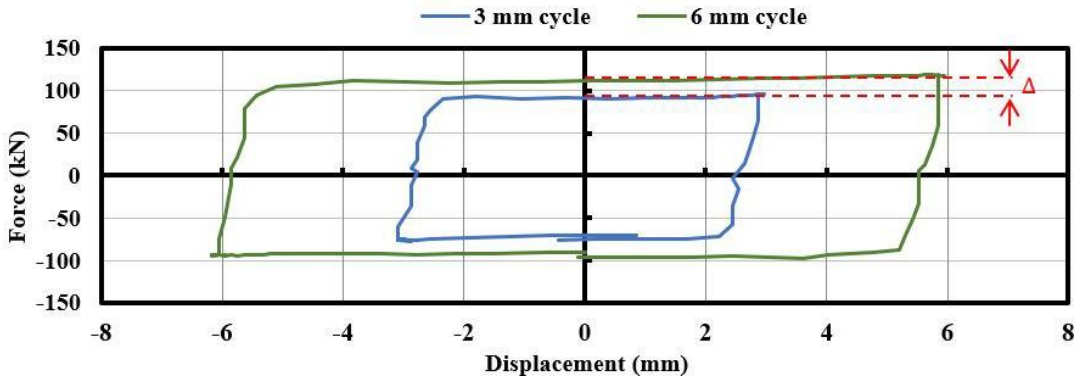

Figure 3-14. Comparison of two early cycles

3.4.1.4. Strength degradation of the SFC braces

Figure 3-6a shows there was some strength degradation when comparing the hysteresis loops of the first testing and the second testing run. The experimental results indicate that the maximum total strength loss between the start of the first run and the end of the second run for an SFC brace was 25%. The total strength loss was the result of the same types of inter-test and intra-test strength loss described in Section 2.4.1.2. Comparing to the AFC braces, the SFC braces tested experienced more significant strength loss, and this was primarily due to more substantial bolt slackening in the SFC bolt assemblies. As mentioned previously, the SFC braces experienced the p-delta effect which caused the SFC details to open and close. When the SFC details opened due to tensile axial force, the top and bottom channels were pushed outwards causing extra tension on the clamping bolts. As the bolts were initially tightened almost to their yielding point, such extra tension would cause the bolts to yield and deform permanently, and together with bolt tilting, prying due to deformed slotted plate, and thermal expansion due to friction heat, the clamping bolts in an SFC brace slackened more severely than those in an AFC brace.

To reduce the impact of p-delta effect and restrict the bracing members from deflecting out-of-plane, additional details can be added to the bracing system. One method to achieve this is to add connecting plates on the sides of the bracing members to connect the two bracing members together. An illustration of this strategy is shown in Figure 3-15 below. The connecting plates can be bolted or welded on to the channel flanges at various locations along the length of an SFC brace.

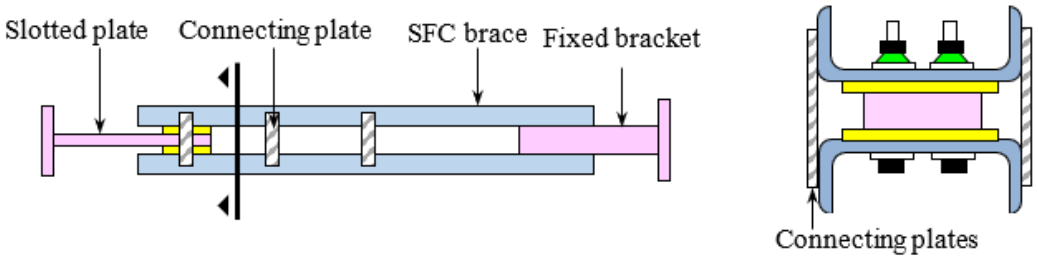

Figure 3-15. Connecting plates to restrict out-of-plane deflections of the bracing members

3.4.2. SFC in a singly braced frame

3.4.2.1. Hysteretic behaviour of the singly braced frame

The SFC braces were tested in the same bare frame as the AFC braces. The hysteretic behaviour of the bare frame is described in Section 2.4.2.1 and Figure 2-27. The plot below consists of the testing results of two brace specimens (Figure 3-16). Two runs of testing were conducted for each specimen. After the first specimen was tested twice, the bolts, shims and the slotted gusset was replaced before the testing of the second brace specimen took place.

The singly braced frame produced stable hysteresis loops when it was equipped with an SFC in the brace and the dissipation mechanism was developed in the same stages as those observed in the SFC brace tests, described in Figure 3-6b in Section 3.4.1.1. Both brace specimens produced similar results, especially in the second runs where the sliding interfaces were smoothened with no severe surface degradation, and bolt slackening had reached a steady state. The slotted gussets were not initially out-of-straightness like the slotted plates used for the SFC brace tests, therefore the stage IV curves of the frame tests are mostly smooth.

The maximum strength degradation from the first run to the second run for the frame tests was approximately 15%. The strength degradation was mostly due to bolt slackening, and the slight material degradation at the sliding interfaces indicates the surfaces were smoothened, which made sliding easier. In general, the strength degradations observed from the frame tests were lower than those observed during the testing of the SFC braces alone. This was because the slotted gussets were not initially out-of-straightness like the slotted plates used for the SFC brace tests, as the welding that applied to the slotted gussets was not heavy for the size of the gussets, therefore they did not deform due to welding heat. The slotted gussets might also be overdesigned by using an effect length factor of 2, therefore little to no buckling occurred in the slotted gussets.

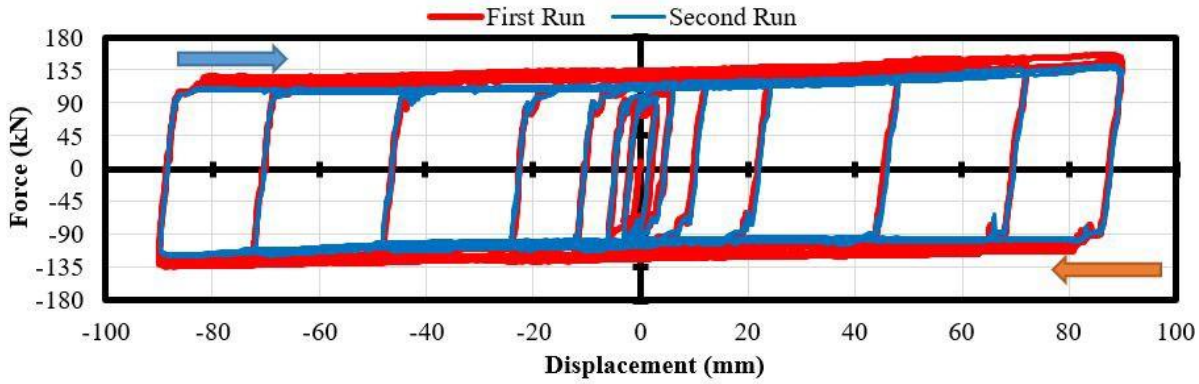

Figure 3-16. Hysteretic behavior of the singly braced frame with an SFC brace

The peak sliding force for the SFC braced frame ranged between 118 kN and 156 kN as shown in Figure 3-16 above, this indicates that the difference in the peak sliding forces between the braced frame and the SFC brace by itself is approximately the strength of the bare frame. Also comparing with the bare frame results described in section 2.3.2.1, by equipping the SFC brace, the energy dissipation mechanism and frame strength were significantly improved without yielding any major structural components, including the channel bracing members. Also by completing the experiments described above, it can be confirmed that the SFC details within a bracing system could be easily assembled and replaced with low material cost.

3.5. Effective coefficient of friction

The SFC brace test results were used to assess the effective friction coefficient (EFC) of the SFC brace configuration shown in Figure 3-1. Equation 2.1 is used to calculate the EFC. As mentioned in Section 2, Chanchi *et al.* [2013] has provided a reference EFC for SFC of 0.45.

Figure 3-17 below shows the average EFC at various sliding displacements for the first and second runs of the SFC brace tests. In the first runs, where brand new bolts, slotted plate and shims were used, the EFC of the SFC braces ranged from 0.315 to 0.34. In the second run, where the clamping bolts were slackened and slight material degradations had occurred at the sliding interfaces, the EFC ranged from 0.289 to 0.297. The second runs produced lower EFC values due to strength degradation which has been described in the previous section. In general, the EFC values estimated from the SFC brace tests were significantly lower than that stated by Chanchi *et al.* [2013]. This could be attributed to the combination of bracing member flexibility, bolt slackening and bolt yielding. Both bolt slackening and yielding reduced the clamping force provided by the bolts, but the true clamping force could not be determined and a value of 95

kN (M16 bolt proof load) was assumed when calculating the EFC using Equation 2.1. These factors could suggest the estimated EFC values from the SFC brace tests were not the true friction coefficients between the slotted plate and the shims, instead they were the EFC under the influence of sub-system flexibility, prying, and bolt slackening/yielding. For design, based on the test results presented in this section, it is recommended to use an average of 0.31 as the EFC. The understrength and overstrength factors shall be taken as 0.7 and 1.4, respectively, to cover the lower and upper bound of the peak sliding force of an SFC brace.

Comparing to the average EFC of AFC braces, the SFC brace average EFC is 72% higher. The higher EFC also attributed to the observation that the SFC brace specimens experienced higher strength degradations than the AFC brace specimens described in Chapter 2, as greater friction at an interface accelerates surface wear.

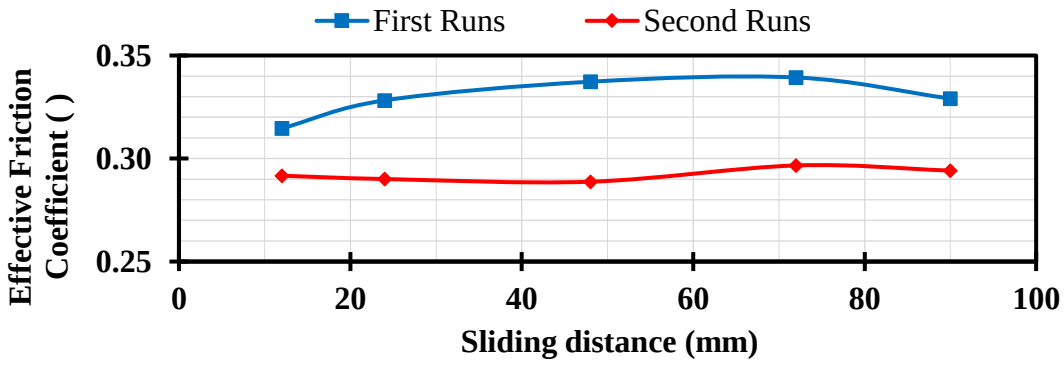

Figure 3-17. Effective coefficient of friction of SFC braces

3.6. Design recommendations of SFC braces

Step 1: Prediction of sliding force.

The dependable sliding force of an SFC brace ($\phi_u F_s$) can be defined using Equation 1.1.

$$\phi_u F_s = \phi_u \times n_b \times n_s \times \mu \times N_{tf} \quad (1.1)$$

Where:

ϕ_u = Understrength factor to account for the overestimation of μ, use 0.7 as recommended by MacRae & Clifton [2015]

n_b = Number of bolts

n_s = Number of sliding surfaces

μ = Friction coefficient, use 0.31 for Bisalloy 500 – Mild Steel interface

N_{tf} = Proof load of bolt used

For a configuration shown in Figure 3-1, both n_b and n_s shall be taken as 2, and N_{tf} is 95 kN for M16 bolts.

The overstrength of an SFC brace can be defined by Equation 1.1

$$\phi_o F_s = \phi_o \times n_b \times n_s \times \mu \times N_{tf} \quad (1.1)$$

Where:

ϕ_o = 1.4 as recommended by MacRae & Clifton [2015]

The brace overstrength shall be used to carry out the capacity design of the bracing members and, slotted gusset and other sub-assembly and primary structural components.

Step 2: Bracing member design

For a bracing member that consists of two channel sections as shown in *Figure 3-1*, Equations 2.2 – 2.19 presented in Section 2.5 shall be used for the design of each channel. The design axial force shall be taken as half of what is calculated using Equation 1.1.

Step 3: Slotted gusset design

Thornton Buckling Capacity Method [Thornton, 1984] using a Whitmore width, and maximum Thornton length shall be used for the design of the slotted gusset, as it is more than conservative than other available gusset designs [Westeneng *et al.*, 2016]. The maximum Thornton length of the slotted gusset is taken from the far end of the slots to the edge on the opposite end, as shown in Figure 3-18 below. It is recommended to use an effective length factor of 2. The design Whitmore width of the slotted gusset shall be taken as the width of the flange, as shown in Figure 3-18. Due to the special layout of the slotted gusset, a conservative design approach

was adopted to ensure the slotted gusset would not buckle under design load and affect the general hysteretic behavior of the friction braced frame, because the focus of the frame tests was to examine the mechanisms of the SFC brace, instead of the brace – gusset – frame interactions. Therefore, it is worth to note that the slotted gussets used in this experimental study might be overdesigned.

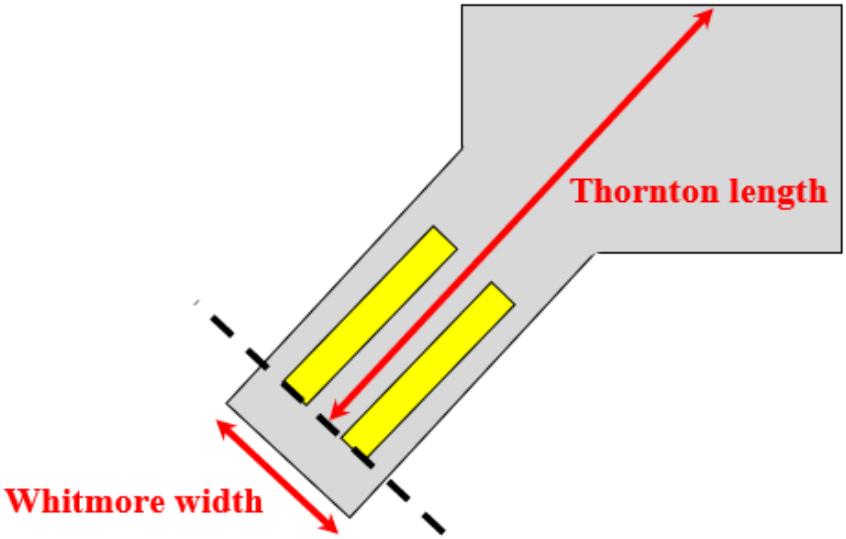

Figure 3-18. Design Thornton length and Whitmore width of the slotted gusset used for the SFC brace in a frame

3.7. SFC brace modelling

The hysteretic behaviour of SFC braces can be predicted using the friction theory of Coulomb. This implies that the hysteresis loop can be described by two stages: (i) a first stage with a vertical trend where the force increases with no displacement of the slotted plate. This stage represents the case before the sliding mechanism of the slotted plate is activated, and (ii) a second stage representing the sliding of the slotted plate by a horizontal trend with no force increment and delimited by the strength of the connection (Figure 3-19). In this model the prying forces, the buckling issues on the slotted plate, and the limited sliding of shims and the slotted plate are not considered given that the post-yielding zone of the hysteresis loop is considered flat. In order to more accurately represent the hysteretic behaviour of SFC braces the need of including prying forces, buckling on the slotted plate, and the limited sliding of the slotted plate and shims are required. Alternatively, the *AFC* numerical model proposed as a part of Chapter 2 can also be used to model SFC brace performance by making the values of K_1 and K_2 equal.

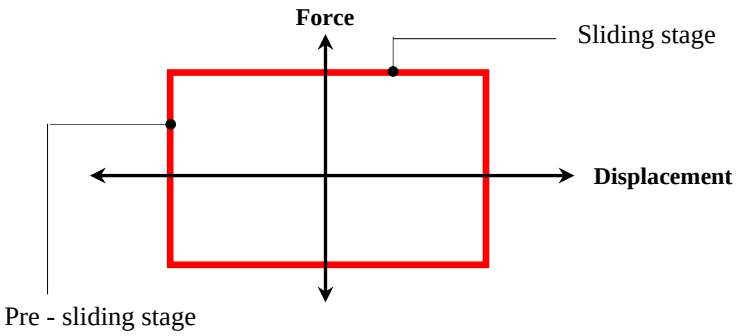

Figure 3-19. Idealised model of an SFC brace

3.8. Alternative SFC brace configuration

Figure 3-20 below demonstrates another method to assemble an SFC brace in a singly braced frame by using an I-section as the bracing member, and a set of SFC details that is illustrated in Figure 3-20a. The SFC details consist of two slotted plates, four shims and two cap plates. The two slotted plates are used to sandwich the I-section brace, the shims are placed on both sides of each slotted plate to high wear resistance sliding interfaces, and the cap plates are placed on the two outer sides of the SFC details. The SFC details and the I-section brace are clamped together using grade 8.8 galvanised bolts which are tightened to their proof load. This configuration substitutes the slotted gusset with two slotted plates and one normal type gusset that does not have an extended flange. It is also worth noting that due to the difference in thickness between the brace web and the top gusset, a packing plate may need to be welded on each side of the brace web. If total thickness of the brace web and shims is greater than that of the gusset, then the packing plates would be inserted between the slotted plates and the gusset.

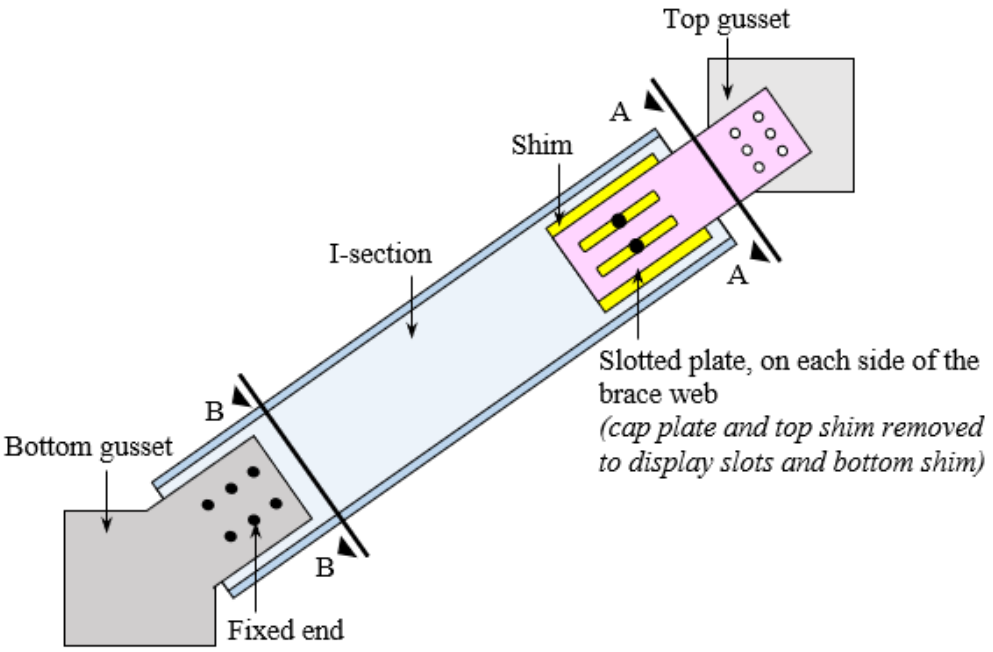

a. SFC brace side view

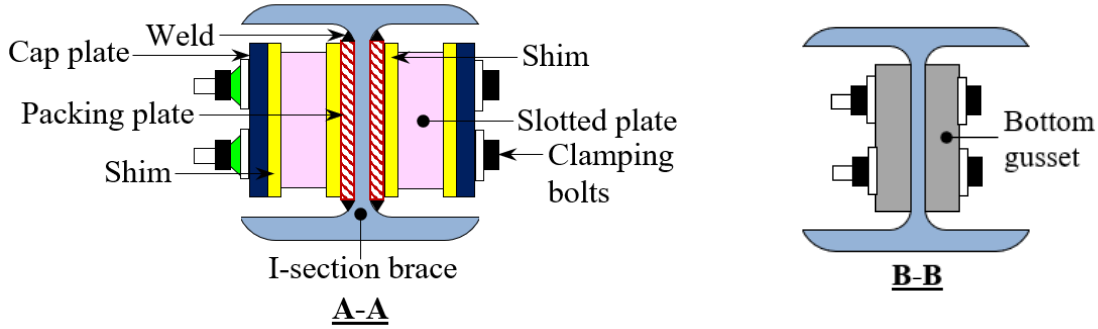

b. Top connection

c. bottom connection

Figure 3-20. Alternative SFC brace configuration

This alternative SFC brace configuration is suitable for a bracing system that requires large peak sliding force because it has four sliding interfaces, therefore theoretically it doubles the original SFC brace configuration that was used in the experiment. This alternative configuration also reduces the p-delta effect that exhibited by the original configuration due to the double slotted plates are likely to be stiffer than the double channel bracing members without additional detailing.

The downside of this configuration is it allows less construction tolerance than the original configuration because it uses more components, and the bottom connection consists of two gussets with flanges. The flanges need to be fabricated precisely to the correct angle and the bolt-holes on the gusset flanges and slotted plates need to be drilled at the exact required

locations. Bolt-hole misalignments at the top and bottom brace-to-gusset connections can lead to misalignment of the slots, which could affect the installation of the clamping bolts and the performance of the SFC brace.

3.9. Conclusions

Based upon the experiments undertaken and the results presented within this Chapter, the following conclusions can be drawn.

- The hysteretic behaviour of SFC brace by itself and SFC braced frame was stable and almost rectangular. The sliding mechanism exhibited slight stiffness changes before full sliding was developed as a result of the clamping bolts slipping across the bolt-hole tolerance. Changes in stiffness occurred only over a short distance. Therefore, they did not have a significant impact on the overall brace behavior.

- Strength degradation of SFC braces was estimated as 15%, for the case where no change of the SFC components or bolt re-tensioning was made after subjecting braces to up to 40 cycles distributed across the full stroke of the connection. Reductions in strength were mainly attributed to (i) loss of bolt tension presented as sliding surfaces degrade, and (ii) reduction of bolt clamping force due to bolt yielding as a result of the p-delta effects, which induced excessive tensile loads on the clamping bolts.

- SFC bracing members deflected out-of-plane as a result of the p-delta effects. The p-delta effect can be reduced by adding connecting plates on the sides of the bracing members.

(ix) The SFC braced frame produced similar hysteretic behavior as when the SFC braces were tested alone. The post-yielding stiffness of the braced frame at full sliding was slightly sloped due to (i) the elastic deformations of the frame components, and (ii) the clamping bolts were bearing on the slotted hole sides as the brace bent in-plane due to frame actions.

(x) SFC braces also increased the ductility of frames allowing them to undergo high drifts without yielding any frame member and with low damage on the brace.

(xi) The measured average effective coefficient of friction from the experiments was 0.31, this was lower than initially estimated effective friction coefficient of 0.45. Therefore, it is recommended to instead use an average effective friction coefficient of 0.31 for SFC as a

part of a bracing system, while the recommended understrength and overstrength factors should remain as 0.7 and 1.4, respectively.

(xii) An SFC brace configuration that is different to the configuration used in the experiments has been proposed as an alternative methodology to assemble an SFC brace. Comparing to the original experimental configuration, the alternative configuration consists of more sliding interfaces and is therefore able to achieve larger peak sliding force while using the same amount of clamping bolts of the same size.

(xiii) SFC braced frames can be considered as low damage structural systems given that stable hysteretic behaviour could be achieved over an amount of cycles comparable to a typical severe earthquake, and also because SFC braced frames could dissipate seismic energy via friction and exhibit large drifts without yielding any member or component of the primary structural system.

3.10. Recommended future research on AFC and SFC braces

Additional experimental studies on AFC and SFC braces are recommended to investigate the following:

- Testing using larger clamping bolts such as M20s and M24s. By subjecting the friction braces to high axial forces, the performance stability of friction braces can be investigated to determine if high load demand could accelerate strength and material degradations, especially in AFC braces due to their asymmetrical cross-sections.

- Testing friction braces under high velocity, high acceleration, ground motion loading. This is essential because velocity may have an impact on the effective friction coefficient of a friction connection. Therefore, by obtaining this information the design strategy of a friction brace can be significantly improved. This is also important information that can be incorporated into the numerical modelling method of friction devices.

- Currently coating is not recommended for friction braces due to low wear resistance of most coating options. However, it is important to carry out a research on the coating of friction connections to prevent rusting of components, which can lead to unstable performance of friction connections.

Additionally, the numerical AFC and SFC models can be improved by incorporating strength degradations as well as changes in effective friction coefficient due to variations in velocity.

4. EFFECT OF DAMPER SUB-SYSTEM STIFFNESS ON THE RESPONSE OF A SINGLE DEGREE OF FREEDOM SYSTEM EQUIPPED WITH A VISCOUS DAMPER

A subset of the results presented within this chapter has been submitted to the following conferences/journals. The work presented within this chapter is an extended version of the information presented within these publications.

Xie, R. M., Rodgers, G. W., & Sullivan, T. J. Influence of Damper Sub-System Stiffness on the Structural Performance of a System Equipped with a Viscous Damper. Australian Earthquake Engineering Society Annual Technical conference, Newcastle, Australia, November 29-December 1.

Xie, R.M., Rodgers, G.W., Sullivan, T.S. (2019) "Effect of Damper Sub-System Stiffness on the Response of a Single Degree of Freedom System Equipped with a Viscous Damper" Submitted to the Journal of Earthquake Engineering, (Under Review).

Chapters 2 and 3 have presented investigations into the use of AFC and SFC connections within structural bracing. However, viscous dampers are also an attractive option within dissipative bracing systems. This chapter presents a numerical investigation into viscous dampers as supplemental dampers.

There are many methods available to design a structure equipped with viscous dampers. A common approach in New Zealand is to adopt the Direct Displacement-Based Design (DDBD) method [Puthanpurayil *et. al*, 2019]. Sullivan and Lago [2012] has proposed a design framework using DDBD, and the framework's procedure is illustrated in Figure 4-1. The framework states that once the required damper constants are determined for the design displacement profile of a building, capacity design is to be carried out for the primary structure and the damper-structure connections, which are also known as the damper sub-systems. Such design philosophy is similar to most available guidelines, where the focus is to size (i) dampers to achieve a given level of damping, and (ii) structural components to achieve sufficient strength and/or displacement capacity. However the influence of the damper sub-systems flexibility on the overall hysteretic behaviour of the structure is not considered.

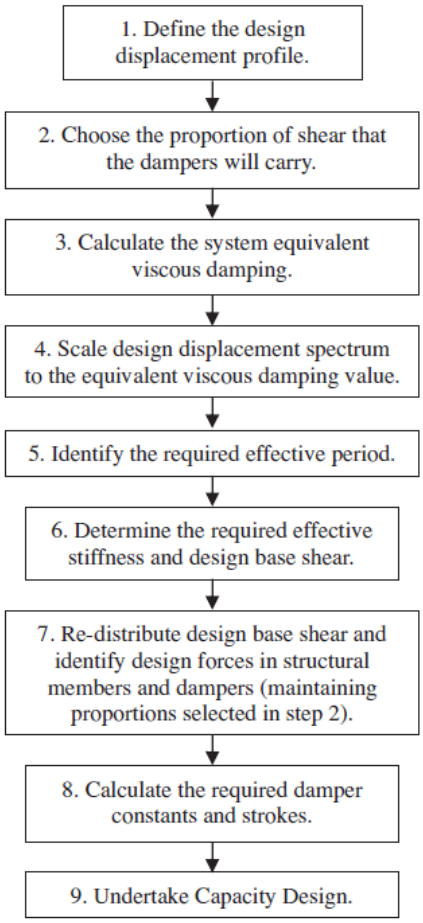

Figure 4-1. DDBD framework proposed by Sullivan and Lago [2012]

An experimental study of a multi-story steel frame building equipped with nonlinear viscous dampers carried out by Dong *et al.* [2016] demonstrated that the elastic deformation of the damper sub-systems affected the stiffness of the structure, as well as its effective damping. The damper sub-system flexibility also caused the phase shift between the damper and the primary structure to change, which suggests the damper sub-system flexibility has an impact on the overall structural response. Therefore, the scope of this chapter is to investigate and quantify the influence of the sub-system stiffness on the overall response of a structural system, in order to propose a guideline to account for this damper sub-system flexibility.

This study utilises a numerical SDOF structure-damper model in OpenSees. Using this model, the following computational investigations are carried out in order to achieve the scope.

Step 1, a free vibration analysis is carried out as the first step to investigate the effect of sub-system stiffness on the damped structural frequency.

Step 2, the SDOF model is subject to a sinusoidal excitation to investigate the effects of sub-system flexibility on the response of system components. This step looks into the phasing of the viscous damper response relative to the structural response, and how it changes as the stiffness of the sub-system changes.

Step 3, parameter studies are undertaken by simulating the SDOF model to a series of ground motions. This step investigates the overall structural response at different sub-system stiffness levels that are ranged from having the same stiffness as the primary structure, to a high stiffness level where the sub-system can be assumed as essentially rigid.

At the completion of the three steps described above, the following questions will be answered:

(i) What is the effect on structural response when the damper sub-system deviates from the rigid assumption?

(ii) What is the minimal level required such that the sub-system stiffness has no significant effect on the overall structural response?

Next, a design example is carried out to determine whether the critical sub-system stiffness level defined based on the analytical results is realistic, and finally, a modification to the Sullivan & Lago [2012] design framework is proposed.

The computational results of some parametric studies that are not included in the main content are included in Appendix F. These results are not additional topics for discussions instead they are support analysis to validate the results presented in the main contents of this chapter.

4.1. Numerical SDOF model

As shown in Figure 4-2, to investigate damper stiffness effects, an equivalent elastic SDOF structural model has been developed that consists of a linear elastic spring in parallel with a viscous dashpot that represents inherent structural damping of 5%. In parallel to this simple, well-known SDOF model, the supplemental damping system is modelled as viscous damper element in series with an elastic spring, otherwise known as the Maxwell model. The viscous dashpot is defined by a damping coefficient C_d and velocity exponent constant α_d. The linear elastic spring in series with the supplemental damper represents the damper sub-system stiffness, and it is defined by a value of K_d. The structural component of the SDOF model is

defined by an elastic material which is connected in parallel with the Maxwell component, which represents the structural lateral resisting system stiffness and has a stiffness of K_s.

A viscous dashpot, representing the inherent damping of the structural system, is connected in parallel with both the structural and Maxwell components. For this study, the inherent structural damping is modelled as linear elastic damping (velocity exponent, $\alpha_i = 1$) using a damping constant representing 5% of critical damping. This 5% of critical value is kept constant for all analyses, while the level of damping provided by the supplemental damping is increased. The SDOF model also consists of two nodes. Node 1 is fully fixed and node 2 is only allowed to displace laterally (in the Z-direction shown in Figure 4-2). Despite the simplicity of the model, it represents a more direct relationship between the structural component, the viscous damper, and the sub-system, without the influence of other factors that would be present in a multi-degree of freedom system.

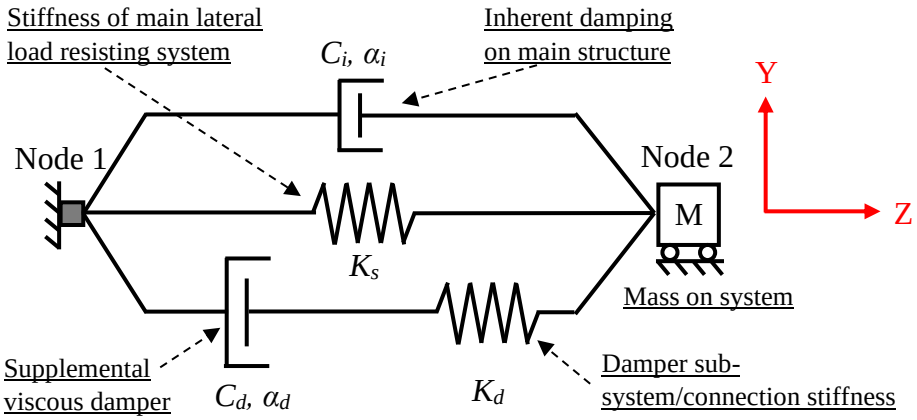

Figure 4-2. Numerical SDOF model

While the system will be solved within OpenSEES for overall system displacement, Z, the displacements and velocities of each component (dashpot and connecting spring) of the damper sub-system can be determined by Equation (4.1) and (4.2), respectively.

$$Z = Z_{dd} + Z_{ds} \tag{4.1}$$

$$v = v_{dd} + v_{ds} \tag{4.2}$$

Where Z_{dd}, Z_{ds}, v_{dd} and v_{ds} are damper sub-system dashpot displacement, the damper sub-system spring displacement (representing elastic flexibility of the damper sub-system), damper sub-system dashpot velocity and the damper sub-system spring velocity, respectively. Velocity is the time derivative of displacement, therefore $v_{dd} = dZ_{dd}/dt$.

In general, the damper force can be calculated using Equation (1.2). For the case of a Maxwell model where the damper is connected in series to a spring, the force within the supplemental damping sub-system dashpot (F_d) must equal the supplemental damping sub-system spring force (F_s), as shown in Equation (4.3).

$$F_d = C_d|v_{dd}|^{\alpha_d}.sign(v_{dd}) = F_s = K_d Z_{ds} \tag{4.3}$$

The Maxwell model can be solved within OpenSEES as part of the numerical integration scheme. There are also solution methods available to solve the damper sub-system, including those presented in Rodgers *et al.* [2012, 2016]

To conduct the numerical time-history analysis for this study, this SDOF model is implemented into OpenSEES [Mazzoni *et al*., 2006]. In OpenSEES, the Maxwell model is represented using the *ViscousDamper* material in the OpenSEES database. It is an uni-axial material that is coded and implemented by Akcelyan *et al*. [2018]. The *ViscousDamper* material models the viscous dashpot and the sub-system spring as a single material, which allows users to define C_d, α_d, and K_d. The *ViscousDamper* material also minimises the numerical issues experienced by other researchers in the past where a conventional nonlinear viscous dashpot was utilised while analysing viscous dampers [Lago, 2011]. As shown in Figure 1-15a, line 1 represents the force-velocity relationship of a nonlinear damper with velocity exponent, α, less than 1.0. At low velocities, the damper force increases rapidly as velocity increases, such that the tangent line to the force-velocity curve is almost vertical and tends to infinity. This rapid change in damping force upon load reversals can lead to numerical instability and cause the solution to fail to converge. While using the new *ViscousDamper* material, this issue can be avoided by simply reducing the integration step size. In this research, a maximum time step of 0.0002s is found to be adequate for earthquake excitation described later in Section 4.3.

4.2. Numerical investigation using sinusoidal excitation

4.2.1. Effect of sub-system stiffness on the structural damped frequency

An initial investigation has been conducted to consider the relationship between sub-system stiffness and overall system response. The damped frequency ω_d can be calculated using Equation (4.4), where ω_n is the undamped frequency defined by Equation (4.5), and ζ is the damping ratio defined by Equation (4.6). In a design where the sub-system is assumed to be rigid, the overall stiffness of the system is only governed by the structural stiffness K_s, which means for Equations (4.5) and (4.6), K is directly related to the structural period T_n.

$$\omega_d = \omega_n\sqrt{1-\zeta^2} \tag{4.4}$$

$$\omega_n = \sqrt{K/M} \tag{4.5}$$

$$\zeta = (T_n C_d)/(4\pi M) \tag{4.6}$$

Where the term M represents the system mass, which is lumped and applied at node 2. For this study, a mass of 1000 tonne is used. Equation (4.6) is only valid for linear viscous dampers and therefore this section of study only considers a linear viscous damper.

Based on the mathematical equations above, the ratio of ω_d/ω_n equal to 1 when the system is undamped (ζ = 0), and the ratio gradually decreases (frequency reduces and periods lengthen) as damping ratio increases, as shown in Figure 4. If the damper sub-system is modelled in OpenSEES to be either rigid or very stiff, the modelled system response should produce a similar curve to the analytical solution given by Equation (4.4). This analysis with higher damper sub-system stiffness provides a benchmark of the OpenSEES model against a known analytical solution, where high damper sub-system stiffness values produce modelled response behaviour that approaches the expected analytical trends. For this initial analysis, T_n = 1 and 2 seconds are considered. For each period T_n, stiffness ratios (K_d/K_s ratios) of 1, 1.5, 5, 10, 100 and 200 are selected. For the excitation protocol, the model is initially subject to a single pulse of acceleration that lasts for one second and the system undergoes free vibration for another 19

seconds to produce a 20 seconds time-history plot, which is then used to calculate ω_d. The results for the two periods considered are shown in Figure 4-3 below.

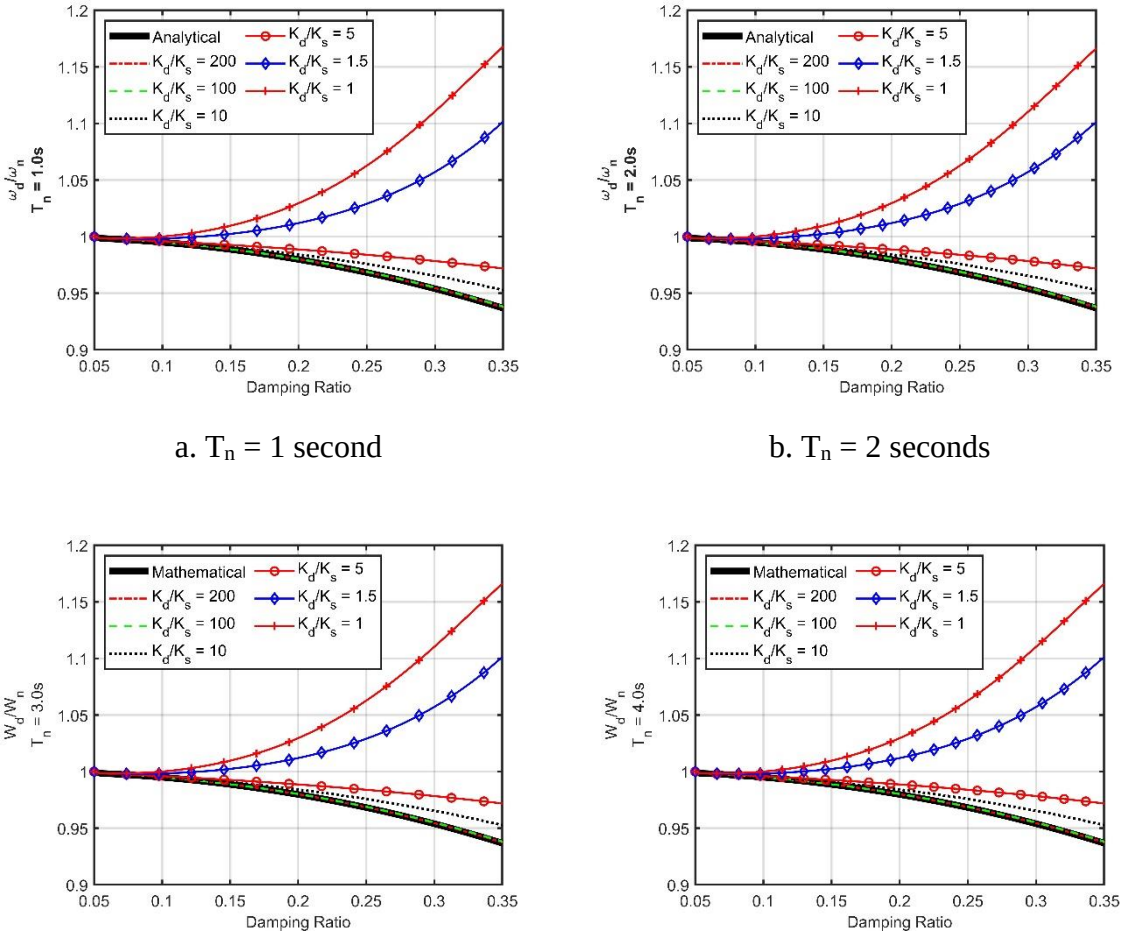

a. T_n = 1 second

b. T_n = 2 seconds

c. T_n = 3 seconds

d. T_n = 4 seconds

Figure 4-3. ω_d/ω_n ratios at different K_d values.

Figure 4-3a and bshow the same trends for all stiffness ratios for T_n = 1 to 4 seconds. The key observation from Figure 4 is that a structure model augmented with a damper with rigid (or very stiff, in this case, K_d/K_s = 100 and 200) support will experience a shift to lower frequency (longer period) as the damping ratio is increased. However, if the damper sub-system flexibility is considered, the trend can be seen to reverse for more flexible systems (K_d/K_s less than 5), where the damped structural frequency is seen to increase (shortening period) as the damping ratio is increased. This observation is important as the consideration of damper sub-system stiffness (that is often neglected in design) leads to an opposite trend to that which would be seen using the rigid connection assumption.

From the results shown in Figure 4-3, the sub-system stiffness K_d needs to be 100 times the structure stiffness K_s (K_d/K_s = 100) for the system damped frequency to be within 1% relative error of the analytical solution. However, the errors between the analytical solutions and computation model remain relatively low for stiffness ratios larger than 5. Once the stiffness ratio drops below 5, the model response is much more sensitive to the change of K_d. The deviations between the simulated response behaviour and the reference analytical model seen from the results are caused by the added flexibility of the damper sub-system relative to the overall system. This result agrees with the "brace effect" described by Dong *et al*. [2016], that was mentioned earlier.

4.2.2. Effects of sub-system flexibility on the response of system components subject to sinusoidal excitation

As shown in the experimental and model results previously presented in Figure 4-2, the phasing of the viscous damper response relative to the structural response is affected by the damper sub-system flexibility. The inherent elastic flexibility of the damper sub-system in series with the viscous dashpot results in a displacement and velocity profile for the damper which becomes partially out-of-phase with the main system's motion.

This section explores this phenomenon by presenting the differences in displacement time-history responses between the structural component, viscous damper and sub-system when the model is subject to a sinusoidal excitation. This analysis is repeated three times at stiffness ratios of K_d/K_s = 0.5, 1.5, and 200 to observe the changes in the out-of-phasing between the three system components. The damping ratio and structural natural period (T_n) are set at 20% and 3 seconds, respectively. The sinusoidal acceleration protocol input at the support node is shown in Figure 5a. Each analysis runs for a total of 20 seconds. The model is excited using the sinusoidal acceleration protocol for the first eight seconds and the system then vibrates freely for the remaining 12 seconds.

The results obtained from the analyses described above are plotted in Figure 4-4b, c and d, where the displacements of the structural system, viscous damper and damper sub-system are normalised using the maximum absolute displacement of the structural system. At a stiffness ratio of 0.5, the displacement response of all three components are out of phase with each other, as shown in Figure 4-4b. Since the damper sub-system elastic displacement and the damper displacement must always add up to the overall structural displacement at any given time, if

out-of-phasing occurs then one component must lead the response while the other component lags. As shown in Figure 4-4b, the sub-system displacement is triggered earlier while the damper displacement occurs later. This phase offset in the displacement response of the damper-structure systems reduces with increasing stiffness ratio as shown in Figure 4-4c, whereas the viscous damper displacement response curve is seen to become more in phase with the structural component displacement response. When the stiffness ratio reaches 200, the sub-system is practically rigid (barely deforming) and the viscous damper displacement response profile is in phase with the structural component displacement response, as shown in Figure 4-4d, where the damper curve is seen to overlap the structural system curve.

Viscous damper forces are related to velocity, whereas structural forces are related to displacement. Therefore, when the displacement response of the damper and structure are in-phase, the forces produced by these two systems are out-of-phase, a trait which is desirable as it limits the combined forces transmitted to the foundations. As such, when the damper sub-system flexibility leads to the displacement response of the damper and structure becoming out-of-phase, as seen in Figure 4-4b, the implication is that the forces of these two systems are becoming more in-phase, which may lead to an increase in the maximum combined force transmitted to the foundations.

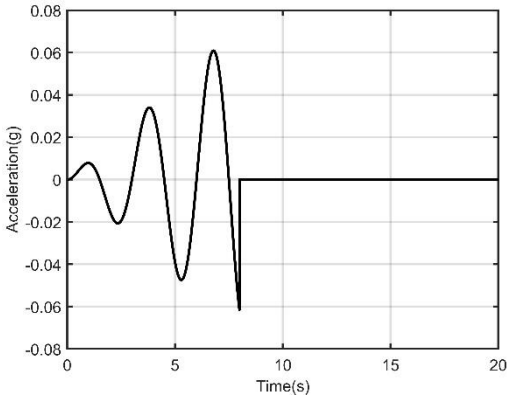

a. Sinusoidal excitation protocol

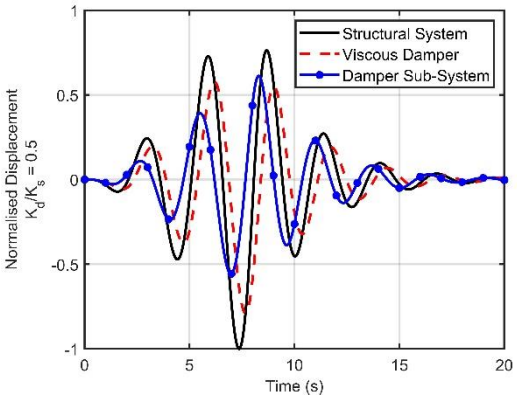

b. K_d/K_s = 0.5

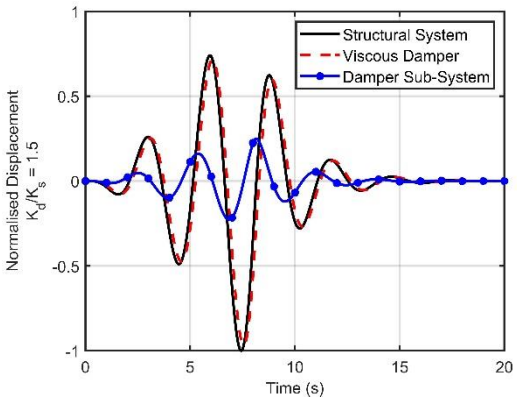

c. K_d/K_s = 1.5

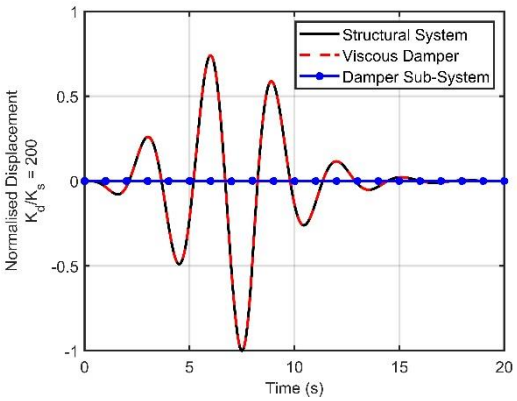

e. K_d/K_s = 200

Figure 4-4. Displacement time-history plot for stiffness ratio of 0.5, 1.5, and 200

4.3. Impact of sub-system flexibility on system response to earthquake excitation

Recalling that viscous dampers are increasingly used in practice to control the response of structures to earthquake motions, this section looks to quantify the impact of sub-system flexibility on the response of SDOF systems subject to earthquake excitation. The impact on systems with linear viscous dampers is first examined and then the impact on systems with nonlinear viscous dampers is investigated.

4.3.1. Linear viscous dampers

4.3.1.1. Ground motion, parameter selections and modelling method

For the linear viscous damper analysis, the SDOF model described in Figure 4-2 is subject to 10 pairs of two-horizontal-component ground motions (20 ground motions in total). The set of ground motions was selected for a general site in Christchurch, New Zealand with subsoil class D and an occurrence possibility of 2% in 50 years by Yeow *et al*. [2018]. The GmRot50 values, which are the geometric mean calculated from the 50th percentile values of the geometric means of all non-redundant rotation angles, of these ground motions were conditioned at 2 seconds period, as shown in Figure 4-5. It is worth to note that the ground motion records scaled by Yeow *et al*. [2018], GmRot50 values are calculated for periods 0.5s, 1s, 1.5s, 2s, 3s, 4s, 5s and 6s only.

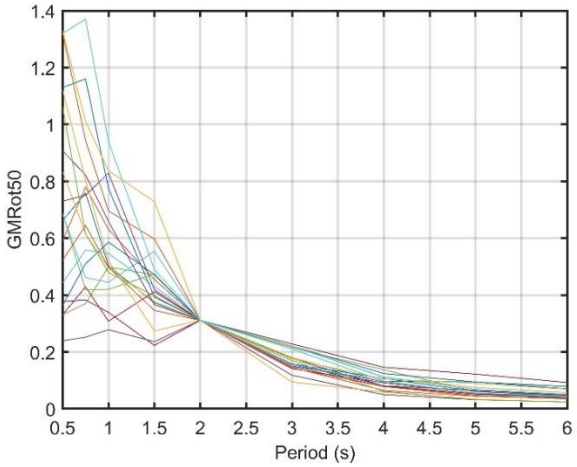

Figure 4-5. GmRot50 spectra for ground motions selected by for ground motions selected by Yeow *et al.*, [2018] using the GCIM method and a conditioning period of 2s.

Stiffness ratios of K_d/K_s = 1, 1.5, 5, 10 and 200 are selected. The inherent system damping is set at 5% of critical and the supplemental damping is defined so that the analysis is undertaken for a range of total system damping ratio from 5% to 35%, representing 0% to 30% supplement damping contributed by the viscous damper. Structural periods, T_n, of 0.25, 0.5, 0.75, 1, 2, and 3 seconds are considered.

For each ground motion simulation, the initial step is to identify the elastic spectral displacement demand at 5% damping, S_d, and spectral acceleration, S_a, at the period of the

system for the selected ground motion. The next step is to input a supplemental damping constant, C_d, value into the model in OpenSEES to run the time-history analysis at a selected stiffness ratio and structural period. The input C_d value can be converted into an equivalent damping ratio using Equation (4.6). For each time-history analysis, the lateral displacement of node 2, and the reaction force of node 1 are recorded. The node 1 reaction force can also be referred to as the base shear force of the overall system. It is the sum of the instantaneous structural system forces, inherent damping forces, and forces from the supplemental damping system. To present the results, at each damping ratio, the maximum absolute displacement, X_0, and base shear force, V_b, are extracted from the time-history data. These two values are normalised using the 5% spectral responses, S_d and S_aM, respectively. For the following sections of this paper, the normalised displacement, X_0/S_d, is defined as the displacement reduction factor (DRF) and the normalised base shear, V_b/S_aM, is defined as the base shear reduction factor (BSRF). Once simulations are completed for all 20 ground motions, the median value is identified and plotted against the total damping ratio.

4.3.1.2. Displacement results

Using the modelling procedure described above, the median DRF-damping ratio curves obtained for the six selected structural periods are plotted in Figure 4-6. It can be seen that for a system possessing linear viscous dampers, the response is not sensitive to the change of stiffness ratio (SR) for structural periods less than 1 second. At T_n = 1 second, differences in DRF between SR = 1 and 200 becomes noticeable only for total damping ratios higher than 25%. For T_n = 2 and 3 seconds, the curves for SR = 1 and 1.5 start to show significant variation across different SR's above 15% damping, and differences in the DRF increase with increases in damping. It is also noted from the results that for all the selected periods, if the SR is greater than 5, the deviations from the high rigidity SR = 200 case in terms of displacement response are less than 5%, suggesting that this stiffness ratio could be a suitable target for design.

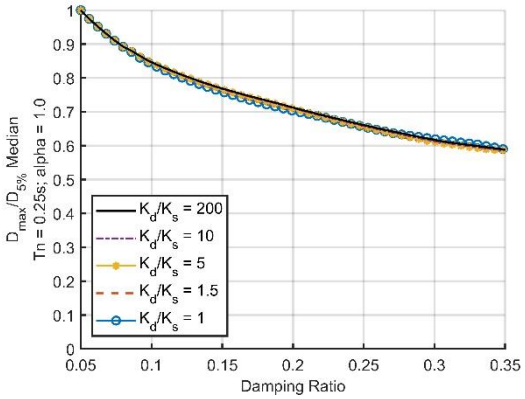

a. T_n = 0.25 second

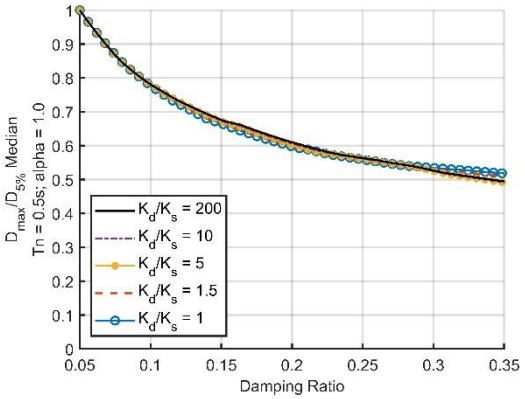

b. T_n = 0.5 second

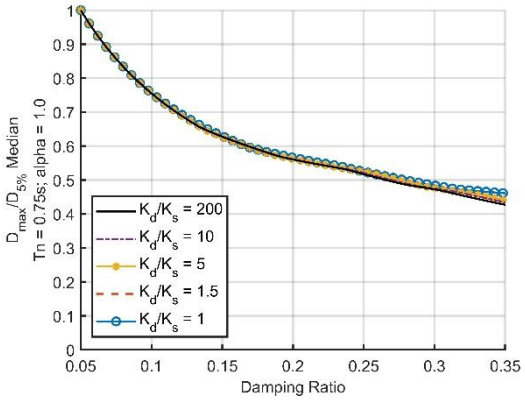

c. T_n = 0.75 second

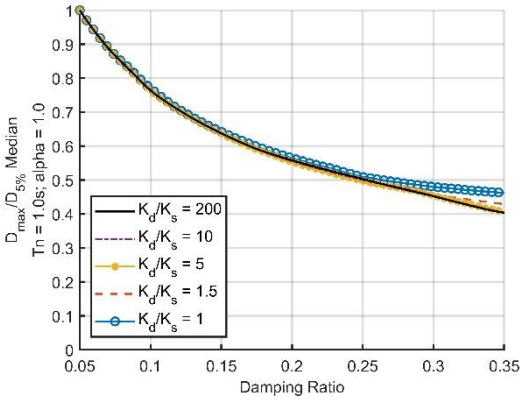

d. T_n = 1 second

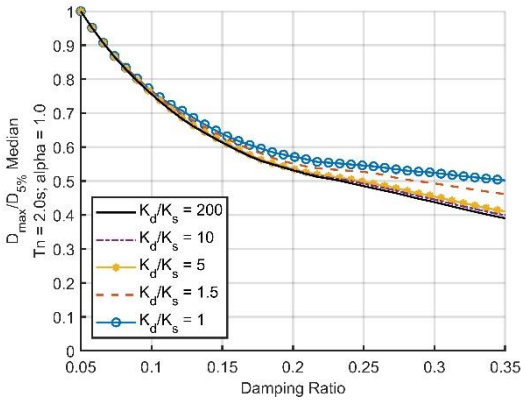

e. T_n = 2 seconds

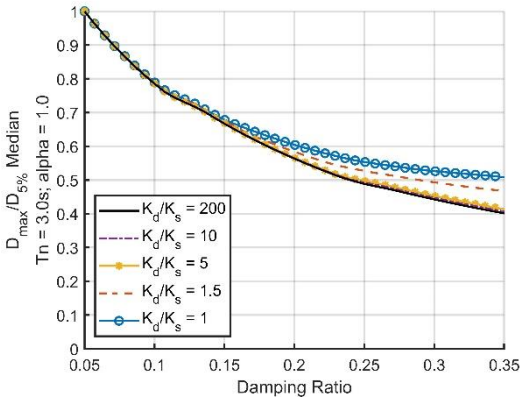

f. T_n = 3 seconds

Figure 4-6. Median DRF-damping ratio curves for linear viscous dampers (α = 1), at the selected structural periods, using the CHCH records selected by Yeow *et al.*, [2018]

4.3.1.3. Total system force results

The median BSRF-damping ratio curves for the six selected structural periods are plotted in Figure 4-7. Unlike the displacement response, differences in BSRF between low and high stiffness ratios exist even at low periods such as T_n = 0.2s and become quite significant for structural periods larger than 0.75s. As shown in Figure 4-7d, e, and f, for the cases of SR = 1 and 1.5, the base shear response starts to show large variation across different stiffness levels for damping ratios higher than 10%. In Figure 4-7e and f, even for high stiffness cases of SR = 5 and 10, there are difference of up to 10% in BSRF between them and the SR = 200 case.

Although viscous dampers are designed to limit structural displacement, it is important to acknowledge the variations in base shear due to sub-system flexibility because this should be considered in capacity design when verifying foundations, connections and other parts of the lateral load resisting system. Based on the results obtained, it would appear if the damper sub-system stiffness is equal to that of the structural system, the total reaction forces transmitted to the foundation may increase by up to 33%. This increase is partially attributed to the fact that the damper and structure displacement response will be partially out-of-phase due to the influence of damper sub-system stiffness. The out-of-phase in displacement response leads to the response force for the damper and structure becoming more in-phase and leading to larger total reaction forces.

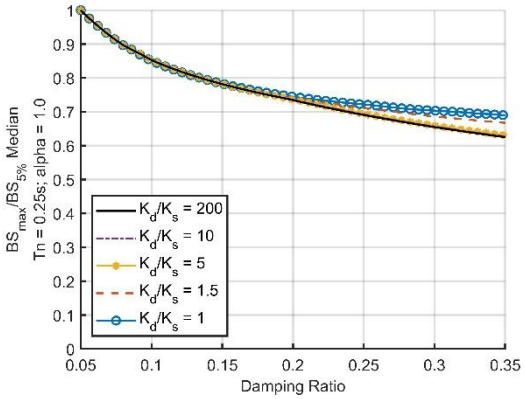

a. T_n = 0.25 second

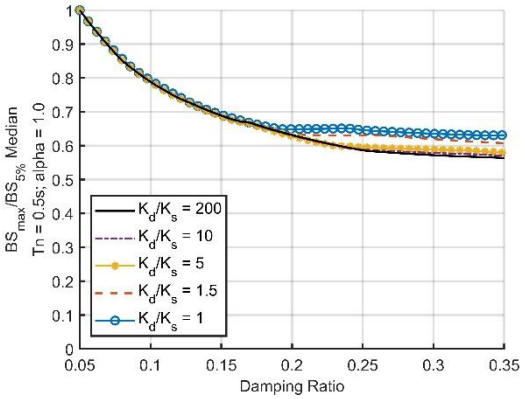

b. T_n = 0.5 second

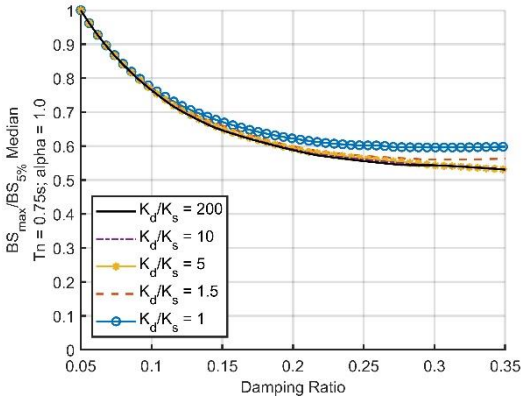

c. T_n = 0.75 second

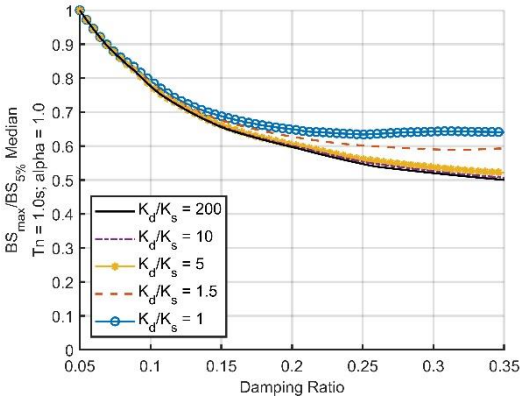

d. T_n = 1 second

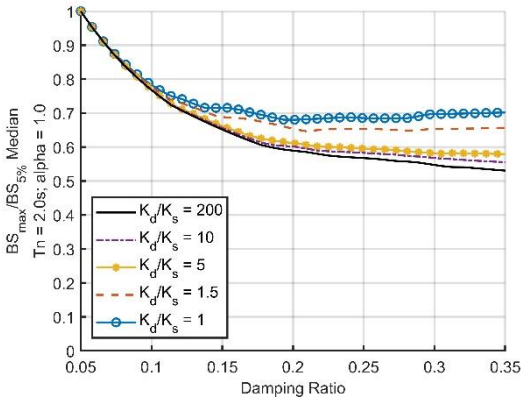

e. T_n = 2 seconds

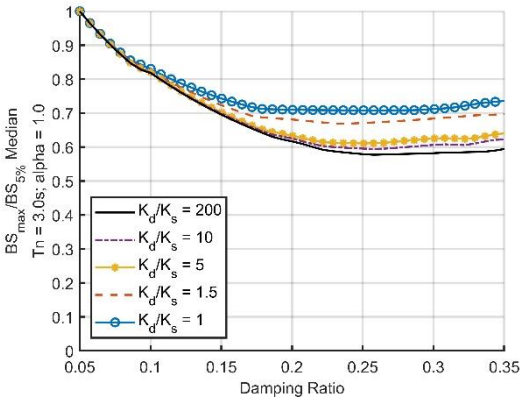

f. T_n = 3 seconds

Figure 4-7. Median BSRF-damping ratio curves for linear viscous dampers (α = 1) and the selected structural periods, using the CHCH records selected by Yeow *et al.*, [2018]

4.3.2. Nonlinear viscous dampers

4.3.2.1. Modelling approach for systems of nonlinear viscous dampers

The modelling and analysis method for the SDOF system with nonlinear viscous dampers is similar in principle to that described in Section 4.3.1. To this extent, the same structural model and the same ground motions are used, and the same stiffness ratios and structural periods are considered. However, to calculate the equivalent damping ratio based on an input damping coefficient Equation (4.6) is no longer appropriate in this case as it is only valid for linear viscous dampers. To calculate the equivalent linear damping ratio for a nonlinear viscous damper, there are a few methods available in the current literature. Lago [2011] made a comparison between four well-known methods, such as Soong and Constantinou [2014], Seleemah and Constantinou [1997], Pekcan *et al*. [1999] and Lin *et al*. [2008]. The comparison concluded that methods proposed by Pekcan *et al*. [1999] and Lin *et al*. [2008] produced more conservative solutions than the other two methods. For this study, the power-based formulation described in Pekcan *et al*. [1999] is used as an initial step to determine the equivalent linear damping ratio at an input damping coefficient, C_d, value for a nonlinear damper. The Pekcan *et al*. [1999] formulation is defined in Equation (4.7).

$$\zeta = \frac{1}{1+\alpha}\frac{C_d X_0^{\alpha-1} T_n^{2-\alpha}}{(2\pi)^{2-\alpha} M} \tag{4.7}$$

Where X_0 is the maximum displacement response and all the other parameters have been defined previously.

As shown in the equation above, the equivalent linear damping ratio is a function of the maximum displacement response X_0. Therefore, in order to utilise the Pekcan *et al*. [1999] formulation into the modelling procedure for nonlinear viscous damper, the following steps were adopted.

Step (i), identify spectral demands at 5% inherent linear viscous damping as described in Section 4.3.1..

Step (ii), analysis is conducted first on the near-rigid case (SR = 200). In OpenSEES, for a given ground motion, SR and structural period, input a trial C_d value and run the time-history analysis, then extract X_0 and V_b from the result. Substitute C_d and X_0 into Equation (4.7) to find the equivalent damping ratio.

Step (iii), trial different values of C_d until the target equivalent damping ratio is reached, e.g. 30%.

Step (iv), divide the C_d at 30% equivalent damping into 50 equal increments and repeat step (ii) for a range of C_d values from $C_{d,30\%}/50$ to $C_{d,30\%}$, as several damping coefficients are required to plot the DRF or BSRF versus damping ratio curves.

Step (v), calculate the DRF and BSRF values using the method described in Section 4.3.1..

Step (vi), As the research findings should not be constrained to a specific damping definition (such as the power-based formulation of Equation (4.7)), the actual equivalent viscous damping is computed by matching the DRF calculated for the nonlinear damper at SR = 200 to the linear damper DRF at SR = 200, and from this, the linear damping ratio required to achieve the same DRF is identified. The nonlinear DRF is then plotted against the actual linear damping ratios instead of the damping ratios approximated using Equation (4.7). The procedure is the same for plotting BSRF.

Step (vii), for the analysis of the lower stiffness cases (SR = 1, 1.5, 5, and 10), the input C_d values are the same as those used for the near-rigid case (SR = 200). The DRF and BSRF are plotted against the actual linear damping ratios for the near-rigid case. By adopting this method, it allows the differences in DRF and BSRF between different stiffness cases (but the same supplement damper, C_d) to be easily observed.

For the displacement response, the seven steps described above are repeated for α = 0.2, 0.4 and 0.6. However, only α = 0.2 is run for all six structural periods used in the linear viscous damper analysis. This value is presented in the most detail as it represents the largest variation from the linear results previously presented and also broadly represents a likely lower bound on the velocity exponent for nonlinear viscous dampers applied in structural engineering applications.

4.3.2.2. Displacement results

The median DRF-damping ratio curves obtained from the analysis approach described above are plotted for the nonlinear viscous damper cases with α = 0.2, 0.4 and 0.6 and various period values in Figure 4-8, Figure 4-9, and Figure 4-10, respectively. The nonlinear viscous damper system responses generally follow similar trends as the linear viscous damper system, but results are found to be more sensitive to the change of sub-system stiffness. At low structural periods of 0.25 second and 0.5 second, the differences in DRF between all stiffness levels are insignificant, but as the structural period becomes larger than 0.75 second, the curves for all SR cases start to separate at damping ratios around 10%. As shown in Figure 4-8f, at T_n = 3 seconds, the displacement response is affected by the sub-system stiffness even for relatively high damper sub-system stiffness cases, such as SR = 5 and 10. For a damping ratio of 35% and a vibration period of 3s, if the damper sub-system stiffness matches the structural system stiffness (i.e. K_d/K_s = 1) the median peak displacement is seen to be 40% greater than the rigid damper case (with K_d/K_s = 200). Comparing Figure 4-9 and Figure 4-10 to Figure 4-8, an increase in α value is seen to slightly reduce the sensitivity of the system to the change of sub-system stiffness as the lower stiffness curves move closer to the curve for the rigid case. However, the variation with alpha is not seen to be very large.

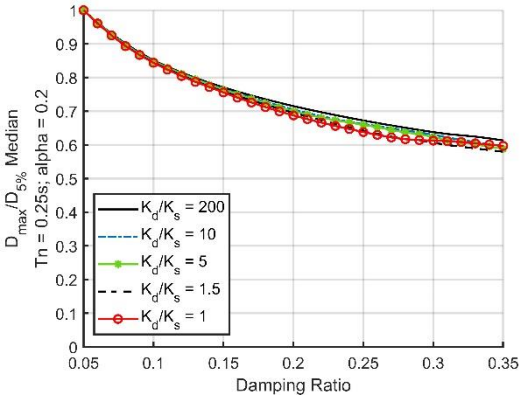

a. T_n = 0.25 second

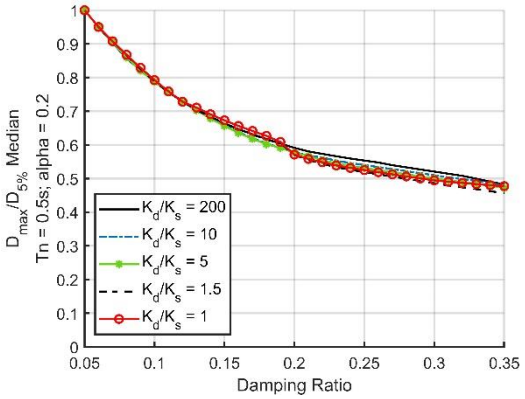

b. T_n = 0.5 second

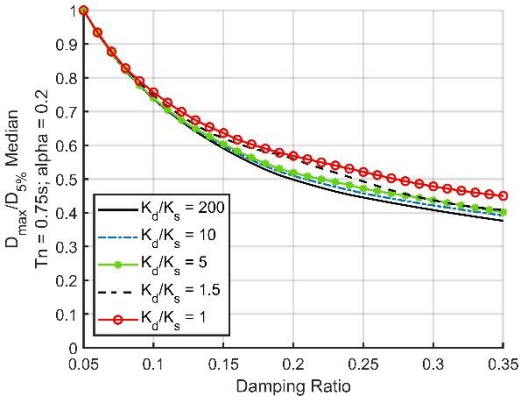

c. T_n = 0.75 second

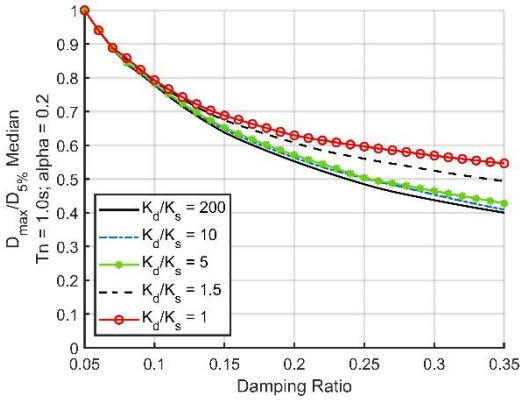

d. T_n = 1 second

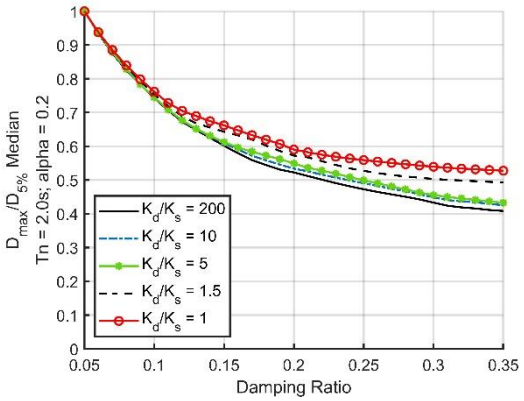

e. T_n = 2 seconds

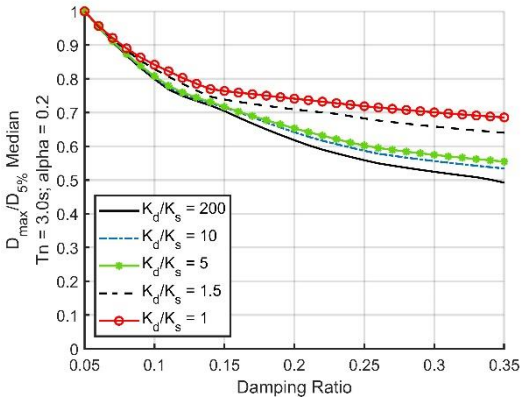

f. T_n = 3 seconds

Figure 4-8. Median DRF-damping ratio curves for the selected structural periods, for a nonlinear viscous damper with α = 0.2, using the CHCH records selected by Yeow *et al.*, [2018]

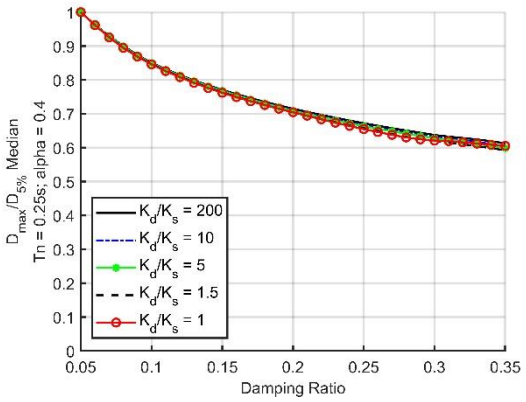

a. T_n = 0.25 second

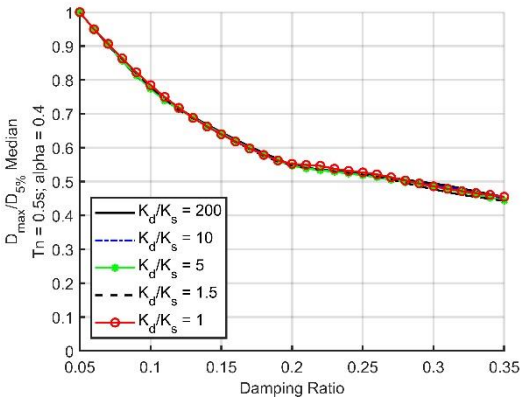

b. T_n = 0.5 second

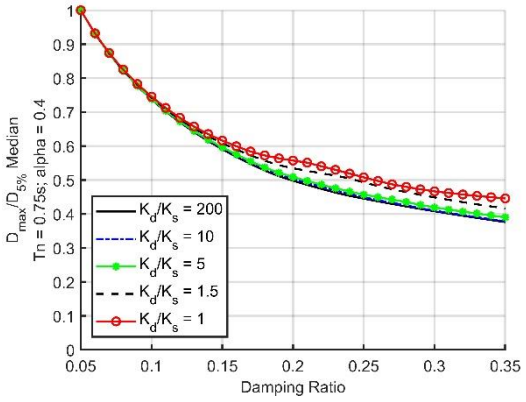

c. T_n = 0.75 second

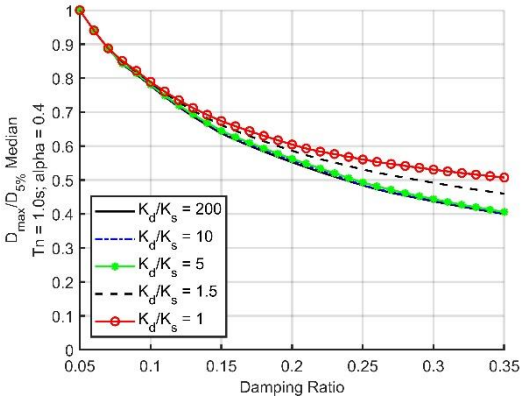

d. T_n = 1 second

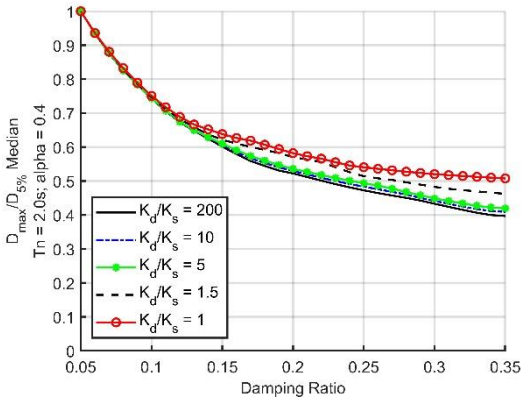

e. T_n = 2 seconds

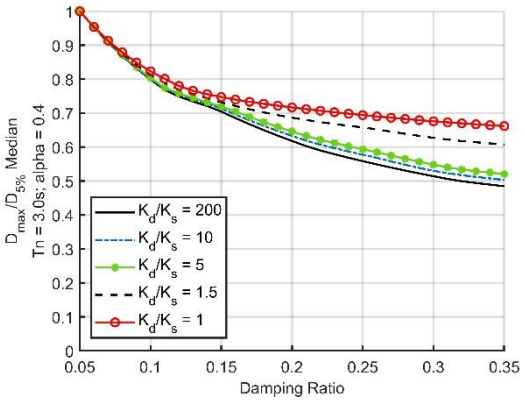

f. T_n = 3 seconds

Figure 4-9. Median DRF-damping ratio curves for the selected structural periods, for a nonlinear viscous damper with α = 0.4, using the CHCH records selected by Yeow *et al.*, [2018]

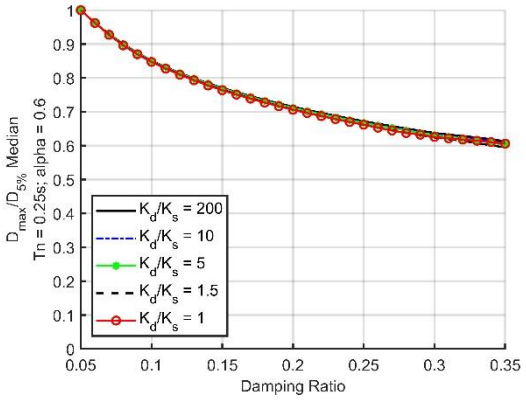

a. T_n = 0.25 second

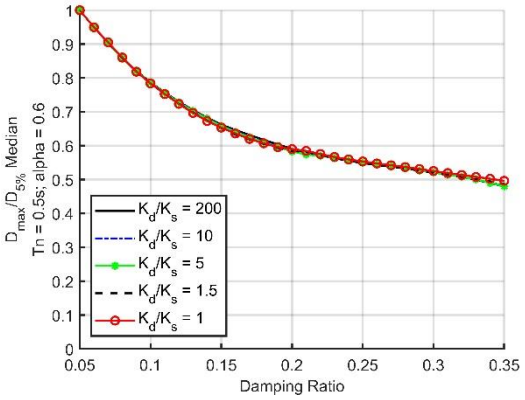

b. T_n = 0.5 second

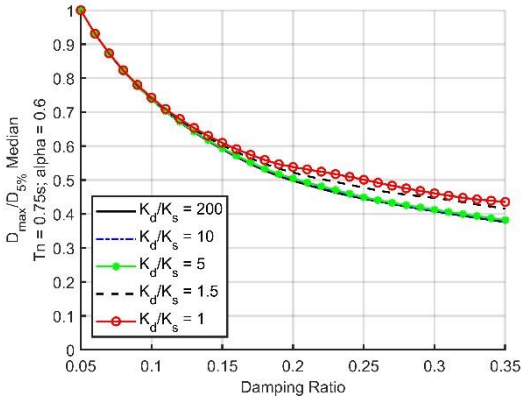

c. T_n = 0.75 second

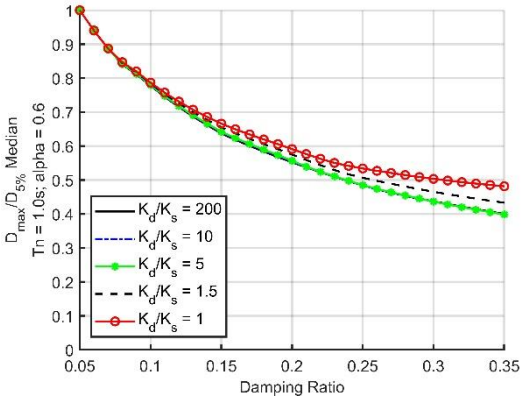

d. T_n = 1 second

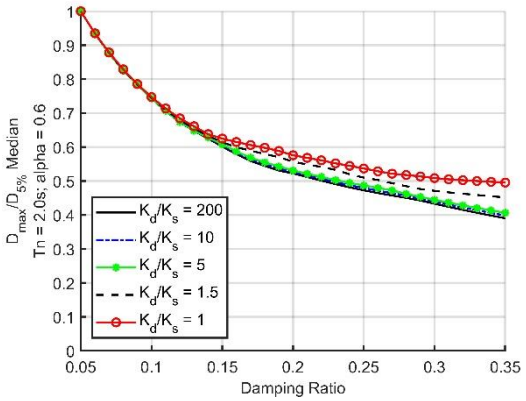

e. T_n = 2 seconds

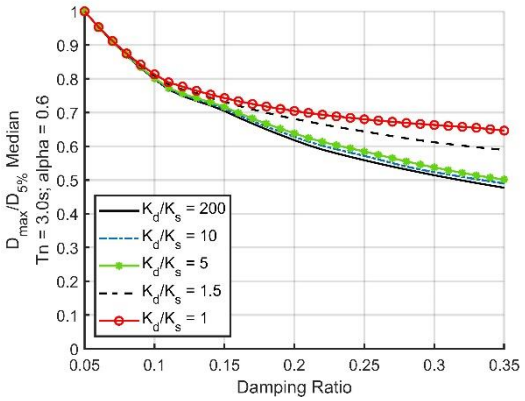

f. T_n = 3 seconds

Figure 4-10. Median DRF-damping ratio curves for the selected structural periods, for a nonlinear viscous damper with α = 0.6, using the CHCH records selected by Yeow *et al.*, [2018]

4.3.2.3. Total system force results

Figure 4-11 plots the median BSRF-damping ratio curves at a structural period of 3 seconds for alpha values of α = 0.2, 0.4 and 0.6. The variations in BSRF between alpha values are similar to those observed in the DRF results, where at higher α values of 0.4 and 0.6, the variations in force responses across all SR ratios are less than those observed at α = 0.2. For example, considering 35% total damping and damper sub-system stiffness of SR = 1, the BSRF is 25% higher than the SR = 200 case when α = 0.6, whereas for the α = 0.2 case, the BSRF is 35% higher than the SR = 200 case.

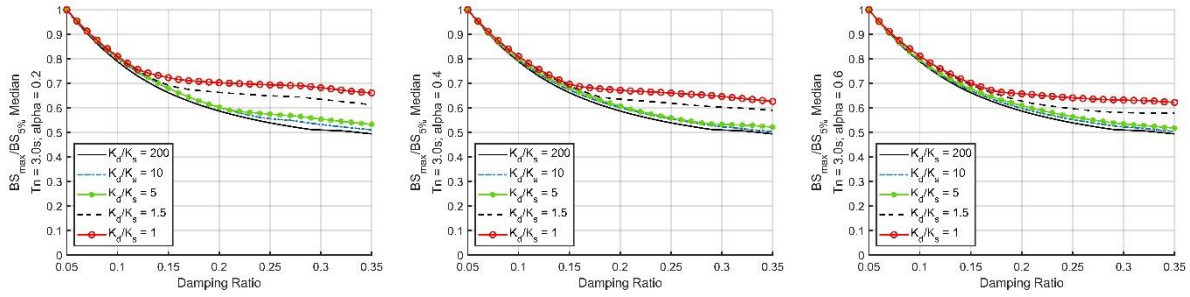

a. Median BSRF-damping ratio curves for α = 0.2

b. Median BSRF-damping ratio curves for α = 0.4

c. Median BSRF-damping ratio curves for α = 0.6

Figure 4-11. Median BSRF-damping ratio curves for Tn = 3 seconds, at α = 0.2, 0.4 and 0.6, using the CHCH records selected by Yeow *et al.*, [2018]

4.3.3. Dispersions of displacement ratio factors

The above results presented are based on median values in order to provide a generalised trend of the structural system's behaviour at various stiffness levels and damping ratios. However, for these median plots to be meaningful, it is important to consider how much spread there is in the results away from the median values. If the dispersion of the 20 ground motion simulation results is large, then by only plotting the median values would not be enough to make valid statements on the structural system's general response. Another reason to consider the result dispersions is to investigate whether the sub-system flexibility affects the dispersions, because it may be possible that spread is either increased, decreased or unchanged by considering different levels of damper sub-system stiffness.

To plot the dispersion-damping ratio relationships, the following steps are taken:

(i) For each ground motion, obtain the maximum DRF at each damping ratio using the methodology described in section 4.3.1.2 for linear dampers, and section 4.3.2.1 for nonlinear dampers.

(ii) At each damping ratio, calculate the natural log of the maximum DRF's for all the 20 ground motions.

(iii) Calculate the standard deviation of the 20 log values to provide an indication of the result dispersion at one damping ratio.

(iv) Repeat step (i) to (iii) for all damping ratios from 5% to 30%.

Figure 4-12 to Figure 4-15 below show the dispersion-damping ratio plots for the system at different stiffness levels and natural periods. It can be seen from all the plots that the dispersion is zero at 5% total damping. This result is because, at this level of damping, the DRF is always 1 due to the DRF is calculated by normalising the system's displacement with its displacement at 5% inherent damping, or zero supplement damping.

In general, when the supplement damping is introduced to the system, the dispersion of the structural responses from different ground motions starts to increase. For most plots, dispersions are higher as damping increases. The rate of the increase is high initially and begins to gradually reduce when the total damping is higher than approximately 7%. It can also be seen from the plots that the stiffness of the sub-system does not have any obvious impact on the dispersions for damping ratios lower than 15%. For damping ratios larger than 15%, the differences in dispersions between stiffness levels are generally higher at lower alpha values. This is shown in *Figure 4-12* below where the variations in dispersions across all stiffness levels are the most significant at $\alpha = 0.2$, when comparing to those at $\alpha = 0.6$, $\alpha = 0.4$ and $\alpha = 1.0$. However, there is no clear trend in the dispersion-SR relationship, which suggests a high SR does not necessarily result a low dispersion, or vice versa.

Another crucial finding from the dispersion plots is that the standard deviations for the 20 ground motions are low, with the maximum being 0.32 at a high damping of 35%. This information indicates the median values are good representations of the system's general behaviours under ground motions with those characteristics described in Section 4.3.2.2.

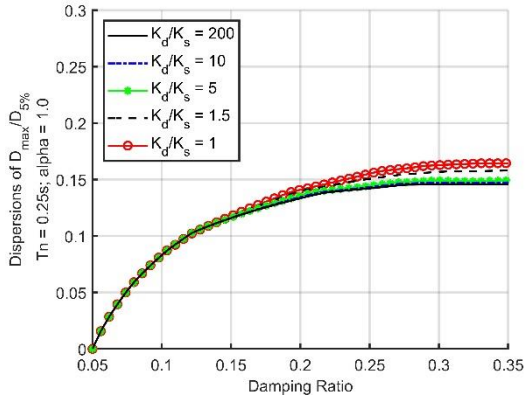

a. T_n = 0.25 second

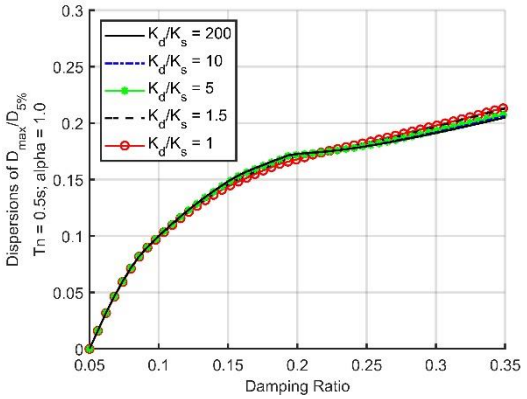

b. T_n = 0.5 second

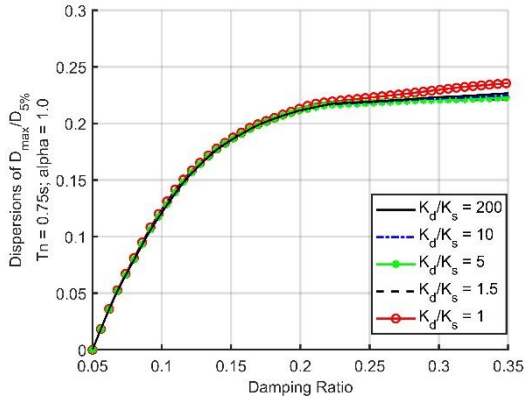

c. T_n = 0.75 second

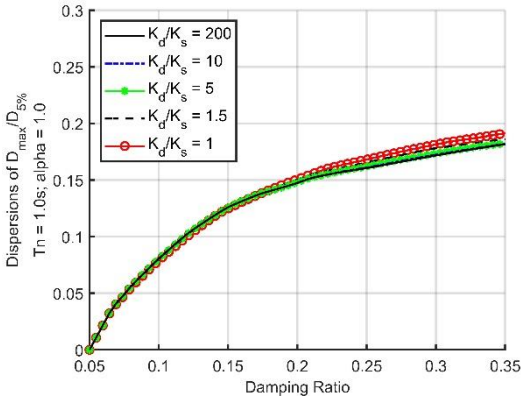

d. T_n = 1 second

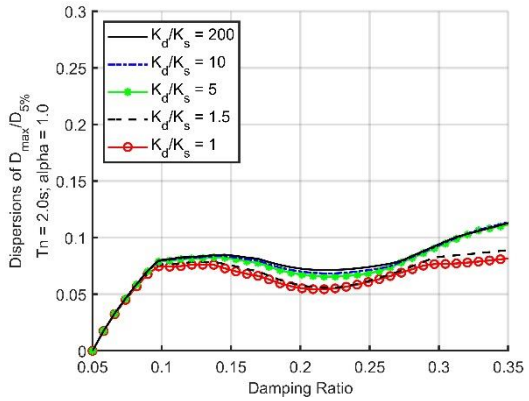

e. T_n = 2 seconds

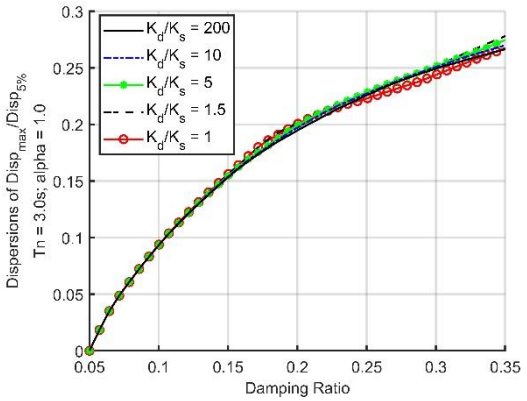

f. T_n = 3 seconds

Figure 4-12. Dispersion curves of DRF-damping ratio obtained using the CHCH records selected by Yeow *et al.*, [2018], for linear viscous dampers, at the selected structural periods. α = 1.0

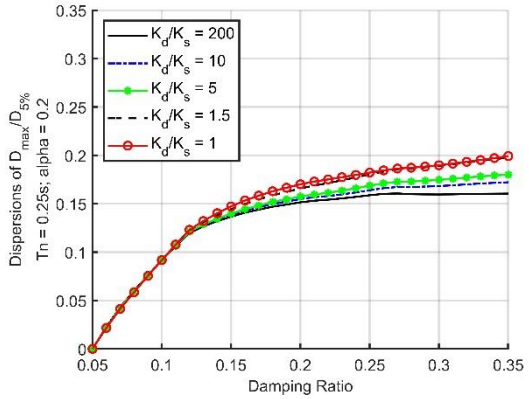

a. T_n = 0.25 second

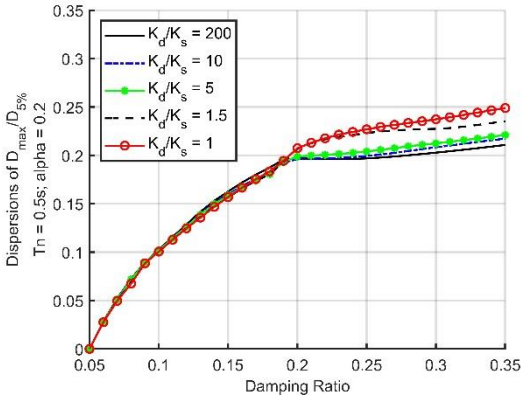

b. T_n = 0.5 second

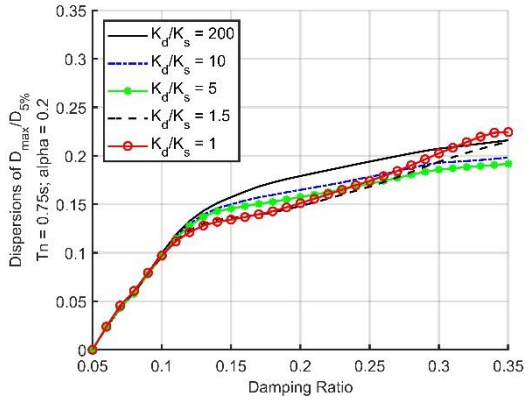

c. T_n = 0.75 second

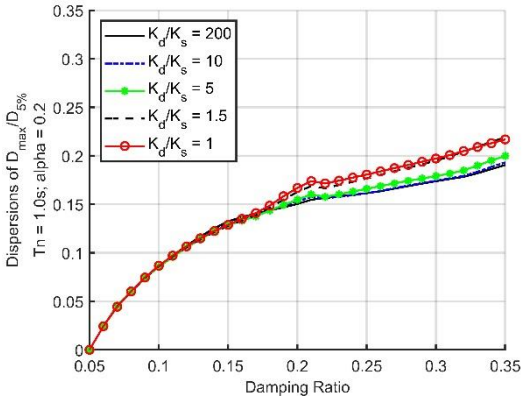

d. T_n = 1 second

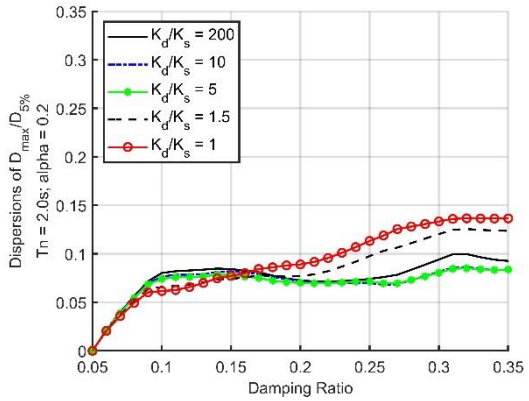

e. T_n = 2 seconds

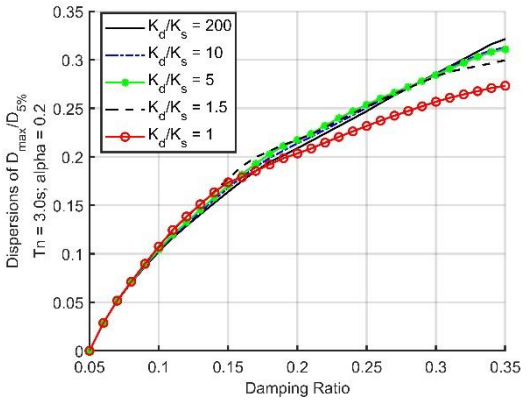

f. T_n = 3 seconds

Figure 4-13. Dispersion curves of DRF-damping ratio for the selected structural periods, obtained using the CHCH records selected by Yeow *et al.*, [2018] for a nonlinear viscous damper with α = 0.2

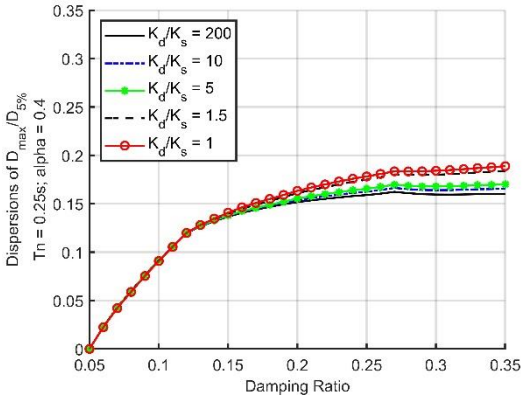

a. T_n = 0.25 second

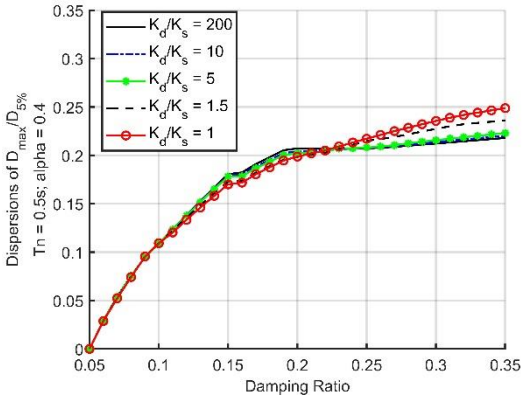

b. T_n = 0.5 second

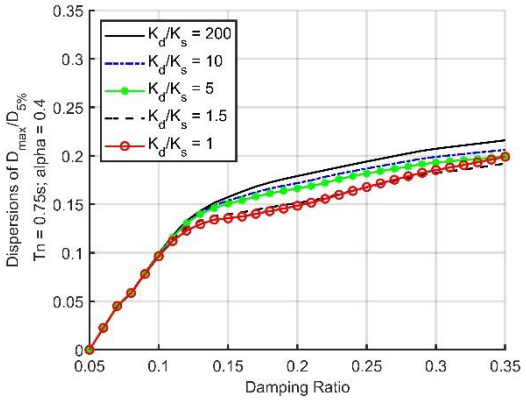

c. T_n = 0.75 second

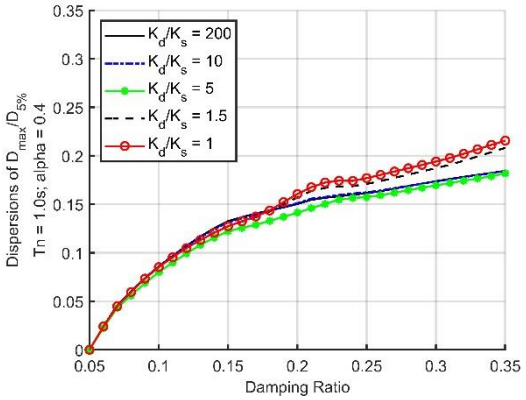

d. T_n = 1 second

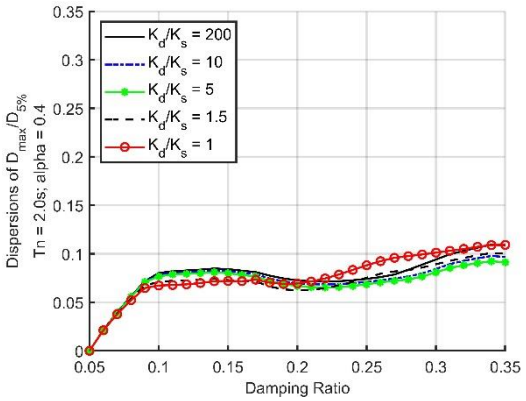

e. T_n = 2 seconds

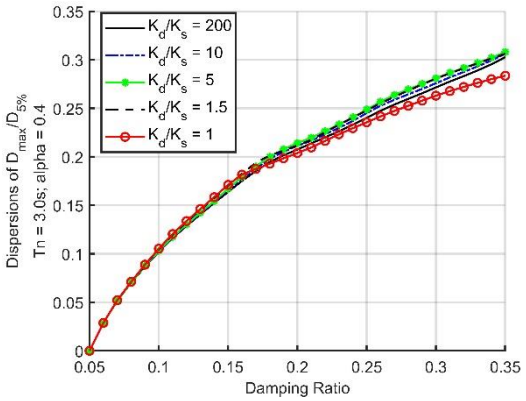

f. T_n = 3 seconds

Figure 4-14. Dispersion curves of DRF-damping ratio for the selected structural periods, obtain using the CHCH records selected by Yeow *et al.*, [2018], for a nonlinear viscous damper with α = 0.4

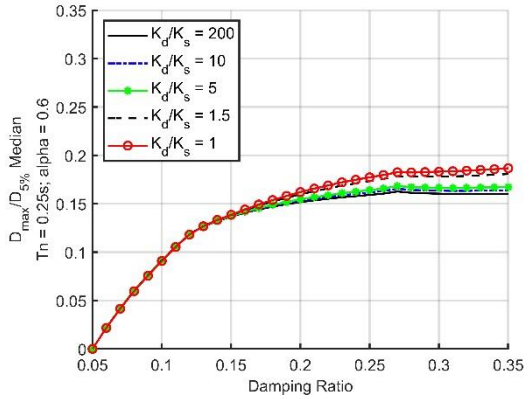

a. T_n = 0.25 second

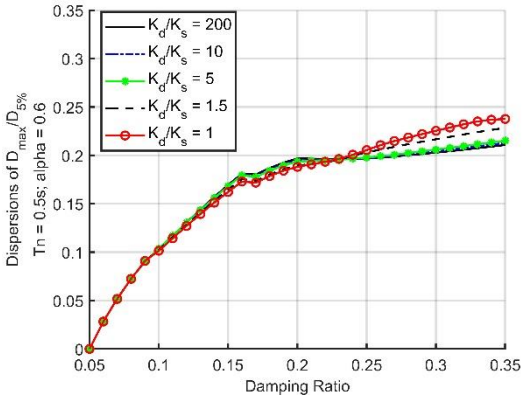

b. T_n = 0.5 second

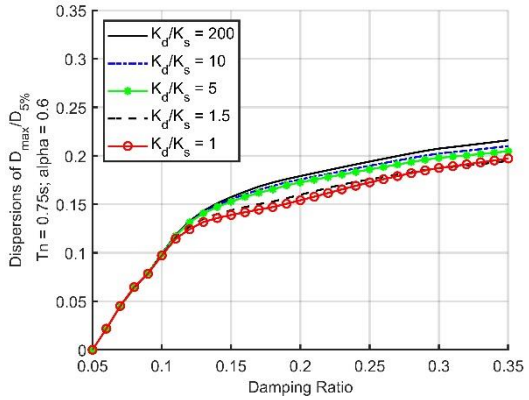

c. T_n = 0.75 second

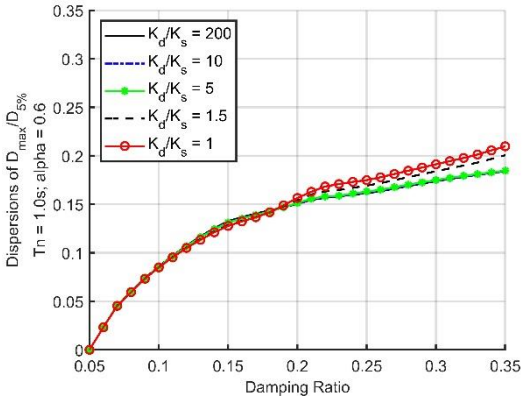

d. T_n = 1 second

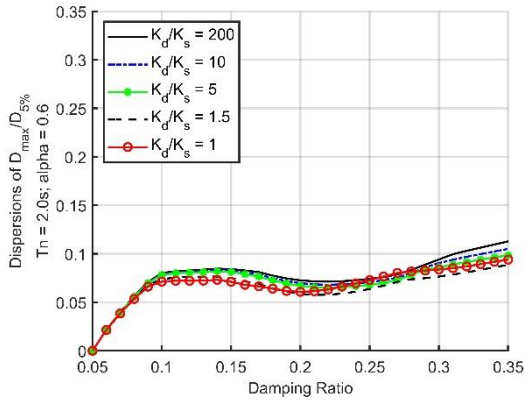

e. T_n = 2 seconds

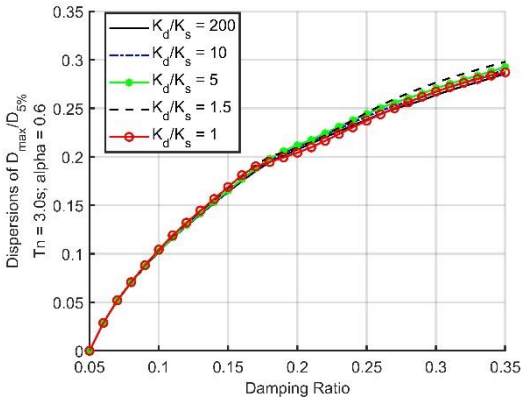

f. T_n = 3 seconds

Figure 4-15. Dispersion curves of DRF-damping ratio for the selected structural periods, obtained using the CHCH records selected by Yeow *et al.*, [2018], for a nonlinear viscous damper with α = 0.6

Figure 4-13e Figure 4-14e and Figure 4-15e above show that the dispersions at T_n = 2 seconds exhibit distinctly different trends comparing to the dispersions at other natural periods. Firstly, at T_n = 2 seconds the dispersions are lower for damping ratios greater than 7%, and at 35% damping the maximum dispersion is 0.14. Secondly, dispersions at T_n = 2 seconds tend to increase up until approximately 12% damping, then start to decrease until damping reaches around 20% before they rise again. Overall, the dispersions at this natural period do not vary significantly with increasing damping, for damping ratios above 10% the dispersions range between 0.06 and 0.14. Recall from Section 4.3.1.1 that the 20 ground motions used for the above parametric studies have the GmRot50 values that are conditioned at 2 seconds period, which indicates the input spectral acceleration demands dispersion at T = 2s is also the lowest comparing to other periods. This is illustrated in Figure 4-16 below, where the spectral acceleration demands at T = 2s are more concentrated together, except for three cases, which results in lower standard deviations comparing to the other selected periods. For this reason, low dispersions in the analytical results are expected.

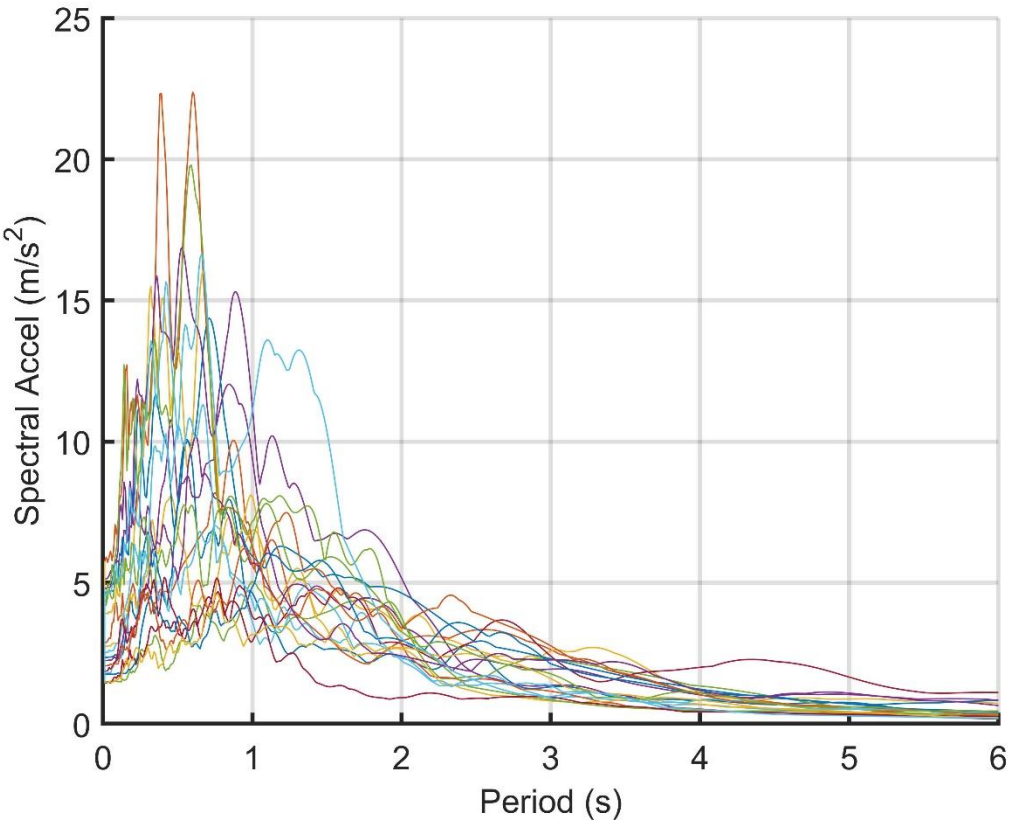

Figure 4-16. Acceleration response spectra for the CHCH ground motion components used in this study

Figure 4-3 in Section 4.2.1 shows the ω_d/ω_n ratios at different stiffness levels. It can be seen the sub-system stiffness can either increase or reduce the damped period of the overall system. For example, if a system with flexible damper sub-system, the damped period is seen to be shortened, and this trend is reversed for a system with rigid damper sub-system. Figure 4-16 above shows that the dispersion of the spectral accelerations changes most drastically before and after the conditioning period. Therefore, if the undamped period of the system is the same as the conditioning period, adding supplemental damping can shift the system period either to the left or right of the conditional period depending on the stiffness of the damper sub-system, causing significant changes to the system's acceleration. Therefore, the damper sub-system stiffness has the most impact on the DRF dispersions if the system's natural period is the same as the conditioning period. In this case, T_n = 2 seconds as shown in Figure 4-13 to Figure 4-15.

4.4. Ground motion simulation results from FEMA P695 ground motions

To further validate the results presented above in Section 4.3, an extension set of ground motion simulations have been conducted using the SDOF model presented in Figure 4-2. The aim of the extended ground motion simulations is to carry out a sensitivity study to determine whether a different set of ground motions influences the results presented in Section 4.3. The ground motions used are 22 pairs of FEMA P695 'far-field' ground motions (44 ground motions in total) [FEMA, 2009], as presented in Table 2 below. These ground motions are not conditioned to a specific period.

Table 4-1. FEMA P695 'far-field' ground motions [FEMA, 2009]

ID No.	Earthquake			Recording Station	
	M	Year	Name	Name	Owner
1	6.7	1994	Northridge	Beverly Hills - Mulhol	USC
2	6.7	1994	Northridge	Canyon Country-WLC	USC
3	7.1	1999	Duzce, Turkey	Bolu	ERD
4	7.1	1999	Hector Mine	Hector	SCSN
5	6.5	1979	Imperial Valley	Delta	UNAMUCSD
6	6.5	1979	Imperial Valley	El Centro Array #11	USGS
7	6.9	1995	Kobe, Japan	Nishi-Akashi	CUE
8	6.9	1995	Kobe, Japan	Shin-Osaka	CUE
9	7.5	1999	Kocaeli, Turkey	Duzce	ERD
10	7.5	1999	Kocaeli, Turkey	Arcelik	KOERI
11	7.3	1992	Landers	Yermo Fire Station	CDMG
12	7.3	1992	Landers	Coolwater	SCE
13	6.9	1989	Loma Prieta	Capitola	CDMG
14	6.9	1989	Loma Prieta	Gilroy Array #3	CDMG
15	7.4	1990	Manjil, Iran	Abbar	BHRC
16	6.5	1987	Superstition Hills	El Centro Imp. Co.	CDMG
17	6.5	1987	Superstition Hills	Poe Road (temp)	USGS
18	7.0	1992	Cape Mendocino	Rio Dell Overpass	CDMG
19	7.6	1999	Chi-Chi, Taiwan	CHY101	CWB
20	7.6	1999	Chi-Chi, Taiwan	TCU045	CWB
21	6.6	1971	San Fernando	LA - Hollywood Stor	CDMG
22	6.5	1976	Friuli, Italy	Tolmezzo	--

4.4.1. Displacement Reduction Factors

For the simulations using the 44 FEMA P695 ground motions, the same methodologies described in Section 4.3.1.1 and 4.3.2.1 are used for linear dampers and nonlinear dampers, respectively. The median DRF's are used to plot Figure 4-17 (linear damper DRF's) and Figure 4-18 (nonlinear damper DRF's, α = 0.2).

In general, comparing to the results from the CHCH ground motion simulations, similar trends can be seen from the FEMA simulations. The trends are: (i) damper sub-system stiffness has less impact on systems with low natural periods, the figures below show that at T_n = 0.25 second the system's DRF's do not vary more than 6% when the SR reduces from 200 to 1. (ii) Damper sub-system stiffness has insignificant effect at low damping ratios, less than 12%. This can be

explained using Figure 4-3, where the ω_d/ω_n ratios of different stiffness levels only start to disperse when the damping ratio is higher than 12%. (iii) If SR is greater than 5, the differences in DRF's are less than 4% when comparing to the SR = 200 case, and (iv) damper sub-system stiffness has more impact on the overall system behaviour if the viscous damper is nonlinear.

The only difference in the results between the CHCH and FEMA simulations is the SR = 1 curves produced from the FEMA simulations are further apart from the SR = 200 curves. This could simply be due to a wider set of ground motions of various characteristics are used for the FEMA simulations. For these reasons, the discussions made so far in this chapter on the relationships between the damper sub-system stiffness and the overall structural response are valid, and they are not especially sensitive to the characteristics of the specific set of ground motions used.

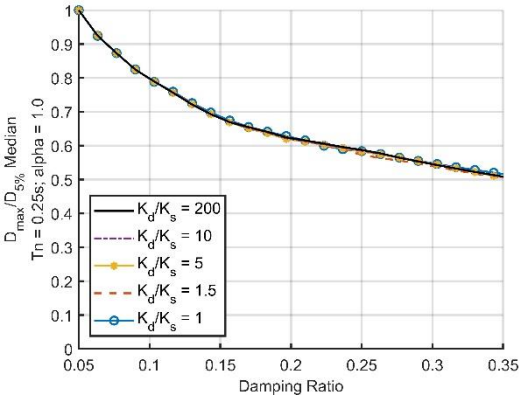

a. T_n = 0.25 second

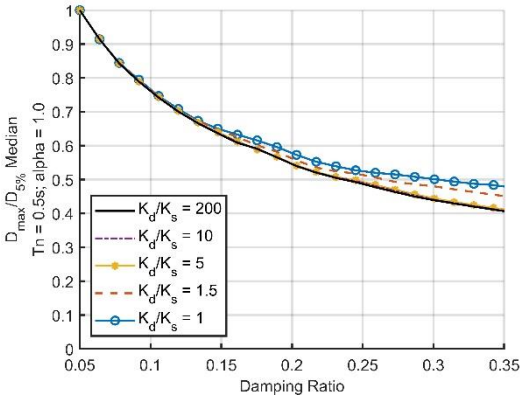

b. T_n = 0.5 second

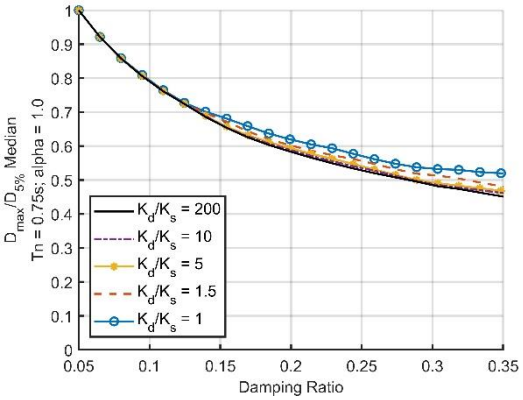

c. T_n = 0.75 second

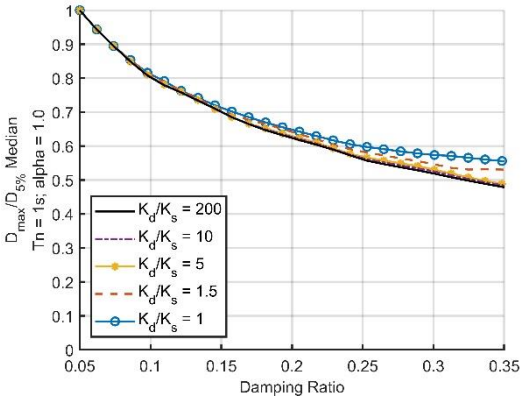

d. T_n = 1 second

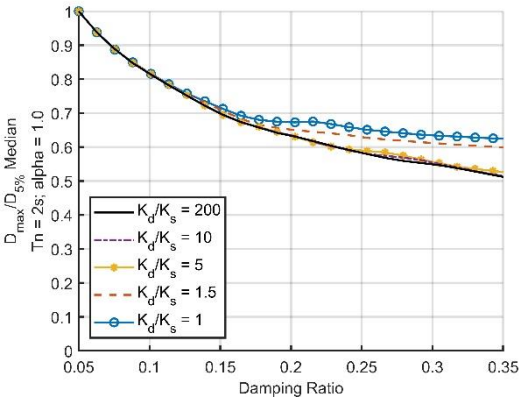

e. T_n = 2 seconds

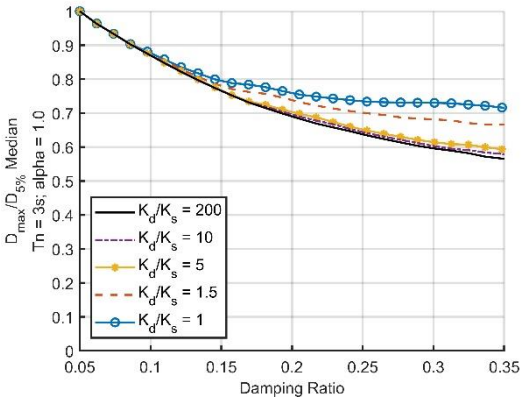

f. T_n = 3 seconds

Figure 4-17. α = 1.0, FEMA P695 ground motion simulations

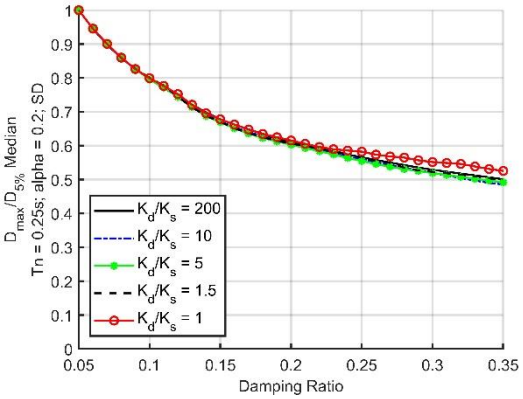

a. T_n = 0.25 second

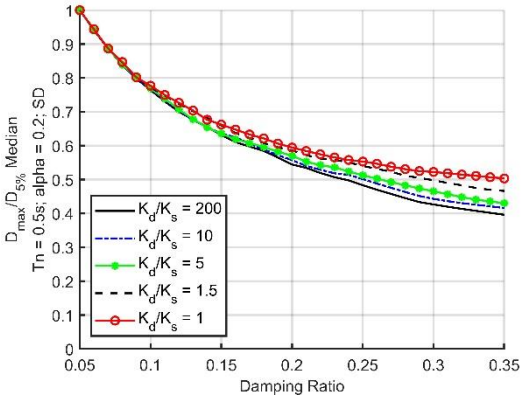

b. T_n = 0.5 second

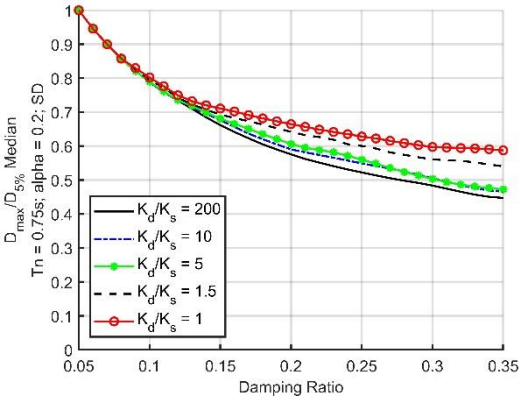

c. T_n = 0.75 second

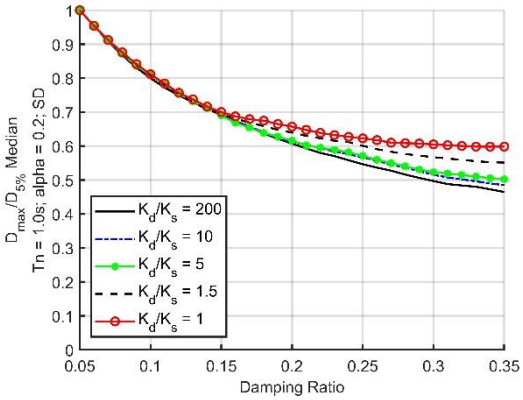

d. T_n = 1 second

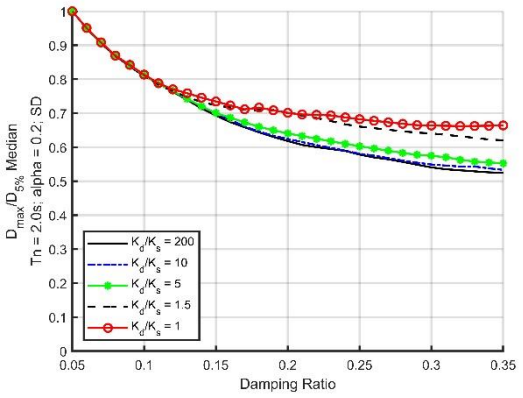

e. T_n = 2 seconds

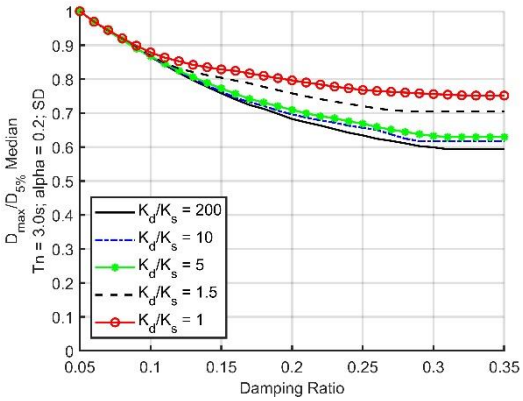

f. T_n = 3 seconds

Figure 4-18 . α = 0.2, FEMA P695 ground motion simulations

4.4.2. DRF dispersions

DRF Dispersions from the FEMA simulations have also been calculated using the method described in Section 4.3.3. The dispersions are plotted in Figure 4-19 for the linear damper system and Figure 4-20 for the nonlinear damper system with α = 0.2. The plots show that the standard deviations of the FEMA simulation results increase with damping ratio, and at 35% damping, which is the highest damping ratio considered for this analytical study, the standard deviations are lower than 0.3. This indicates low dispersions among the results at a given structural period, and the median values presented in the previous section are reasonable representations of the system's general behaviour when it is subject to the FEMA ground motions. It is also worth to note that the atypically low dispersions seen at T_n = 2s for the CHCH ground motions is no longer present here for the FEMA ground motions, this is because the FEMA ground motions are not conditioned to a certain period.

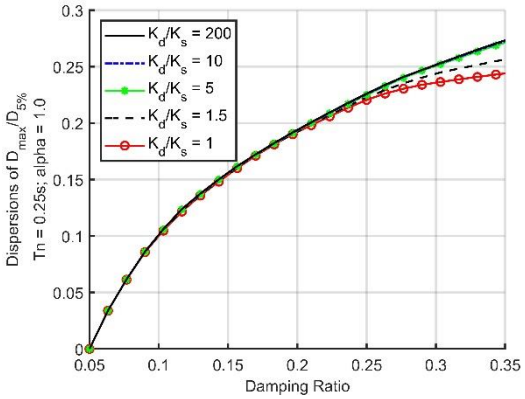

a. T_n = 0.25 second

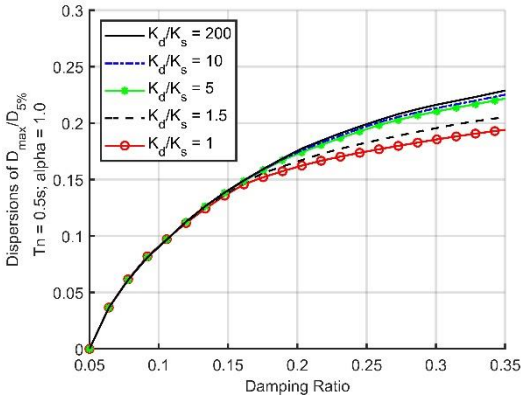

b. T_n = 0.5 second

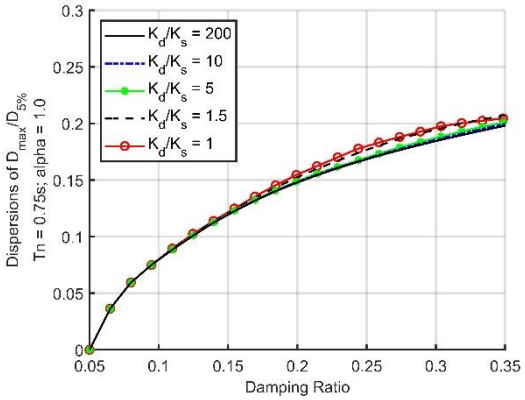

c. T_n = 0.75 second

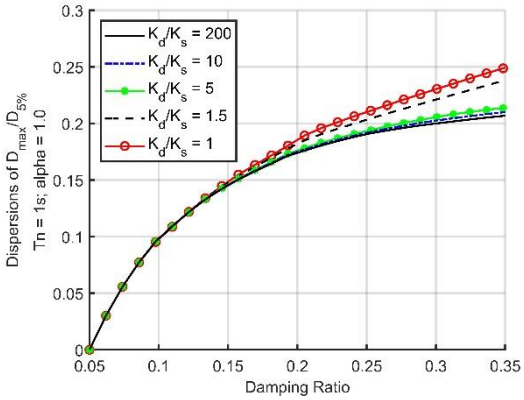

d. T_n = 1 second

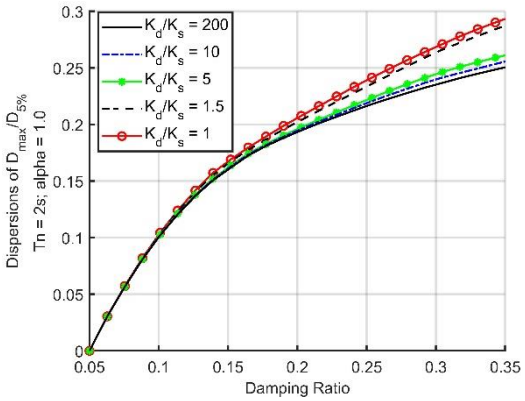

e. T_n = 2 seconds

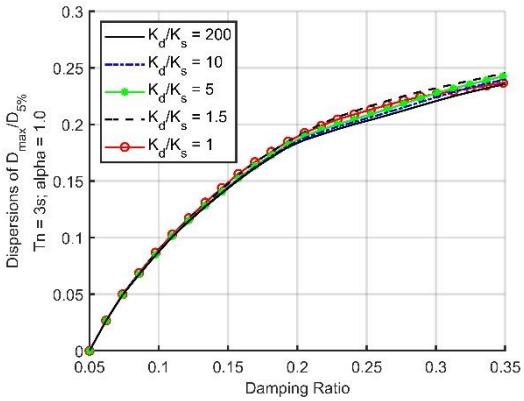

f. T_n = 3 seconds

Figure 4-19. α = 1.0, Dispersions, FEMA simulations

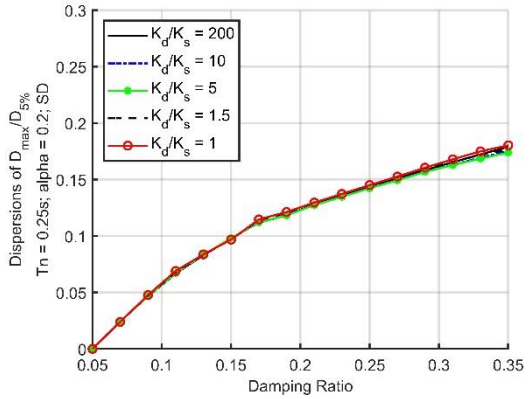

a. T_n = 0.25 second

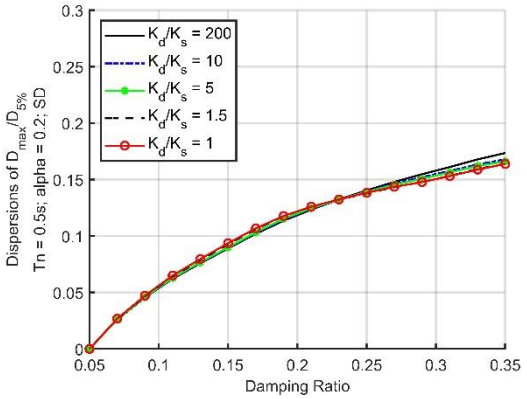

b. T_n = 0.5 second

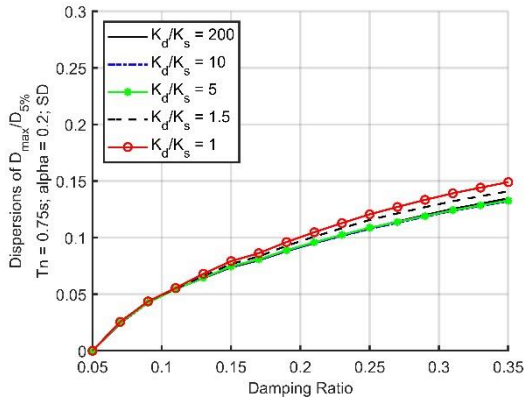

c. T_n = 0.75 second

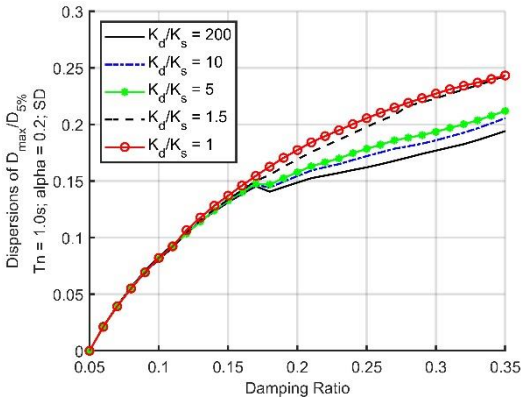

d. T_n = 1 second

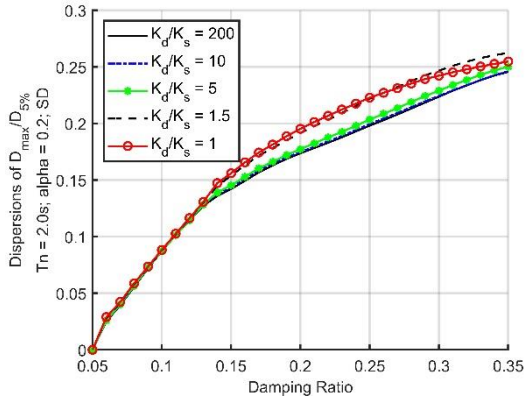

e. T_n = 2 seconds

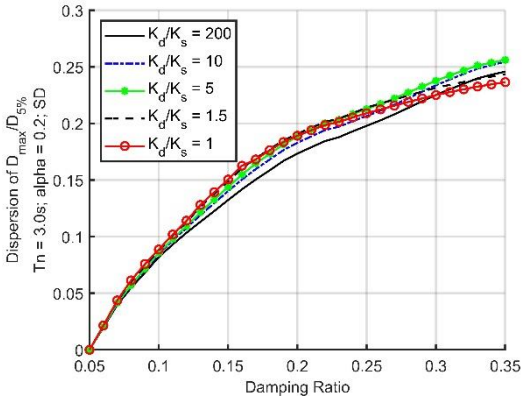

f. T_n = 3 seconds

Figure 4-20. α = 0.2, Dispersions, FEMA simulations

From Figure 4-20d above, the spread in dispersions between different stiffness levels is more significant at 1 second period comparing to the other periods. Figure 4-21 below plots the

elastic spectral acceleration spectra of the FEMA records. It can be seen from the plot that T = 1s sits on a steeper slope of the median curve comparing to the other selected periods, this indicates any change in period due to damper sub-system flexibility could result in a more significant change in demands. It is worth to note that T = 0.25s also sits on a steep slope on the median spectral acceleration curve as shown in Figure 4-21 below. However, as indicated by the results presented in this chapter, structures with low periods such as 0.25s and 0.5s are not significantly affected by the damper sub-system flexibility, therefore there is no obvious difference in dispersions between stiffness ratios for T = 0.25s.

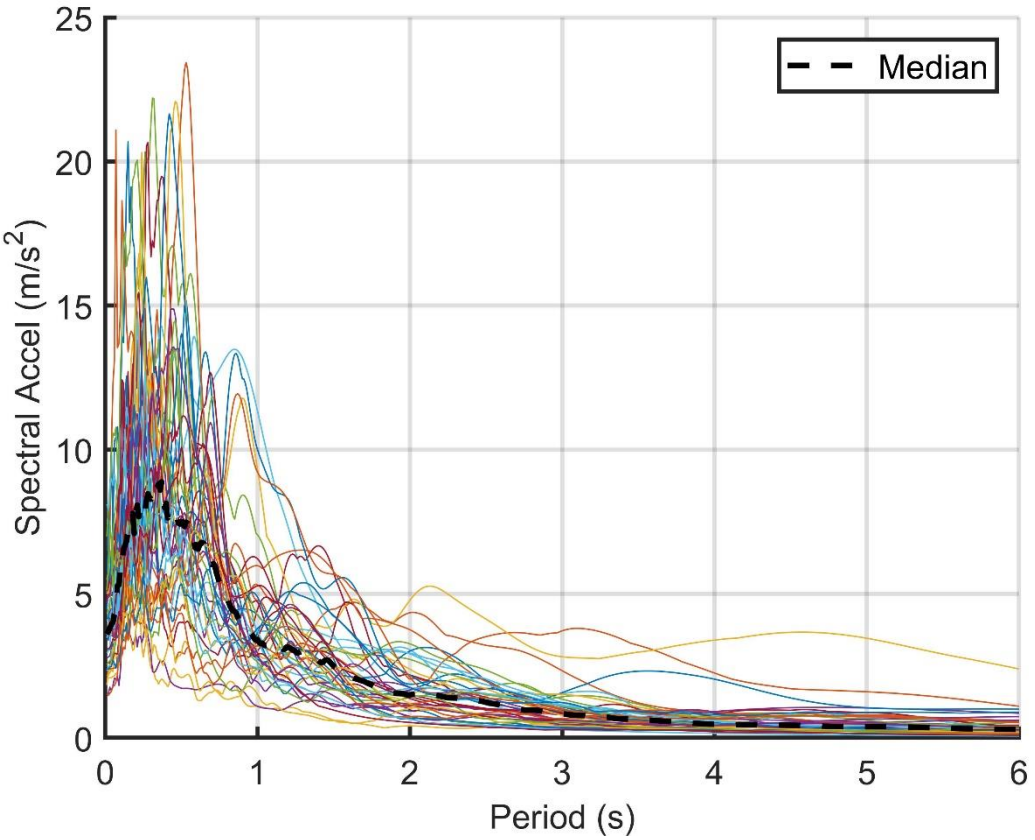

Figure 4-21. Elastic spectra of FEMA P695 records

4.4.3. Displacement Reduction Factors considering damper stiffness

Another common nondimensional parameter to reflect the damper sub-system stiffness is the ratio of $K_d/(\omega * C_d)$, where ω is the frequency of the displacement history between the two ends of the brace-damper assembly. In order for the assumption of rigid damper sub-assembly to be accurate, K_d needs to be stiff with respect to the dashpot stiffness $\omega * C_d$, irrespective of the

structural stiffness. For a SDOF system with a linear damper, the sub-system-to-damper stiffness ratio (R) can be re-written as Equation (4.8).

$$R = \frac{K_d}{2\zeta K_s} = \frac{K_d}{C_d \omega} \tag{4.8}$$

The simulations described in Section 4.4.1 are repeated for a range of R values using the same FEMA P695 ground motions. In contrast to the simulations carried out in Section 4.4.1, where every curve presented in Figure 4-17 is for a fixed value of the damper sub-system K_d and also a fixed K_d/K_s ratio for any give period, the new simulations in this Section use fixed R values which require K_d to be changed for every damping ratio ζ. The results of these simulations are presented in Figure 4-22.

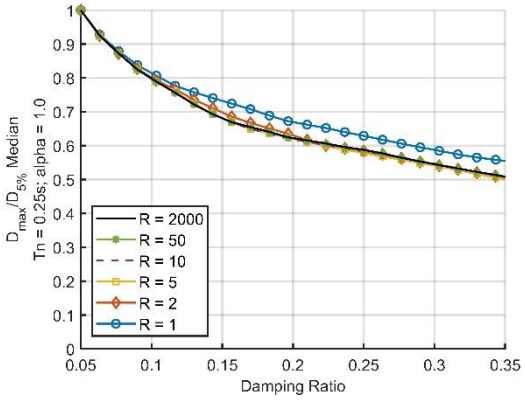

a. T_n = 0.25 second

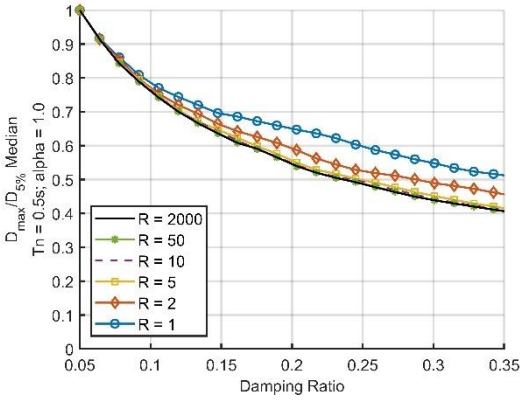

b. T_n = 0.5 second

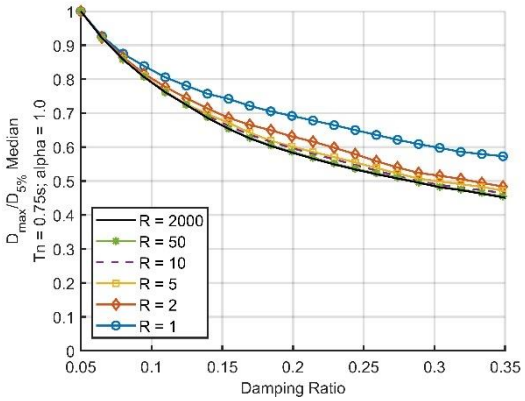

c. T_n = 0.75 second

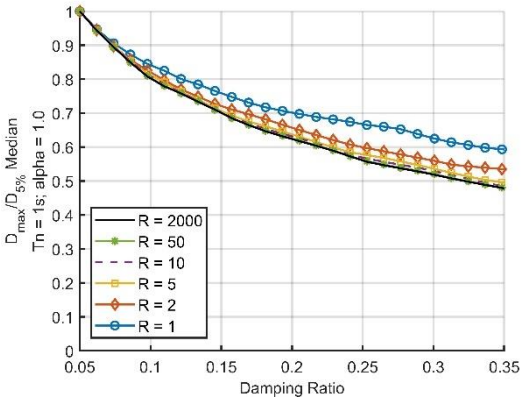

d. T_n = 1.0 second

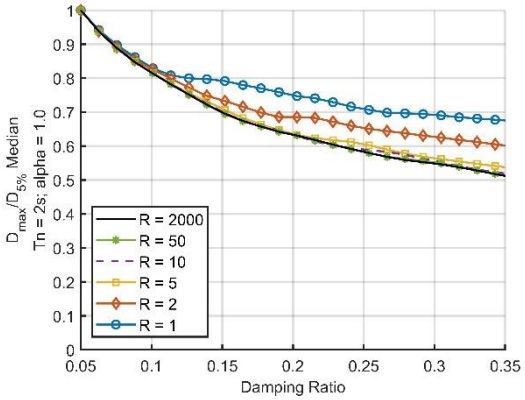

e. T_n = 2.0 seconds

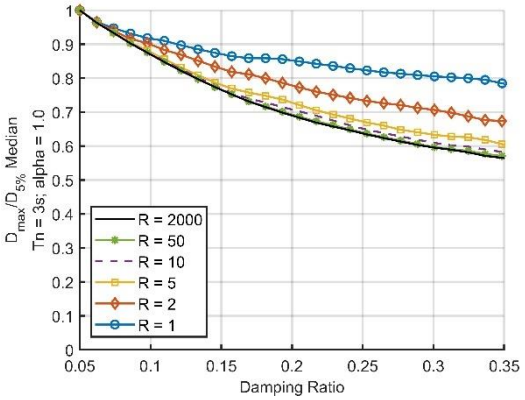

f. T_n = 3.0 seconds

Figure 4-22. DRF based on various R values; α = 1.0, FEMA P695 ground motion simulations

Results presented in Figure 4-22 show similar trend as those shown in Figure 4-17, and for the two almost rigid cases of the two sets of results, R = 2000 and SR = 200, the DRF curves are identical. This findings suggest that by using the sub-system-to-damper stiffness ratio, R, as the parameter to reflect the sub-system stiffness would lead to similar conclusions as if the sub-system-to-structure stiffness ratio, SR, is used. It should be noted in Figure 4-22a the R = 1 case generates significantly higher DRF's than the other R cases. When R = 1, the equivalent K_d/K_s ratio at 30% damping is 0.6, indicating a very flexible sub-system which may not satisfy the capacity design criteria, and therefore such low R value may not be a practical case.

4.5. Design recommendations

Based on the results and discussions presented in the previous sections of this chapter, this section proposes a modification to current design frameworks. Since the main purpose of viscous dampers is to limit seismic structure displacement, and flexible damper sub-systems can reduce the effectiveness of the dampers, leading to smaller reductions in displacement response. Therefore, empirical displacement reduction ratio (DRF) amplification factors are proposed based on the structure's natural period and sub-system to primary structure stiffness ratio. This section also suggests the critical SR's where a designer should consider the damper sub-system flexibility. A design example is also carried out to support these recommendations.

4.5.1. Amplification factors

This work has shown that in general, by ignoring the sub-system stiffness in the design process the effectiveness of the viscous dampers may be overestimated and the base shear demand may be underestimated. Both deviations from the design assumptions are non-conservative and warrant further consideration. To provide a better and clearer understanding of the results presented in Section 4, the DRF amplification factors can be plotted by normalising the DRF for the stiffness ratio cases of 1, 1.5, 5, and 10 to the DRF of the near-rigid case (SR = 200). By doing so, the differences in displacement response between the high stiffness case (SR = 200) and the low stiffness cases can be quantified. The resulting response amplification factors essentially represent a variation in response from the rigid-connection assumption often applied in design. To present this information, the DRF amplification factors are grouped by stiffness ratio (SR) and results for T_n = 0.25, 0.5, 0.75, 1, 2 and 3 are plotted together. Figure 4-23 shows the DRF amplification factors for the linear viscous damper system for SR = 1, 1.5,

and 5. Figure 4-24 shows cases for the nonlinear viscous damper system with SR = 1, 1.5, 5 and 10.

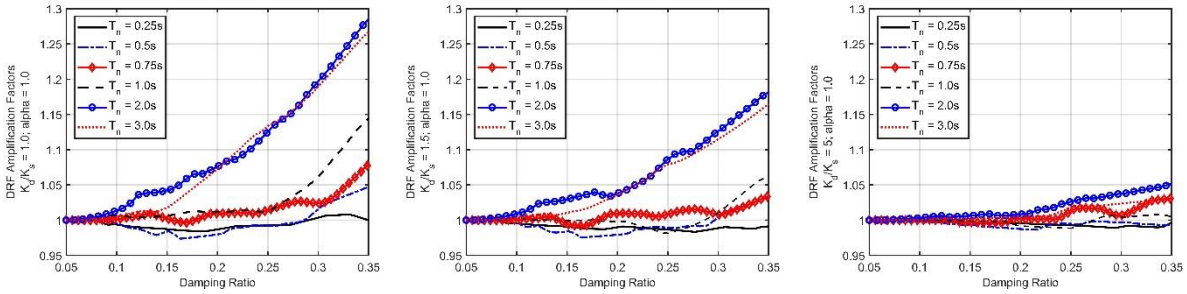

a. SR = 1 b. SR = 1.5 c. SR = 5

Figure 4-23. DRF amplification factors of linear damper systems for various structural periods, at SR = 1, 1.5 and 5

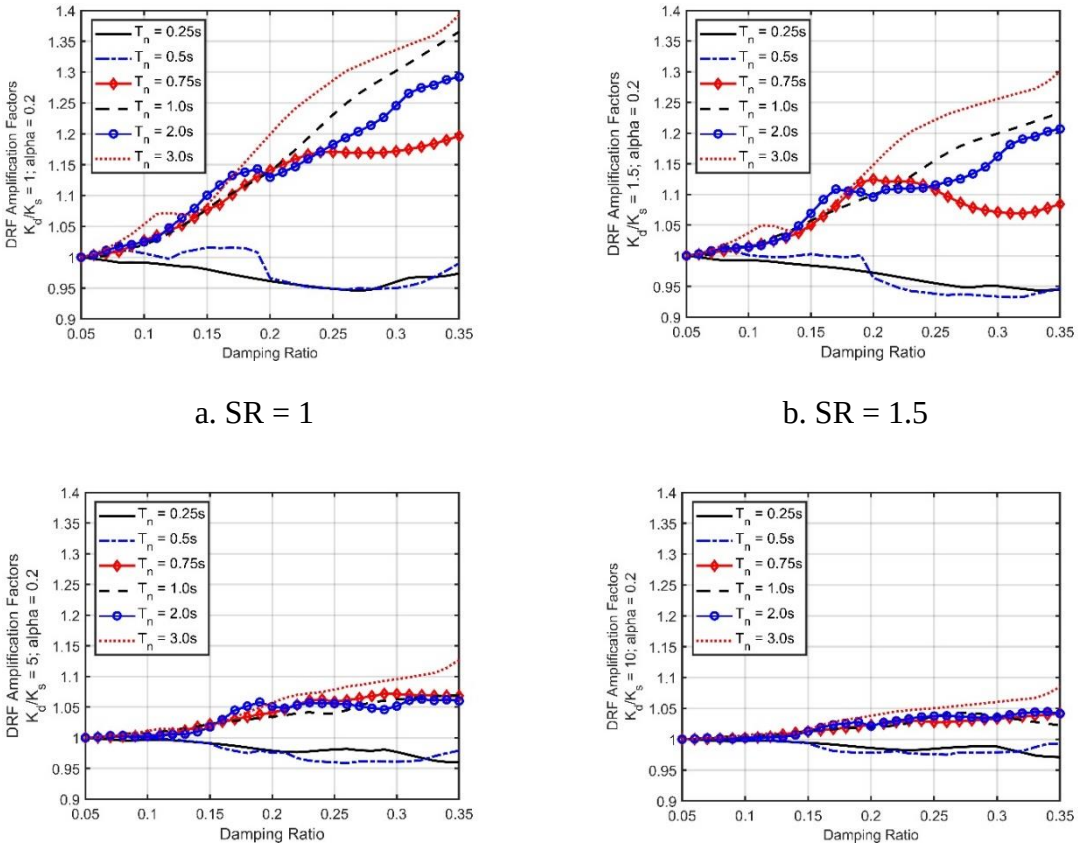

a. SR = 1 b. SR = 1.5

c. SR = 5 d. SR = 10

Figure 4-24. DRF amplification factors of nonlinear damper systems with α = 0.2, for various structural periods, at SR = 1, 1.5, 5 and 10

For the linear damper system, the peak DRF amplification factors for structural periods 0.5s and above reduce significantly as the stiffness ratio increases from 1 to 1.5 and to 5. At SR = 5, the highest DRF amplification factor for all stiffness cases are below 1.05, which indicates when a sub-system flexibility at this level is introduced, the overall system displacement response is amplified by no larger than 5%. Similar trends are shown for the nonlinear damper system where larger SR values lead to lower DRF amplification factors. However, the nonlinear damper system is more sensitive to the sub-system flexibility. As shown in Figure 4-24c, when SR = 5, and damping is 20% or more, the displacement responses for structural periods 0.75s and above are at least 5% higher than the SR = 200 case. In Figure 12d, when the stiffness ratio is increased to 10, the DRF amplification factors for structural periods 2s and less are reduced below 1.05, while the 3s system peaks at 1.08 for 35% damping. Also shown in Figure 4-24, systems with structural periods less than 0.75s are insensitive to the sub-system stiffness levels, for both linear damper systems and nonlinear damper systems. The T_n = 0.25 and 0.5s systems also introduced less than 5% additional total system reaction force (base shear).

In light of the above, in order for the rigid sub-system assumption to be appropriate in design, the structural system should either possess a short period (high structural stiffness), or the damper sub-system needs to be 5 times stiffer than the structural lateral resisting system if a linear viscous damper is to be used, or 10 times stiffer if a nonlinear viscous damper is to be used.

4.5.2. Extended considerations of BSRF amplification factors

The results presented in Section 4.3 suggest damper sub-system flexibility reduces base shear reductions from damping. To highlight the impact of damper sub-system flexibility on base shear demand, amplification factors of base shear reduction factors (BSRF) can be plotted using the same methodology described in 4.5.1, where the BSRF of a lower stiffness ratio (SR) is divided by the BSRF of the system with near-rigid damper sub-system (SR = 200). For this investigation, a system period of 3s is selected, and the BSRF amplification factors are plotted for SR = 1, 1.5, 5 and 10. Figure 4-25 below presents the results for α = 0.2, 0.4, 0.6 and 1.0.

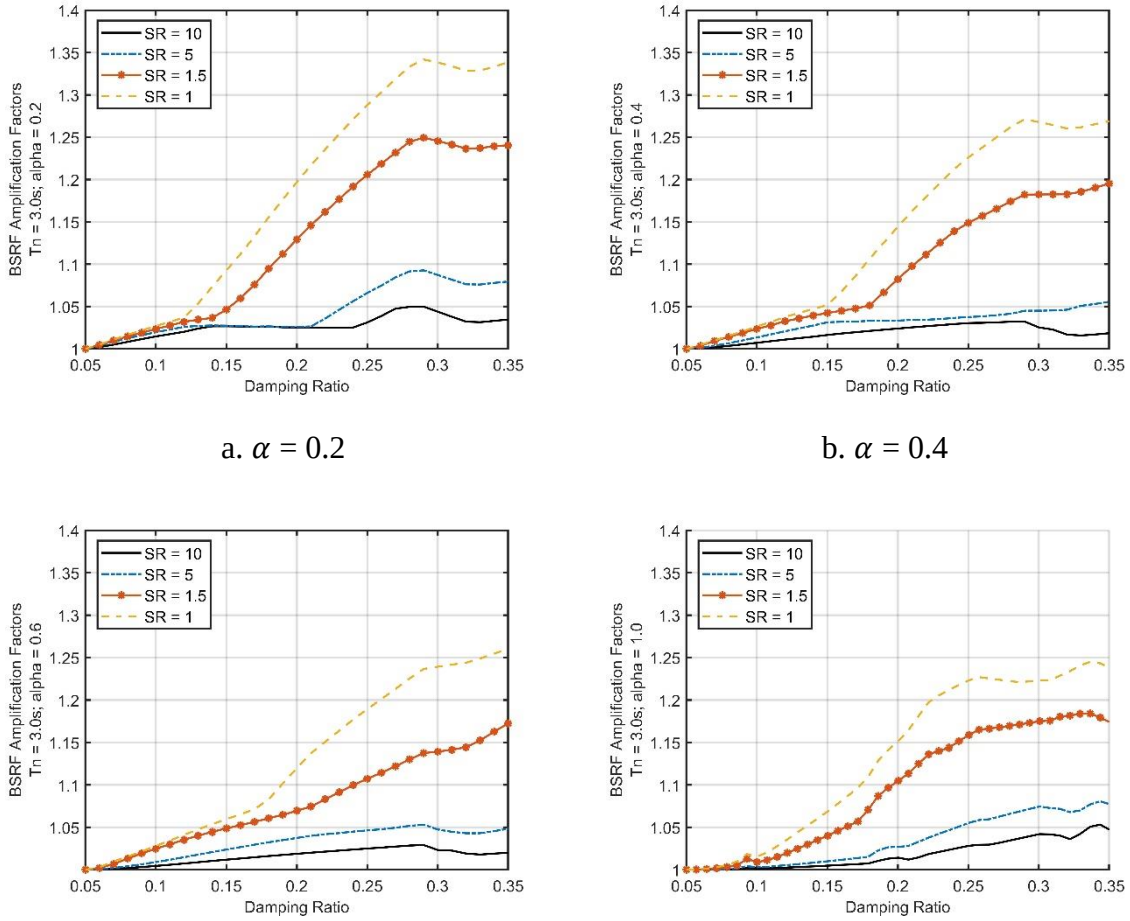

a. α = 0.2

b. α = 0.4

c. α = 0.6

d. α = 1.0

Figure 4-25. Base shear amplification factors for *Tn* = 3s.

4.5.3. Design example

4.5.3.1. Single storey frame design example

To investigate whether the recommended stiffness ratios are realistic, a capacity design example of a single-storey frame equipped with a diagonal linear viscous damper brace is carried out. This frame is assumed to have the same lateral stiffness and damper properties as the ground floor frame of the case study structure modelled in Sullivan & Lago [2012].

Although it has been stated earlier that damper sub-system stiffness has insignificant impact to low period/rise structures, this is a quick hand-calculation example to indicate the likely sub-system to primary structure stiffness ratio if a conventional capacity design process is carried out. If the ratio is lower than recommended, the design example can state if it is practical to

stiffen the sub-system to the recommended ratio. It is also worth to note that this is not a detailed design, therefore many component dimensions are reasonably assumed.

The numerical model presented in Sullivan & Lago [2012] shows the flexural stiffness of the ground floor frame is 31.5 kN/mm, and the damper force is 450 kN. Using this information, the capacity design of the damper sub-system is carried out by undertaking the following steps:

- Assume pin-pin brace connections, so the damper and its sub-system are subject to axial demand only.

- Consider an overstrength factor of 1.5 for the viscous damper, and an understrength factor of 0.9 for the sub-system components. This gives an axial demand of 675 kN on the sub-system due to damper overstrength.

- For the bracing member, consider a Grade C350LO hollow cylinder. The chosen section is 168.3x4.8 CHS, with an axial stiffness of 123.5 kN/mm.

- The gussets are designed using the Thornton method with the maximum Thornton length and a Whitmore width.

- Other sub-system components, including connecting plates and bolts, are designed according to NZS3404 [1997].

- The sub-system components can be modelled as springs in series, and the equivalent sub-system stiffness can be calculated using Equation (4.9) below, where K_i is the stiffness of each component, and n is the number of components.

$$\frac{1}{K_{eq}} = \sum_{i=1}^{n} \frac{1}{K_i} \tag{4.9}$$

Detailed calculations of the steps above are presented in Appendix G. By using the damper sub-system stiffness of the ground floor frame is 91.3 kN/mm. This results in a K_d/K_s ratio of 2.9, which is lower than the recommend SR of 5 for a linear damper system. The calculation results indicate that the CHS bracing member contributes to almost 80% of the total sub-system flexibility, as shown in Table 4.2 below. Therefore, the most effective strategy to enhance the

sub-system stiffness is to stiffen the bracing member, and it can be done by either increasing the cross-sectional area or reducing the length.

Table 4-2. Damper sub-system component flexibilities

Sub-system	**Stiffness, K (kN/mm)**	**Flexibility, 1/K (mm/kN)**	**% of total sub-system flexibility**
Brace	123.5	0.00810	73.97
Bottom connecting plate	2727	0.00037	3.35
Bottom gusset	11333	0.00009	0.81
Top Gusset	11333	0.00009	0.81
Top connecting plate	2727	0.00037	3.35
Bolt group A	1960	0.00051	4.66
Plates A and B	6485	0.00015	1.41
Bolt groups B and C	2237	0.00045	4.08
Plates C and D	6485	0.00015	1.41
Bolt groups D and E	1484	0.00067	6.16

Illustrations and locations of the sub-system components listed in the table above are presented in APPENDIX G, page 0.

To achieve the SR of 5 or higher for the ground floor frame, a larger section such as 273.1x12.7CHS can be used as the bracing member. This section allows the SR to reach 6.6. Although this comes with a higher construction cost, it can be easily achieved as it is a common size and does not require special fabrication. However, if a nonlinear damper is used and a SR of 10 is the target to achieve near-rigid damper sub-system, the minimum cross-sectional area required to achieve such high stiffness level is 67,000 mm^2. This seems to be an impractical strategy as this is not a common profile size in New Zealand and a welded section is required.

In this case, instead of attempting to achieve the SR, it is more practical to apply the displacement amplification factors proposed in Section 4.5.1. This can be done by dividing the design displacement profile by the design displacement reduction factor, f_m, so the actual the displacement reduction that is amplified by the damper sub-system flexibility is lower than the allowable limit. Based on this recommendation a modification to the design flowchart can be proposed, as shown in Figure 4-26 below. At the end of Step 10, if the stiffness ratio K_d/K_s lower than the target SR, Step 11 should be undertaken to account for the phasing effects. Step 11a gives designer the option of increasing the damper sub-system stiffness K_d until the

desirable stiffness ratio K_d/K_s is reached, and Step 11b considers modifying the design displacement by incorporating the design displacement reduction factor f_m.

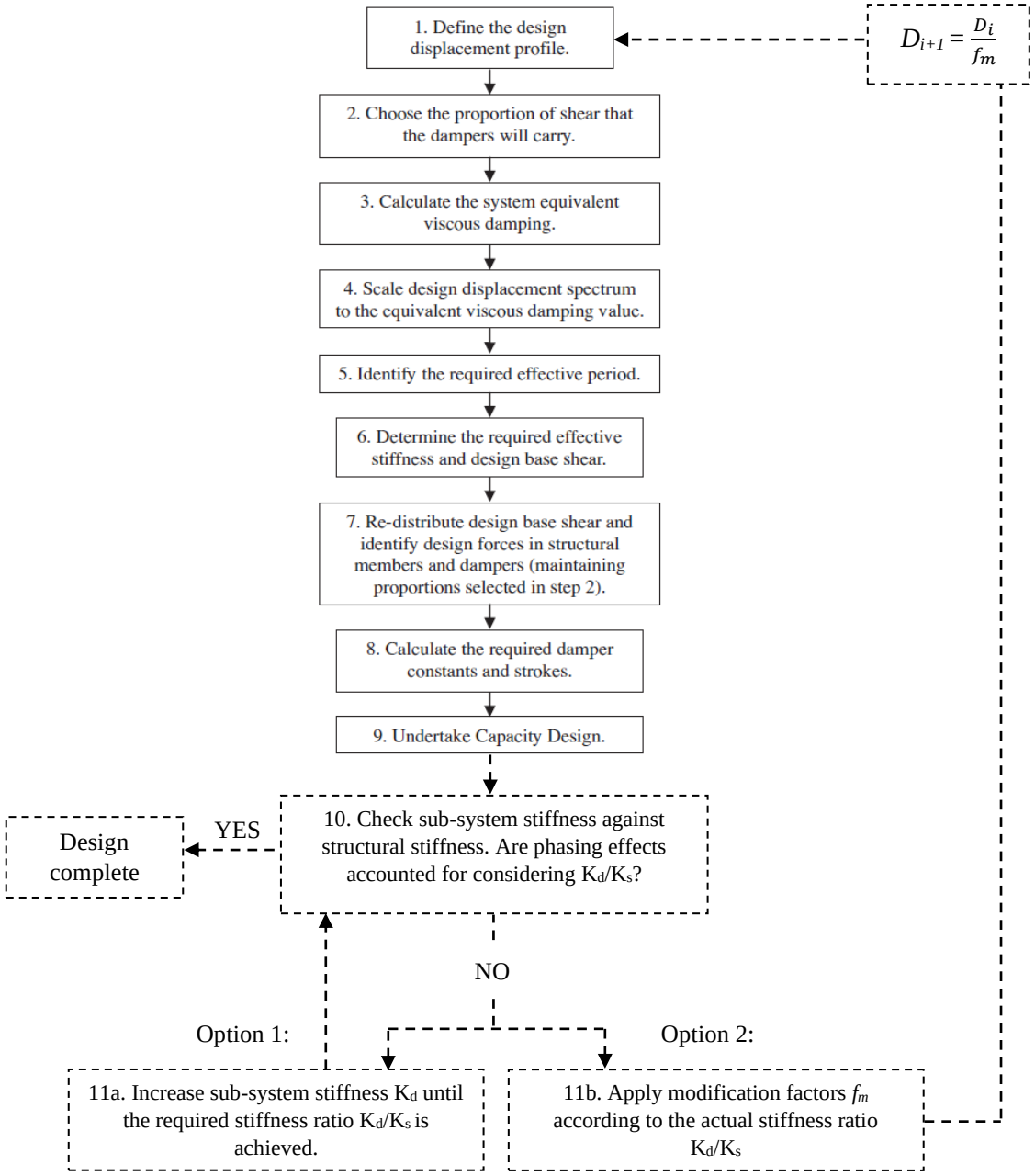

Figure 4-26. Modified design frame based on which proposed by Sullivan & Lago [2012]

An empirical equation has been developed based on test results to provide designers a convenient and practical method to calculate the design displacement reduction factor, f_m, in the design process if the stiffness ratio has been defined. The relationship between f_m and stiffness ratio can be defined using Equation (4.10).

$$f_m = \zeta \times 1.31SR^{-0.656} + 0.94SR^{0.0246} \quad (4.10)$$

To investigate the accuracy of this equation, f_m is normalised using the DRF amplification factors presented in Figure 4-24 $\left(\frac{f_m}{DRF\ amp.factor}\right)$. The normalised values are plotted in Figure 4-27 below. These plots can be referred as an assessment of systematic bias introduced by Equation (4.10). Low structural periods of 0.25s and 0.5s are excluded from the plots as damper sub-system flexibility does not have significant impact on such structures.

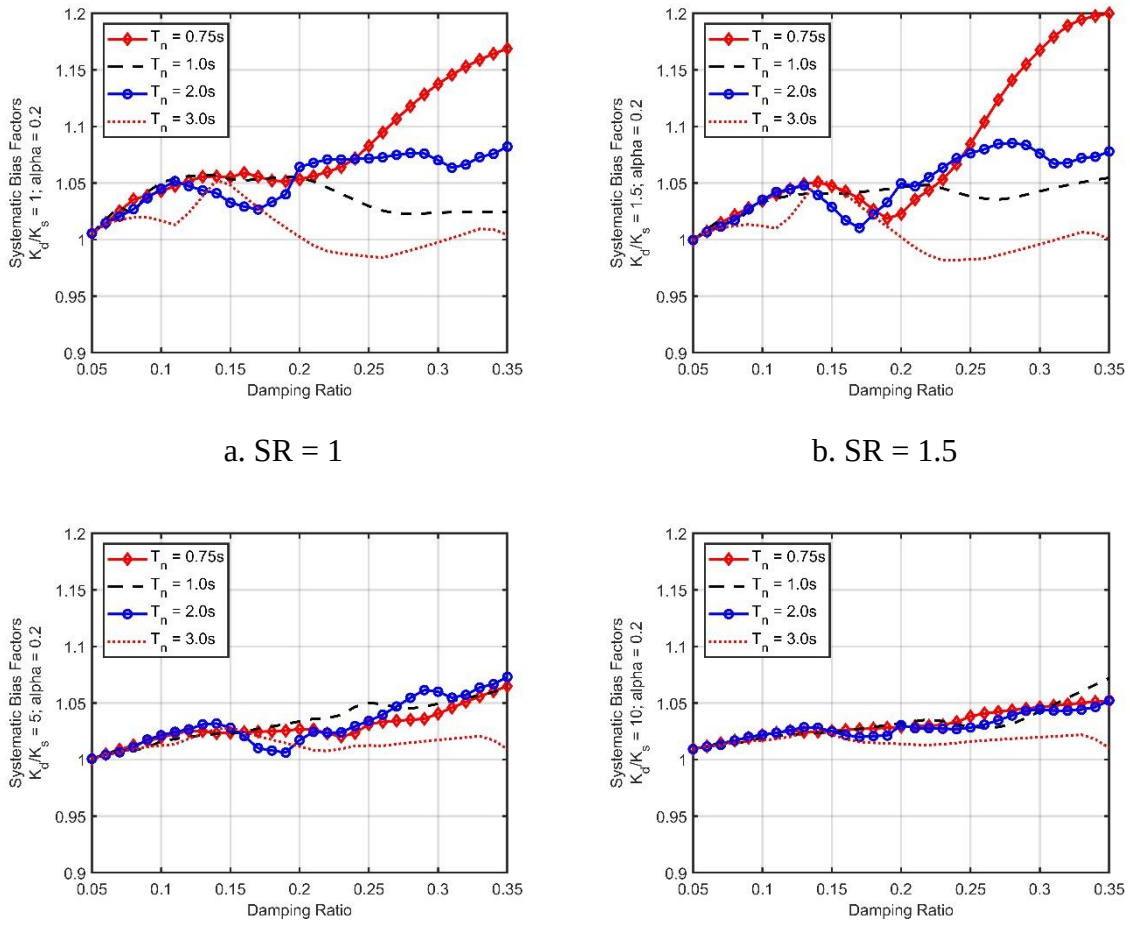

a. SR = 1

b. SR = 1.5

c. SR = 5

d. SR = 10

Figure 4-27. Systematic bias factors obtained as dividing Equation (4.10) by the observed amplification factors presented in Figure 4-24, for α = 0.2, SR = 1, 1.5, 5, and 10

It is worth to note this equation is highly influenced by the characteristics of the ground motion records used to carry out the analytical work in this chapter. A different set of ground motion

could potentially alter the curves of the displacement amplification factors presented in Figure 4-23 and Figure 4-24, thus potentially changing the form and constants of Equation (4.10). For this reason, this methodology currently adopts a conservative approach to minimise the overestimations of displacement reduction capacity of a viscous damper under the influence of sub-system flexibilities. It can be seen that the results present in Figure 4-27 are mostly above, therefore the systematic bias is intentionally on the conservative side.

4.5.3.2. Extended design considerations for a MDOF system

In reality, a system equipped with viscous dampers is most likely to have multi degrees of freedom (MDOF), therefore it is important to extend the design example presented in the section above to provide a guidance on calculating the stiffness ratio for a MDOF system.

The following steps can be used if a multi-storey, multi-degree-of-freedom system is considered in design.

- Estimate the storey stiffness K_{si} using Equation (4.11) below, where V_i is the storey shear force and d_i is the storey displacement, and i represents the i-th storey.

$$K_{si} = \frac{V_i}{d_i - d_{i-1}} \tag{4.11}$$

- After capacity design is completed for each storey, calculate the sub-system stiffness of each storey. This process follows the same calculation philosophy as presented in the design example in Appendix G. For each storey, the equivalent sub-system stiffness is known as K_{di}.

- Calculate the average structural stiffness $[K_s]$ of all storeys by constructing the stiffness matrix using Equation (4.12) below.

$$[K_s] = \begin{bmatrix} k_{si} + k_{si+1} & -k_{si+1} & \cdots & \cdots & \cdots \\ -k_i & k_{si} + k_{si+1} & -k_{si+1} & \ddots & \vdots \\ \vdots & \ddots & \ddots & \ddots & \vdots \\ \vdots & \ddots & -k_{n-1} & k_{sn-1} + k_{sn} & -k_n \\ \cdots & \cdots & \cdots & -k_n & k_n \end{bmatrix} \tag{4.12}$$

- Repeat the same step above to calculate the average sub-system stiffness [K_d] of all storeys using the K_{di} of each storey.

- The average stiffness ratio of the multi-storey structure can be calculated by taking the determinant of the two stiffness matrices, as shown in Equation (4.13) below. The determinant produces a scalar which defines the SR of the multi-storey building.

$$SR = Det[K_s^{-1}\, K_d] \tag{4.13}$$

It is common for multi-storey structures to have different sizes for columns, beams and braces throughout the height of the building due to inconsistent storey shear and damper forces at different levels. Therefore, in addition to calculating the average SR, it is also worth checking the individual storey SR, as it may be substantially different to the average SR of the entire structure. To calculate the individual storey SR, similar steps can be carried out as those presented in the Section 4.5.3.1. The storey stiffness of each level can be calculated by dividing the storey force by the inter-storey drift at yielding. The storey stiffness is compared against the damper sub-system stiffness of the same level to determine the individual storey SR.

It is worth noting that this Section provides a high-level recommendation on taking sub-system stiffness into consideration when designing MDOF systems. In reality, many factors could affect SR. For example, a diagonal damper brace could induce extra axial demand on the columns when comparing to a horizontal damper system, leading to axial deformations of the columns, which indicates the damper brace orientation could dictate the load demand flow paths, as well as K_s. Additionally, as seen in Section 4.5.3.1, the components of the sub-assembly could have a significant impact on K_d. Therefore, more comprehensive studies and investigations are required to improve the design recommendations provided in this Section so the SR could be more accurately computed for MDOF systems.

Section 4.4.3 states the sub-assembly-to-damper ratio R can also be used as an alternative to SR to address the effect of brace stiffness on the overall structural response. However, R is also depended on K_d and K_s, therefore, more study is required to produce a guideline for calculating both R and SR for a MDOF system. Additionally, it is also recommended to carry out optimisation analysis as a future research work to determine whether R or SR is the most suitable parameter to be used in structural design that considers damper sub-system stiffness.

4.6. Conclusions

(i) Chapter 4 has described numerical investigations aimed at quantifying the extent to which the damper sub-system stiffness can affect the overall displacement response and total base shear force for a structural system subject to earthquake excitation. Results from both sinusoidal and ground motion simulations indicate that if the sub-system to primary lateral load resisting system stiffness ratio is less than 5 for linear dampers, and less than 10 for nonlinear dampers, the overall system response can be significantly affected by the sub-system flexibility. Results from ground motion simulations show that at stiffness ratios (i.e. the damper sub-system stiffness to total structural stiffness) K_d/K_s = 1, 1.5, and 5, both the median peak displacement response and the total system force can be 5% to 40% higher than the response of a damper system with a stiffness ratio of 200.

(ii) The ground motion simulation results also lead to the recommendation that designers take sub-system flexibility into consideration if more than 5% supplemental damping, or 10% total damping, is to be introduced to the structural system. By plotting the DRF amplification factors for different structural periods at various stiffness ratios, it is recommended that for structures with natural periods larger than 0.5s, the linear viscous damper sub-system be provided with a stiffness that is five times greater than the structural stiffness, and the sub-system of a nonlinear viscous damper is required to be at least ten times stiffer than the stiffness of the structural lateral resisting system.

(iii) For cases where it is not practical to achieve the two threshold stiffness ratios mentioned above, it is recommended to use a modified design framework which adopts an iterative process and accounts for damper sub-system flexibility by using the displacement amplification factors to reduce the design displacement profile.

(iv) Design examples and recommended considerations have been presented for both single storey and multi-storey systems to calculate damper sub-system to primary structure stiffness ratios.

4.7. Recommended future research work

Based upon the research presented on the results obtained, the following areas of future work are identified:

(i) Expand the ground motion profile and carry out more ground motion simulations to improve the accuracy of Equation (4.10), which is used to calculate the required displacement amplification factor based on the damper sub-system to primary structure stiffness ratio.

(ii) Carry out a detailed case study design using the modified framework described in Figure 4-26 to further validate the recommended method to account for damper sub-system flexibility in the design of a system equipped with viscous dampers.

(iii) Extend numerical studies to 2D and 3D MDOF modelling to advance this analysis.

(iv) Conduct similar parametric studies as described in this chapter on the impact of brace sub-system flexibility on the overall structural performance for systems that are equipped with other energy dissipaters, such as friction connections, and buckling restrained braces.

(v) Once the above study is completed and better understanding on a wider range of energy dissipation mechanisms is achieved, it is essential to carry out a comparative study of these energy dissipaters to provide a better guidance on selecting the most efficient energy dissipation mechanism based on design criteria.

5. KEY FINDINGS

5.1. Overview

The motivation of the research topic "Improved Modelling and Implementation Guidance of Energy Dissipation Devices" is to carry out required research in order to improve the understanding of the mechanisms of current energy dissipation devices, and propose new practical construction and design recommendations that can be easily applied by designers. Friction connections and viscous dampers have been selected as the study subjects as they are commonly used energy dissipators in New Zealand as well as other seismic regions around the world, and the current design guidelines for these devices have the potential for improvements.

This chapter concludes the findings obtained through the experimental and analytical studies carried out for this research topic. The findings from the experimental study of friction connections include the mechanism of friction braces, design considerations, recommended assembly methodology and retrofit strategy, and a proposal for a new OpenSees AFC model. For viscous dampers, the findings include (i) recommended modelling method of viscous dampers in OpenSees, (ii) the impact of damper sub-system stiffness on the overall behaviour of a structural system equipped with viscous dampers, and (iii) the procedure to account for damper sub-system flexibility while using the currently available design guidelines.

Both devices have their advantages and disadvantages, and sometimes it is not clear which is the more suitable device to use for new builds and existing structures. Therefore, at the end of this chapter, based on the findings obtained from this research topic a comparison is made between friction braces and viscous dampers. This is an attempt to help designers to select the most appropriate device based on their design criteria.

5.2. Energy dissipation mechanisms

5.2.1. Mechanism of friction braces

The energy dissipation mechanism of an AFC brace can be illustrated using Figure 5-1. The mechanism can be divided into four stages. The full sliding mechanism is developed at the beginning of stage IV, and the force at full sliding mechanism is referred to as the peak sliding force, which is mathematically defined within the design procedure presented in Section 2.6.

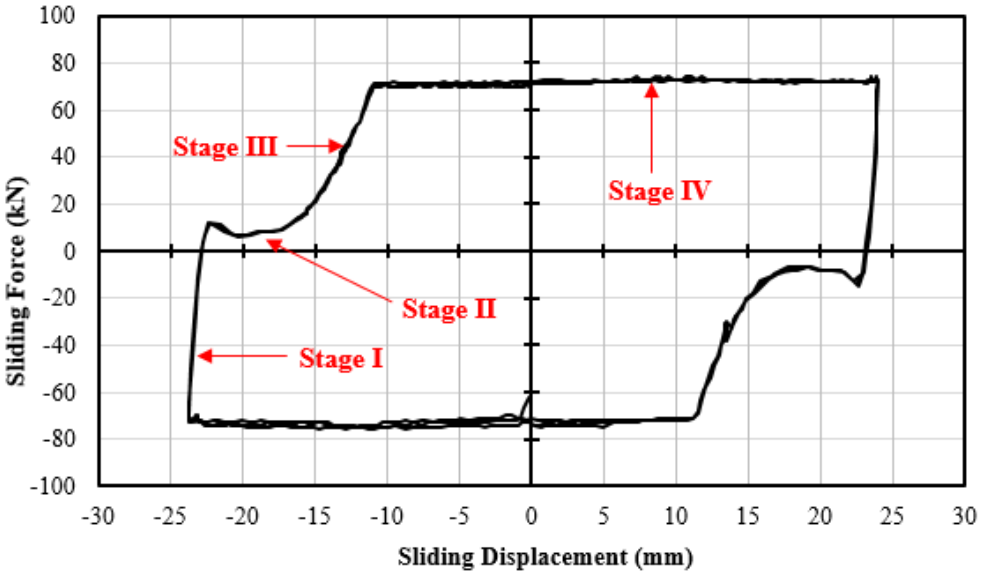

Figure 5-1. Dissipation mechanism of an AFC brace

In the first stage, the stiffness of the brace is high as it mostly depends on the axial stiffness of the slotted plate and the bracing member. In the second stage, the stiffness of the brace reduces drastically as clamping bolts tilt due to the eccentric configuration of the brace, and they slide across the oversize bolt-hole in the bracing member and the cap plate. In the third stage, the clamping bolts are locked in place and bear against the bolt-hole edges of the bracing member and cap plate. It is important to note that the stage III stiffness is lower than that of stage I, as it mostly depends on the flexural stiffness of the clamping bolts. At the fourth stage, the peak sliding force is reached, and sliding is activated on both sides of the slotted plate, and the slotted plate can be driven up to the length of the slots with little to no increment in the applied axial force.

AFC braces experience strength degradation as a result of bolt slackening. The strength degradation observed from the experiment was approximately 10% after 48 cycles of axial load reversals. Heavy material degradation at the sliding interfaces can lead to unstable performance when a friction brace is in full sliding, which means its peak sliding force becomes unpredictable. Based on the experimental results, the peak sliding force of an AFC brace could vary up to 70 kN (230%) when the slotted plate was heavily degraded.

The energy dissipation mechanism of an SFC brace is outlined in Figure 5-2 below.

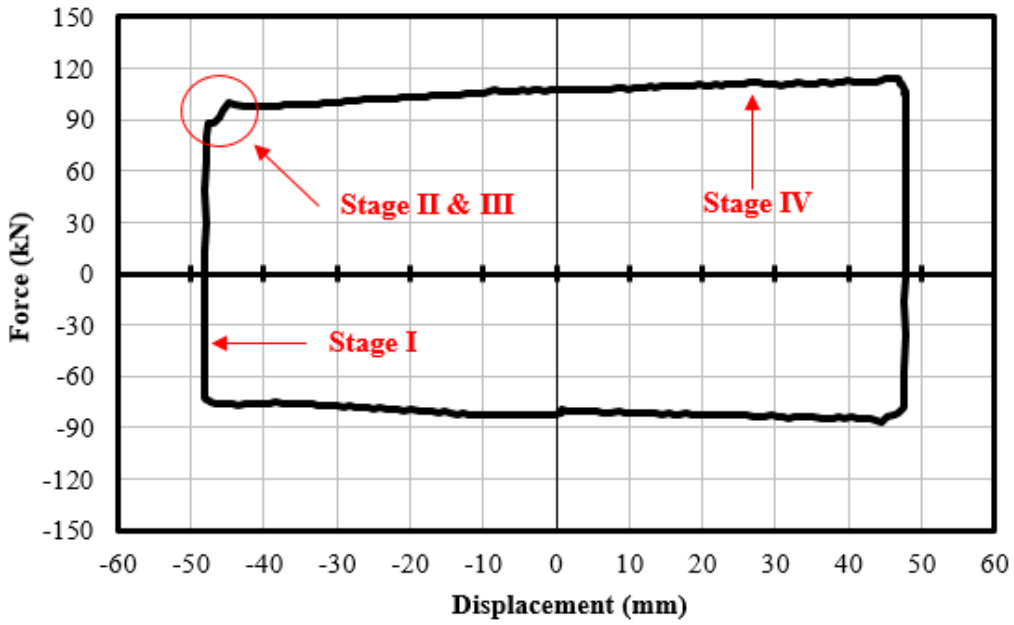

Figure 5-2. Dissipation mechanism of an SFC brace

The mechanism can be divided into the same four stages as those of the AFC brace mechanisms. However, unlike AFC braces, stage II and III for an SFC brace occur over a short sliding distance, approximately 2 – 3 mm, immediately prior to stage IV, full sliding. This is because the cross-section profile of an SFC brace is concentric, and the clamping bolts are subject to double shear. Therefore, there is no induced eccentric axial load that leads to premature bolt tilting and slipping.

The maximum strength degradation of the SFC brace configuration tested in Chapter 3 was 25%. The high strength degradation was mainly attributed to the p-delta effect which pushed the top and bottom bracing members outwards, which induced additional tensile load on the clamping bolts and caused them to yield. The strength degradation could possibly be reduced by adopting an alternative configuration that is described in Section 3.8, as well as by providing additional detailing along the length of the bracing members as described in Section 3.4.1.4.

5.2.2. Mechanism of viscous dampers

In Chapter 4, the mechanism of a viscous damped system under the influence of damper sub-system flexibility is examined. In general, a flexible damper sub-system could lead to underestimations of structural forces and displacement, as shown in Figure 5-3 below, which plots the responses of a system with flexible damper sub-system, which has a sub-system to primary structure stiffness ratio (SR) equal to 1, and a system with high rigidity damper sub-

system (SR = 200) under sinusoidal excitations. The displacements and forces are normalised using the peak displacement and force of the SR = 200 system, and it can be seen that the flexible damper sub-system amplified the maximum structural force and displacement by approximately a factor of 1.2 and 1.25, respectively. Therefore, the Chapter 4 study can conclude that it is not conservative to neglect damper sub-system flexibility in the design process of a structure equipped with viscous dampers.

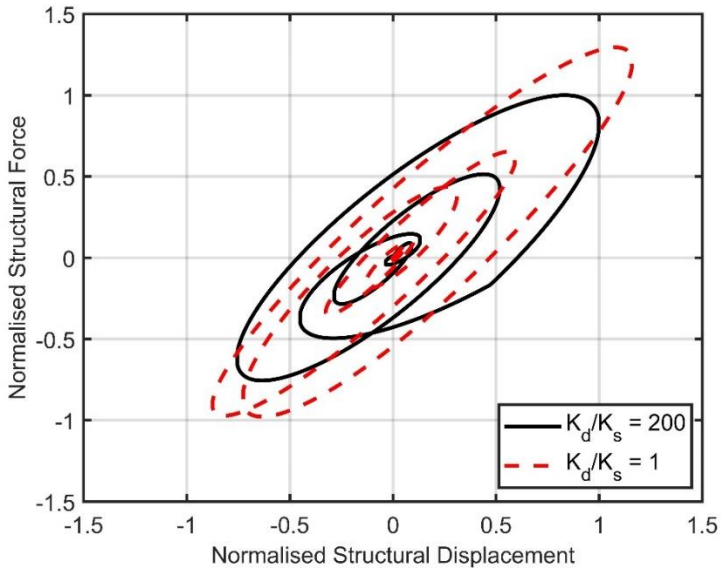

a. Normalised force and displacement relationship comparisons between SR = 1 and 200.

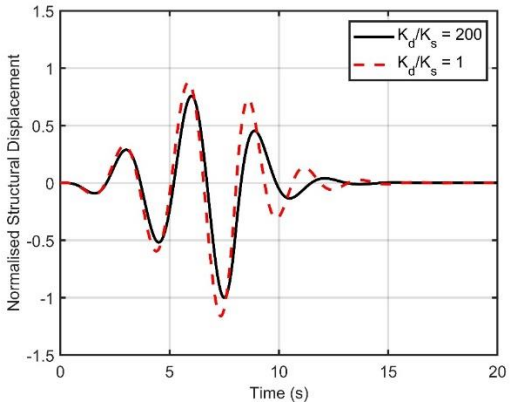

b. Normalised structural displacement time-history plot.

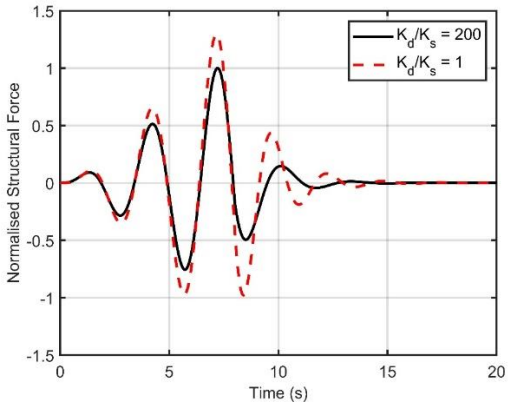

c. Normalised structural force time-history plot.

Figure 5-3. Changes in structural response due to sub-system flexibility.

A series of ground motion simulations using a SDOF viscous damped system has also been conducted as a part of the Chapter 4 study, and the results obtained can further validate the argument made above. However, Figure 5-4 below shows the damper sub-system flexibility has less impact on low period structures, and it may be acceptable for designers to not consider the SR if the structure has a period of 0.25s and lower.

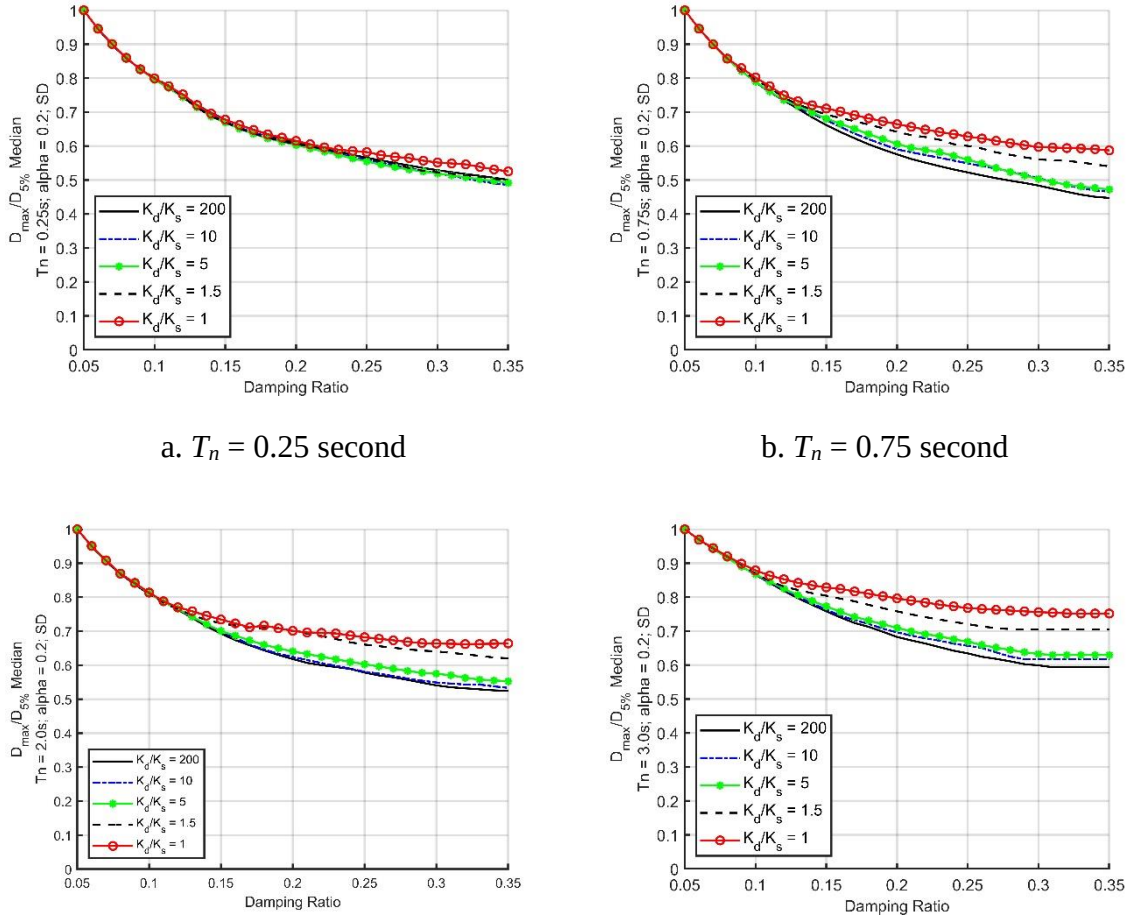

a. T_n = 0.25 second

b. T_n = 0.75 second

e. T_n = 2 seconds

f. T_n = 3 seconds

Figure 5-4. Ground motion simulation results

5.3. Influence of detailing and construction approach

5.3.1. Friction braces

The experimental studies of SFC and AFC braces adopted the assembly recommendations provided by Chanchi *et al.*, [2013 and 2014] have yielded good results. These recommendations include using high Brinell hardness Bisalloy 500 shims, and grade 8.8 galvanised bolts that are tightened to their proof loads. An overview of the AFC and SFC

assemblies constructed by Chanchi *et al.*, [2013 and 2014] is shown in Figure 5-5 below. For the case an SFC brace, the fixed plates shown in Figure 5-5a are swapped for a pair of channel sections as bracing members, as illustrated in Figure 5-5b.

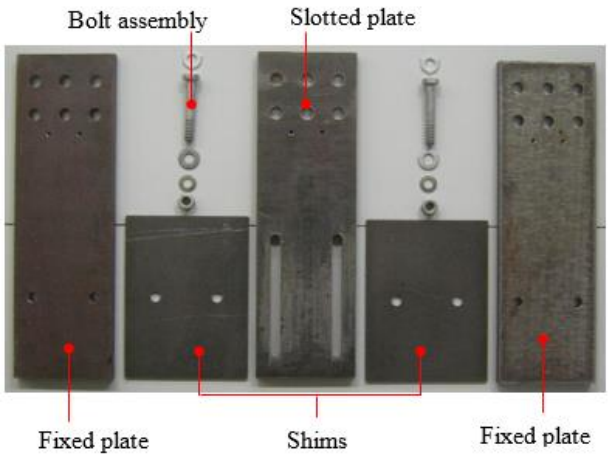

a. SFC assembly by Chanchi *et al.*, [2013].

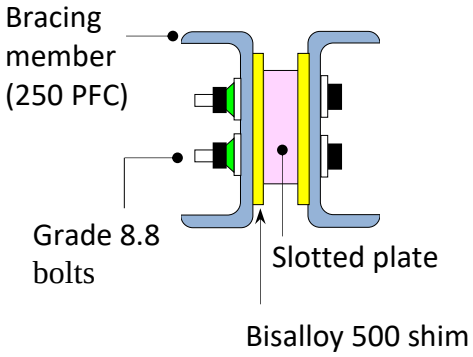

b. SFC brace assembly.

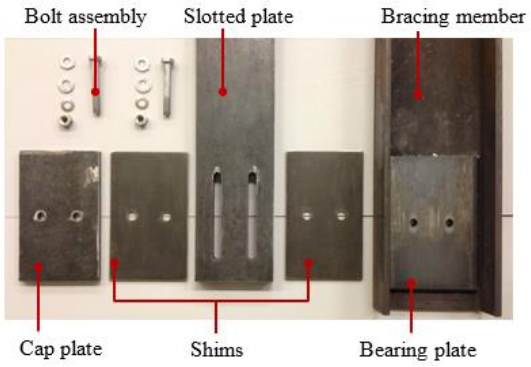

c. AFC brace assembly by Chanchi *et al.*, [2014].

Figure 5-5. SFC and AFC brace assemblies recommended by literatures.

In addition to the general features described above, a number of detailing and construction issues can affect the energy dissipation mechanism of friction braces.

Prior to assembling the components, all sliding surfaces need to be mechanically cleaned to remove mill scale, as the mill scale on raw metal surfaces generally have low wear resistance, and changes to sliding surface conditions can alter the sliding mechanism of a friction connection and potentially lead to unstable hysteretic performance. Currently coating is not recommended at sliding interfaces. As indicated by the research work carried out by Chanchi *et al.,* [2019], there is currently lack of evidence to support a type of coat that has high wear resistance, and also does not significantly reduce the coefficient of friction.

To improve assembly consistency, lubrication should be applied to the clamping bolts prior to tightening, as lubrication reduces friction between the bolt threads and nut threads, thus minimises the torsion in the bolts induced during the tightening process.

It is important to ensure the clamping bolts can be easily fit through the slots and bolt-holes within the connection details by hand, and they should not be touching the edges of the slots and bolt-holes before any sliding take place. Therefore, precise fabrication is required for all components, which also include the bracing members and gusset plates. Bolt-hole misalignments and initial out-of-straightness of these components could lead to the slotted holes being out of alignment with the bolt-holes in the shims, cap plate and the bracing members. This misalignment could result in the clamping bolts being forced into the slots, and under such condition, the clamping bolts could yield prematurely as they are subject to high moment-shear-axial interactions.

It is recommended to assess surface conditions and replace bolts after 6000 mm of cumulative travel. This recommendation is based on the experimental observations that bolt slackening after several cycles of sliding could lead to strength degradation, and severe material degradation could significantly affect the performance stability of friction connections. However, this recommendation is currently based on quasi-static test results, and it is difficult for practitioners to consider cumulative lateral displacement of a structure during the design process. Therefore, to make this recommendation more practical, shake table tests using ground motion excitations are recommended as an attempt to (i) measure degradations in terms of ground motion characteristics, and (ii) investigate the amplification in strength and material degradation due to high accelerations and velocities.

There are no major restrictions on the potential configurations of the friction brace, as long as the required components that are outlined in Figure 5-5 above included in the friction connection details. However, for an AFC brace, to minimise the eccentricity between the bracing member and the AFC details, as well as to maximise the allowable construction tolerance, the configuration tested in Chapter 2 is recommended, and this is illustrated in Figure 5-6 below.

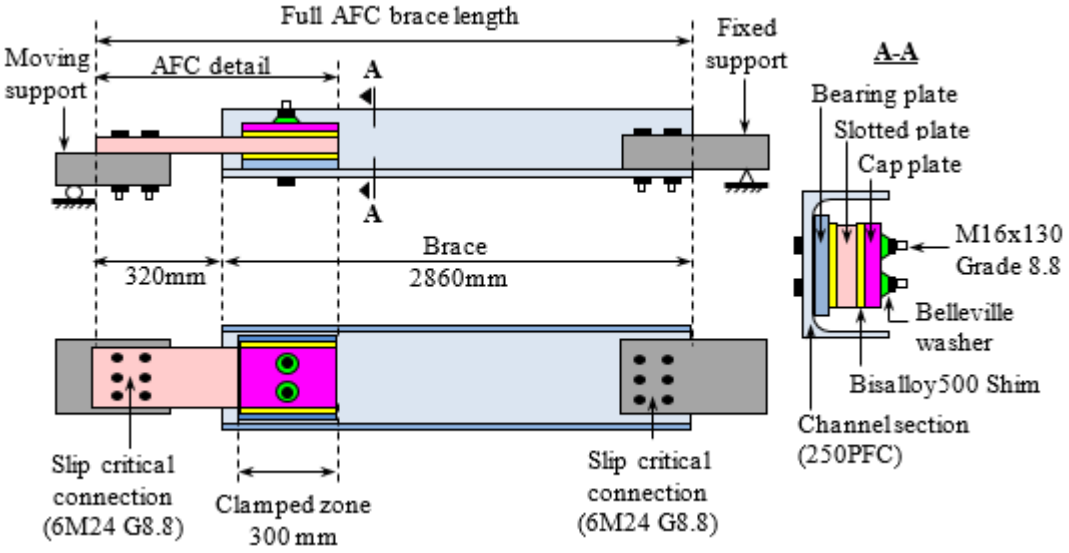

Figure 5-6. AFC brace assemblies recommended by this thesis

The most important feature of an SFC brace is to have a symmetrical cross-section, so the axial force is transferred from the friction connection details to the bracing member(s) without eccentricity. This configuration leads to substantially reduced prying effects, more stable hysteretic behaviour, and less cycle-to-cycle degradation. Two examples of cross section configurations are presented in Figure 5-7. The experimental study of the configuration illustrated in Figure 5-7a is described and discussed in Chapter 3.

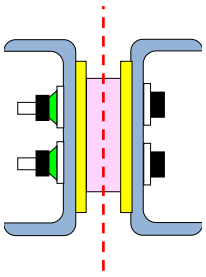

a. SFC cross section

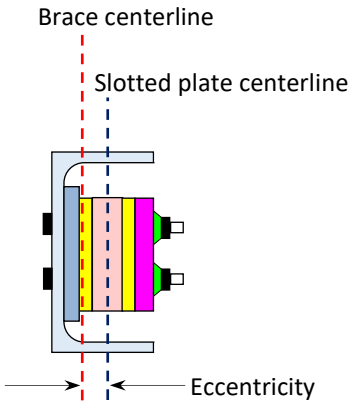

c. AFC cross section

Figure 5-7. Comparison between an SFC and AFC cross section

In general, having more bolts and sliding interfaces can increase the peak sliding force of a friction brace. It may also improve the performance stability of a friction brace, because if many clamping bolts are used and one of the bolts is over or under tightened, it would not impact the overall behaviour of the bracing system as significantly as if only two or three clamping bolts are used. However, as mentioned earlier, friction brace components require relatively precise fabrication to ensure stable and predictable performance. Therefore, to have more bolts and sliding interfaces, more bolt-holes and components are required, thus reducing the friction brace's construction tolerance.

For both types of friction braces, it is important to minimise component initial out-of-straightness to reduce the impact of prying and p-delta effect as discussed in Chapter 2 and 3. Therefore, the plates and bracing member(s) of a friction brace need to be of high quality.

5.3.2. Viscous dampers

For a structure equipped with linear viscous dampers, in order to minimise the impact on the overall structural response due to sub-system flexibility, the minimum damper sub-system stiffness recommended is five times the lateral stiffness of the primary structure. For the case of a nonlinear viscous damper system, the damper sub-system to primary structure stiffness ratio should be at least 10.

If a designer wishes to adopt the current design framework and utilise the assumption that the damper sub-system is rigid, the designer should achieve the recommended stiffness ratios by using stiffer sub-system components. This is explained in more details in Section 5.4.2 below.

5.4. Design recommendations

The following design recommendations aim to improve the existing design methods for friction dissipators and viscous dampers, by incorporating the improved understanding of the energy dissipation mechanism of the two devices.

5.4.1. Friction braces

The peak sliding force can be calculated using Equation (1.1), and it is shown below. The design peak friction force ϕF_s is governed by the under or overstrength factor ϕ, number of clamping bolts n_b, number of sliding interfaces n_s, tension provided by the clamping bolts N_{tf} (as indicated in Section 5.3.1 that the tension should equal to the proof load of the clamping bolts), and the effective friction coefficient μ_{eff}. Effective friction coefficient to be used in design for AFC is 0.18, and for SFC is 0.31. 0.7 and 1.4 shall be used as the understrength and overstrength factors, respectively, to cover the lower and upper bound of the peak sliding force.

$$\phi F_s = \phi \times n_b \times n_s \times N_{tf} \times \mu_{eff} \quad (1.1)$$

For AFC braces, the Stage II stiffness can be approximated as zero, and stage III stiffness can be approximated as the total cantilever flexural stiffness of the clamping bolts, which can be defined using Equation (5.1), where n_b is the number of clamping bolts, and l_p is the grip length, or total thickness of the friction connection details. Bolts with higher L/d ratios will reduce the stage III stiffness.

$$\frac{P}{\Delta} = K = n_b \times EI_b/l_p \tag{5.1}$$

For SFC braces, stage II and stage III occur close to the peak sliding force and only over a short distance, therefore it is suitable for designers to neglect these two stages.

It is worth to note that under-tensioned clamping bolts, excessive permanent deformations and fractures of bolts can completely change the hysteretic behaviour of friction braces, and under such conditions their performance would be difficult to predict. Therefore, it is important to tighten the clamping bolts to their proof load, and replace the bolts after a seismic event.

Capacity design should be carried out so that the bracing member has a strength that is higher than the friction connection overstrength, which is calculated by multiplying the 1.4 overstrength factor by the peak sliding strength defined by Equation 1.

Gusset plates that are used to attach a friction brace to a frame shall be designed based on the friction connection overstrength. Thronton Buckling Capacity method [Thornton, 1984], using a Whitmore width and maximum Thronton length is recommended when designing the gusset plates of a friction braced frame, as this method has been defined as the most conservative by several experimental studies, such as Yam and Cheng [1993]. An effective length factor of 2 shall be used when considering the gusset plate compressive strength.

The beams and columns of a friction braced frame need to be designed such that they would remain elastic after the (stage IV) full sliding is triggered in the friction connection. This is recommended so yielding only occurs within the friction connection, and the energy dissipation of the frame only relies on friction, and not the yielding of the primary structural components.

It is also important to consider the maximum travel of a friction brace shall not be greater than 90% of the slot length to avoid the clamping bolts bearing against the edges of the slots, as high bearing stress could cause the bolts to severely deform and eventually fracture, which would lead to a complete loss of capacity in the friction brace. To avoid this, either the maximum structural drift needs to be limited, or the slots in the friction connection details need to be long enough to accommodate the maximum structural design drift. Extra slot length for additional run-out for safety is also recommended.

5.4.2. Viscous dampers

Direct Displacement Based Design (DDBD) is a common method to design viscous dampers for existing buildings and new builds. This method determines viscous damper coefficients using design displacement profiles of the primary structure, and capacity design is carried out for damper sub-systems and primary structural components based on viscous damper force and moment demands. An example of a simplified DDBD method is presented in Sullivan & Lago [2012].

Once the capacity design is completed, it is important to calculate the damper sub-system stiffness and compare it against the stiffness of the primary structure. If the damper sub-system to structure stiffness ratio is less than the values recommended previous in Section 5.3.2, designers can increase the stiffness of the damper sub-system. It has been noted for the example case-study presented, from Table 4-2 that the major source of damper sub-system flexibility is the bracing member that connects the damper to one of the end connections. Therefore, the most effective procedure to achieve the recommended stiffness ratios is to increase the axial stiffness of the bracing member, which can be done by either increasing the cross-sectional area or reduce its length. The practicality of this recommendation is dependent on the configuration and characteristic of the frame and its bracing system. As shown in Section 4.5.3.1, for the case of a singly braced frame which has a width-to-height ratio of 1.9, it is not difficult to achieve a SR of 5 by increasing the size of the bracing member, but it is not practical to achieve a SR of 10 as a welded built-up section would be required. Therefore, for cases that are not practical to achieve the recommended stiffness ratios, an alternative design framework is proposed.

The alternative design framework is a modified version of the framework initially proposed by Sullivan and Lago [2012]. This modified framework takes an iterative approach. In the first iteration, a design displacement is defined, and at the end of the design process, a SR is determined. If the SR is too low, then a DRF reduction factor f_m can be calculated using Equation (4.10) described in Chapter 4. At the start of the second iteration, the design displacement from the first iteration is reduced by f_m, so the structure is designed to a smaller displacement to account for the reduced amount of displacement due to the damper sub-system flexibility. The same design process as the first iteration is carried out to determine a new SR. The iterative process continues until the SR is equal or above the recommended level.

The same observations regarding the importance of phasing effects are also applicable to other methods proposed for the design of systems with viscous dampers, such as those of Chrisopoulos *et al.*, [2006] and Silvestri *et al.*, [2010]. As such, if designers wish to use such methods, similar modifications to those presented in Chapter 4 should also be made.

5.5. Numerical modelling

5.5.1. Friction braces

For numerical analysis there is currently no suitable model that simulations a hysteretic behaviour that is similar to that of an AFC. Therefore, a new OpenSees multi-linear uniaxial material model is proposed as part of this research work. This numerical model considers the reduced stiffness in stage II and III as described in Chapter 2 and Section 5.2.1 above, and it produces a flat curve when the defined peak sliding force is reached. Figure 5-8 shows the hysteretic response of this friction model during a displacement-controlled simulation.

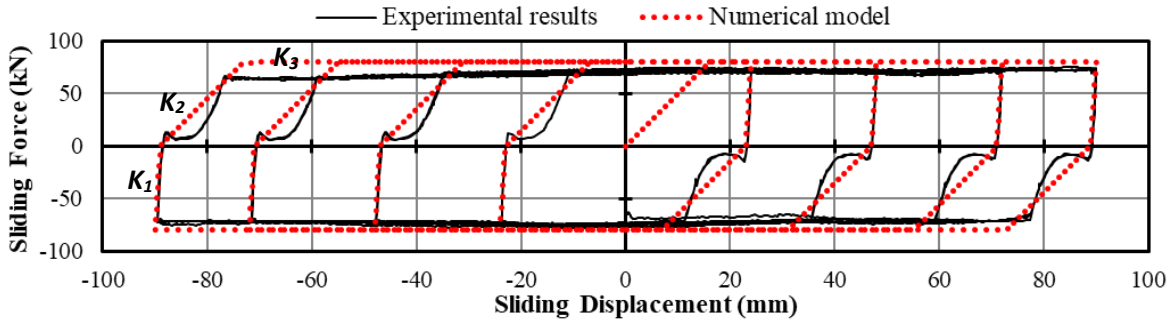

Figure 5-8. Comparison between the AFC model and AFC brace experimental results

In the figure above, K_1 represents the stage I stiffness, K_2 approximates the stage II and III stiffness, and K_3 is the stiffness at full sliding, which is zero. It can be seen from the figure above that the model provides a reasonable approximation of the hysteretic behaviour of an AFC. However, it is worth noting that this is a simplified model. Therefore, it does not capture peak force degradations and stage II and III stiffness degradations due to bolt slackening and sliding surface degradations. The model currently also assumes accelerations do not affect the peak sliding force. Despite a few shortcomings, this model provides an improvement to the modelling of Asymmetrical Friction Connections in OpenSees, and a practitioner can use it to carry out force and displacement-controlled simulations.

For the modelling of an SFC, it is appropriate to utilise the classic Coulomb model of friction as the hysteretic behaviour of an SFC can be approximated as an bi-linear model, which has an almost vertical pre-sliding stiffness and a flat curve as the stiffness of the model when full sliding is triggered. A comparison between the Coulomb model response and the experimental SFC brace hysteresis loops is presented in Figure 5-9 below, and it can be seen the Coulomb model provides a reasonable approximation.

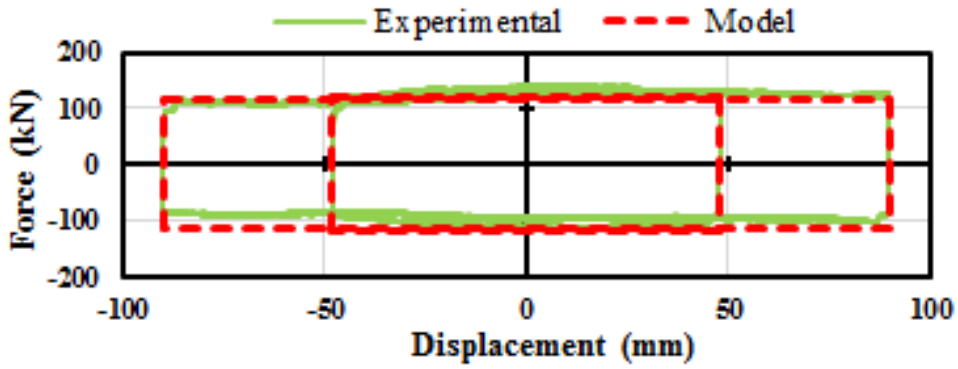

Figure 5-9. Comparison between the Coulomb model and SFC brace experimental results

Like the AFC OpenSees model, the Coulomb model also does not consider peak sliding force degradations, and the influence of velocity and acceleration on the peak sliding force. There are several friction models within the OpenSees platform that are velocity dependent, however more detailed studies are required, including high velocity/acceleration experimental studies on friction connections, before incorporating the velocity dependent models in the modelling of friction braces.

5.5.2. Viscous dampers

To model a viscous damper material in OpenSees, there are two options, the first is to use a uniaxial material model identified as the *Viscous* model. This model represents a classic viscous damper dashpot and it is coded based on the viscous damping force equation defined by Equation (1.2). Although it offers efficient computational process for linear damping system, it does not work well with nonlinear dampers, particularly those with low velocity exponent α values. For low velocity exponent α values, at low velocities damper force changes rapidly with small increments in velocity (Figure 5-10), which can lead to numerical instability and convergence errors. Therefore, the second option which is a uniaxial material model named *ViscousDamper* coded by Akcelyan *et al.*, [2018], is recommended. The *ViscousDamper*

model simulates a Maxwell viscous model where a viscous damper is connected in series with a spring, and the spring's stiffness represents the damper sub-system stiffness. It uses an ODE solver that may not be as efficient as the *Viscous* model, but it minimises the numerical issue. However, using the alternative ODE solver convergence errors may still be present if the integration time step is large. Therefore, to avoid the computational errors described above, a maximum time step of 0.0002s is recommended when using the *ViscousDamper* material model in ground motion simulations.

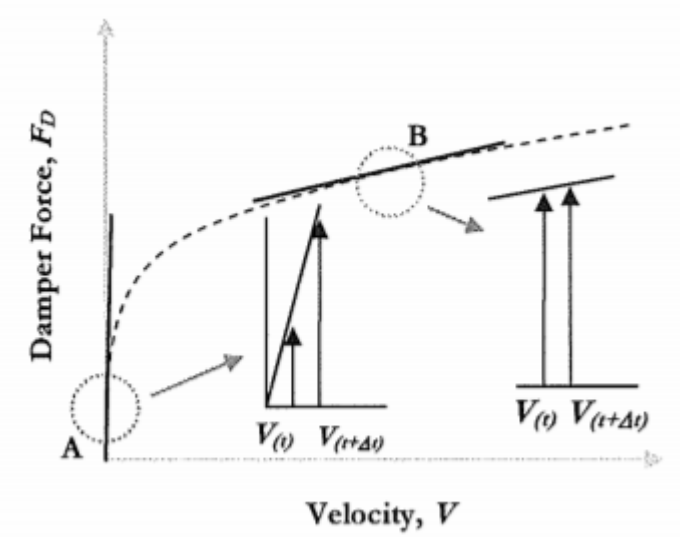

Figure 5-10. Force-displacement of a nonlinear damper with low α value (e.g. 0.2), and its associated numerical issues [Lago, 2011]

5.6. Comparative discussions

In this section, the two types of friction braces are compared against each other, and the friction braces are then compared against viscous dampers. The aim of this section is not to state which device is the best out of the three devices but instead it highlights the advantages and disadvantages of the devices. Practitioners can utilise this information to select the most optimal device for their design.

5.6.1. AFC vs SFC

While using the same number of sliding interfaces and clamping bolts of the same size, comparing to AFC brace, SFC braces possess: (i) greater peak sliding forces that are on average 72% higher than those of AFC braces due to higher having an average effective friction coefficients, and (ii) higher pre-sliding stiffness with negligible stiffness changes, whereas

AFC braces experience significant stiffness reduction before full sliding is triggered, as highlighted in Figure 5-1 in Section 5.2.1. To increase the peak sliding force of an AFC brace, more clamping bolts can be used. However, due to the offset between the AFC details and bracing member, a higher force induces higher prying in the AFC brace, which could accelerate strength and material degradation. Therefore, SFC braces can have more stable performance than AFC braces at high axial load demands.

From the experimental study results presented in Chapter 2 and 3, SFC braces experienced higher peak sliding force degradation than AFC braces. This difference was due to (i) the observation that SFC braces underwent higher material degradation due to a higher efficient friction coefficient, and (ii) excessive tension applied to the clamping bolts as the bracing members deflected outwards which caused the bolts to yield, but this could be reduced by improving the detailing of SFC braces as discussed in Chapter 3.

The configuration of the AFC brace testing specimens presented in Chapter 2 requires one channel bracing member, one slotted plate, two shims, one cap plate, and one bearing plate. The configuration of the SFC brace testing specimens presented in Chapter 3 requires two channel bracing members, one gusset with a slotted flange, and two shims. The slotted gusset that is used for the SFC brace configuration requires precise fabrication to ensure the flange is at the correct angle and the slots are cut at the correct locations. The alternative SFC brace configuration proposed in Section 3.8 does not require a slotted gusset, but it consists of more components than the AFC brace configuration described in Chapter 2, including one additional slotted plate, bottom gusset, cap plate, and two extra shims, and all the extra components need to be fabricated precisely. Therefore, in general the construction tolerance for SFC braces is lower than that for AFC braces.

As indicated above, SFC braces require larger and/or more components than AFC braces, and therefore the material cost of an SFC brace is likely to be higher than that of an AFC brace. Also, since AFC braces have less components, it is easier to assess surface conditions and replace deteriorated components after a seismic event.

In summary, at low design axial demand, if a practitioner prefers cheaper and easier construction and repairs, it is recommended to used AFC braces. However, if the axial demand is high, SFC braces should be selected. It is worth nothing that currently there are not enough experimental results to confidently determine the critical axial demand at which an SFC brace

produces more stable performance than an AFC brace for a large accumulative sliding distance, as the AFC and SFC braces tested all equipped with two M16 clamping bolts. Therefore, testing of both types of friction braces using larger clamping bolts is required to obtain this information.

5.6.2. Viscous dampers vs friction braces

Viscous dampers and friction braces can both achieve similar hysteretic behaviour in both tension and compression. Viscous dampers are velocity dependent, while friction braces exhibit velocity independent elasto-plastic hysteresis, where the peak sliding force is based on the applied bolt tension and it is largely independent of displacement amplitude and velocity. Despite their difference in velocity dependency, viscous dampers have similar elasto-plastic hysteresis loops to those of a friction brace at low velocity exponent α values, therefore a viscous damper is able to dissipate similar amount of energy to a friction brace. Comparing to friction braces, viscous damper hysteresis loops are smoother in general, as they are not dependent on material conditions like friction braces. Also, unlike friction braces, viscous dampers do not experience sudden stiffness changes due to bolt slipping.

Practitioners should be aware that friction braces, or friction connections in general are sensitive to surface conditions and treatments, as well as the assembly process. Fabrication and assembly errors can lead to unstable performance and premature failure of the clamping bolts. It is also important to note that friction braces require consistent monitoring, which includes rust monitoring, and maintenance that involves bolt and plate replacements may be required after an earthquake to ensure friction braces continue to perform stably during subsequent earthquakes. Conversely, viscous dampers do not require maintenance under design loads and their performance can remain predictable and reliable over a large number of cyclic loadings without component replacements.

It is important to note that friction braces themselves do not possess reliable self-centring characteristics, and the self-centring of a building that is equipped with friction brace can only rely on the elasticity of the columns and beams, as well as the weight of the building. Therefore, it is possible for a friction braced structure to retain residual tension or compression forces at the end of an earthquake, leading to an increased chance of residual displacements and altered performance on subsequent loading. On the contrary, viscous dampers are less likely to lead to residual displacements as their velocity dependence means that they do not support residual force once the structure stops moving.

Friction connections in general require less space for installation and it is possible to convert an existing conventional brace to a friction brace without replacing the entire bracing system. For example, if a conventional brace is damaged during an earthquake, the damaged portion of the brace can be removed and replaced using a set of friction details. The size and strength of the friction connection can be easily adjusted according to the existing bracing configuration. Therefore, friction braces can be considered a more immediate retrofit strategy with locally available materials for existing buildings, for which the goal is to achieve similar energy dissipation mechanism in both tension and compression loadings. Whereas to install a viscous damper to an existing structure as a retrofit or strengthening strategy, the existing bracing system most likely needs to be replaced, and the design of a new bracing system needs to be carried out, especially the existing bracing system may not meet the recommended damper sub-system-to-structure stiffness ratios as mentioned in Section 5.3.2.

On a component level, viscous dampers do not allow much manufacturing tolerance and the precision required during the fabrication process of a viscous damper is greater than a friction brace. However, these tight tolerances are wrapped up with the purchased product, and practitioners do not have much control over the quality of a viscous damper, as it is the sole responsibility of the manufacturer, and the installation of a viscous damper is often a simple process. Friction brace components do not necessarily require as much machining because they are standard conventional plates and bolts. Although surface cleaning is required before the assembly of a friction brace, it does not require intense cost and labour. However, the installation of a friction brace requires tight tolerance as all bolt-holes and slots need to be drilled and cut at the correct locations to allow the friction brace to perform as predicted.

It is difficult to define the cost difference between viscous dampers and friction braces. On the component level, a viscous damper is more expensive, but the phasing effects induced by the viscous damper might indicate the total force demands on the structure foundation are less, requiring either less foundation work in a new build, or it may prevent the need to strengthen the foundation of an existing structure in a retrofit application. Therefore, a practitioner should consider the structural system as a whole when estimating cost, instead of comparing viscous dampers and friction braces on a component level. However, this could be a significantly challenging process.

Comparing the design process of a friction braced structure to a system equipped with a viscous damper, it may be easier to incorporate the design of a friction brace into standard structural

design, as friction brace behaviours are similar to conventional design with sacrificial damage. Conversely, the velocity-dependent nature of viscous dampers makes them more difficult to be incorporated into a standard design process. However, as mentioned earlier, the mechanism of friction connections is not yet fully understood, and more experimental study is required. Therefore, at this stage it is difficult to state which device has a more robust design framework.

6. CONCLUSIONS

This thesis presents the findings of the research carried out to achieve better understanding in the energy dissipation mechanism of friction braces and viscous dampers, which lead to an improved design frame for structures equipped with friction braces and viscous dampers.

Experimental study has been carried on AFC and SFC braces under quasi-static loading conditions. The braces were tested by themselves as well as within a steel single storey frame. The results have shown that:

(i) The brace and frame tests produced stable hysteretic behaviour while there was little to no material degradation. The hysteresis loops were repeatable and almost rectangular. Strength degradation for AFC and SFC braces was estimated as 10% and 15%, respectively, for the cases where no change of the friction connection components or bolt re-tightening was applied over 42 cycles of load reversals. Reductions in strength were attributed to loss of bolt tension and surface degradation, which was exacerbated by prying due to bracing member flexibilities.

(ii) The measured average effective coefficient of friction from the experiments was 0.18 for AFC braces and 0.31 for SFC braces. These were lower than the initially suggested effective friction coefficient by literatures that were 0.21 and 0.45 for AFC and SFC, respectively. A general design guideline of AFC and SFC braces has been provided.

(iii) An OpenSees numerical hysteresis model has been proposed based on the experimental results as a part of this study to model the general hysteretic behavior of friction braces. A comparison between the model response under a displacement-controlled simulation and the experimental hysteresis loops of an AFC brace specimen, and it shows the hysteresis model provides a reasonable approximation of the brace's hysteretic behavior.

(iv) AFC and SFC braced frames can be considered as low damage structural systems given that stable hysteretic behaviour could be achieved over an amount of cycles comparable to a typical severe earthquake, and also because friction braced frames could dissipate seismic energy via friction and exhibit large drifts without yielding any member or component of the primary structural system.

This thesis has also described numerical investigations aimed at quantifying the extent to which the damper sub-system stiffness can affect the overall displacement response and total base shear force for a structural system subject to earthquake excitation. Results from both sinusoidal and ground motion simulations indicate that if the sub-system stiffness is less than 10 times the stiffness of the main lateral load resisting system, the overall system response can be significantly affected by the sub-system flexibility. Results from ground motion simulations show that at stiffness ratios (i.e. the damper sub-system stiffness to total structural stiffness) K_d/K_s = 1, 1.5, and 5, both the median peak displacement response and the total system force can be 5% to 40% higher than the response of a damper system with a stiffness ratio of 200.

The ground motion simulation results also lead to the recommendation that designers take sub-system flexibility into consideration if more than 5% supplemental damping is to be introduced to the structural system. By plotting the DRF amplification factors for different structural periods at various stiffness ratios, it is recommended that for structures with natural periods larger than 0.5s, the linear viscous damper sub-system be provided with a stiffness that is five times greater than the structural stiffness, and the sub-system of a nonlinear viscous damper is required to be at least ten times stiffer than the stiffness of the structural lateral resisting system. A design example has been carried out to present how the damper sub-system to main structure lateral stiffness ratio can be calculated. Additionally, a modified design frame has been proposed as a part of this study to account for damper sub-system stiffness.

Finally, key findings of this thesis have been concluded in Chapter 5, and comparisons have made between AFC and SFC braces, as well as between friction braces in general and viscous dampers. In this chapter, the advantages and disadvantages of each system are highlighted to assist readers to select the more ideal device based on their design criteria.

REFERENCES

AISC, A. (2005). 360-Specification for Structural Steel Buildings; American Institute of Steel Construction.

Akcelyan, S., Lignos, D. G., & Hikino, T. (2018). Adaptive numerical method algorithms for nonlinear viscous and bilinear oil damper models subjected to dynamic loading. *Soil Dynamics and Earthquake Engineering*, *113*, 488-502.

AS/NZS1252 (2016). High-strength steel bolts with associated nuts and washers for structural engineering. *Standards New Zealand, Wellington*.

Borzouie, J., MacRae, G., Chase, G. J., & Clifton, C. (2014). Experimental studies on cyclic behaviour of steel base plate connections considering anchor bolts post tensioning. In *Proceedings of the 2014 New Zealand Society of Earthquake Engineering Conference, Christchurch, New Zealand*.

Borzouie, J., MacRae, G. A., Chase, J. G., Xie, R., Golondrino, J. C., & Clifton, G. C. (2015). Cyclic performance of Asymmetric Friction Connections with grade 10.9 bolts. *The Bridge and Structural Engineer*, *45*(1), 53-62.

Buchanan, A. H., Bull, D., Dhakal, R. P., MacRae, G. A., Palermo, P., & Pampanin, S. (2011). Base Isolation and Damage-Resistant Technologies for Improved Seismic Performance of Buildings, Report to the Royal Commission for the Canterbury Earthquakes, New Zealand, August 2011.

Butterworth, J. W. (1999). Seismic damage limitation in steel frames using friction energy dissipators. In *Proceedings of the 6th International Conference on Steel and Space Structure, Singapore* (pp. 1-2).

Castaldo, P., & De Iuliis, M. (2014). Optimal integrated seismic design of structural and viscoelastic bracing-damper systems. *Earthquake engineering & structural dynamics*, *43*(12), 1809-1827.

Cavallaro, G. F., Latour, M., Francavilla, A. B., Piluso, V., & Rizzano, G. (2018). Standardised friction damper bolt assemblies time-related relaxation and installed tension variability. *Journal of Constructional Steel Research*, *141*, 145-155.

Chanchi, J., MacRae, G. A., Chase, J. G., Rodgers, G. W., & Clifton, G. C. (2013). Hysteretic behaviour of Symmetrical Friction Connections using steel shims of different grades. In *Pacific Structural Steel Conference, Singapore*.

Chanchi, J., MacRae, G. A., Chase, J. G., Scott, A., Rodgers, G. W., & Bell, D. K. (2013, Feburary). Recent research on two low damage dampers applicable to steel framing system. In *Proceedings of the 2013 Steel Innovations Conference, Christchurch, New Zealand*.

Chanchí, J. C., Xie, R., MacRae, G., Chase, G., Rodgers, G., & Clifton, C. (2014, March). Low-damage braces using asymmetrical friction connections (AFC). In *NZSEE Conf., The New Zealand Society for Earthquake Engineering, Wellington, New Zealand*.

Chanchi Golondrino, J., Xie, R., MacRae, G. A., Chase, J. G., Rodgers, G. W., & Clifton, C. (2015). Low damage brace using a Symmetrical Friction Connection (SFC) detail. In *NZSEE Conf., The New Zealand Society for Earthquake Engineering, Wellington, New Zealand*.

Chen, Y. T., & Chai, Y. H. (2011). Effects of brace stiffness on performance of structures with supplemental Maxwell model-based brace–damper systems. *Earthquake Engineering & Structural Dynamics*, *40*(1), 75-92.

Chimeh, M. N., & Homami, P. (2012). Efficiency of bracing systems for seismic rehabilitation of steel structures. In *Proceedings of the 15th World Conference On Earthquake Engineering. Libosa, Portugal*.

Chou, C. C., Liu, J. H., & Pham, D. H. (2012). Steel buckling-restrained braced frames with single and dual corner gusset connections: seismic tests and analyses. *Earthquake Engineering & Structural Dynamics*, *41*(7), 1137-1156.

Christopoulos, C., Filiatrault, A., Uang, C. M., & Folz, B. (2002). Posttensioned energy dissipating connections for moment-resisting steel frames. *Journal of Structural Engineering*, *128*(9), 1111-1120.

Christopoulos, C., Filiatrault, A., & Bertero, V. V. (2006) *Principles of Passive Supplemental Damping and Seismic Isolation*, Pavia, IUSS Press.

Clifton, G. C. (2005). *Semi-rigid joints for moment-resisting steel framed seismic-resisting systems* (Doctoral dissertation, ResearchSpace@ Auckland).

Cook, J. (2018). *Design, testing and simulation of grip 'n'grab ratcheting, tension-only devices for seismic energy dissipation systems.* (Doctoral dissertation, University of Canterbury, Christchurch, New Zealand).

Dong, B. (2016). *Large-scale experimental, numerical, and design studies of steel MRF structures with nonlinear viscous dampers* (Doctoral dissertation, Lehigh University).

Dong, B., Sause, R., & Ricles, J. M. (2016). Seismic response and performance of a steel MRF building with nonlinear viscous dampers under DBE and MCE. *Journal of Structural Engineering*, *142*(6), 04016023.

Elwood, K. J., Marquis, F., & Kim, J. H. (2015, November). Post-earthquake assessment and repairability of RC buildings: lessons from Canterbury and emerging challenges. In *Proceedings of the tenth pacific conference on earthquake engineering, Sydney, Australia*.

FEmA, P. (2009). 695. *Quantification of building seismic performance factors", prepared by the Applied Technology Council (ATC) for the Federal Emergency Management Agency, Washington, DC*.

Filiatrault, A., & Cherry, S. (1987). Performance Evaluation of Friction Damped Braced Steel Frames Under Simulated Earthquake Loads. *Earthquake Spectra*, *3*(1), 57-78.

Filiatrault, A., & Cherry, S. (1988). Comparative performance of friction damped systems and base isolation systems for earthquake retrofit and aseismic design. *Earthquake engineering & structural dynamics*, *16*(3), 389-416.

Fitzgerald, T. F., Anagnos, T., Goodson, M., & Zsutty, T. (1989). Slotted bolted connections in aseismic design for concentrically braced connections. *Earthquake Spectra*, *5*(2), 383-391.

Fu, Y., & Kasai, K. (1998). Comparative study of frames using viscoelastic and viscous dampers. *Journal of Structural Engineering*, *124*(5), 513-522.

Gledhill, S. M., Sidwell, G. K., & Bell, D. K. (2008, April). The damage avoidance design of tall steel frame buildings-Fairlie terrace student accommodation project, Victoria university of Wellington. In *New Zealand Society of Earthquake Engineering Annual Conference* (pp. 11-13).

Gluck, N., Reinhorn, A. M., Gluck, J., & Levy, R. (1996). Design of supplemental dampers for control of structures. *Journal of structural Engineering*, *122*(12), 1394-1399.

Golondrino, J. C., MacRae, G., & Clifton, C. (2012). Behaviour of Asymmetrical Friction Connections using different shim materials. In *Proceedings of the New Zealand Society for Earthquake Engineering Conference*.

Golondrino, J. C., Xie, R., MacRae, G. A., Chase, G., Rodgers, G., & Clifton, C. (2015). Braced frame using asymmetrical friction connections (AFC). In *8th Conference on Behaviour of Steel Structures in Seismic Areas (STESSA)*.

Golondrino, C. J. (2019). *Hysteretic behaviour of Asymmetric Friction Connections (AFCs).* (Doctoral dissertation, University of Canterbury, Christchurch, New Zealand).

Golondrino, J. C. C., MacRae, G. A., Chase, J. G., Rodgers, G. W., Scott, A. C. N., & Clifton, G. C. (2019, June). Steel Building Friction Connection Seismic Performance–Corrosion Effects. In *Structures* (Vol. 19, pp. 96-109). Elsevier.

Grigorian, C. E., & Popov, E. P. (1994). *Energy dissipation with slotted bolted connections* (Report 94-02). UCB/EERC., Earthquake Research Center, University of California, Berkeley.

Gross, J. L. (1990). Experimental study of gusseted connections. *Engineering Journal*, *27*(3), 89-97.

Hatami, M., MacRae, G. A., Rodgers, G. W., & Clifton, G. C. (2019) Numerical and experimental study on friction connection performance-asymmetric and symmetric (AFC/SFC). In *Proceedings of 2019 Pacific Conference on Earthquake Engineering, Auckland, New Zealand.*

Ito, Y., Toyoda, J., & Nagata, S. (1979). Interface pressure distribution in a bolt-flange assembly. *Journal of Mechanical Design*, *101*(2), 330-337.

Kim, J., Choi, H., & Min, K. W. (2003). Performance-based design of added viscous dampers using capacity spectrum method. *Journal of Earthquake Engineering*, *7*(01), 1-24.

Lago, A. (2011). *Seismic design of structures with passive energy dissipation systems.* (PhD Dissertation, ROSE School, IUSS Pavia).

Latour, M., Piluso, V., & Rizzano, G. (2015). Free from damage beam-to-column joints: Testing and design of DST connections with friction pads. *Engineering Structures*, *85*, 219-233.

Lavan, O., & Levy, R. (2005). Optimal design of supplemental viscous dampers for irregular shear-frames in the presence of yielding. *Earthquake engineering & structural dynamics*, *34*(8), 889-907.

Lavan, O., & Levy, R. (2006). Optimal design of supplemental viscous dampers for linear framed structures. *Earthquake engineering & structural dynamics*, *35*(3), 337-356.

Lavan, O., & Levy, R. (2009). Simple iterative use of Lyapunov's solution for the linear optimal seismic design of passive devices in framed buildings. *Journal of Earthquake Engineering*, *13*(5), 650-666.

Lavan, O. (2012). On the efficiency of viscous dampers in reducing various seismic responses of wall structures. *Earthquake Engineering & Structural Dynamics*, *41*(12), 1673-1692.

Lavan, O. (2015). A methodology for the integrated seismic design of nonlinear buildings with supplemental damping. *Structural Control and Health Monitoring*, *22*(3), 484-499.

Lavan, O. (2015). Optimal design of viscous dampers and their supporting members for the seismic retrofitting of 3D irregular frame structures. *Journal of Structural Engineering*, *141*(11), 04015026.

Lin, Y. Y., Tsai, M. H., Hwang, J. S., & Chang, K. C. (2003). Direct displacement-based design for building with passive energy dissipation systems. *Engineering structures*, *25*(1), 25-37.

Lin, Y. Y., Chang, K. C., & Chen, C. Y. (2008). Direct displacement-based design for seismic retrofit of existing buildings using nonlinear viscous dampers. *Bulletin of Earthquake Engineering*, *6*(3), 535-552.

Londoño, J. M., Neild, S. A., & Wagg, D. J. (2013). A noniterative design procedure for supplemental brace–damper systems in single-degree-of-freedom systems. *Earthquake engineering & structural dynamics*, *42*(15), 2361-2367.

Londoño, J. M., Wagg, D. J., & Neild, S. A. (2014). Supporting brace sizing in structures with added linear viscous fluid dampers: A filter design solution. *Earthquake engineering & structural dynamics*, *43*(13), 1999-2013.

MacRae, G. A. (2008). A New Look at Some Earthquake Engineering Concepts. In *Proceedings of Nigel Priestley Symposium, King's Beach, USA* (pp. 15).

MacRae, G. A., & Clifton, G. C. (2015, September). Research on seismic performance of steel structures. In *Steel Innovations Conference, Auckland, New Zealand*.

MacRae, G. A., Clifton, G. C., Mackinven, H., Mago, N., Butterworth, J., & Pampanin, S. (2010). The sliding hinge joint moment connection. *Bulletin of the New Zealand Society for Earthquake Engineering*, *43*(3), 202.

Mazzoni, S., McKenna, F., Scott, M. H., & Fenves, G. L. (2006). OpenSees command language manual. *Pacific Earthquake Engineering Research (PEER) Center*, *264*.

Pall, A. S., & Marsh, C. (1982). Response of friction damped braced frames. *Journal of Structural Engineering*, *108*(9), 1313-1323.

Park, J. H., Kim, J., & Min, K. W. (2004). Optimal design of added viscoelastic dampers and supporting braces. *Earthquake engineering & structural dynamics*, *33*(4), 465-484.

Pekcan, G., Mander, J. B., & Chen, S. S. (1999). Fundamental considerations for the design of non-linear viscous dampers. *Earthquake engineering & structural dynamics*, *28*(11), 1405-1425.

Pennucci, D., Sullivan, T. J., & Calvi, G. M. (2011). Displacement reduction factors for the design of medium and long period structures. *Journal of Earthquake Engineering*, *15*(S1), 1-29.

Pettinga, J. D., Oliver, S., & Kelly, T. E. (2013) A design office approach to supplemental damping using fluid viscous dampers. In *Proceedings of 2013 Steel Innovations Conference, Christchurch, New Zealand.*

Pollini, N., Lavan, O., & Amir, O. (2017). Minimum-cost optimization of nonlinear fluid viscous dampers and their supporting members for seismic retrofitting. *Earthquake Engineering & Structural Dynamics*, *46*(12), 1941-1961.

Pollini, N., Lavan, O., & Amir, O. (2018). Optimization-based minimum-cost seismic retrofitting of hysteretic frames with nonlinear fluid viscous dampers. *Earthquake Engineering & Structural Dynamics*, *47*(15), 2985-3005.

Puthanpurayil, A. M., Edmonds, A. J., Jury, R. D., & Sharpe, R. D. (2017). Simplified vs. optimal techniques for viscous damper design: some preliminary observations. In *Proceedings of NZSEE conference, Wellington, New Zealand.*

Puthanpurayil, A. M., Lavan, O., & Sullivan, T. J. (2019). Displacement based design approach as a scheme stage methodology for structures with viscous dampers: some preliminary observations. In *Proceedings of NZSEE conference, Wellington, New Zealand.*

Rad, A. A., Hazaveh, N. K., & Holden, T. (2019) Seismic performance of steel buildings with fluid viscous dampers relative to base isolation. In *Proceedings of 2019 Pacific Conference on Earthquake Engineering, Auckland, New Zealand.*

Ramhormozian, S., Clifton, G. C., MacRae, G. A., & Khoo, H. H. (2015). Improving the seismic behaviour of the Sliding Hinge Joint using Belleville Springs. In *8th Conference on Behaviour of Steel Structures in Seismic Areas (STESSA)*.

Ramhormozian, S., Clifton, G. C., MacRae, G. A., & Davet, G. P. (2017). Stiffness-based approach for Belleville springs use in friction sliding structural connections. *Journal of Constructional Steel Research*, *138*, 340-356.

Ramirez, O. M. (2001). *Development and evaluation of simplified procedures for the analysis and design of buildings with passive energy dissipation systems* (Doctoral dissertation, State University of New York, Buffalo).

Reinhorn, A. M., Li, C., & Constantinou, M. C. (1995). *Experimental and analytical investigation of seismic retrofit of structures with supplemental damping: part 1-fluid viscous damping devices* (No. NCEER-95-0001).

Rodgers, G. W., Mander, J. B., & Geoffrey Chase, J. (2012). Modeling cyclic loading behavior of jointed precast concrete connections including effects of friction, tendon yielding and dampers. *Earthquake engineering & structural dynamics*, *41*(15), 2215-2233.

Rodgers, G. W., Mander, J. B., Chase, J. G., & Dhakal, R. P. (2016). Beyond ductility: parametric testing of a jointed rocking beam-column connection designed for damage avoidance. *Journal of Structural Engineering*, *142*(8), C4015006.

Sabelli, R., Mahin, S., & Chang, C. (2003). Seismic demands on steel braced frame buildings with buckling-restrained braces. *Engineering Structures*, *25*(5), 655-666.

Seleemah, A. A., & Constantinou, M. C. (1997). *Investigation of seismic response of buildings with linear and nonlinear fluid viscous dampers*. Buffalo: National Center for Earthquake Engineering Research.

Silvestri, S., Gasparini, G., & Trombetti, T. (2010). A five-step procedure for the dimensioning of viscous dampers to be inserted in building structures. *Journal of Earthquake Engineering*, *14*(3), 417-447.

Singh, M. P., Verma, N. P., & Moreschi, L. M. (2003). Seismic analysis and design with Maxwell dampers. *Journal of Engineering Mechanics*, *129*(3), 273-282.

Soong, T. T., & Costantinou, M. C. (Eds.). (2014). *Passive and active structural vibration control in civil engineering* (Vol. 345). Springer.

Standard, S. S. (2007). NZS 3404: 1997. *Standards New Zealand, Wellington*.

suanPan [Software]. (2019). Retrieved from https://doi.org/10.5281/zenodo.1285221

Sullivan, T. J., & Lago, A. (2012). Towards a simplified direct DBD procedure for the seismic design of moment resisting frames with viscous dampers. *Engineering Structures*, *35*, 140-148.

Takewaki, I., & Yoshitomi, S. (1998). Effects of support stiffnesses on optimal damper placement for a planar building frame. *The Structural Design of Tall Buildings*, *7*(4), 323-336.

Thornton, W. A. (1984). Bracing connections for heavy construction. *Engineering Journal*, *21*(3), 139-148.

Tremblay, R. (1993). *Seismic behavior and design of friction concentrically braced frames for steel buildings* (Doctoral dissertation, University of British Columbia).

Viola, E., & Guidi, F. (2009). Influence of the supporting braces on the dynamic control of buildings with added viscous dampers. *Structural Control and Health Monitoring: The Official Journal of the International Association for Structural Control and Monitoring and of the European Association for the Control of Structures*, *16*(3), 267-286.

Westeneng, B., Lee, C. L., & MacRae, G. (2016, April). Prevention of gusset plate out-of-plane sway buckling failure in buckling restrained braced frames. In *Proc of 2016 NZSEE Conference*.

Wijanto, S. (2012). *Behaviour and Design of Generic Buckling Restrained Brace Systems* (Doctoral dissertation, University of Auckland).

Xie, Q. (2005). State of the art of buckling-restrained braces in Asia. *Journal of constructional steel research*, *61*(6), 727-748.

Xie, R., Chanchi Golondrino, J., MacRae, G. A., & Clifton, G. C. (2018). Braced Frame Symmetrical and Asymmetrical Friction Connection Performance. In *Key Engineering Materials* (Vol. 763, pp. 216-223). Trans Tech Publications.

Xie, R. M., Rodgers, G. W., & Sullivan, T. J. (2019). Influence of Damper Sub-System Stiffness on the Structural Performance of a System Equipped with a Viscous Damper. In *Australian Earthquake Engineering Society Annual Technical conference, Newcastle, Australia.*

Yam, M. C., & Cheng, J. R. (1993). *Experimental investigation of the compressive behaviour of gusset plate connections* (Report SER194). Structural Engineering Report, Department of Civil Engineering, University of Alberta, Edmonton.

Yeow, T. Z., Orumiyehei, A., Sullivan, T. J., MacRae, G. A., Clifton, G. C., & Elwood, K. J. (2018). Seismic performance of steel friction connections considering direct-repair costs. *Bulletin of Earthquake Engineering*, *16*(12), 5963-5993.

APPENDICES

APPENDIX A: AFC brace design example for Section 2.6.

APPENDIX B: Material requests for friction brace and frame tests, for Chapter 2 and 3.

APPENDIX C: AFC brace test setup, for Section 2.2.

APPENDIX D: Source code for the *AFC* numerical model, for Section 2.7.

- APPENDIX D-1: AFCN.h
- APPENDIX D-2: AFCN.cpp

APPENDIX E: Viscous damper OpenSees model used for ground motion simulations in Section 4.3 and 4.4.

- APPENDIX E-1: OpenSees model
- APPENDIX E-2: Matlab file used to launch ground motion simulations

APPENDIX F: Extra parametric studies to support the results in Section 4.2 and 4.3

- APPENDIX F-1: Impact of sub-system flexibility on the phasing of viscous dampers.
- APPENDIX F-2: Validation of the Chapter 4 SDOF model (Figure 4-2) using a CHCH ground motion record [Yeow *et. al*, 2018].

APPENDIX G: Detailed hand calculations for single storey viscous damper frame design example (Section 4.5.3.1).

APPENDIX A. AFC brace design example

This appendix contains a design example carried out on an AFC brace using Equations (2.2) – (2.19).

The following design example carries out a capacity design for an AFC brace with a layout and dimensions that are illustrated in Figure 2.1. The calculations below follow the recommended steps described in Section 2.6, using Equations (1.1) and (2.2) – (2.19).

Step 1: Prediction of sliding force.

For an AFC detail with 2 M16 G8.8 bolts, the parameters from Equation 1.1 are defined as below:

$$\phi = 0.7$$

$$n_b = 2$$

$$n_s = 2$$

$$\mu = 0.18$$

$$N_{tf} = 95\ kN$$

$$\phi F_s = 0.7 \times 2 \times 2 \times 0.18 \times 95\ kN$$

$$\phi F_s = 47.9\ kN$$

This gives a lower bound force that can trigger full sliding in an AFC detail.

Step 2: Design of the bracing member

Design examples for this step is carried out for a 2860 mm long brace.

AFC brace axial demand:

$$N_s^* = \phi_o F_s$$

$$= 1.4 \times (47.9/0.7)$$

$$N_s^* = 112\ kN$$

Check the section compressive capacity using Equation (2.2) and (2.3):

$A_g = 4520\ mm^2$ *(gross cross section area of 250PFC)*

$A_n = A_g - 3 \times A_{hole,\emptyset=25mm}$

$A_n = 3920\ mm^2$

$K_f = 1$ *(form factor for 250PFC)*

$f_y = 300\ MPa$

$\phi_u N_s = 823\ kN$

$\phi_u N_s > N_s^*$ <u>*OK*</u>

Member compressive axial capacity of the brace, Equation (2.4) – (2.6):

$N_c^* = 112\ kN$

$L_e = 1.2 \times 2860\ mm$

$L_e = 3432\ mm$

$r_x = 99.9\ mm$

$$\lambda_{n,x} = \frac{3432\ mm}{99.9\ mm}\sqrt{1}\sqrt{\frac{300\ MPa}{250}}$$

$\lambda_{n,x} = 34.35$

$\alpha_{c,x} = 0.891$

$\phi_u N_{cx} = 0.7 \times 0.891 \times 1 \times 300\ MPa \times 3920\ mm^2$

$\phi_u N_{cx} = 733\ kN$

$r_y = 28.4\ mm$

$$\lambda_{n,y} = \frac{3432\ mm}{28.4\ mm}\sqrt{1}\sqrt{\frac{300\ MPa}{250}}$$

$$\lambda_{n,y} = 132.38$$

$$\alpha_{c,y} = 0.332 \text{ } \textit{(interpolated using Table 6.3.3(1))}$$

$$\phi_u N_{cy} = 0.7 \times 0.332 \times 1 \times 300\ MPa \times 3920\ mm^2$$

$$\phi_u N_{cy} = 273\ kN$$

$$\phi_u N_{cy} < \phi_u N_{cx}$$

$$\phi_u N_c = \phi_u N_{cy}$$

$$= 295\ kN$$

$$\phi_u N_c > N_s^* \quad \underline{OK}$$

Now check the section tensile capacity of the 250PFC bracing member, Equation (2.7):

$$N_t^* = 112\ kN$$

$$\phi_u N_{t,1} = 0.7 \times 4520\ mm^2 \times 300\ MPa$$

$$\phi_u N_{t,1} = 949.2\ kN$$

$$\phi_u N_{t,2} = 0.7 \times 0.85 \times 1 \times 4232\ mm^2 \times 430\ MPa$$

$$\phi_u N_{t,2} = 1082.76\ kN$$

$$\phi_u N_t = \phi_u N_{t,1}$$

$$= 949.2\ kN$$

$$\phi_u N_t > N_t^* \quad \underline{OK}$$

As a conclusion, using Equation (2.8) the governing axial capacity of the 250PFC bracing member is defined as:

$$\phi_u N = \phi_u N_{cy}$$

$$\phi_u N = 295\ kN$$

Check moment capacity of the 250PFC brace considering section strength to satisfy Equation (2.9):

Moment demands on the brace during frame tests:

$$M_x^* = 1.28\ kNm$$

$$M_y^* = 0\ kNm$$

$$M_e^* = 2.2\ kNm$$

M_x^* was computed using SAP2000 based on a first- order analysis of a frame model with the same properties as the experimental frame. The M_x^* from SAP2000 was also checked using SAP2000. M_y^* is zero as no load was applied on to the test frame from the tangential direction, and the out -of-plane deflection of the frame was restrained during the experiment. Equation (2.10) and (2.11) are used to check the section moment capacity of the 250PFC brace.

$$Z_{ex} = 421 \times 10^3\ mm^3, \textit{ for 250PFC.}$$

$$M_{sx} = 126.3\ kNm$$

$$Z_{ey} = 89 \times 10^3\ mm^3, \textit{ for 250PFC.}$$

$$M_{sy} = 26.7\ kNm$$

$$f_1 = \frac{112\ kN}{888.72\ kN} + \frac{1.28\ kNm}{0.7 \times 126.3\ kNm} + \frac{2.2\ kNm}{0.7 \times 26.7\ kNm}$$

$$f_1 = 0.26$$

$$f_1 < 1 \quad \underline{OK}$$

Check moment capacity of the 250PFC brace considering member strength to satisfy Equation 2.11:

Since design compressive force dominates the axial capacity of the brace, f_2 shall be satisfied for member considerations. Moment distribution profile can be estimated based on SAP2000 analysis using pre-selected frame materials before a strength check is carried by through hand calculations:

$\beta_m = 0.408$

Case 1 from Table 5.6.1 of NZS3404:1997 shall be considered for the following calculations due to the linear moment distribution profile of the bracing member.

For 250PFC, the following parameters can be defined. Moment modification factor α_m is calculated using Equation (2.15):

$\alpha_m = 2.5$

$G = 80{,}000\ MPa$

$J = 238 \times 10^3\ mm^4$

$E = 200{,}000\ MPa$

$I_y = 3.64 \times 10^6\ mm^4$

$I_w = 35.9 \times 10^9\ mm^6$

$L_e = 3432\ mm$

Substitute the above parameters into Equations (2.12) – (2.14), and (2.16) – (2.19) the following terms can be calculated:

$M_{oa} = 123.63\ kNm$

$\alpha_s = 0.593$

$M_{bx} = 131.07\ kNm$

$M_{ox} = 81.3\ kNm$

M_{ix} = 108.4 kNm

M_{iy} = 16.5 kNm

With the different member moment capacities defined, f_2 can be calculated using Equation (2.11) to show the overall moment capacity of the 250PFC bracing member satisfies the strength criteria.

$$f_2 = \left(\frac{1.28\ kNm}{0.7 \times 81.3\ kNm}\right)^{1.4} + \left(\frac{2.2\ kNm}{0.7 \times 16.5\ kNm}\right)^{1.4}$$

f_2 = 0.11

f_2 < *1* <u>*OK*</u>

Step 3: Design of slotted plate

Using the same method and equations as the bracing member design:

Axial Strength:

Parameters			**Equations/Tables**
$N^*_{s,c,t}$	=	112 kN	(1.1)
K_f	=	1	(2.3)
A_n	=	3360 mm^2	–
$\phi_u N_s$	=	658 kN	(2.2)
L_e	=	858 mm	(2.6)
λ_{nx}	=	17.47	(2.5)
α_{cx}	=	0.98	NZS3404, table 6.3.3(2)
$\phi_u N_{cx}$	=	645 kN	(2.4)

λ_{ny}	=	98.292	(2.5)
α_{cy}	=	0.495	NZS3404, table 6.3.3(2)
$\phi_u N_{cy}$	=	325 kN	(2.4)
$\phi_u N_t$	=	859 kN	(2.7)
$\phi_u N$	=	325 kN	(2.8)

Moment Capacities:

Parameters			**Equations/tables used**
M_x^*	=	0.76 kNm	SAP2000 analysis
M_y^*	=	0 kNm	–
M_e^*	=	2.2 kNm	–
Z_x	=	172.8 $\times$ 10^3 mm^3	–
M_{sx}	=	48 kNm	(2.10)
Z_y	=	30.72 $\times$ 10^3 mm^3	–
M_{sy}	=	8.6 kNm	(2.10)
f_1	=	0.6	(2.9)
α_m	=	1.2	(2.15)
J	=	922.1 $\times$ 10^3 mm^4	–
I_y	=	491.52 $\times$ 10^3 mm^4	–
I_w	=	0 mm^4	–
M_{oa}	=	311 kNm	(2.17)

α_s = 0.95 (2.16)

M_{bx} = 38 kNm (2.14)

M_{ox} = 25 kNm (2.13)

M_{ix} = 39 $kNm > M_{ox}$ (2.12)

M_{cx} = 25 kNm –

M_{iy} = 5.6 kNm (2.12)

f_2 = 0.46 (2.11)

APPENDIX B. Material requests for friction braces and frame tests

This appendix consists of the material requests submitted to the supply manager Stuart Toase at the University of Canterbury Structures Laboratory. The documents include drawings and dimensions of the components that used for the experimental study of AFC and SFC braces.

Material suppliers were Profile Cutting, John Jones Steel, and Black Fasteners.

DEPARTMENT OF CIVIL AND NATURAL RESOURCES ENGINEERING

UNIVERSITY OF CANTERBURY

Materials Request – First Stage

Submitted to: Stuart Tose

Designers: Robin Xie

Jose Chanchi

Associate Professor Greg MacRae

23rd April 2013

I. FRAME PROFILE

Item	Components	Geometry	Quantity	Grade	See Drawing
1.1	Beam 1	200UC59.5 Length=2100 mm	1	300	A
1.2	Beam 2	200UC59.5 Length=360 mm	2	300	A
1.3	Column	200UC59.5 Length=3030 mm	2	300	A

DRAWING A UNIT: [mm]

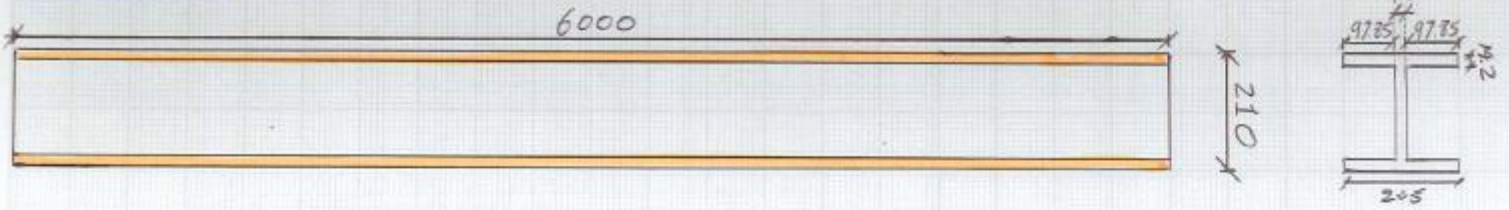

Component	Section Profile	Strength	Length	Quantity
BEAM/COLUMN	200UC59.5	G300	6000mm	1

UNIVERSITY OF CANTERBURY	
SUBJECT:	BEAM/COLUMN
DESIGNERS:	MACRAE; CHANCHI; XIE
DATE:	23/04/2013

II. PLATES

Item	Components	Geometry (mm)	Quantity	Grade	See Drawing
2.1	Plate 1	PL 850X360X50	2	300	B
2.2	Plate 2	PL 415X205X30	1	300	C
2.3	Plate 3	PL 350X205X30	1	300	C

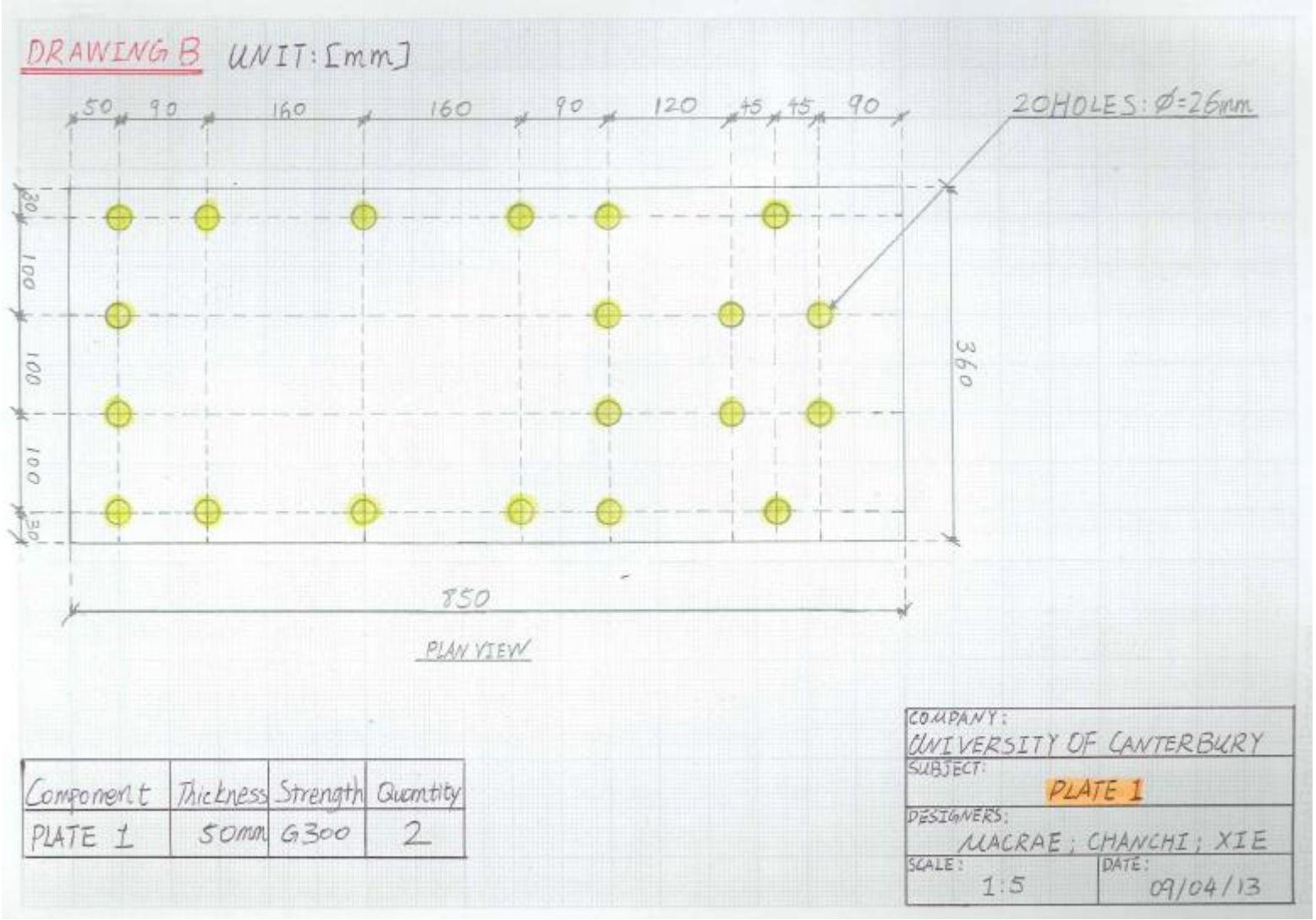
DRAWING B UNIT: [mm]
50 90 160 160 90 120 45 45 90
20HOLES: ∅=26mm
30 100 100 100 30
360
850
PLAN VIEW
Component | Thickness | Strength | Quantity
PLATE 1 | 50mm | G300 | 2
COMPANY: UNIVERSITY OF CANTERBURY
SUBJECT: PLATE 1
DESIGNERS: MACRAE; CHANCHI; XIE
SCALE: 1:5
DATE: 09/04/13

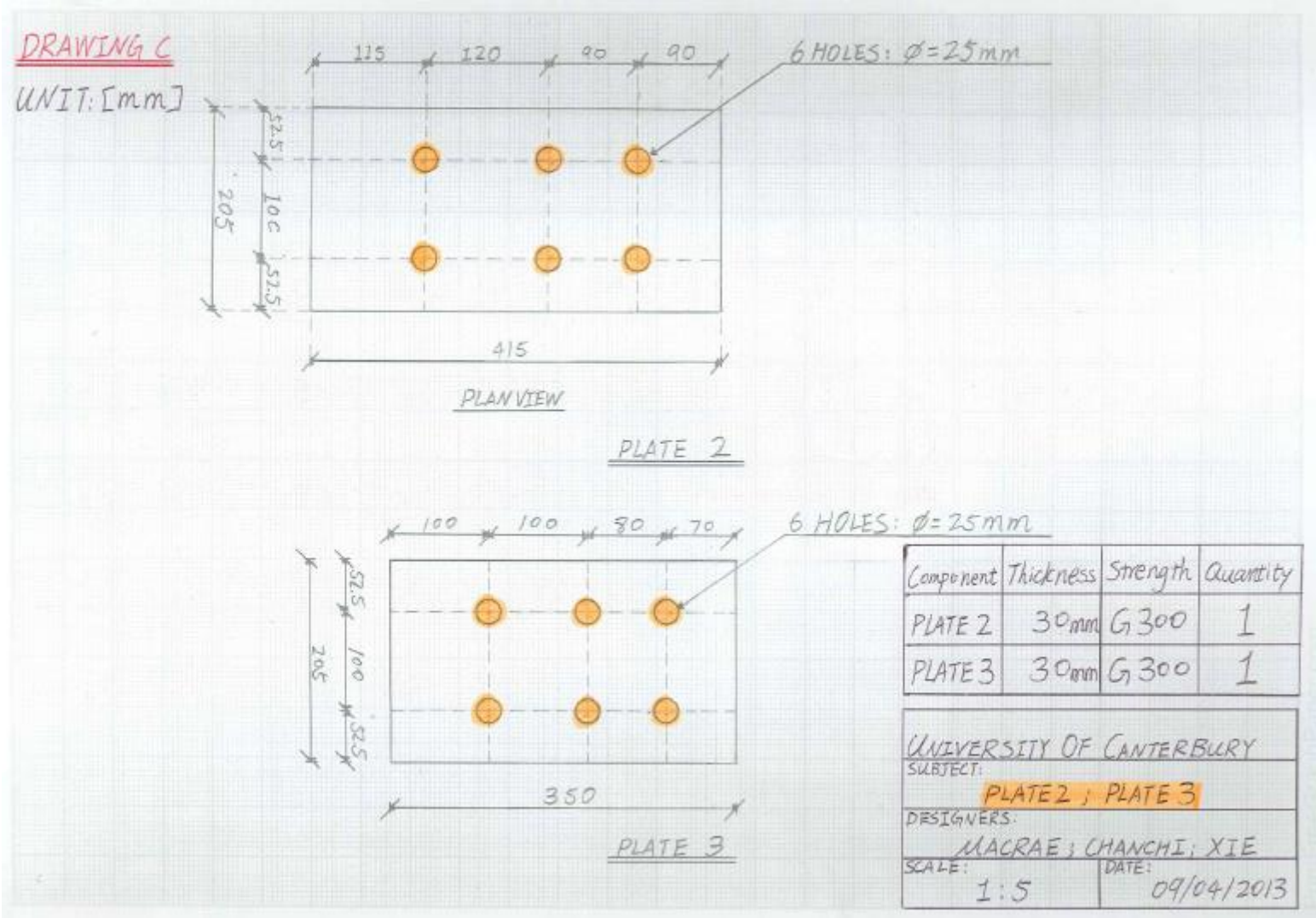
DRAWING C
UNIT: [mm]
115
120
90
90
6 HOLES: Ø=25mm
52.5
100
52.5
205
415
PLAN VIEW
PLATE 2
100
100
80
70
6 HOLES: Ø=25mm
52.5
100
52.5
205
350
PLATE 3
Component | Thickness | Strength | Quantity
PLATE 2 | 30mm | G300 | 1
PLATE 3 | 30mm | G300 | 1
UNIVERSITY OF CANTERBURY
SUBJECT: PLATE2 ; PLATE 3
DESIGNERS: MACRAE ; CHANCHI ; XIE
SCALE: 1:5
DATE: 09/04/2013

III. SHAPED PLATES

Item	Components	Geometry (mm)	Quantity	Grade	See Drawing
3.1	Gusset Plate 1	PL 410X300X40*	1	300	D
3.2	Stiffeners	PL 180X90X16*	24	300	E

**For specific dimensions, please refer to the corresponding drawings.*

DRAWING D UNIT: [mm]

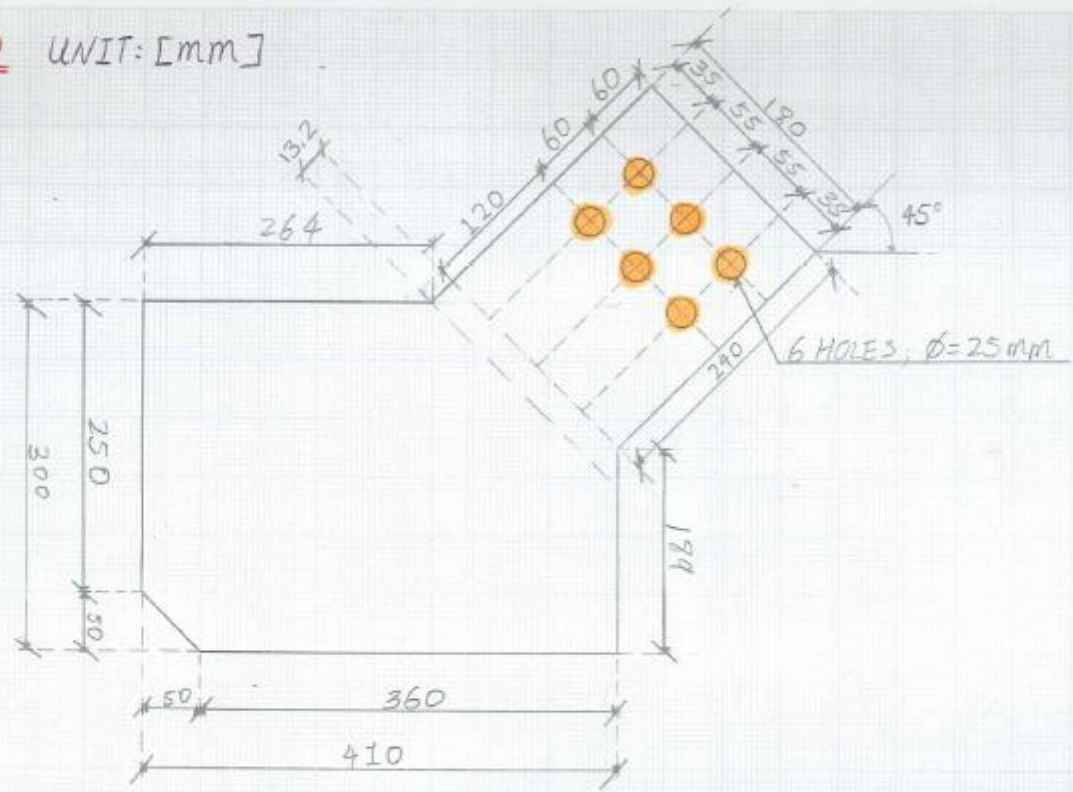

Component	Thickness	Strength	Quantity
GUSSET PLATE 1	40 mm	G300	1

UNIVERSITY OF CANTERBURY

SUBJECT: GUSSET PLATE 1

DESIGNERS: MACRAE; CHANCHI; XIE

SCALE: 1:5

DATE: 10/04/2013

DRAWING E UNIT: [mm]

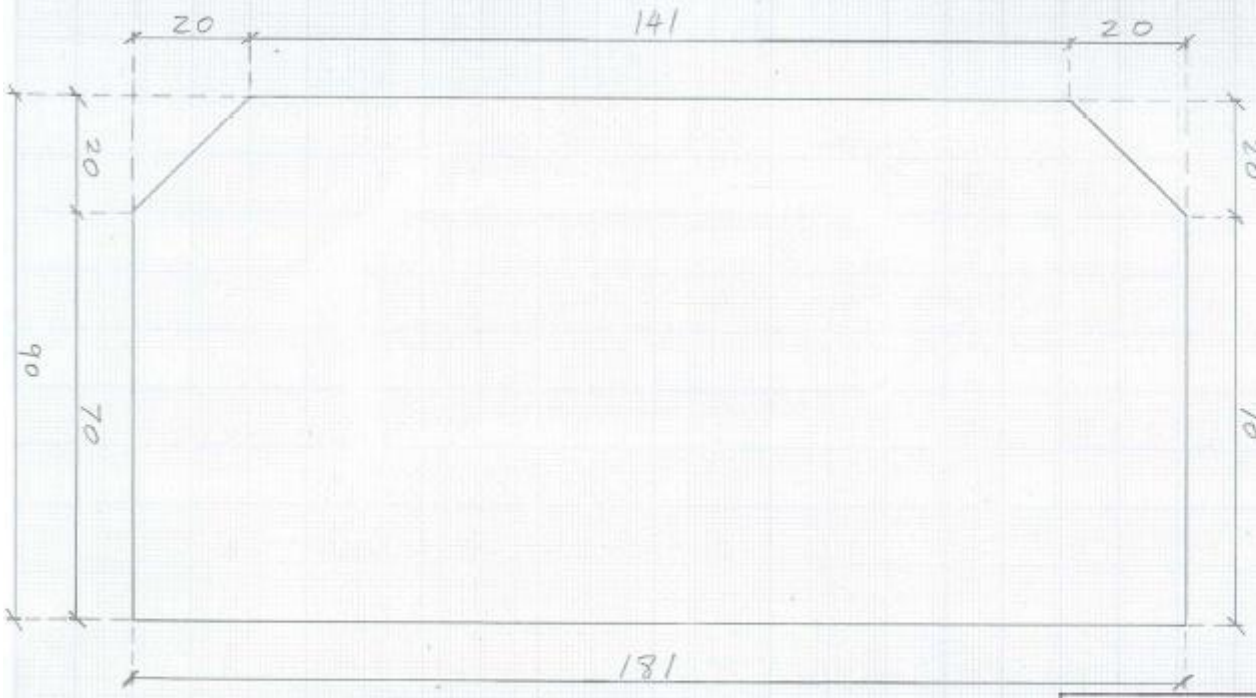

Component	Thickness	Strength	Quantity
STIFFENER	16 mm	G300	24

UNIVERSITY OF CANTERBURY	
SUBJECT: STIFFENER	
DESIGNERS: MACRAE; CHANCHI; XIE	
SCALE: 1:1	DATE: 19/04/2013

IV. BOLTS

Item	Component	Diameter (mm)	Nominal Length (mm)	Grade	Quantity	Type
4.1	M24X150	24	150	8.8	8	Galvanised
4.2	M24X120	24	120	8.8	17	Galvanised
4.3	M24X80	24	80	8.8	14	Galvanised

V. WASHERS & NUTS

Item	Component	Size (mm)	Grade	Quantity	Type
5.1	Flat Washers	M24	8.8	45	Galvanised
5.2	Structural Washers	M24	8.8	45	Galvanised
5.3	Nuts	M24	8.8	39	Galvanised

MATERIAL REQUEST – FIRST STAGE: SUMMARY

I. FRAME PROFILE

Item	Components	Geometry	Quantity	Grade	See Drawing
1.1	Beam 1	200UC59.5 Length=2100 mm	1	300	A
1.2	Beam 2	200UC59.5 Length=360 mm	2	300	A
1.3	Column	200UC59.5 Length=3030 mm	2	300	A

II. PLATES

Item	Components	Geometry (mm)	Quantity	Grade	See Drawing
2.1	Plate 1	PL 850X360X50	2	300	B
2.2	Plate 2	PL 415X205X30	1	300	C
2.3	Plate 3	PL 350X205X30	1	300	C

III. SHAPED PLATES

Item	Components	Geometry (mm)	Quantity	Grade	See Drawing
3.1	Gusset Plate 1	PL 410X300X40*	1	300	D
3.2	Stiffeners	PL 180X90X16*	24	300	E

**For specific dimensions, please refer to the corresponding drawings.*

IV. BOLTS

Item	Component	Diameter (mm)	Nominal Length (mm)	Grade	Quantity	Type
4.1	M24X150	24	150	8.8	8	Galvanised
4.2	M24X120	24	120	8.8	17	Galvanised
4.3	M24X80	24	80	8.8	14	Galvanised

V. WASHERS & NUTS

Item	Component	Size(mm)	Grade	Quantity	Type
5.1	Flat Washers	M24	8.8	45	Galvanised
5.2	Structural Washers	M24	8.8	45	Galvanised
5.3	Nuts	M24	8.8	39	Galvanised

DEPARTMENT OF CIVIL AND NATURAL RESOURCES ENGINEERING

UNIVERSITY OF CANTERBURY

Materials Request – Second Stage

Submitted to: Stuart Tose

Designers: Robin Xie

Associate Professor Greg MacRae

Jose Chanchi

23rd July 2013

I. FRAME PROFILE

Item	Components	Geometry	Quantity	Grade	See Drawing
1.1	Channel	250PFC Length=3000 mm	1	300	A

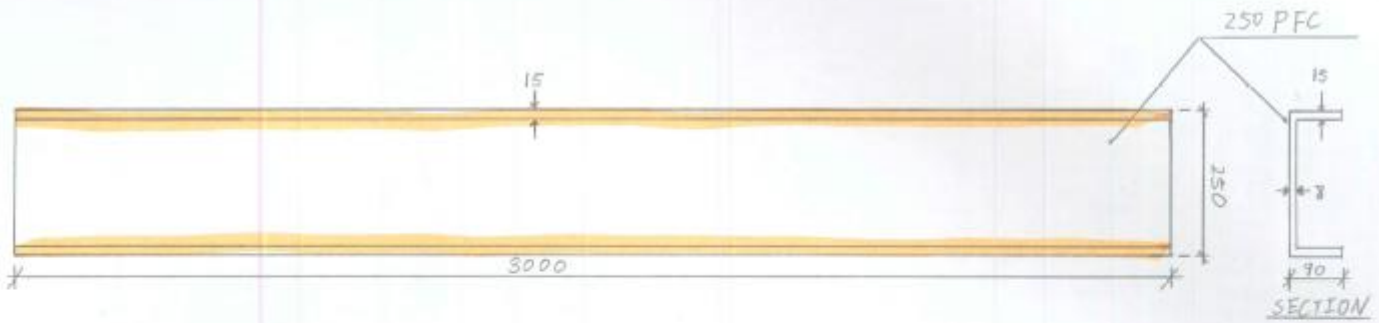

Component	Profile	Strength	Quantity
CHANNEL	250PFC	G300	1

DRAWING A

UNIVERSITY OF CANTERBURY

CHANNEL

DESIGNERS:
MACRAE; CHANCHI; XIE

SCALE: 1:10

DATE: 29/06/2013

II. PLATES

Item	Components	Geometry (mm)	Quantity	Grade	See Drawing
2.1	Plate 4	PL 400X210X32	1	300	B
2.2	Plate 5	PL 360X210X32	1	300	C
2.3	Bearing Plate	PL 300X200X16	1	300	D

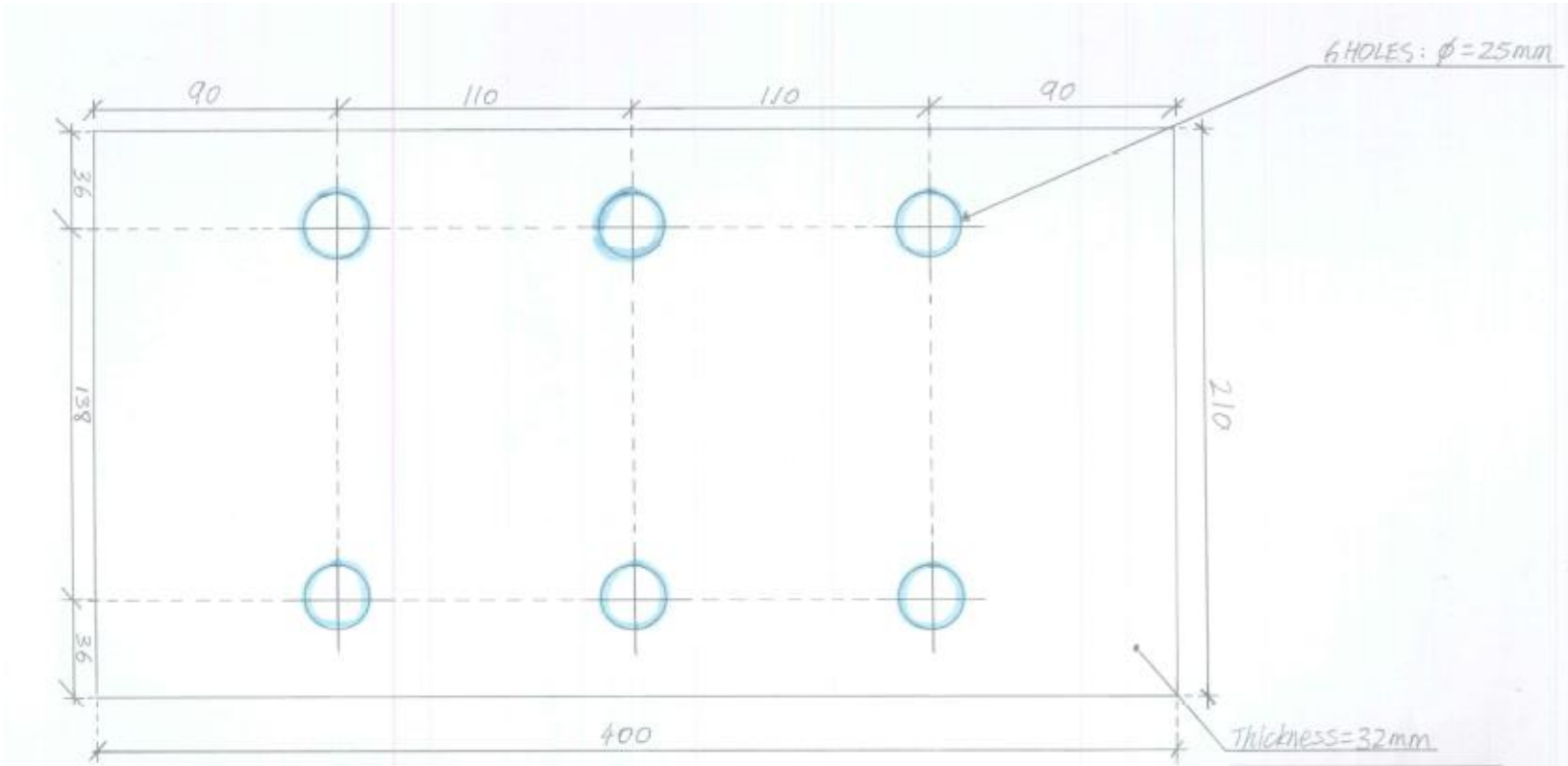

Component	Thickness	Strength	Quantity
PLATE 4	32mm	G300	1

DRAWING B

UNIVERSITY OF CANTERBURY

SUBJECT: PLATE 4

DESIGNERS: MACRAE; CHANCHI; XIE

SCALE: 1:2

DATE: 22/06/2013

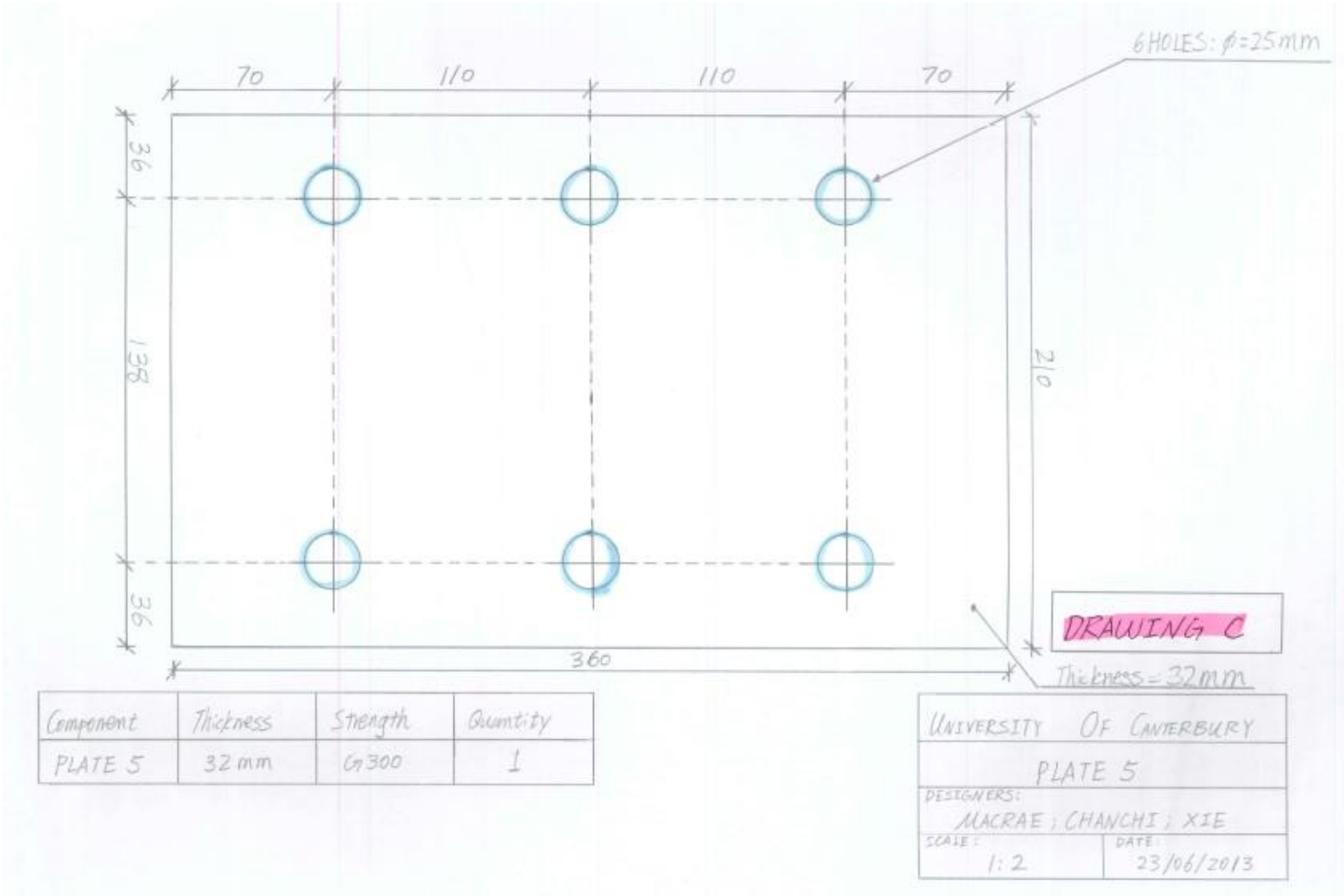

Component	Thickness	Strength	Quantity
PLATE 5	32 mm	G300	1

UNIVERSITY OF CANTERBURY	
PLATE 5	
DESIGNERS: MACRAE ; CHANCHI ; XIE	
SCALE: 1:2	DATE: 23/06/2013

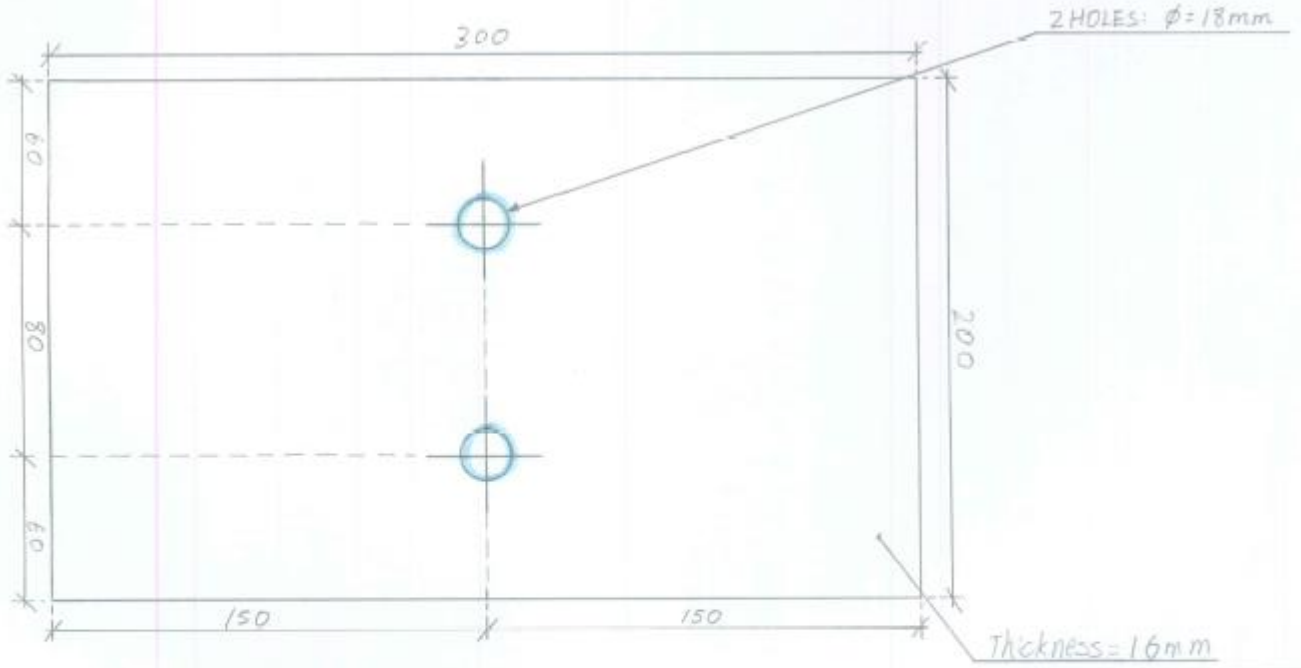

Component	Thickness	Strength	Quantity
BEARING PLATE	16 mm	G300	1

DRAWING D

UNIVERSITY OF CANTERBURY	
BEARING PLATE	
DESIGNERS: MACRAE; CHANCHI; XIE	
SCALE: 1:2	DATE: 23/06/2013

III. SHAPED PLATES

Item	Components	Geometry (mm)	Quantity	Grade	See Drawing
3.1	Gusset Plate 2	PL 345X324X32*	1	300	E

**For specific dimensions, please refer to the corresponding drawings.*

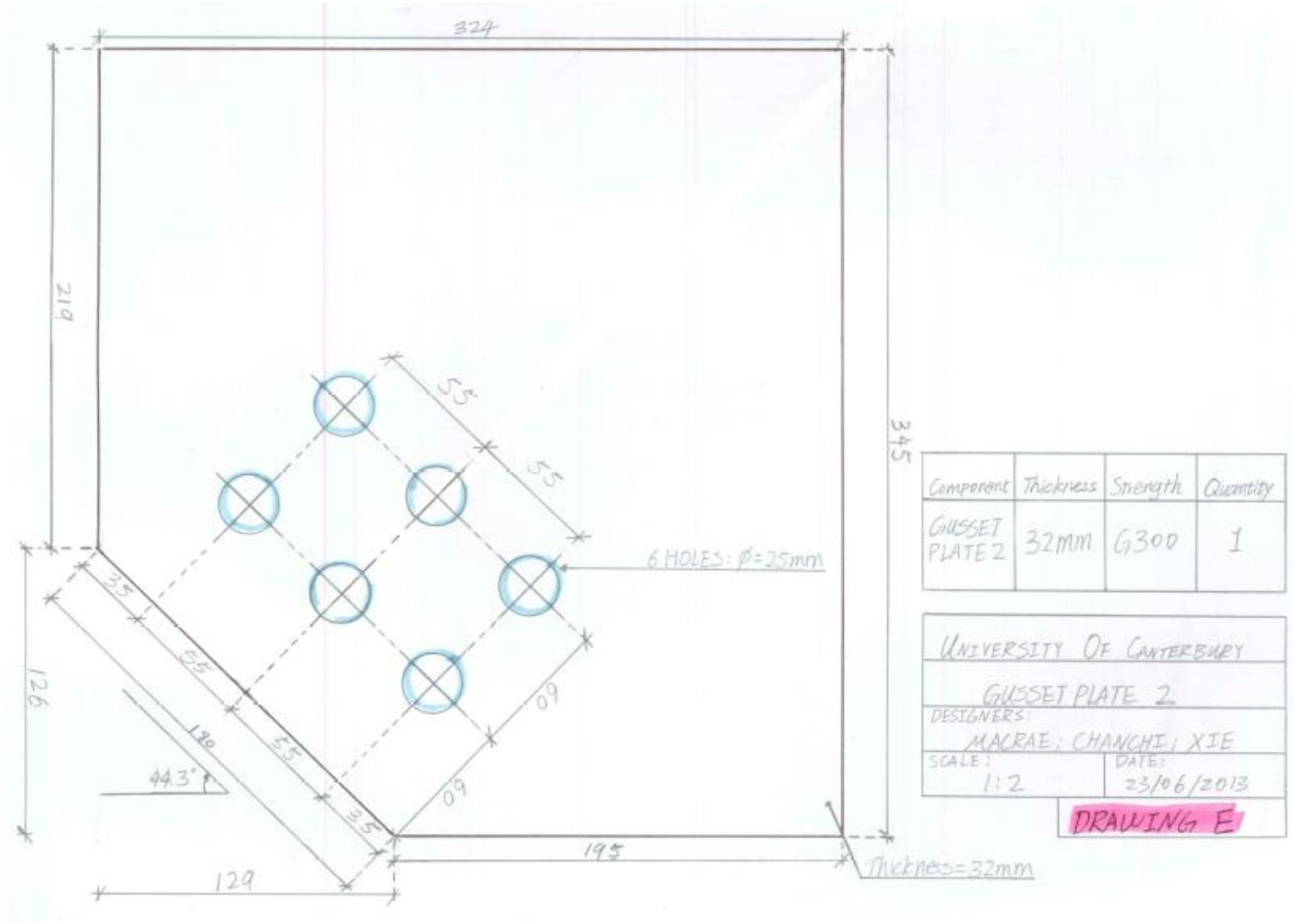

Component	Thickness	Strength	Quantity
GUSSET PLATE 2	32mm	G300	1

UNIVERSITY OF CANTERBURY	
GUSSET PLATE 2	
DESIGNERS: MACRAE; CHANCHI; XIE	
SCALE: 1:2	DATE: 23/06/2013
DRAWING E	

IV. AFC COMPONENTS

Item	Components	Geometry (mm)	Quantity	Grade	See Drawing
4.1	Cap Plate	PL 300X180X16	1	300	F
4.2	Slotted Plate	PL 715X180X32	1	300	G
4.3	Shim	PL 350X205X30	8	Bisalloy 500	H

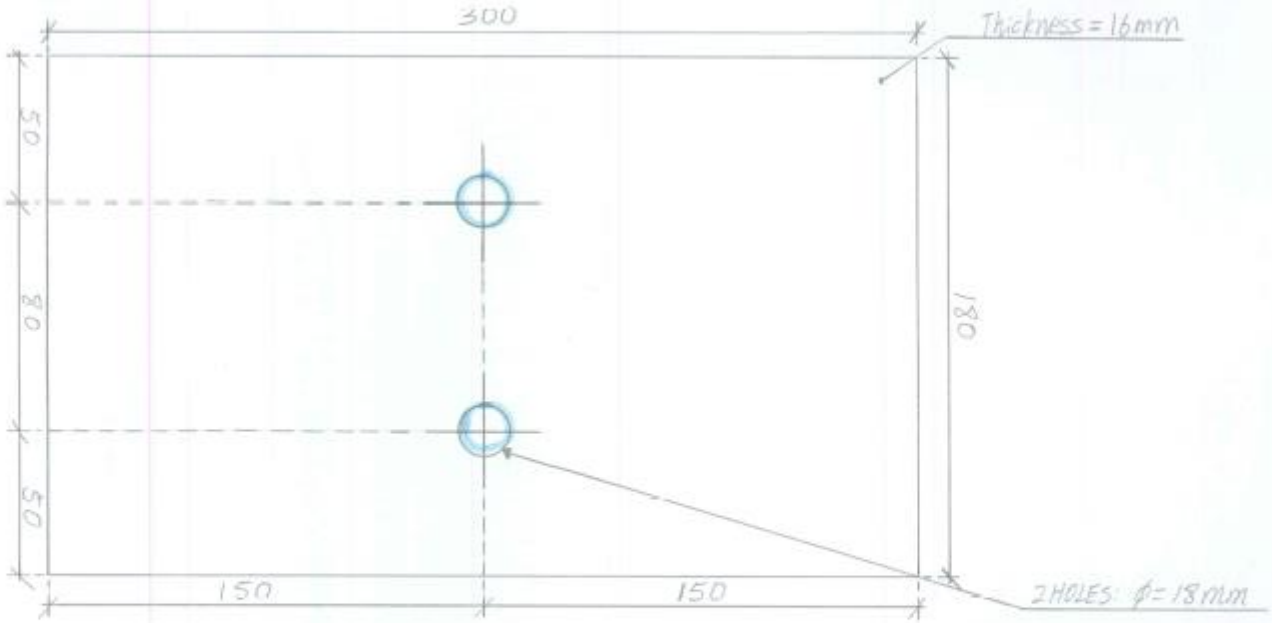

Component	Thickness	Strength	Quantity
CAP PLATE	16mm	G300	2

DRAWING F

UNIVERSITY OF CANTERBURY
CAP PLATE
DESIGNERS: MACRAE; CHANCHI; XIE
SCALE: 1:2 — DATE: 23/06/2013

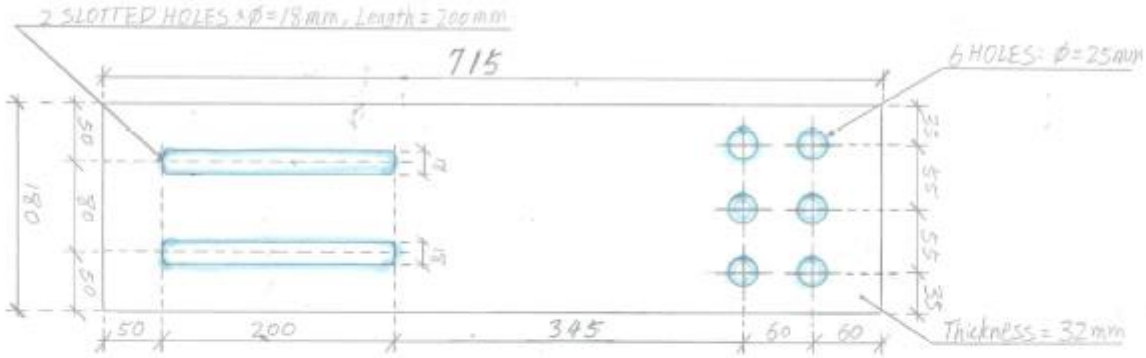

Component	Thickness	Strength	Quantity
SLOTTED PLATE	32 mm	G300	2

DRAWING A

UNIVERSITY OF CANTERBURY	
SLOTTED PLATE	
DESIGNERS: MACRAE ; CHANGHI ; XIE	
SCALE: 1:5	DATE: 23/06/2013

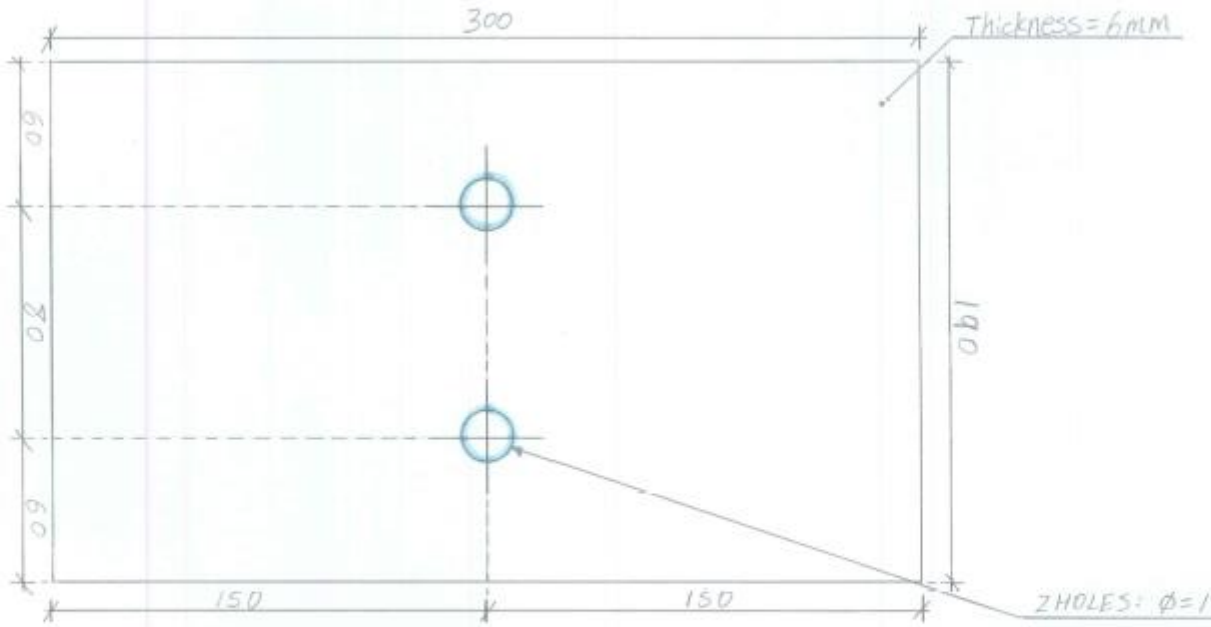

Component	Thickness	Strength	Quantity
SHIM	6 mm	BISALLOY 300	8

DRAWING H

UNIVERSITY OF CANTERBURY	
SHIM	
DESIGNERS: MACRAE; CHANCHI; XIE	
SCALE: 1:2	DATE: 23/06/2015

V. BOLTS

Item	Component	Diameter (mm)	Nominal Length (mm)	Grade	Quantity	Type
5.1	M24X150	24	150	8.8	10	Galvanised
5.2	M24X120	24	120	8.8	40	Galvanised
5.3	M24X110	24	110	8.8	30	Galvanised
5.4	M24X90	24	90	8.8	25	Galvanised
5.5	M24X80	24	80	8.8	30	Galvanised
5.6	M16X130	24	130	8.8	20	Galvanised

VI. WASHERS & NUTS

Item	Component	Size (mm)	Grade	Quantity	Type
6.1	Flat Washers	M24	8.8	150	Galvanised
6.2	Flat Washers	M16	8.8	30	Galvanised
6.3	Structural Washers	M24	8.8	150	Galvanised
6.4	Structural Washers	M16	8.8	30	Galvanised
6.5	Nuts	M24	8.8	150	Galvanised
6.6	Nuts	M16	8.8	30	Galvanised
6.7	Belleville Washers	M16	8.8	30	Galvanised

DEPARTMENT OF CIVIL AND NATURAL RESOURCES ENGINEERING

UNIVERSITY OF CANTERBURY

Materials Request – SFC

Submitted to: Stuart Tose

Designers: Robin Xie

Associate Professor Greg MacRae

Jose Chanchi

22nd September 2014

I. SHAPED PLATES

Item	Components	Geometry	Quantity	Grade	See Drawing
1.1	Gusset 2	PL 345X324X32*	2	300	A

* *For specific dimensions, please refer to the corresponding drawing.*

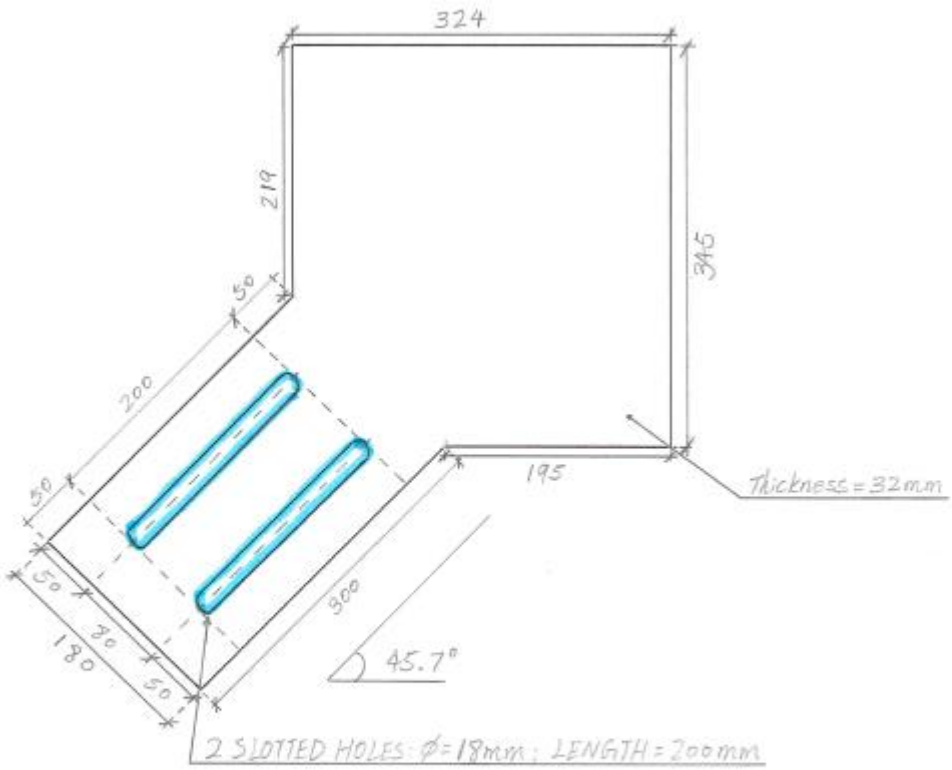

DRAWING A

Component	Thickness	Strength	Quantity
GUSSET PLATE 2	32mm	G300	2

UNIVERSITY OF CANTERBURY	
GUSSET PLATE 2	
DESIGNERS: XIE, MACRAE, CHANCHI	
SCALE: 1:5	DATE: 10/09/2014

II. PLATES

Item	Components	Geometry (mm)	Quantity	Grade	See Drawing
2.1	Plate 4	PL 400X210X32	2	300	B
2.2	Plate 5	PL 360X210X32	2	300	C
2.3	Packing Plate	PL 300X200X3	2	300	D
2.4	Bearing Plate	PL 300X200X16	2	300	E

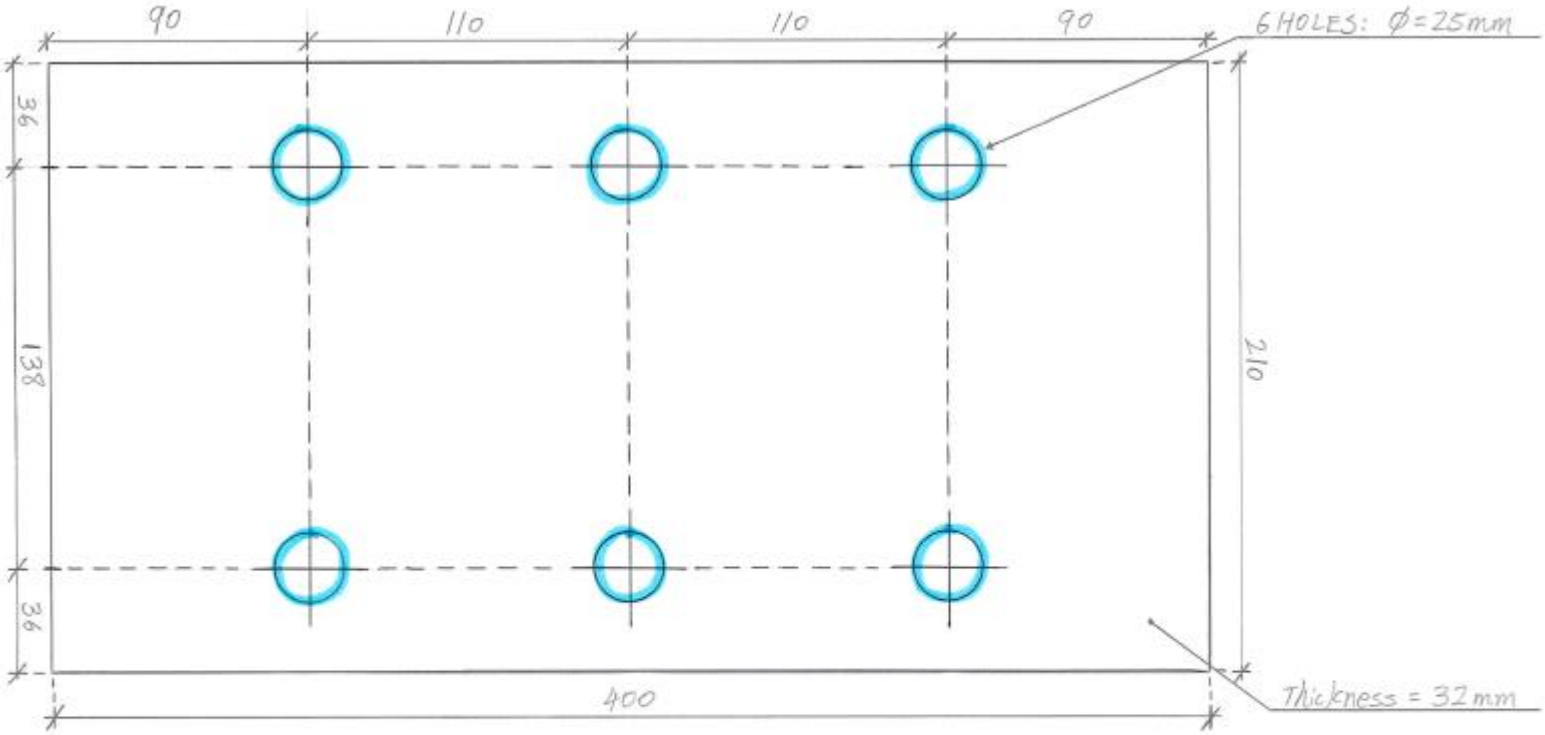

Component	Thickness	Strength	Quantity
PLATE 4	32mm	G300	2

DRAWING B

University Of Canterbury	
PLATE 4	
Designers: XIE; MACRAE; CHANCHI	
Scale: 1:2	Date: 10/09/14

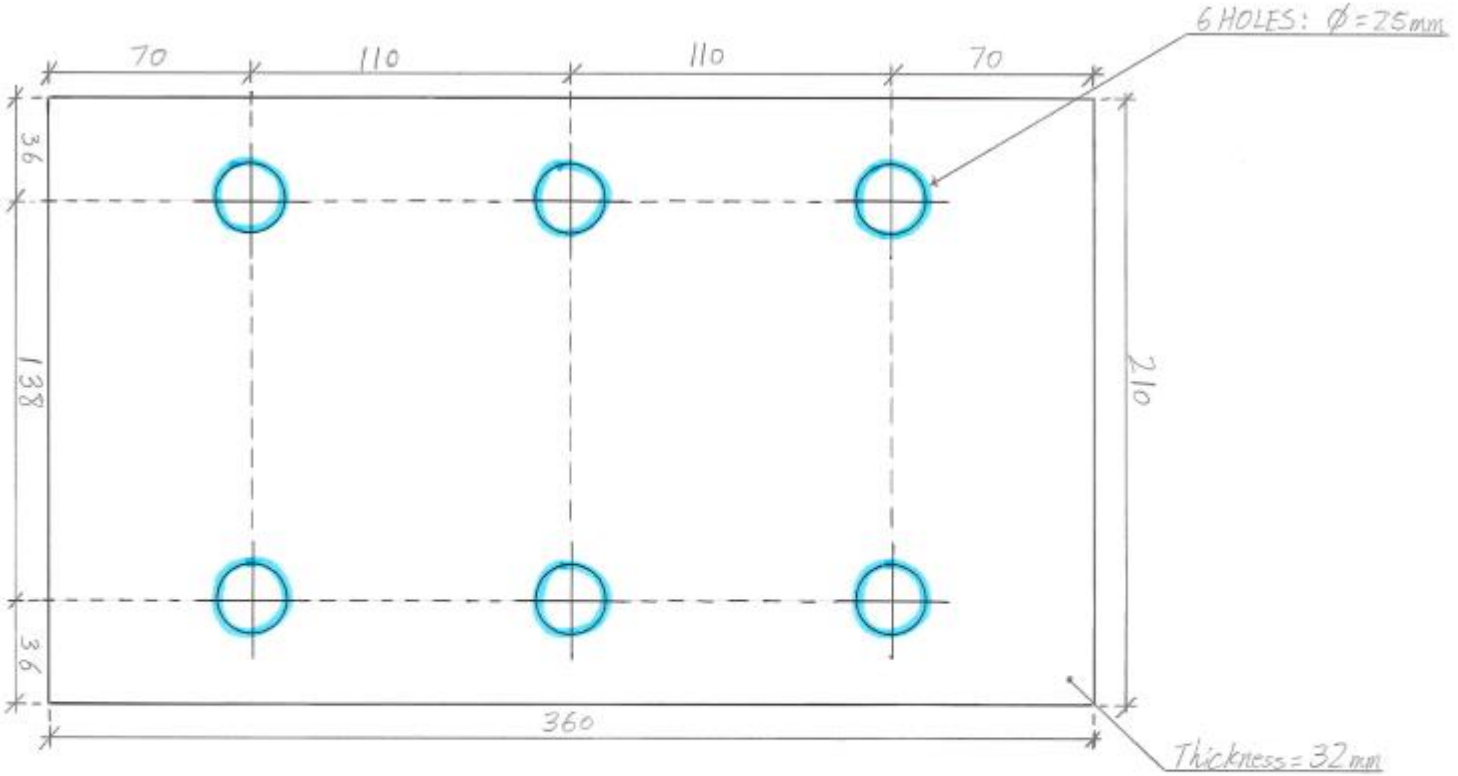

Component	Thickness	Strength	Quantity
PLATE 5	32 mm	G300	2

DRAWING C

University Of Canterbury	
PLATE 5	
Designers: YIE, MACRAE, CHANCHI	
Scale: 1:2	Date: 10/09/2014

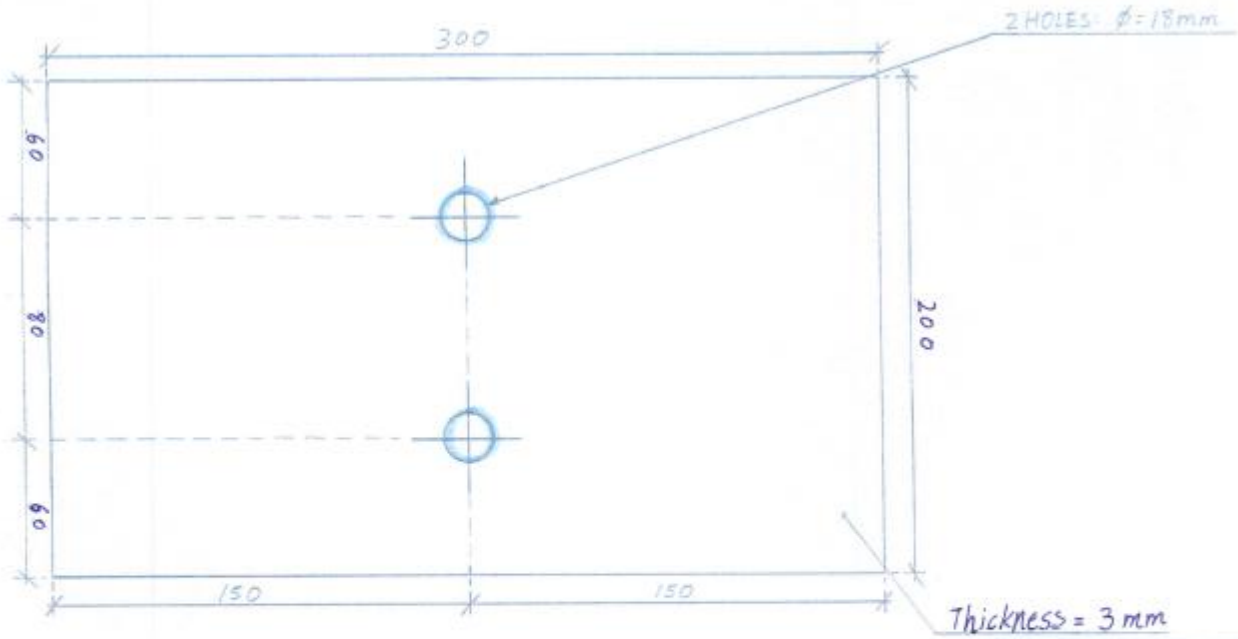

Component	Thickness	Strength	Quantity
PACKING PLATE	3 mm	G300	2

DRAWING D

DRAWING D

UNIVERSITY OF CANTERBURY

BEARING PLATE

DESIGNERS: MACRAE ; CHANGHI ; XIE

SCALE: 1:2

DATE: 25/06/2013

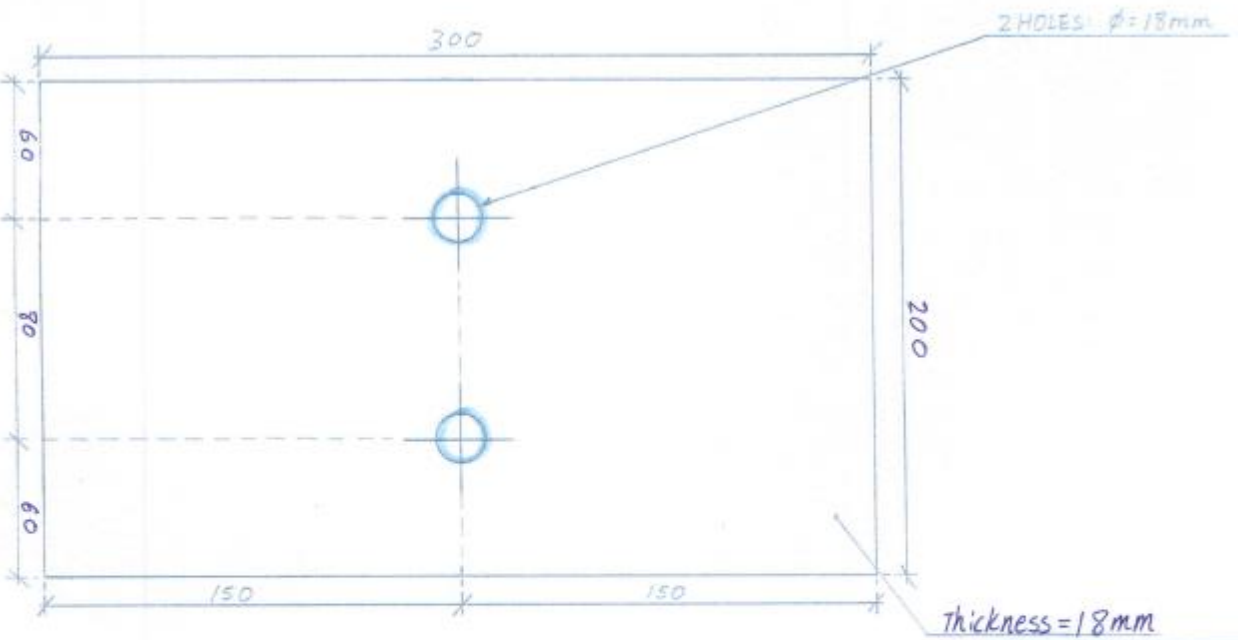

Component	Thickness	Strength	Quantity
BEARING PLATE	16 mm	G300	2

DRAWING E

DRAWING E

UNIVERSITY OF CANTERBURY

BEARING PLATE

DESIGNERS: MACRAE ; CHANCHI ; XIE

SCALE: 1:2

DATE: 23/06/2013

III. BRACE PROFILE

Item	Components	Geometry (mm)	Quantity	Grade	See Drawing
3.1	Channel	250PFC Length = 3500mm	2	300	F
3.2	Rectangular Hollow Section	RHS 100X50X3 Length = 1000mm	1	300	G

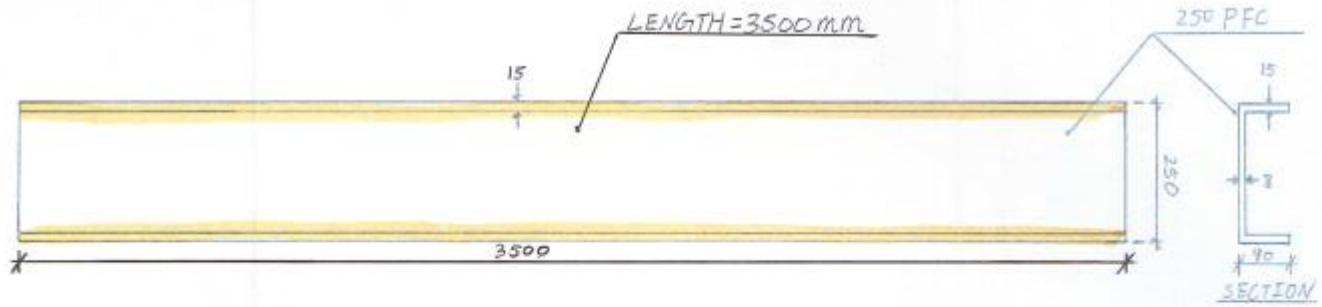

Component	Profile	Strength	Quantity
CHANNEL	250PFC	G300	2

DRAWING F

DRAWING F

UNIVERSITY OF CANTERBURY

CHANNEL

DESIGNERS: MACRAE; CHANCHI; XIE

SCALE: 1:10

DATE: 29/06/2013

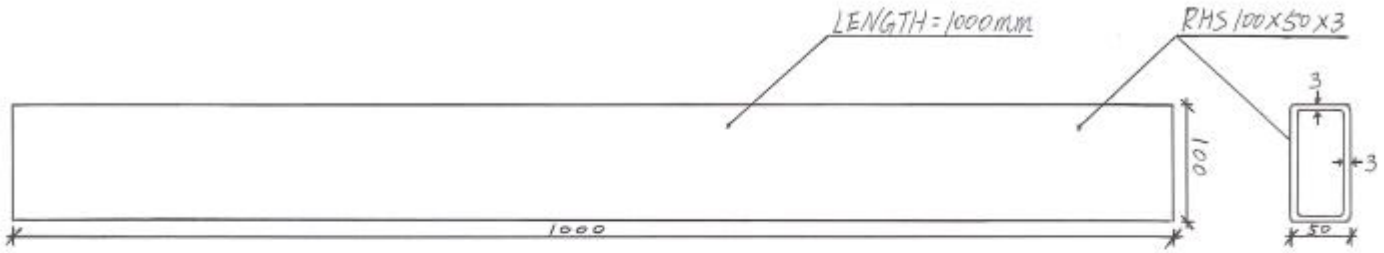

Component	Profile	Strength	Quantity
RHS	RHS 100x50x3	G300	1

DRAWING G!

University Of Canterbury	
Rectangular Hollow Section	
Designers: XIE; MACRAE; CHANCHI	
Scale: 1:5	Date: 10/09/14

IV. SUMMARY

Item	Components	Geometry	Quantity	Grade	See Drawing
1.1	Gusset 2	PL 345X324X32*	2	300	A
2.1	Plate 4	PL 400X210X32	2	300	B
2.2	Plate 5	PL 360X210X32	2	300	C
2.3	Packing Plate	PL 300X200X3	2	300	D
2.4	Bearing Plate	PL 300X200X16	2	300	E
3.1	Channel	250PFC Length = 3500mm	2	300	F
3.2	Rectangular Hollow Section	RHS 100X50X3 Length = 1000mm	1	300	G

APPENDIX C. AFC brace test setup

This appendix contains an illustration of the proposed testing setup for the AFC brace tests. This document was submitted to Mosese Fifita at the University of Canterbury Structures Laboratory.

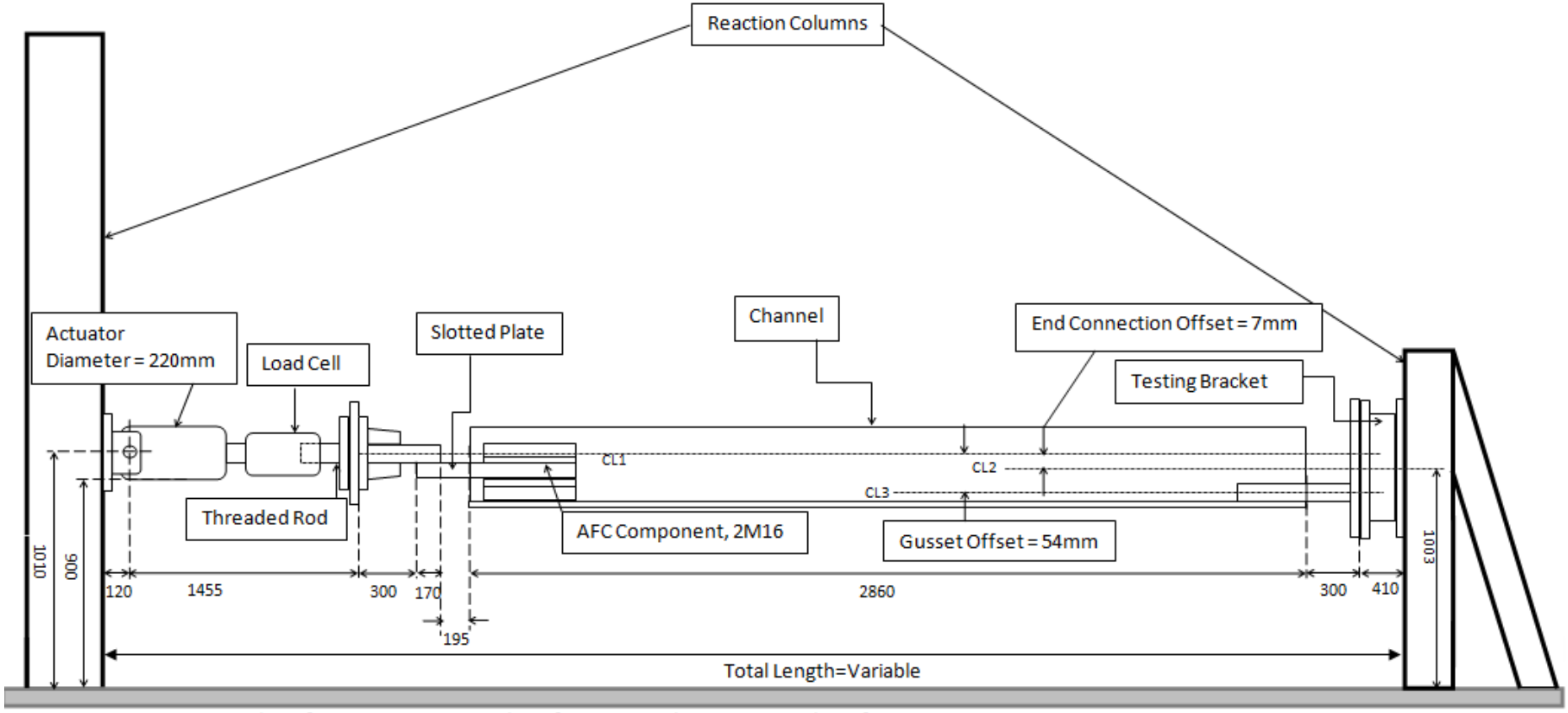

CL1=Centerline of Actuator; CL2=Centerline of Testing Bracket; CL3=Centerline of RHS Gusset

Ground anchor bolts strength check:

Maximum Tensile Force Per Bolt=100kN; N=10 Bolts

Shear Capacity=0.8*0.62*Tensile Capacity

Shear Capacity=0.8*0.62*100kN=49.6kN;

Total Shear Capacity=49.6*10=496kN > 300kN OK

APPENDIX D. Source code for the *AFC* numerical model

This appendix contains the source code that constructs the numerical *AFC* uniaxial model. The source code was completed with assistance provided by T.L. Chang from the University of Canterbury. This hysteresis model has been fully implemented into suanPan [2019], and it can also be used on the OpenSees platform.

APPENDIX D-1. AFCN.h

```
#pragma once
#include "UniaxialMaterial.h"
#include <array>

using std::array;

struct DataAFC {
      const double elastic_modulus;
      const double t_yield_stress;
      const double t_hardening;
      const double t_unloading;
      const double c_yield_stress;
      const double c_hardening;
      const double c_unloading;
      const double t_yield_strain = t_yield_stress / elastic_modulus;
      const double c_yield_strain = c_yield_stress / elastic_modulus;
};

class AFCN final : DataAFC, public UniaxialMaterial {
      double current_stiffness = elastic_modulus, trial_stiffness =
elastic_modulus;

      double current_strain = 0., trial_strain = 0.;
      double current_stress = 0., trial_stress = 0.;
      array<double, 7> current_history{0., 0., 0., 0., 0., 0., 0.},
trial_history{0., 0., 0., 0., 0., 0., 0.};

      static void compute_transition(double&, double&, double, double,
double, double, double, double, double);
      void compute_degradation(double, double);
public:
      AFCN(int,    // unique tag
           double, // elastic modulus
           double, // tension yield stress
           double, // tension hardening modulus
           double, // tension unloading modulus
           double, // compression yield stress
           double, // compression hardening modulus
           double, // compression unloading modulus
      );
      AFCN(const AFCN&) = default;
      AFCN(AFCN&&) = delete;
      AFCN& operator=(const AFCN&) = delete;
      AFCN& operator=(AFCN&&) = delete;
      ~AFCN() = default;

      int setTrialStrain(double, double) override;
      double getStrain() override;
      double getStress() override;
      double getTangent() override;
      double getInitialTangent() override;

      int commitState() override;
      int revertToLastCommit() override;
      int revertToStart() override;
```

```
        UniaxialMaterial* getCopy() override;

        int sendSelf(int, Channel&) override;
        int recvSelf(int, Channel&, FEM_ObjectBroker&) override;

        void Print(OPS_Stream&, int) override;
};
```

APPENDIX D-2. AFCN.cpp

```
#include "AFCN.h"
#include "elementAPI.h"
#include "OPS_Globals.h"

extern "C" _declspec(dllexport) void* OPS_AFCN() {
	int tag, num;
	double prop[8];
	num = 1;
	if(OPS_GetIntInput(&num, &tag) != 0) return nullptr;

	num = 8;
	if(OPS_GetDoubleInput(&num, prop) != 0) return nullptr;

	return new AFCN(tag, prop[0], prop[1], prop[2], prop[3], prop[4],
prop[5], prop[6], prop[7]);
}

void AFCN::compute_transition(double& TY, double& TS, const double TX,
const double XS, const double YS, const double ES, const double XF,
const double YF, const double EF) {
	if(fabs(TX - XS) <= DBL_EPSILON) {
		TY = YS;
		TS = ES;
	}

	if(fabs(TX - XF) <= DBL_EPSILON) {
		TY = YF;
		TS = EF;
	}

	const auto TA = XF - XS;
	const auto TC = TX - XS;
	const auto ESEC = (YF - YS) / TA;
	const auto TB = ESEC - ES;
	const auto R = (EF - ESEC) / TB;
	const auto TD = TB * pow(std::max(fabs(TC / TA), DBL_EPSILON),
R);

	TY = YS + TC * (ES + TD);
	TS = ES + (R + 1.) * TD;
}

void AFCN::compute_degradation(const double yield_strain, const double
stiffness) {
	auto& max_strain = trial_history[1];
	const auto& s_strain = trial_history[3];
	const auto& s_stress = trial_history[4];
	const auto& e_strain = trial_history[5]; // limit strain
	const auto& e_stress = trial_history[6]; // limit stress

	if(degrade == 0.) {
		trial_stiffness = (e_stress - s_stress) / (e_strain -
s_strain);
		trial_stress = s_stress + trial_stiffness * (trial_strain -
s_strain);
```

```
	} else {
		max_strain = std::max(std::max(fabs(trial_strain),
fabs(e_strain)), max_strain);

		const auto factor = .9 * exp(-degrade * max_strain /
fabs(yield_strain));
		const auto s_stiffness = factor * elastic_modulus;
		const auto e_stiffness = stiffness - factor * (stiffness -
elastic_modulus);

		compute_transition(trial_stress, trial_stiffness,
trial_strain, s_strain, s_stress, s_stiffness, e_strain, e_stress,
e_stiffness);
	}
}

AFCN::AFCN(const int T, const double E, const double TYS, const double
THK, const double TUK, const double CYS, const double CHK, const double
CUK, const double DG)
	: DataAFC{fabs(E), fabs(TYS), fabs(THK), fabs(TUK), fabs(CYS),
fabs(CHK), fabs(CUK), fabs(DG)}
	, UniaxialMaterial(T, 0) {}

int AFCN::setTrialStrain(const double t_strain, const double) {
	const auto i_strain = (trial_strain = t_strain) - current_strain;

	if(fabs(i_strain) <= DBL_EPSILON) return 0;

	trial_history = current_history;
	auto& load_sign = trial_history[0];
	auto& r_strain = trial_history[2];
	auto& s_strain = trial_history[3];
	auto& s_stress = trial_history[4];
	auto& e_strain = trial_history[5]; // limit strain
	auto& e_stress = trial_history[6]; // limit stress

	if(current_stress >= 0.)
		if(i_strain >= 0.) {
			if(load_sign <= 0.) {
				s_strain = current_strain, s_stress =
current_stress;
				e_strain = s_strain + ((s_strain -
t_yield_strain) * t_hardening + t_yield_stress - s_stress) /
(elastic_modulus - t_hardening);
				e_stress = (e_strain - t_yield_strain) *
t_hardening + t_yield_stress;
			}
			if(trial_strain < e_strain)
compute_degradation(t_yield_strain, t_unloading);
			else trial_stress = (trial_strain - e_strain) *
(trial_stiffness = t_hardening) + e_stress;
		} else {
			if(load_sign > 0.) r_strain = current_strain -
current_stress / t_unloading;
			if(trial_strain >= r_strain) trial_stress =
current_stress + i_strain * (trial_stiffness = t_unloading);
			else {
				s_strain = r_strain, s_stress = 0.;
```

```
                        e_strain = s_strain + ((s_strain +
c_yield_strain) * c_hardening - c_yield_stress) / (elastic_modulus -
c_hardening);
                        e_stress = (e_strain + c_yield_strain) *
c_hardening - c_yield_stress;
                        if(trial_strain > e_strain)
compute_degradation(c_yield_strain, c_unloading);
                        else trial_stress = (trial_strain - e_strain) *
(trial_stiffness = c_hardening) + e_stress;
                  }
            }
      else if(i_strain <= 0.) {
            if(load_sign >= 0.) {
                  s_strain = current_strain, s_stress = current_stress;
                  e_strain = s_strain + ((s_strain + c_yield_strain) *
c_hardening - c_yield_stress - s_stress) / (elastic_modulus -
c_hardening);
                  e_stress = (e_strain + c_yield_strain) * c_hardening -
c_yield_stress;
            }
            if(trial_strain > e_strain)
compute_degradation(c_yield_strain, c_unloading);
            else trial_stress = (trial_strain - e_strain) *
(trial_stiffness = c_hardening) + e_stress;
      } else {
            if(load_sign < 0.) r_strain = current_strain -
current_stress / c_unloading;
            if(trial_strain <= r_strain) trial_stress = current_stress +
i_strain * (trial_stiffness = c_unloading);
            else {
                  s_strain = r_strain, s_stress = 0.;
                  e_strain = s_strain + ((s_strain - t_yield_strain) *
t_hardening + t_yield_stress) / (elastic_modulus - t_hardening);
                  e_stress = (e_strain - t_yield_strain) * t_hardening +
t_yield_stress;
                  if(trial_strain < e_strain)
compute_degradation(t_yield_strain, t_unloading);
                  else trial_stress = (trial_strain - e_strain) *
(trial_stiffness = t_hardening) + e_stress;
            }
      }

      load_sign = i_strain > 0. ? 1. : -1.;

      return 0.;
}

double AFCN::getStrain() { return trial_strain; }

double AFCN::getStress() { return trial_stress; }

double AFCN::getTangent() { return trial_stiffness; }

double AFCN::getInitialTangent() { return elastic_modulus; }

int AFCN::commitState() {
      current_strain = trial_strain;
      current_stress = trial_stress;
```

```
      current_stiffness = trial_stiffness;
      current_history = trial_history;
      return 0;
}

int AFCN::revertToLastCommit() {
      trial_strain = current_strain;
      trial_stress = current_stress;
      trial_stiffness = current_stiffness;
      trial_history = current_history;
      return 0;
}

int AFCN::revertToStart() {
      trial_strain = current_strain = 0.;
      trial_stress = current_stress = 0.;
      trial_stiffness = current_stiffness = elastic_modulus;
      trial_history = current_history = {0., 0., 0., 0., 0., 0., 0.};
      return 0;
}

UniaxialMaterial* AFCN::getCopy() { return new AFCN(*this); }

int AFCN::sendSelf(int, Channel&) { throw; }

int AFCN::recvSelf(int, Channel&, FEM_ObjectBroker&) { throw; }

void AFCN::Print(OPS_Stream& OUT, int) { OUT << "Test\n"; }
```

APPENDIX E. Codes for the parametric studies on the impact of viscous damper sub-system flexibility using ground motion records

This appendix contains the OpenSees and Matlab codes to run the ground motion simulations described in Chapter 4. The OpenSees code is an example model using a period of 0.25s and a damper-subsystem to main structure ratio of 200. The Matlab codes provided is an example file that used to run one of the CHCH records provided by Yeow *et al.*, [2018].

APPENDIX E-1. OpenSees model

```
wipe

model BasicBuilder -ndm 2 -ndf 2

set Output T_0p25;
file mkdir $Output;

source DynInput.tcl;

#build model

node 1 0 0
node 2 0 0
fix 1 1 1
fix 2 0 1

set g 9810.; #mm/sec^2
set m 100.;
mass  2 $m 0.

set pi [expr acos(-1.0)];

#set damper parameters
set Ci 251.33; #kNs/mm
set ai 1;
set ad 0.2;

#set the structural properties
set Tn 0.25; #sec
set Es [expr pow(2*$pi/$Tn,2)*$m]; #KN/mm
set Cc [expr 2*pow($Es*$m,0.5)];
set ID [expr $Ci/$Cc];

#create structural material
uniaxialMaterial Elastic 1 $Es

#create structural element
element zeroLength 1 1 2 -mat 1 -dir 1

#create spring material
#set elastic damper spring
set Ed [expr $Es*200]; #kN/mm

#create ViscousDamper material with Spring
#uniaxialMaterial ViscousDamper $matTag $Ed $Cd $ad
uniaxialMaterial ViscousDamper 2 $Ed $Cd $ad

#create VD element using ZeroLength
element zeroLength 2 1 2 -mat 2 -dir 1

#create inherent damper
#uniaxialMaterial Viscous $matTag $Cd $ai
uniaxialMaterial Viscous 3 $Ci $ai

#create inherent damping element
```

```
element zeroLength 3 1 2 -mat 3 -dir 1

puts "Model Built"

#timeSeries Path $tsTag -dt (second/step) -filePath (fileName) -factor
(g amplifier)
timeSeries Path 1 -dt $dtx -filePath $outfilex -factor [expr $g];

pattern UniformExcitation 1 1 -accel 1

recorder Node -file $Output/DispKd200Ks$num$outfilex -time -node 2 -dof
1 disp;
recorder Node -file $Output/BSKd200Ks$num$outfilex -time -node 1 -dof 1
reaction;

set f [expr 100];
set dx [expr $dtx/$f];
set y [expr $NPTSx*$f];

wipeAnalysis;
constraints Transformation;
numberer RCM;
system UmfPack;
test EnergyIncr 1.0e-10 100 ;
algorithm  KrylovNewton;
integrator Newmark 0.5 0.25 ;
analysis Transient;
analyze $y $dx

puts "Complete"
wipe
```

APPENDIX E-2. Matlab file

```
clear all; close all; clc
fclose('all');

alpha = 0.2;
Tn = 0.25;
mass = 100;

% Damping coefficient to achieve 40% damping ratio

c = 81610;

% Call ground motion record

k = 6;
i = 10;
j = 2;

l=num2str(k); m=num2str(j); n=num2str(i);
name=strcat('CHCH2p0_',l,'_',n,'_',m,'.txt');
name2=strcat('CHCH2p0_',l,'_',n,'_',m,'.out');
rec1=textread(name,'%s','headerlines',3);
DT1=str2num(rec1{2});
NSPT1=str2num(rec1{1});
rec1=textread(name,'%f','headerlines',4);
fileID = fopen(name2,'w');
fprintf(fileID,' %f\n',rec1(:,1));

% Divide target damping coefficient into 50 increments

incr = c/50;

A = [incr:incr:c];

zeltaI = zeros(1,length(A));

for zd = 1:length(A)

    cd = A(zd);

    count = zd;

    % Input ground motion record and damping coefficient into OpenSees

    fid = fopen('DynInput.tcl', 'w');
    fprintf(fid,'%s','set outfilex ');
    fprintf(fid,'%s\n',name2);

    fprintf(fid,'%s','set NPTSx ');
    fprintf(fid,'%.0f\n',NSPT1);

    fprintf(fid,'%s','set dtx ');
    fprintf(fid,'%f\n',DT1);

    fprintf(fid,'%s','set Cd ');
    fprintf(fid,'%f\n',cd);
```

```
    fprintf(fid,'%s','set num ');
    fprintf(fid,'%.0f\n',count);

    !OpenSees.exe "NLDamper".tcl

    %Calculate damping ratio using the Pekcan et al.,[1999] method

    kfact = 1/(1+alpha);
    uI = num2str(count);
    DispI =
load(['D:\T_0p25\DispKd200Ks',uI,'CHCH2p0_',l,'_',n,'_',m,'.out']);
    DispMI = DispI(:,2);
    x0I = max(abs(DispMI));
    upI = cd*(x0I^(alpha-1))*(Tn^(2-alpha));
    botI = ((2*pi())^(2-alpha))*mass;
    zeltaI(zd) = kfact*upI/botI;

end
```

APPENDIX F. Support parametric studies and analysis using the Chapter 4 SDOF model

APPENDIX F-1. Impact of sub-system flexibility on the phasing of viscous damper

This study is to observe the displacement time-history of the structural element, spring and dashpot at various K_d, and how the behaviour of the viscous damper changes at different spring stiffness. Analysis is carried out for a range of K_d values from 1 to 200000 kN/mm. Damping ratio and natural period are set to 20% and 3 seconds, respectively, as these are common values in design practices. The acceleration protocol is shown in Figure 1a with the maximum acceleration set to be approximately 0.06g. Analysis is run for 20 seconds. The model is excited using the protocol for the first eight seconds and it vibrates freely for the remaining 12 seconds.

For a very soft spring where K_d = 1 kN/mm, the out-of-phasing between the damper and the structural element is at maximum. This can be seen from figure 1b where the spring displacements over time overlaps with structural displacements, whereas the damper barely deforms. The damper-structural out-of-phasing reduces with increasing K_d but the spring is no longer in phase with the structural element (Figure 1c). When the spring is very stiff (K_d = 20000 kN/mm), the damper is completely in phase with the structural element and the spring barely deforms (Figure 1d).

Figure 1e plots the time when each system component passes the location of zero displacement after the maximum acceleration is applied (the 8th time where the displacement curve intersects the horizontal axis). The plot shows results for K_d =1 to 4000 kN/mm and it is consistent with Figure 1b - c. It shows the system is more sensitive to the change of K_d when K_d is smaller than approximately 250 kN/mm. The sensitivity reduces as K_d increases beyond 250 kN/mm and it becomes insignificant when K_d is higher than 2000 kN/mm.

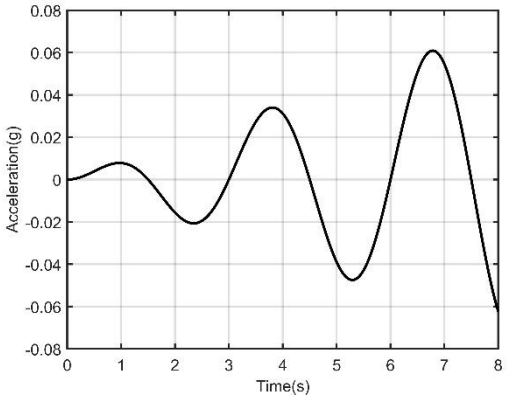

a. Acceleration protocol

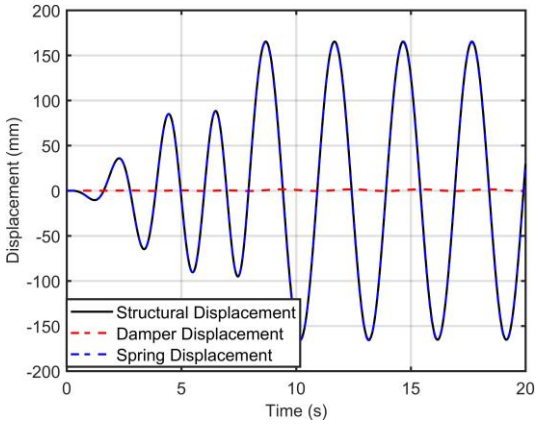

b. Displacement time-history at K_d = 1 kN/mm

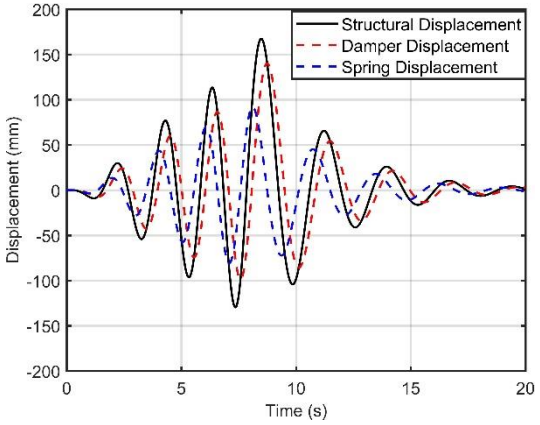

c. Displacement time-history at K_d = 300 kN/mm

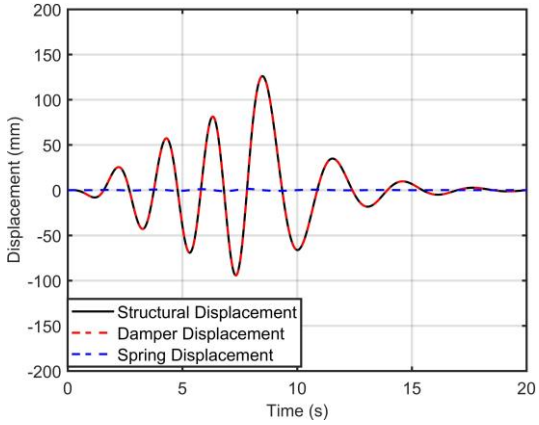

d. Displacement time-history at K_d = 20000 kN/mm

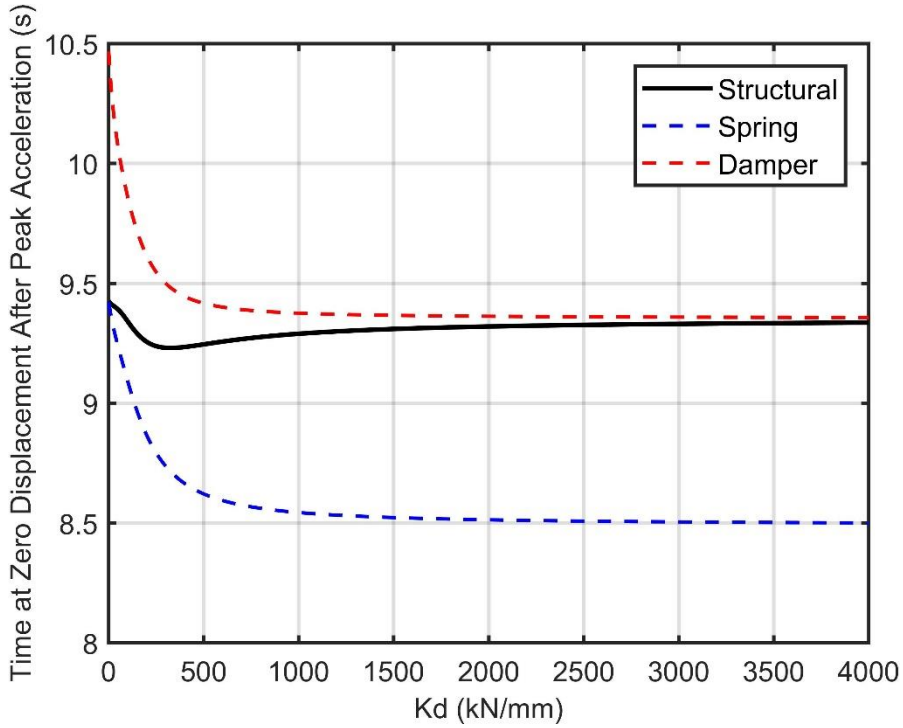

e. Zero displacement time for each element at various K_d values.

Figure 1. Displacement time-history responses under sinusoidal acceleration

The plots below (Figure 2) show the maximum displacements of the three elements at different K_d values. Same as above, 40% damping ratio is chosen and the system natural period is set to three seconds. Figure 1a is used as the acceleration protocol, and the maximum acceleration for each analysis is set to approximately 0.06g. As a part of the parametric studies, different acceleration frequencies (f) and natural periods for the structural element (T_n) are used. It is worth noting for the figures below, that the maximum displacements of the damper and the spring do not necessarily add up to that of the structural element due to out-of-phasing.

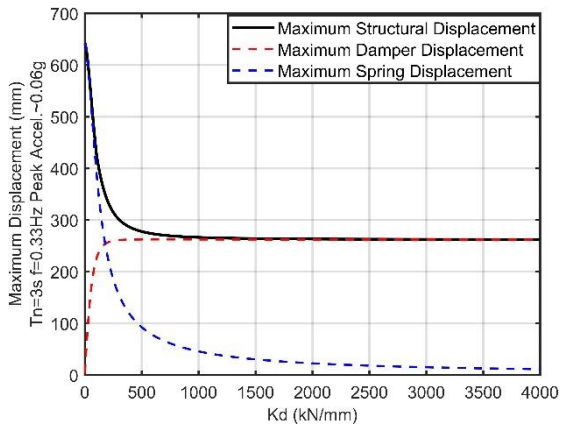

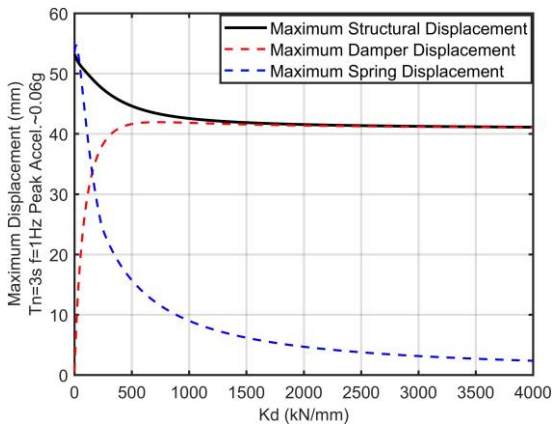

a. Maximum displacements at T_n = 3 s and f = 0.33 Hz

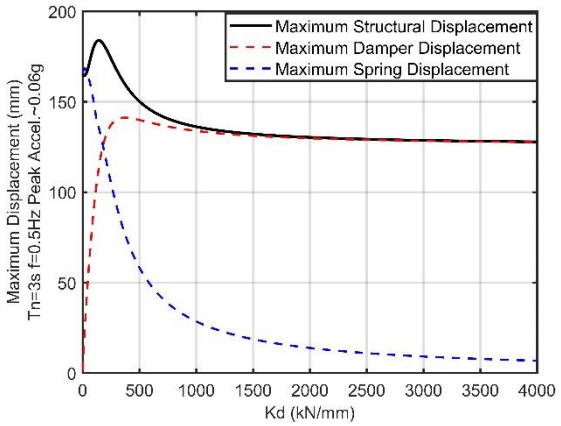

b. Maximum displacements at T_n = 3 s and f = 1 Hz

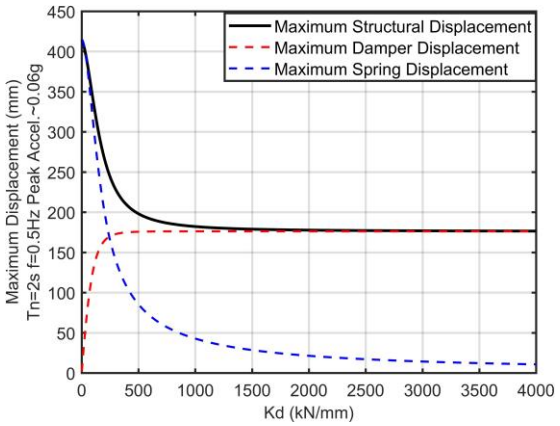

c. Maximum displacements at T_n = 3 s and f = 0.5 Hz

d. Maximum displacements at T_n = 2 s and f = 0.5 Hz

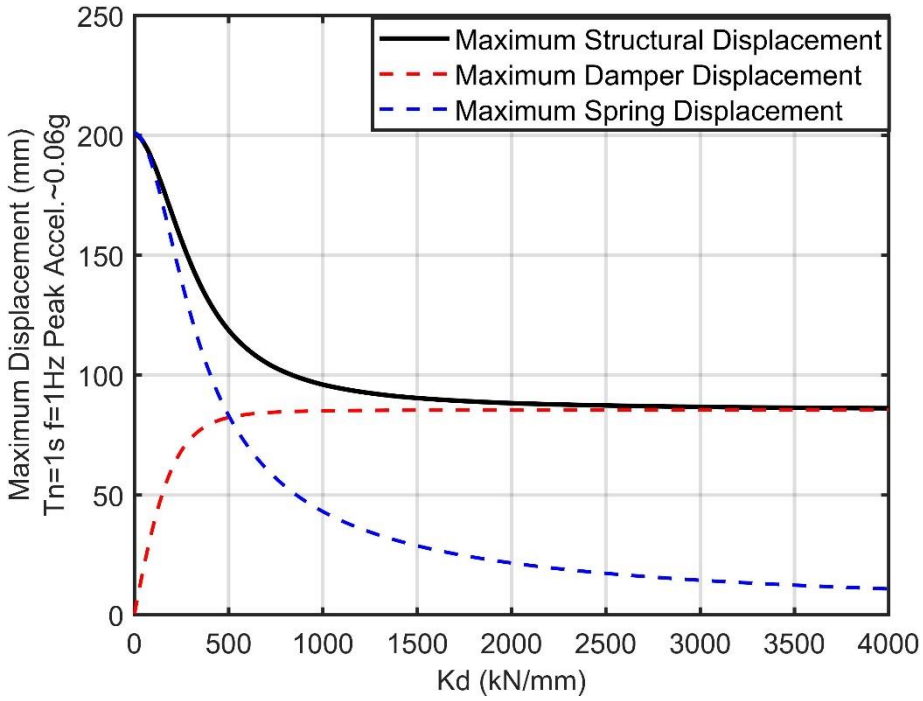

e. Maximum displacements at T_n = 1 s and f = 1 Hz

Figure 2. Maximum displacements of each component obtained from the corresponding displacement time-history response

APPENDIX F-2. Validation of the Chapter 4 SDOF model using a CHCH ground motion record

The SDOF model is tested using a ground motion acceleration input as shown in figure 42. The region of the ground motion is Christchurch (subsoil class D) with a hazard level of 6 [Yeow *et al.*, 2018]. The damping ratio of the model is set to 20% with a period of 3 seconds. The force-displacement hysteresis response of the viscous damper element is shown in Figure 3. The hysteresis loops are almost oval, and they follow the same principle rules for a linear damper as shown in Figure 1-14. This result confirms the SDOF model behaves stably when it is subject to ground motion accelerations.

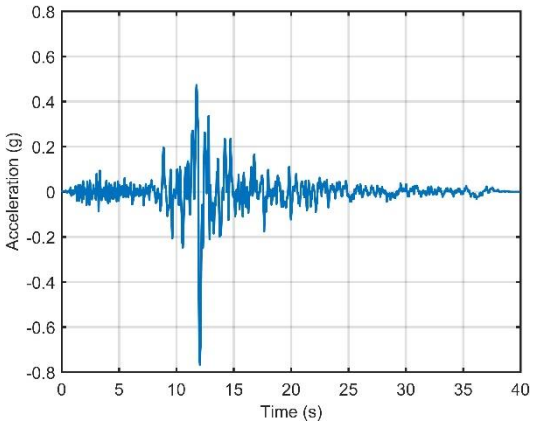

a. Ground motion acceleration

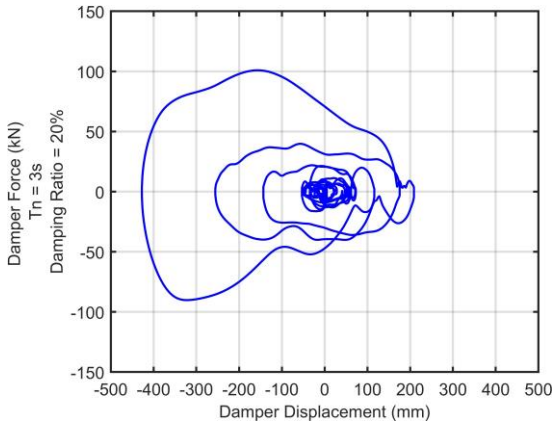

b. Viscous damper hysteresis response under ground motion

Figure 3. Validation of the Chapter 4 SDOF model using a ground motion record

APPENDIX G. Detailed hand calculations for single storey viscous damper frame design example

The hand calculation script in the following pages are an example of the design consideration highlighted in Section 4.5.3 where the lateral damper sub-system to primary structure stiffness ratio should be considered. More background of the calculations can be found in Section 4.5.3.1.